Segregating neuronal and glial membrane injury in an anti-GM1 antibody-mediated neuropathy

Clare Ile Campbell BSc (Hons)

A thesis submitted in fulfilment of the requirements of the University of Glasgow for the degree of Doctor of Philosophy

Institute of Infection, Immunity, and Inflammation

College of Medical, Veterinary and Life Sciences

University of Glasgow

December 2021

Abstract

Guillain-Barré syndrome is a post-infectious autoimmune disorder affecting the peripheral nervous system. Broadly, it presents as acute motor axonal neuropathy (AMAN) and acute inflammatory demyelinating polyneuropathy (AIDP). Although segmental demyelination is the predominant characteristic of AIDP, secondary bystander axonal injury can occur and is associated with poor prognosis. The pathogenesis of AIDP and secondary bystander axonal injury are poorly understood in comparison to the established mechanisms involved in primary axonal degeneration in AMAN. The most common preceding infection is with *Campylobacter jejuni* which is associated with anti-GM1 ganglioside autoantibodies. GM1 antibodies primarily bind to the motor axolemma but have also been demonstrated to bind to the paranodal Schwann cell loops. It is currently unknown whether the pathological phenotype mediated by anti-GM1 antibodies arises from injury to one or other, or both membranes in AMAN and AIDP. Current animal models are unable to segregate primary injury from the consequences of cell-specific membrane injury because GM1 is expressed on both neural membranes. To address this, we used *GalNAc-T$^{-/-}$-Tg(neuronal)* and *GalNAc-T$^{-/-}$-Tg(glial)* mice to selectively target the axonal and glial membrane, respectively, with a single anti-GM1 antibody. We investigated the effects of complement-mediated injury at the distal motor neuromuscular junction (NMJ) and distal node of Ranvier (NoR). Results demonstrated that injury to the axonal membrane in *GalNAc-T$^{-/-}$-Tg(neuronal)* mice resulted in a significant reduction of axonal integrity at the NMJ and disruption to voltage gated sodium channels at the NoR. In contrast, it was established that targeted injury to the glial membrane caused significant impairment to the axo-glial junction at the paranode, resulting in disruption to the paranodal loops. Complement inhibition attenuated injury to the paranodal loops, suggesting that targeting the complement pathway therapeutically would be effective in treating demyelinating neuropathies. Furthermore, targeted injury to the glial membrane subsequently led to secondary injury to the axon at the distal NoR. Overall, these transgenic mice offer many potential roles in the investigation of anti-ganglioside antibody mediated binding and injury at specific membrane sites; particularly to study the downstream mechanism(s) of primary and secondary axonal degeneration to help inform the development of targeted treatments.

Dedication

I dedicate this thesis to all the experimental animals used throughout this thesis.

Monument to the laboratory mouse **-** Siberia, Russia.

Acknowledgement

I would first like to thank my supervisor, Professor Hugh Willison for believing in me and giving me this incredible opportunity. I have learned and grown so much as a scientific researcher throughout these last 4 years. Thank you for all of your time, patience, advice, and encouragement and the use of your incredible analogies to help explain things to me – it is greatly appreciated!
I am extremely grateful to my second supervisor, Dr Rhona McGonigal. I cannot thank you enough for all your support, knowledge, advice, and friendship over the last 4 years. I am so fortunate to have had the privilege to work alongside you and gain my node of Ranvier knowledge from the best expert in the field.

To the incredible team who I've worked alongside for the last 4 years: Jen, aka. lab queen! You really are the fountain of all knowledge. Thank you so much for teaching me all the lab techniques, helping me grow up DG2, performing the electron microscopy processing and analysis (was so worth it for the stunning images), endless advice and always lending an ear when I needed it. Maddy, thank you for always putting a smile on my face and lighting up every room you enter. I am so grateful for all your help, advice and friendship through my PhD and helping me iron out all my problems. Sue, thank you for all your advice on experiments, especially sharing your complement knowledge. Denggao, thank you for all the hard work in keeping our mice in check and the endless amount of PCR that you do. And finally thank you to all previous Willison lab members. In particular, thank you to Amy for welcoming me with open arms. My experience in Genoa at the PNS conference is a memory I will never forget. Thank you to all the staff at the CRF for all the help with the animals and taking such good care of them, it is much appreciated.

I would like to thank Argenx for providing funding for this project and for giving me the opportunity to collaborate with them. Special thanks to Inge Van de Walle for her help and support throughout. All work has been approved by Argenx.

To Colin, I am so grateful that I carried out my PhD alongside you. Thank you for all the laughs and memories over the years... oh, and the constant IT help! It's been greeeaaattt!! What!? To the rest of the Neuro crew (past and present), thank you for getting me through these last 4 years with the hilarious lunch break chats, reciting memes (yes Becky, I'm talking to you.. Oh ya ham!!), sporcles in the office, trips to The Aragon, and the great craic on our nights out. Very fortunate to have made friends for life!

To my incredible family, thank you so much for your endless support and encouragement which you always provide, but especially over these last 4 years. Thank you for engaging with all my chat about nerves and gangliosides and pretending that you were interested! I am so fortunate to have you all by my side and I love you all very much.
To my beautiful niece Rosie, although you don't realise it, your gorgeous smiles and adorable laugh made any work problems/stresses disappear.

Steven a ghràidh, tapadh leat airson an turas seo a ghabhail còmhla rium thairis air na trì bliadhna a dh'fhalbh. Cha phàigh taing thu airson na thug thu dhomh de ghaol 's de thaic, airson na deòir a shuathadh air falbh agus airson gàire a chuir air m' aodann cho tric. Tha gaol agam ort.
Mòran taing Maureen for translating!

Author's Declaration

All experiments are the work of the author unless specifically stated otherwise.

Clare Ile Campbell BSc (Hons)

University of Glasgow

December 2021

Table of Contents

List of Figures and Tables

Figures

Tables

Abbreviations

ACh	acetylcholine
AGAb(s)	anti-ganglioside antibody/antibodies
AIDP	acute inflammatory demyelinating polyneuropathy
AIS	axon initial segment
AMAN	acute motor axonal neuropathy
AMSAN	acute motor and sensory axonal neuropathy
AnkB	ankyrin-B
AnkG	ankyrin-G
BBB	blood-brain barrier
BBE	Bickerstaff brainstem encephalitis
BBG	bovine brain ganglioside
BNB	blood-nerve barrier
BSA	bovine serum albumin
BTx	bungarotoxin
C. jejuni	*Campylobacter jejuni*
CAM	cell adhesion molecules
Caspr	contactin associated protein
CFP	cyan fluorescent protein
CIDP	chronic inflammatory demyelinating polyneuropathy
CMAP	compound muscle action potential
CMV	cytomegalovirus
CNS	central nervous system
CR1	complement receptor type 1
CSF	cerebrospinal fluid
CTB	cholera toxin subunit B
DAF	decay accelerating factor
DML	distal motor latency
DMSO	dimethyl sulfoxide
EAN	experimental allergic neuritis
ECM	extracellular matrix
ELISA	enzyme-linked immunosorbent assay
EtOH	ethanol

FCS	foetal calf serum
Gal-C	galactocerebroside
GalNAc	N-acetylgalactosamine
GalNAc-T	β1-4 N-acetylgalactosaminyltransferase/GalNAc transferase
GBS	Guillain-Barré syndrome
GlcCer	glucosylceramide
Glc-T	glucosyltransferase
H. influenza	*Haemophilus influenza*
IgG	immunoglobulin G
IgM	immunoglobulin M
IP	intraperitoneally
IVIg	intravenous immunoglobulin
IV	intravenously
Kv	voltage-gated potassium channels
LacCer	lactosylceramide
LOS	lipo-oligosaccharide(s)
mAb	monoclonal antibody
MAC	membrane attack complex
MASP	mannan-binding lectin-associated serine proteases
MBL	mannose-binding lectin
MBP	myelin basic protein
MCP	membrane cofactor protein
MFS	Miller Fisher syndrome
MMN	multifocal motor neuropathy
nAChR	nicotinic acetylcholine receptors
Nav	voltage-gated sodium channels
NeuAc	sialic acid
NF186/155/140	neurofascin-186/155/140
NFH	neurofilament heavy
NGS	normal goat serum
NHS	normal human serum
NMJ	neuromuscular junction
NoR	node(s) of Ranvier

NrCAM	neuronal cell adhesion molecule
OD	optical density
pan-Nfasc	pan-neurofascin
PBS	phosphate buffered saline
PE	plasma exchange
PFA	paraformaldehyde
PLP	proteolipid promoter
PNS	peripheral nervous system
pSC	perisynaptic Schwann cell(s)
RCA	regulators of complement activation
RCF	reversible conduction failure
ROI	region of interest
RR	respiratory rate
RT	room temperature
SNAP	sensory nerve action potential
TAG-1	transient axonal glycoprotein-1
TS	triangularis sterni
TV	tidal volume
WBP	whole-body plethysmography

1 Introduction

1.1 Guillain-Barré syndrome

In 1859, the first description of ascending paralysis was published by Jean Baptist Octave Landry (Landry, 1859). However, due to the limitations of definitive diagnostic data in Landry's publication, it is Guillain, Barré and Strohl who are credited with the first description of the disease in 1916 (Guillain et al., 1916), hence the name Guillain-Barré syndrome (GBS). GBS is now recognised as the most common cause of acute peripheral neuropathy worldwide (Goodfellow and Willison, 2016).

The incidence rate of GBS is between 1 and 2 cases per 100,000 people/year. Rate increases with age, with a slightly higher incidence rate in males compared to females (Sejvar et al., 2011). GBS commonly presents clinically with paraesthesia and weakness of the distal limbs. This is accompanied with rapidly progressive ascending paralysis, which is normally symmetrical in pattern. Upon clinical examination, tendon reflexes are usually reduced or absent in the affected limbs. Ascending paralysis can affect the respiratory muscles and approximately 30% of patients require mechanical ventilation (Dhadke et al., 2013). Autonomic dysfunction occurs in up to two-thirds of cases, urinary retention and constipation are rare at the onset, however, they commonly develop at the nadir of the disease (Lehmann et al., 2012). Disease nadir is reached by 4 weeks, and recovery can range from weeks to months, depending on the severity of the disease. Despite the fact most patients make a full recovery, up to 20% of patients remain significantly disabled but a higher proportion of patients have sequelae, including chronic sensory-motor symptoms, pain and fatigue. There is a mortality rate of ~5%, therefore, GBS has significant ramifications to health services worldwide due to its high morbidity and significant mortality (Eldar and Chapman, 2014, Goodfellow and Willison, 2016).

1.1.1 Variants of GBS

GBS was initially believed to be a homogenous syndrome characterised as a demyelinating disorder. With the development of electrodiagnostic equipment and immunological techniques, GBS was found to be a heterogenous disease which can present with varying clinical pathology. Broadly, GBS consists as four main subtypes: acute inflammatory demyelinating polyneuropathy (AIDP); acute motor axonal

neuropathy (AMAN); acute motor and sensory axonal neuropathy (AMSAN) and Miller Fisher syndrome (MFS); however, GBS rarely presents as a 'pure' variant and often presents with varying overlap in clinical features that are typical of other variant forms (reviewed by (Leonhard et al., 2019)).

1.1.1.1 Acute inflammatory demyelinating polyneuropathy

The prime subtype of GBS is AIDP and is the predominant variant across Europe and North America accounting to almost 90% of GBS cases (Hadden et al., 1998, Kaida, 2016). It is characterised pathologically by segmental demyelination with mononuclear cell infiltration (Haymaker and Kebnohan, 1949). Autopsy analysis from patients with AIDP have demonstrated the deposition of complement products on the outer surface of Schwann cells and the presence of macrophages in fibres undergoing extensive demyelination (Asbury et al., 1969, Hafer-Macko et al., 1996b). It is believed that the pathogenesis of AIDP involves the binding of autoantibodies to a yet unidentified antigen located on the surface of Schwann cells, resulting in complement activation (Figure 1.1). The demyelination can be widespread, however, in the early stages it is commonly limited to nerve roots and distal intramuscular nerves where they lie outwith the protection of the blood-nerve barrier (BNB). Long term recovery from AIDP is generally good, due to the plasticity of Schwann cells and their ability to dedifferentiate to a repair phenotype, and remyelinate denuded axons [reviewed by (Nocera and Jacob, 2020)]. However, the axons can become injured as a consequence of acute demyelination and inflammation through unknown mechanisms, termed by-stander injury, and the presence of this secondary axonal degeneration can result in a poor long-term prognosis (Asbury et al., 1969, Feasby et al., 1993).

1.1.1.2 Acute motor axonal neuropathy

In 1986, Feasby and colleagues described cases of axonal degeneration without the presence of demyelination or lymphatic inflammation. They hypothesised that they had discovered a pure axonal variant of GBS (Feasby et al., 1986). This concept was not widely accepted until some years later. A supporting study was published by Yuki and colleagues (1990), reporting 2 patients who had severe acute motor neuropathy with poor recovery, suggestive of axonal loss. Additionally, a study from China was published describing a GBS-like syndrome, predominantly in children, which demonstrated severe motor

neuropathy with preserved sensory nerve action potentials. The authors named this syndrome 'Chinese paralytic syndrome', as it differed to the GBS cases which were described in America and Europe (McKhann et al., 1991). Autopsy results from patients with Chinese paralytic syndrome demonstrated that this was not the typical demyelinating GBS, but instead, found that there was extensive Wallerian-like degeneration of motor axons, and they thereby termed this disease AMAN, an axonal variant of GBS (McKhann et al., 1993). AMAN is more common in East Asia than in Western Countries, accounting to 65% of GBS cases in Northern China alone (Ho et al., 1995). During the large study carried out in China, they found that there was a rise in cases in the summer months, particularly in children from rural areas who lived in close proximity to animals (McKhann et al., 1993). An explanation for this was provided later when AMAN was found to be commonly linked to a preceding bacterial infection found in chickens (Li et al., 1996, Yuki et al., 1990).

The discovery of a 'new' variant of GBS sparked lots of interest, and it was not long before the pathogenesis of this subtype was understood. Antibodies were found in patient serum to ganglioside and ganglioside-like epitopes (McKhann et al., 1991), which are thought to bind to antigens present at the node of Ranvier (NoR) and internodal axolemma of motor fibres, as illustrated in Figure 1.1 (Hafer-Macko et al., 1996a). These antibodies result in complement deposits and infiltration of macrophages into the periaxonal space leading to axonal damage (Griffin et al., 1995). There have been contrasting findings regarding the recovery time in AMAN patients. McKhann (1993) reported the rapid recovery of patients, but on the other hand, Yuki reported the poor recovery of patients with an axonal phenotype (Yuki et al., 1990). In 1998, a unique electrodiagnostic feature of AMAN was discovered – reversible conduction failure (RCF). The authors suggested that this is caused by impaired physiological conduction at the NoR as a result of antibody binding (Ho et al., 1997, Kuwabara et al., 1998), or localised NoR injury caused by antibody and complement activation (Hafer-Macko et al., 1996a). On the other hand, a poor recovery is thought to be due to the progression of the immune reaction, leading to axonal damage and Wallerian-like degeneration (Kuwabara et al., 1998, Uncini et al., 2013).

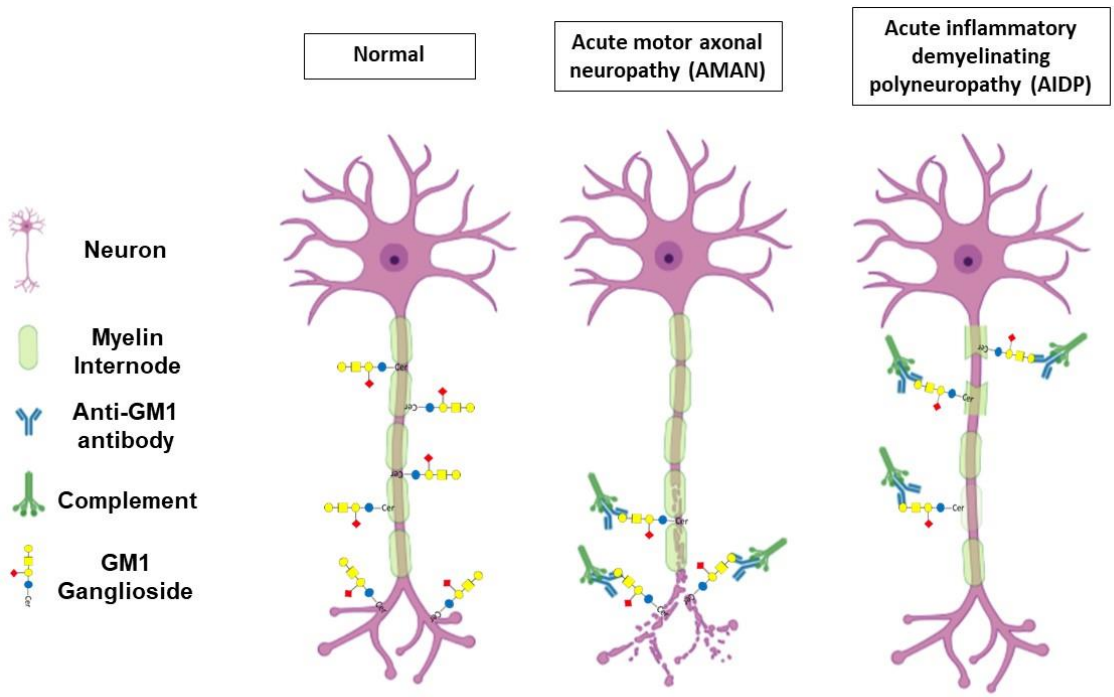

Figure 1.1: AMAN and AIDP pathogenesis. Diagram illustrating a normal myelinated neuron with complex gangliosides expressed on both axonal and glial membranes. In AMAN, antibodies bind to gangliosides on axonal membranes resulting in axonal degeneration. In AIDP, pathogenesis is less defined, but believed to result from anti-ganglioside antibodies activating complement, leading to segmental demyelination and detachment of the paranodal loops. Created using BioRender.

1.1.1.3 Acute motor and sensory axonal neuropathy

When Feasby and colleagues first described a case of pure axonal degeneration, they reported a rapid fall in compound muscle action potential (CMAP) and sensory nerve action potential (SNAP) (Feasby et al., 1986). However, the axonal cases reported by McKhann et al., (1993), displayed a fall in CMAP without a change in SNAP. Therefore, they concluded that these demonstrated two different variants of axonal GBS, a pure motor axonal variant (AMAN), and an axonal neuropathy which affects both motor and sensory nerves, termed AMSAN (McKhann et al., 1993). It was found that there is a close pathological relationship between AMSAN and AMAN, which is consistent with antibody-mediated pathogenesis. Griffin concluded that AMAN and AMSAN belong to a spectrum of disease where there is a direct immune attack on axonal antigens, and AMSAN pathology represents the most severe case (Griffin et al., 1996). The incidence rate of AMSAN is very low in comparison to AIDP and AMAN [reviewed by (Uncini and Yuki, 2009)]. It is not clear why antibodies only bind to motor axons in some cases but bind to both motor and sensory axons in other cases, especially if the same antigen is responsible

for disease in both AMAN and AMSAN. Evidence suggests that there is no quantitative difference in the presence of GD1a, GD1b and GM1 gangliosides between motor and sensory axons (Ogawa-Goto et al., 1990). However, it has been demonstrated that some anti-ganglioside antibodies (AGAbs) preferentially bind to motor fibres and not to sensory fibres (Gong et al., 2002). It is known that steric hinderance can affect the ability of an antibody to bind to different membrane environments (Greenshields et al., 2009). Therefore, it is possible that the steric presentation of the epitope is more accessible on motor nerve membranes than it is on sensory nerve membranes, which could account for the motor predominance in AMAN [reviewed by (Kaida, 2016)].

1.1.1.4 Miller fisher syndrome

In 1956, Charles Miller Fisher described three cases of acute neurologic illness characterised clinically by a triad of symptoms: ataxia, areflexia and ophthalmoplegia (Fisher, 1956). He observed an elevated rise in cerebrospinal fluid (CSF) protein in the later stages of the illness in one of the cases, and thereby declared it a close relation to GBS. This is now widely recognised as MFS. Although MFS is commonly considered a variant of GBS, it is rather unique and differs from the 'typical' characteristics of GBS in that it is a descending paralysis which presents with facial weakness and sometimes shows signs of central nervous system (CNS) involvement. In the first report of MFS, Fisher described that one of the patients was drowsy, relating to brainstem activity, during the acute phase of the illness. The involvement of the CNS has sparked debate over whether MFS is truly a variant of GBS, or whether it is more closely associated with Bickerstaff brainstem encephalitis (BBE). BBE is a rare inflammatory disorder of the CNS in which drowsiness is a key characteristic. BBE shares common clinical features with MFS and it has been suggested that MFS and BBE belong to the same group of disorders as a syndrome of ophthalmoplegia, ataxia and areflexia (Matsumoto et al., 2002, Petty et al., 1993).

1.1.1.5 Chronic neuropathies

Chronic inflammatory demyelinating polyneuropathy (CIDP) is a heterogenous sensory and motor neuropathy which is considered as part of a spectrum of inflammatory demyelinating polyneuropathies. Antibodies directed towards components of the paranode have been implicated in the pathogenesis of CIDP (Querol et al., 2014, Querol

et al., 2013). This neuropathy bears some similarities to GBS such as, elevated CSF protein content, symmetrical weakness in both proximal and distal muscles, and reports of a preceding infection in 16-32% of patients. The main difference between CIDP and GBS is that CIDP is associated with a progressive or relapsing-remitting time course (Eldar and Chapman, 2014, Said, 2006). However, CIDP can have an acute or subacute onset which is often confused and misdiagnosed as GBS (Dionne et al., 2010, Hughes et al., 1992, Ruts et al., 2010).

Another chronic neuropathy which is important to note is multifocal motor neuropathy (MMN). This is an asymmetrical neuropathy which targets motor nerve fibres and is characterised by conduction block. There is a high association with immunoglobulin M (IgM) AGAbs, such as anti-GM1 antibodies, present in 30-80% of cases (Eldar and Chapman, 2014). It is believed that these AGAbs result in complement activation and the resulting pathologic effects (Piepers et al., 2010, Yuki et al., 2011), thereby, implicating similarities between AMAN and MMN.

1.1.2 Diagnosis

The accurate and early diagnosis of GBS is crucial to prevent life-threatening complications and to aid prompt administration of treatment to improve the long-term prognosis. Electrophysiology is an essential diagnostic tool used to diagnose GBS and to help differentiate between the different subtypes. The electrodiagnostic criteria for differentiating between AMAN and AIDP has evolved over the years (Albers et al., 1985, Asbury and Cornblath, 1990, Ho et al., 1995, Hadden et al., 1998). There is continuous development of diagnostic criteria, but the diagnostic criteria set by Ho, (1995) and Hadden (1998), illustrated in Table 1.1, are commonly used in clinical practice to differentiate between AMAN and AIDP (Uncini and Kuwabara, 2012).

	Albers et al. (1985)	Cornblath (1990)	Ho et al. (1995)	Hadden et al. (1998)
Criteria for AIDP	At least one of the following in ≥ 2 nerves	Must have 3 of the following:	Must have one of the following in ≥ 2 nerves during first 2 weeks of illness	At least one of the following in ≥ 2 nerves
Conduction velocity	Reduction in conduction velocity	Reduction in conduction velocity in ≥ 2 motor nerves	Reduction in conduction velocity	Reduced motor conduction velocity
Distal Latency	Prolonged distal latencies	Prolonged distal latencies in ≥ 2 nerves	Prolonged distal latencies	Prolonged distal latency
Temporal dispersion	Unequivocal temporal dispersion	Abnormal temporal dispersion in ≥ 1 motor nerve	Unequivocal temporal dispersion	Not specified
Conduction block	Proximal to distal amplitude ratio <0.7	Partial or severe conduction block in ≥ 1 motor nerve	Not specified	Proximal to distal amplitude ratio <0.5
F-wave latency	Prolonged F-wave latency	Absent F-waves or prolonged minimum F-wave latencies in ≥ 2 motor nerves	Prolonged F-wave latency	Prolonged F-wave latency
Criteria for AMAN			No evidence of demyelination as specified above	None of the above features, except one demyelinating feature allowed in one nerve
			Reduced compound muscle action potential	Reduced compound muscle action potential in ≥ 2 nerves

Table 1.1 Diagnostic criteria for AIDP and AMAN (modified from (Uncini and Kuwabara, 2012)).

The key electrophysiologic features of AIDP are reduced nerve conduction velocity; prolonged distal motor latency (DML); prolonged or absent F-wave; conduction block, defined as the failure of action potential propagation; and extensive temporal dispersion, characterised by an abnormal duration of CMAP. In AIDP, conduction block is due to acute demyelination (paranodal loop detachment) and secondary axonal degeneration. Whereas, reduced nerve conduction velocity, prolonged DML and extensive temporal dispersion are correlated to the remyelinating phase (Uncini and Yuki, 2009). On the

other hand, the characteristic features of AMAN are reduced or absent distal CMAP with the absence of demyelinating features (Ho et al., 1995). However, using Hadden's criteria (1998), they considered that there may be a prolonged F-wave or reduced conduction velocity in the presence of axonal degeneration, and so they suggested that a reduced CMAP paired with one demyelinating feature, in one nerve, is still diagnosed as AMAN. It was later reported that conduction block was a feature present in distal and intermediate nerve segments in AMAN cases with AGAbs (Kuwabara et al., 1998). They found that the conduction block promptly resolved without the development of excessive temporal dispersion (termed RCF). At early stages of the disease, differentiation between RCF (present in AMAN) and conduction block (characteristic of AIDP) is difficult, and so sequential electrophysiologic recordings are desired to distinguish between the two subtypes.

Unfortunately, there are no clinical biomarkers of GBS that can be used to aid diagnosis. However, albumino-cytological dissociation (elevated protein concentration in CSF without a rise in cell numbers) is a key characteristic of GBS [reviewed by (Lehmann et al., 2012)], but this is also linked with other peripheral neuropathies such as CIDP and so is not an exclusive biomarker for GBS. Additionally, some variants of GBS are associated with AGAbs and so this can be used in addition to an increase in protein CSF. In the last couple of years, a new biomarker of axonal damage in acquired peripheral neuropathies has been found (Khalil et al., 2018). Studies have shown that the levels of serum neurofilament light chain are correlated with disease severity in GBS (Altmann et al., 2020, Martín-Aguilar et al., 2020). Thus, serum levels of neurofilament light chain offer a valuable prognostic biomarker of GBS (Martín-Aguilar et al., 2020).

1.1.3 Antecedent infections

In 1958, the association between an infectious trigger and GBS was first described by Campbell who reported that 60% of polyneuritis cases had preceding respiratory symptoms and 10-20% had recent diarrhoea (Campbell, 1958). However, determining the causative pathogen proved to be difficult due to a couple of reasons: 1) the delay between infection and diagnosis of GBS, and 2) as GBS is a highly heterogenous disorder, then the pathogen may only be responsible for the onset of disease in a small minority of cases, thereby making it difficult to find a significant association. Various pathogens have

been associated with GBS, such as, *Campylobacter jejuni (C. jejuni), mycoplasma pneumonia, haemophilus influenza* (*H. influenza*), cytomegalovirus (CMV), Epstein-Barr virus and influenza virus (Jacobs et al., 1998, Schonberger et al., 1976). In more recent times, the outbreak of Zika virus in Brazil in 2015 was linked to a rise in the number of GBS cases in the affected areas (Barbi et al., 2018). Furthermore, during the recent pandemic there has been speculation regarding an association between GBS and COVID-19 (Caress et al., 2020); however, evidence suggests that there is no causal link (Keddie et al., 2021).

A causal link between *C. jejuni* and *H. influenzae* and the development of MFS was discovered in 2005, found to be responsible for around 33% of MFS cases (Koga et al., 2005). The most widely understood preceding infection relating to GBS is *C. jejuni*. The first reported link between *Campylobacter* bacterial infections and GBS was published in 1982 (Rhodes and Tattersfield, 1982). Following on from this discovery, Kaldor and Speed (1984) performed a serological study to determine the occurrence of post-infectious GBS, focussing on *C. jejuni*. They found that 38% of GBS patients in their study had serological evidence of a recent *C. jejuni* infection, also noting that these patients had a severe phenotype compared to GBS patients without any evidence of a recent infection. This finding was replicated in subsequent reports which provided evidence that *C. jejuni* infections commonly precede GBS and are associated with axonal degeneration, slow recovery and severe disability (Rees et al., 1995b, Yuki et al., 1990). Additionally, confirmation of a *C. jejuni* infection was found in 76% of AMAN cases and 42% of AIDP cases, thereby corroborating the association between *C. jejuni* infection and production of the axonal variant of GBS (Ho et al., 1995). *C. jejuni* enteritis is the most common preceding infection in GBS in both Western countries and Asia (Koga et al., 2001).

1.1.4 Molecular mimicry

Following the discovery of the association between GBS and a preceding infection, Yuki and colleagues reported patients with elevated levels of AGAbs and suggested that these were involved in the pathogenesis of AMAN (Yuki et al., 1990). The mechanism of action was believed to be via a process called molecular mimicry, whereby the foreign particle shares a common epitope with antigens present on peripheral nerves, resulting in cross-activation of autoreactive T or B-cells (see Figure 1.2). Yuki demonstrated that lipo-

oligosaccharides (LOS), which coat the outer surface of *C. jejuni*, reacted with anti-GM1 antibodies and that the terminal tetrasaccharide of the purified LOS was identical to that of GM1 (a complex ganglioside) (Yuki et al., 1993b). This hypothesis was further confirmed when Yuki and colleagues developed the first animal model of AMAN by injecting rabbits with anti-GM1 antibodies, or with *C. jejuni* LOS isolated from a patient with AMAN (Yuki et al., 2001, Yuki et al., 2004). The work performed by Yuki and colleagues was critical in our understanding of the pathogenesis of AMAN and opened the field to the investigation of AGAbs and their role in GBS.

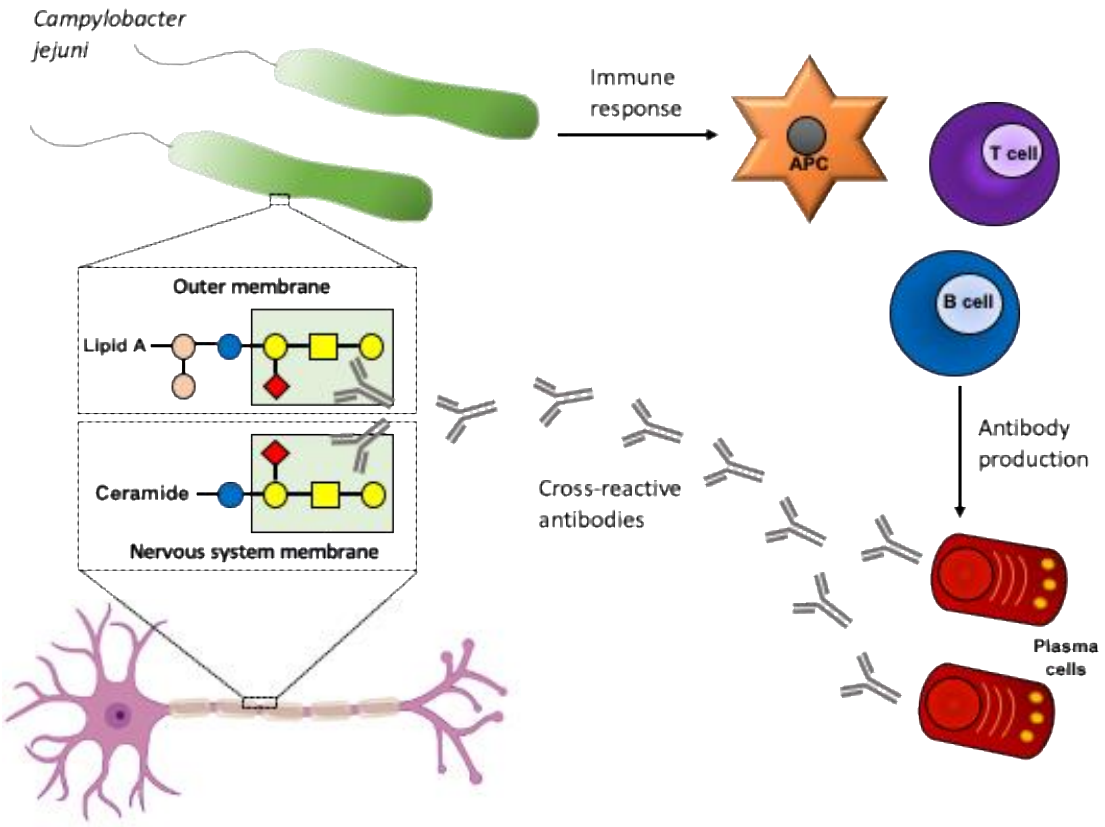

Figure 1.2: Molecular mimicry. *Campylobacter jejuni (C. jejuni)* infection results in an immune response by the host. The antibodies which are produced from plasma cells bind to lipo-oligosaccharides located on the outer membrane of *C. jejuni.* These lipids share a structural resemblance to gangliosides (referred to as molecular mimicry) that are highly expressed on nervous system membranes. Antibodies can cross-react and bind to the gangliosides leading to complement activation and injury. Modified from (Van Den Berg et al., 2014).

1.1.5 Anti-ganglioside antibodies

Auto-antibodies against gangliosides, mostly of immunoglobulin G (IgG) subtype, are the main pathogenic factors of GBS and are present in the sera of ~60% patients. It was considered that antibodies were involved in the pathogenesis of GBS following the success of plasma exchange (PE) treatment (Brettle et al., 1978). It was not until a decade later that Ilyas and colleagues determined the antigens which were being targeted by autoantibodies were gangliosides, present on neural membranes (Ilyas et al., 1988). They noted that the presence of AGAbs occurred early in the acute phase of GBS and fell over time, therefore, indicating that they were not a secondary immune response. Following from this discovery, Yuki reported 2 cases of AMAN following *C. jejuni* infection with anti-GM1 antibodies present in their sera (Yuki et al., 1990). The mechanism of how these autoantibodies arose was later described to occur through molecular mimicry (as described in section 1.1.4). Both AMAN and AMSAN have been associated with antibodies to GM1, GD1a and GD1b gangliosides (Yuki et al., 1992, Kuwabara et al., 1998, Ho et al., 1999, Yuki et al., 1999, Kaida et al., 2000, Ogawara et al., 2000). Antibodies to GM1, GD1a and GD1b have been found to predominantly stain motor fibres, in particular, GM1 and GD1b bind to motor nerve terminals, and GM1 is also enriched at the NoR (Ganser et al., 1983, Gong et al., 2002, Hansson et al., 1977). Therefore, this provides an explanation for the predominant motor phenotype which is found in these subtypes. In 1992, the first report was published demonstrating the presence of anti-GQ1b antibodies in sera from a patient diagnosed with MFS (Chiba et al., 1992). This finding was corroborated by Willison and colleagues (1993) who found that 100% of patients studied had high anti-GQ1b antibody titres in their sera. The association between MFS and GQ1b is now well established with 90% of patients having antibody titres to GQ1b. Moreover, MFS is also associated with antibodies to GT1a gangliosides (Chiba et al., 1993). The location of GQ1b ganglioside was studied by Chiba and colleagues (1993) who demonstrated that GQ1b was predominantly located at the paranodal regions of oculomotor nerves in comparison to other nervous system tissues, compatible with the clinical association of anti-GQ1b antibodies with acute ophthalmoplegia. Anti-GQ1b antibodies have also been associated with BBE supporting the theory that MFS and BBE are linked and belong to the same group of diseases (Yuki et al., 1993a). It is hypothesised that anti-GQ1b antibodies bind to oculomotor nerves, permeate the blood-brain barrier (BBB), and bind to the brainstem resulting in CNS symptoms (Shahrizaila and Yuki, 2013), possibly through retrograde

transport along oculomotor nerves (Cunningham et al., 2016). A significant relationship between AGAbs and AIDP is less established, however, a subclass of AIDP patients do have AGAbs present in their sera, particularly IgG anti-GM1 antibodies (Rees et al., 1995a, Sinha et al., 2007). Despite this, the antigen which is targeted in AIDP is largely unknown. AIDP pathogenesis is still considered to be mediated by antibodies due to the success of PE and intravenous immunoglobulin (IVIg) as treatments for GBS, and the presence of complement deposits in patient autopsy. Due to primary injury to the myelin sheath in AIDP, it is likely that the antigen is located on the plasmalemma of Schwann cells (Hafer-Macko et al., 1996b). Although the target antigen has yet to be determined, there have been several studies which implicate IgG antibodies to myelin glycolipids, such as galactocerebroside (Gal-C) or LM1, in the pathogenesis of AIDP (Kuwahara et al., 2011, Samukawa et al., 2014, Samukawa et al., 2016, Yako et al., 1999). More recently, anti-moesin antibodies, which target the Schwann cell microvilli at the NoR, have been found in sera from AIDP patients who had a preceding CMV infection, but a pathogenic role has yet to be determined (Sawai et al., 2014). Nodal and paranodal proteins have also been suggested as possible targets in AIDP (Doppler et al., 2016, Ng et al., 2012, Devaux et al., 2012).

More recently, antibodies to ganglioside complexes, consisting of two different gangliosides, were discovered as new target antigens in GBS. Ganglioside complexes are formed when the carbohydrate group of two gangliosides interact with each other on the plasma membrane, forming a novel binding epitope (Kaida et al., 2004). Despite the lack of evidence confirming an association between single ganglioside antibodies and AIDP, a study which screened the sera from GBS patients against a large cohort of single and complex gangliosides using a combinatorial glycoarray technique, demonstrated a higher frequency of antibodies against ganglioside complexes in AIDP cases compared to axonal cases (Rinaldi et al., 2013). It was found that there was a high frequency against ganglioside complexes containing sulfatide. As sulfatide is concentrated within the myelin membrane then this could be a possible target antigen for AIDP, but further research is required to explore this possibility. Using microarray, some AGAbs have been shown to bind to ganglioside complexes, but not to the individual glycolipids. On the other hand, there are some complexes which obscure the antibody-binding site (Halstead et al., 2016, Kaida et al., 2008). This suggests that the antibodies are targeted to new conformational epitopes that differ from the binding epitope of single gangliosides. Furthermore, there is

evidence which demonstrates that the glycolipid environment can influence the ability of an AGAb to bind and have neuropathogenic effects. A study performed by Greenshields and colleagues (2009) investigated the pathological effects of two mouse anti-GM1 monoclonal antibodies (mAb; DG1 and DG2) and they discovered that DG2 was able to bind mouse motor nerve terminals and exert complement-mediated neuropathology. On the other hand, DG1 was unable to bind GM1 in living neuronal membrane and therefore, prevented injury to the nerve terminal (see Figure 1.3). Following neuraminidase treatment (digests GD1a creating *de novo* GM1), DG1 was able to bind GM1 on live tissue, thus suggesting that 'native' GM1 is masked by *cis*-interaction with GD1a, thereby preventing binding of some anti-GM1 antibodies (Greenshields et al., 2009). One such trait which can influence the binding is the topographic orientation of the carbohydrate head group of the glycolipids (Rinaldi et al., 2010). Hence, it is likely that within lipid rafts, the orientation of the carbohydrate group of gangliosides and the interaction with other gangliosides, can attenuate or enhance auto-antibody binding.

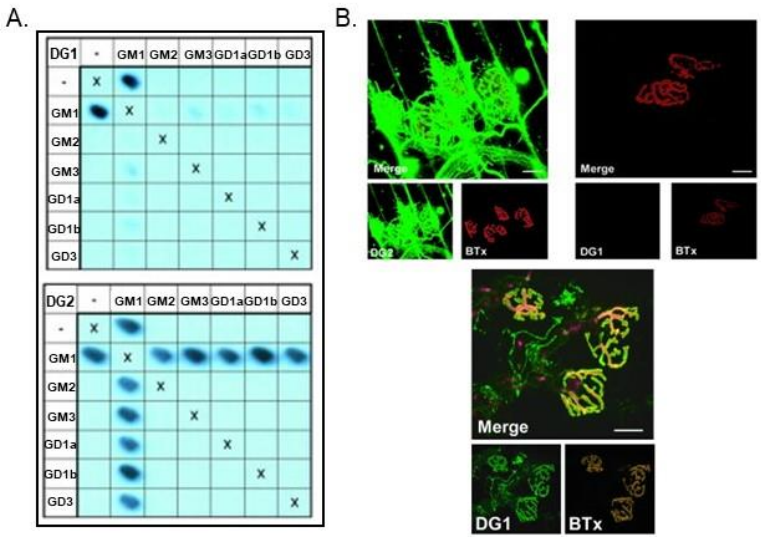

Figure 1.3: Differential binding of anti-GM1 antibodies in live neuronal membranes. A) PVDF glycoarrays demonstrate that DG1 (upper panel) binds to GM1 alone but does not bind GM1 complexes. DG2 (lower panel) binds to both GM1 and GM1 complexes. B) Confocal images of mouse triangularis sterni neuromuscular junctions (NMJ); DG2 binds to the NMJ in living nerve-muscle preparations (left panel), but DG1 staining is absent from the NMJ in live tissue (right panel). DG1 staining is present at the NMJ following neuraminidase treatment (lower panel). Modified with permission from (Greenshields et al., 2009).

1.1.6 Treatment

Plasmapheresis, or PE therapy, was introduced as a possible treatment for GBS in 1978 (Brettle et al., 1978). However, it was not until 1985 when the results of a large clinical trial conducted in North America and Canada demonstrated the positive effects of PE in patients with GBS that the treatment was established (Guillain-Barré Syndrome Study Group, 1985). As a result, PE was the first proven effective treatment for GBS patients. Further clinical trials have shown that treatment with PE accelerates recovery time and improves the clinical outcome at 1 year (Hughes et al., 2007). PE therapy works by removing pathological substances, such as autoantibodies, through replacing the plasma (Reeves and Winters, 2014). In 1988, the first study demonstrating beneficial effects of IVIg treatment in patients with severe GBS was published (Kleyweg et al., 1988). Results from a large scale randomised clinical trial showed that IVIg was as successful as PE therapy when treating patients with GBS (Van der Meché et al., 1992). The precise mechanism of action of IVIg is unknown, but it is thought to have a combined effect on complement inactivation, neutralisation of autoantibodies, cytokine inhibition, and saturation of Fc receptors on endoneurial macrophages (Dalakas, 2002). Currently, the treatment which is widely used when treating GBS patients is IVIg. This treatment is favoured over PE therapy because it is more widely available, and more comfortable for the patient (van Doorn, 2013). However, a high percentage of patients still require ventilation and have poor long-term recovery, therefore, the development of a new and targeted treatment is required.

1.2 Peripheral nervous system

As mentioned previously, GBS results from an autoimmune mediated attack to the peripheral nerves. This section will outline the basic anatomy and structure of peripheral nerves. The nervous system is divided into two components; CNS, made up of the brain and the spinal cord, and the peripheral nervous system (PNS), consisting of all the nerves that leave the spinal cord. The function of the PNS is to communicate messages to and from the CNS as it forms a connection between every muscle and organ in the body with the brain (Catala and Kubis, 2013).

1.2.1 Axon

Motor axons are responsible for transmitting information in the form of an action potential, from the CNS to effector organs, such as muscles and glands. The anatomy of the peripheral nerve is outlined in Figure 1.4. Within the PNS, both unmyelinated and myelinated axons are coated in a protective sheet of connective tissue known as the endoneurium. Located at the innermost layer of the endoneurium are small capillaries which contain endothelial tight junction molecules, forming the BNB (Kanda, 2013). Individual axons are then bundled together forming fascicles, which are enclosed by the perineurium. The function of the perineurium is to maintain the homeostasis of the endoneurial fluid that surrounds each individual nerve. Furthermore, fascicles are embedded in the epifascicular epineurium, dense connective tissue of which the outer layers condense to form the epineurium (Stewart, 2003).

The CNS and PNS are protected by a barrier. In the CNS, protection is offered by the BBB which serves to prevent toxins, pathogens, and inflammatory cells from gaining entry to the brain. However, the BBB can be altered or lost during neurological diseases which contributes to the pathology and disease progression (Daneman and Prat, 2015). On the other hand, the PNS is protected by the BNB which restricts movement of blood components to the PNS parenchyma. Additionally, the BNB actively exchanges material between the endoneurial microenvironment – the connective tissue surrounding the myelin sheath - and the surrounding extracellular space, to maintain PNS homeostasis. Destruction of the BNB results in the infiltration of mononuclear cells, toxic substances, and immunoglobulins into the endoneurium, which is a crucial step in the development of immune mediated peripheral neuropathy, such as GBS (Kanda, 2013). There are certain structures within the PNS which are particularly vulnerable to immune mediated attack, such as the dorsal root ganglia (contains cell bodies of sensory neurons) (Sheikh and Amato, 2010), spinal roots, the neuromuscular junction (NMJ) and the distal segments of myelinated fibres that innervate them (Brown and Snow, 1991), as they lie outwith the protection of the BNB and so are exposed to circulating factors.

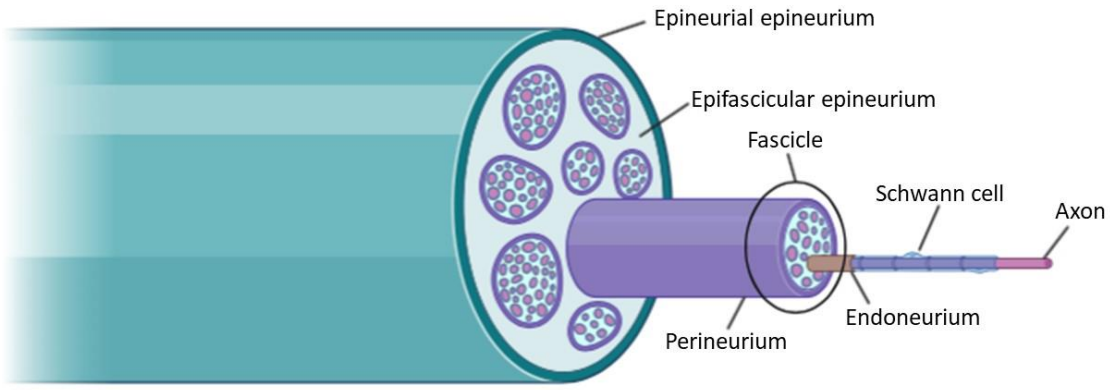

Figure 1.4: Peripheral nerve anatomy. The myelinated axon is enclosed in a sheet of connective tissue called the endoneurium. Individual axons are bundled together forming a fascicle which is enwrapped by the perineurium. Fascicles are embedded in connective tissue, the epifascicular epineurium, and the outer layers form the sheath, referred to as the epineurial epineurium. Diagram created using BioRender.

1.2.1.1 Axon regeneration

One major difference between the PNS and CNS, is that axons in the PNS can regenerate. Following injury to the peripheral nerve, the portion of the axon distal to transection becomes fragmented and degenerates; this process is known as Wallerian degeneration. During this active process, glial cells dedifferentiate and enter a repair phenotype where they function to clear up axonal and myelin debris. Clearance of debris removes inhibitory factors and allows the axon segment proximal to the injury site to form growth cones, allowing axons to regenerate and re-innervate their targets (Llobet Rosell and Neukomm, 2019, Huebner and Strittmatter, 2009).

1.2.1.2 Axonal cytoskeleton

The underlying cytoskeleton has an array of functions which are essential to maintain the integrity of axons [reviewed by (Kevenaar and Hoogenraad, 2015)]. The cytoskeleton, composed of microtubules, actin filaments and neurofilaments (explained in full in section 1.2.4.1), is required for axon formation and axonal transport. Axonal protein transport is particularly important for cytoskeleton remodelling during growth and regeneration but is also required for maintenance of neuronal polarity and synapse function. The cytoskeleton is responsible for internal organisation of proteins and provides mechanical support to allow the nerve to perform essential functions, such as saltatory conduction. Additionally, the cytoskeleton forms the structural basis of

specialised axonal structures, such as the axon initial segment (AIS) and the NoR. Destruction to the cytoskeleton can be extremely detrimental to the function and integrity of the cell, contributing to the pathophysiology of many peripheral neuropathies (for reviews see (Kevenaar and Hoogenraad, 2015, Leterrier et al., 2017)).

1.2.2 Myelin

In the PNS, axons greater than 1 μm in diameter are myelinated by Schwann cells. Myelin is believed to play a few roles, the most important function being that it insulates the axon which increases the rate of electrical impulse conduction. Additionally, it is also believed that myelin offers neurotrophic support which is essential for the functional integrity and long-term survival of axons. There are two main types of Schwann cells: myelinating and non-myelinating. Unmyelinated axons are grouped together in bundles called Remak fibres, by non-myelinating Schwann cells. Furthermore, some non-myelinating Schwann cells migrate to the NMJ where they become terminal Schwann cells, or perisynaptic Schwann cells (pSC) (Ioghen et al., 2020, Nave, 2010). On the other hand, myelinating Schwann cells wrap larger diameter axons forming the myelin sheath. In the PNS, each Schwann cell forms a myelin internode and there is a 1:1 relationship between the Schwann cell and axon. This differs to the CNS, where the myelinating glial cell, called the oligodendrocyte, can ensheath multiple axons. There is a break in the myelin sheath between each internode which forms the NoR [reviewed by (Nave, 2010, Salzer, 2015)].

The Schwann cell enwraps the axon forming compact myelin along the internode. Located laterally are the non-compact cytoplasmic loops which form an axo-glial junction with the axolemma forming the paranodal loops. Located within the glial cytosol are the Schmidt-Lanterman incisures, long channels which connect the cytosol to the periaxonal space. These structures are believed to be important for metabolic exchange between the Schwann cell and the axon. As the myelin sheath is very dense and functions to insulate the axon, it restricts the axon from gaining nutrients from the endoneurium and so it is hypothesised that the glial cell takes over this role and forms metabolic interactions with the axon (Nave, 2010). The Schwann cell membrane is rich in lipid rafts which consists of cholesterol, sulfatide, caveolin and gangliosides (Nave, 2010, Salzer, 2015).

1.2.3 Nodes of Ranvier

The NoR are highly specialised structures that occur at frequent intervals along the axon, appearing as a gap in the myelinated internodes (Figure 1.5). As they do not have the protection of myelin, they are exposed to the extracellular environment and so can be vulnerable to injury. These structures are responsible for the saltatory conduction of action potentials along the nerve (explained in more detail in section 1.2.3.4) and so injury to this area can lead to electrophysiological disruption, such as conduction block (Devaux, 2014). The NoR are composed of three compartments: the node (which will be referred to as the nodal gap), paranode and juxtaparanode (Figure 1.5).

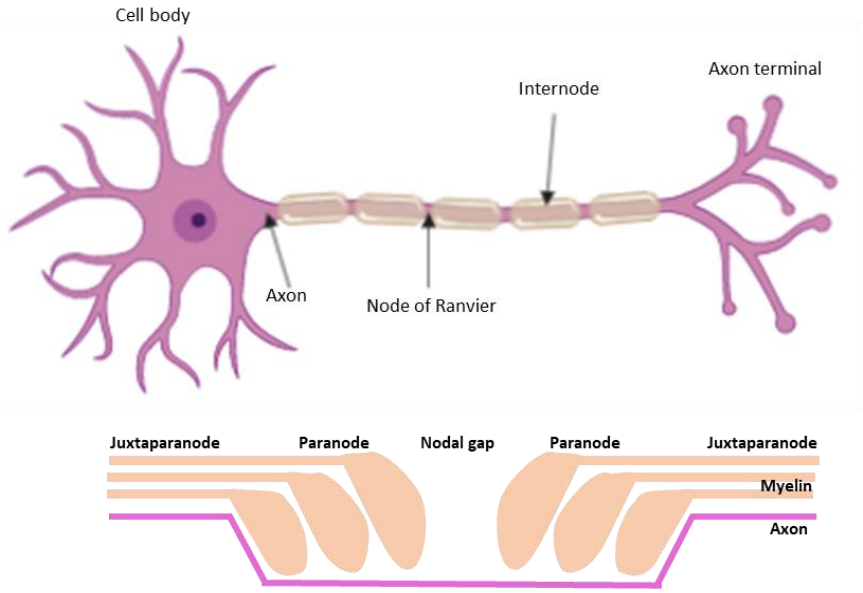

Figure 1.5: Schematic diagram of the peripheral nerve and node of Ranvier. The axon leaves the cell body and travels to its target where it forms the axon terminal. Schwann cells are responsible for myelinating the axon and forming internodes. The unmyelinated gap between two internodes is referred to as the node of Ranvier (NoR), responsible for saltatory conduction. The NoR consists of three domains: the nodal gap, the paranodes and the juxtaparanodes. Modified from (McGonigal and Willison, 2021). Created using BioRender.

1.2.3.1 Nodal gap

The axonal membrane, located between two adjacent myelinated internodes, is the nodal gap (Figure 1.5). High density clustering of voltage-gated sodium channels (Nav) and voltage-gated potassium channels (Kv) on the nodal axolemma is a prerequisite for the function of the nodal gap in saltatory conduction (Poliak and Peles, 2003). In the PNS, Schwann cells are completely covered by a basal lamina, rich in extracellular matrix (ECM)

proteins and cell adhesion molecules (CAM), and the outermost layer of the Schwann cell extends microvilli which contacts the axonal membrane at the nodal gap (Figure 1.6) (Landon and Williams, 1963, Scherer et al., 2001).

1.2.3.2 Paranode

The paranodes, which lie adjacent to the nodal gap, is where the Schwann cell cytoplasmic paranodal loops are connected to the axolemma forming the paranodal junction or the axo-glial junction (Figure 1.5). When viewed down an electron microscope, these junctions appear as electron dense bands, termed transverse bands, which have a similar appearance to invertebrate septate junctions. It is believed that the paranodes function as a barrier, preventing the lateral diffusion of axolemma proteins and separating the ion channels located in the node from those located in the juxtaparanode (Rasband and Peles, 2016).

1.2.3.3 Juxtaparanode

Juxtaparanodes begin at the innermost axo-glial junction at the paranode and extend into the internode (Figure 1.5). They are characterised by high density clustering of Kv1.1/1.2, believed to function in the re-polarisation of the axon and maintaining the internodal resting potential (Carroll, 2017).

1.2.3.4 Saltatory conduction

Action potentials are generated at the AIS (located at the proximal axon, where the axon leaves the neuron) by Nav that permit the influx of sodium ions, resulting in the depolarisation of the cell. In myelinated axons, the action potential then ‘jumps’ from node to node, re-polarising at each nodal gap (mediated by dense clusters of Nav), travelling down the full length of the axon. This process is referred to as saltatory conduction. Myelination has evolved over time to increase the conduction velocity of action potentials, therefore reducing the metabolic requirements for neuronal activity (see review by (Carroll, 2017)).

1.2.4 Proteins at the NoR

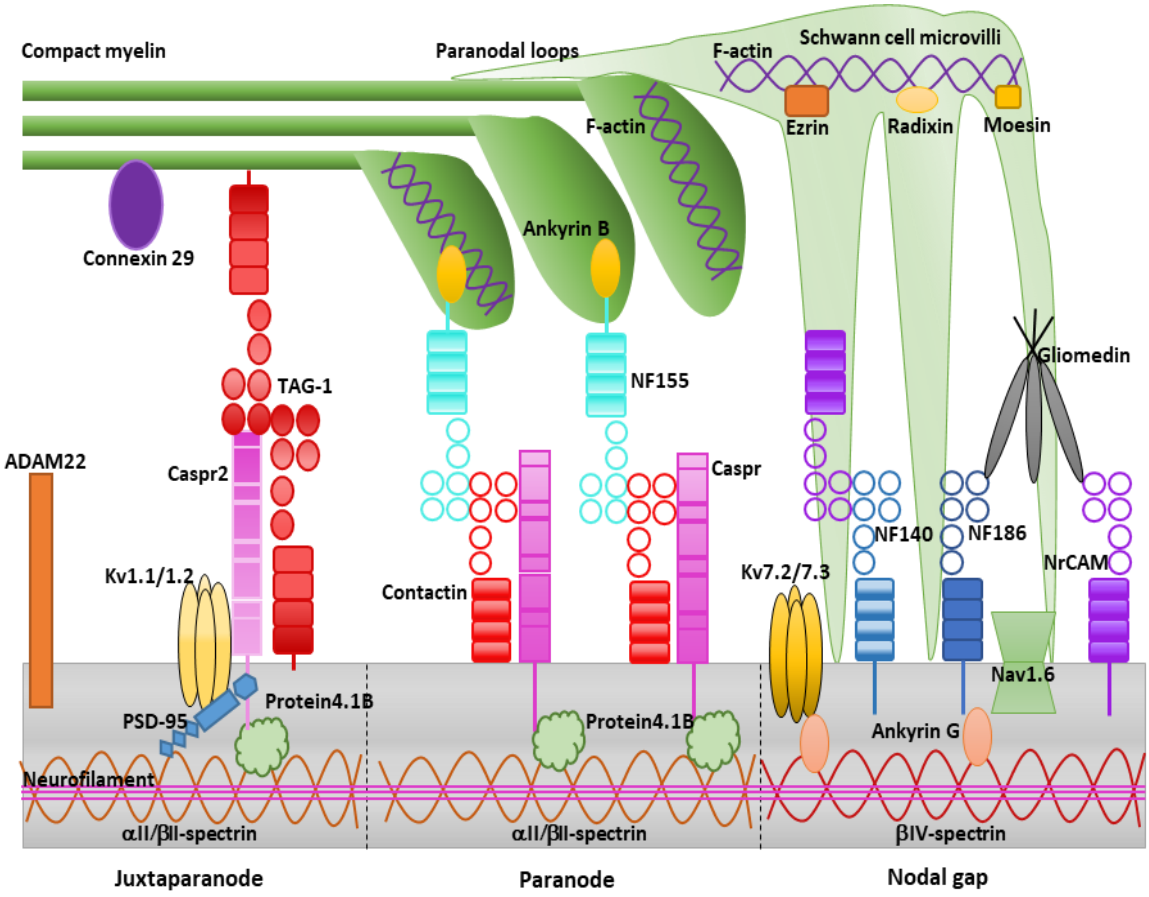

Figure 1.6: Proteins located at the node of Ranvier. The node of Ranvier (NoR) is highly specialised and consists of three compartments: the nodal gap, the paranode and the juxtaparanode. Key proteins at the nodal gap are voltage-gated sodium channels (Nav), involved in saltatory conduction, cell adhesion molecules (CAM; NF186), cytoskeletal proteins (ankyrin G) and extracellular matrix proteins (NrCAM and gliomedin). The axo-glial junction is located at the paranode and consists of contactin associated protein (Caspr), contactin and NF155. Specialised anchoring proteins (ankyrin B and protein 4.1B) tether these proteins to the underlying cytoskeleton. Voltage-gated potassium channels (Kv) are found at the juxtaparanode along with CAM (TAG-1 and Caspr2) and scaffolding proteins (PSD-95 and protein 4.1B).

1.2.4.1 Nodal gap proteins

Axonal Cytoskeleton

The most abundant protein in the cytoskeleton is neurofilament, located in the cytoplasm along the length of the axon and present in all compartments of the NoR (Kevenaar and Hoogenraad, 2015). Neurofilaments are composed of subunits of light, medium and heavy molecular weights and function to control the diameter of the axon and hence, axonal conduction (Yuan et al., 2012, Leterrier et al., 2017). Except for neurofilament, the axonal cytoskeleton differs across each compartment of the NoR. At the nodal gap, the

cytoskeleton comprises of βIV-spectrin, a member of the spectrin family which functions to provide mechanical support and mediates anchoring of nodal membrane proteins through direct interaction with ankyrin-G (AnkG) (Berghs et al., 2000). AnkG has a critical role in the specific subcellular localisation of membrane-associated proteins and tethering these proteins to the cytoskeleton. The presence of neurofascin, either nodal or paranodal, is necessary for the clustering of AnkG and ion channels at the nodal gap (Amor et al., 2017). In turn, AnkG binding is required for localisation of βIV-spectrin to the axonal cytoskeleton at the nodal gap (Yang et al., 2007). Additionally, the membrane-associated proteins at the nodal gap share a conserved AnkG binding domain, hence AnkG functions to scaffold these proteins to the cytoskeleton. Therefore, taken together, the evidence suggests that AnkG is essential for the organisation of the nodal gap (Rasband and Peles, 2020).

Voltage gated channels

The propagation of action potentials occurs at the nodal gap due to the clustering of high concentrations of Nav and Kv. The clustering of Nav at the nodal gap is critically important for saltatory conduction. There are various isoforms of Nav, the most prominent are Nav1.2 and Nav1.6. During development, Nav1.2 is expressed at the nodal gap but switches to Nav1.6 following myelination (Boiko et al., 2001). Although Kv1 are enriched at the juxtaparanode, different Kv isoforms are also present at the nodal gap (Kv7.2/7.3). The Kv are responsible for the repolarisation of the nodal membrane and regulation of axonal excitability (reviewed by (Freeman et al., 2016, Nelson and Jenkins, 2017, Pinatel and Faivre-Sarrailh, 2021)).

As explained previously, high density clustering of Nav at the nodal gap is a requirement for re-polarising the action potential during saltatory conduction. The high concentration of Nav at the nodal gap compared to the internode reduces the axonal capacitance. Additionally, it results in the necessary concentration of sodium ions required to regenerate the action potential. Initiation of Nav1.6 and Kv7.2/7.3 clustering is determined by ECM molecules (gliomedin and neuronal CAM (NrCAM)), located in Schwann cell microvilli, interacting with neurofascin-186 (NF186) at heminodes during myelination. Stabilisation of the node then occurs following the formation of the paranodal junction; NF186 binds to AnkG which then interacts with and recruits Nav1.6 and Kv7.2/7.3 and tethers these proteins to βIV-spectrin. The paranodal junction then

functions as a barrier, restricting Nav and Kv to the nodal gap (for review, see (Nelson and Jenkins, 2017, Freeman et al., 2016)).

Cell adhesion molecules

The CAM situated at the nodal gap consist of NF186 and NrCAM. During development (prior to myelination), NF186 functions as an attachment site for AnkG and βIV spectrin, which subsequently recruit Nav and Kv via axo-glial interactions (reviewed by (Rasband and Peles, 2020)). However, Amor and colleagues (2017) demonstrated that NF186 is not essential for Nav clustering; upon deletion of NF186, paranodal mechanisms take over the role of clustering AnkG and Nav to the nodal gap. The impact of the loss of neuronal neurofascin was demonstrated to have an effect in the long-term maintenance and stabilisation of Nav (Desmazieres et al., 2014). The function of NrCAM is less established compared to NF186. In a study by Custer and colleagues (2003), they examined the consequence of genetic elimination of NrCAM and found that the clustering of Nav was significantly delayed. In addition, they also found that the recruitment of AnkG to the nodal gap was also significantly delayed (Custer et al., 2003). Therefore, given the major role of AnkG in the assembly of the nodal gap (discussed above), it is not clear whether the delay in Nav clustering is due to the absence of NrCAM or delayed localisation of AnkG. More recently, it has been suggested that NrCAM might play a role in the transport of NF186, as it was demonstrated that NF186 and NrCAM are co-transported anterogradely during myelination (Bekku and Salzer, 2020, Rasband and Peles, 2020).

In addition to NF186 and paranodal neurofascin-155 (NF155), there is a third neurofascin isoform, neurofascin-140 (NF140). This isoform was first discovered by Bennet and colleagues (1993), but only recently has the localisation and function of the protein been determined. During development, NF140 is expressed on the neuronal membrane prior to NF186; expression is then downregulated during myelination. Furthermore, NF140 recruits Nav, βIV-spectrin and AnkG to the nodal gap. Thus, suggesting that NF140 complements the function of NF186 during development (Zhang et al., 2015).

Schwann cell microvilli proteins

In the PNS, the Schwann cell microvilli extend processes and contact the axonal membrane at the nodal gap. The microvilli express an array of ECM proteins which are involved in axo-glial interactions required for assembly of the nodal gap (Rasband and Peles, 2016). The cytoskeletal protein located in Schwann cell microvilli is F-actin (Trapp

et al., 1989). F-actin is linked to the membrane via ezrin, radixin and moesin, also referred to as ERM proteins (Scherer et al., 2001). Furthermore, gliomedin is a transmembrane protein secreted from the surface of Schwann cell microvilli (Eshed et al., 2005). It has been shown that gliomedin contains an olfactomedin domain which interacts with NF186 and NrCAM on the nodal axolemma. The presence of gliomedin at Schwann cell microvilli is required for the clustering of nodal proteins at the nodal gap (Eshed et al., 2005). In addition to NrCAM being expressed on the nodal membrane, it is also present at the Schwann cell microvilli and is considered to promote node assembly by mediating axon-glia interactions along with gliomedin [reviewed by (Rasband and Peles, 2020)].

1.2.4.2 Paranodal proteins

Cytoskeletal proteins

The paranodal axonal cytoskeleton includes αII-spectrin, βII-spectrin, and protein 4.1B. It has been shown that protein 4.1B anchors contactin associated protein (Caspr) to αII/βII-spectrin, thereby stabilising the axo-glial junction (Ghosh et al., 2018). Zhang and colleagues (2013) demonstrated that a loss of paranodal βII-spectrin results in the invasion of juxtaparanodal proteins to the paranode, despite an intact axo-glial junction. Therefore, this strongly suggests that the underlying cytoskeleton is crucial for maintaining a boundary between the juxtaparanode and the nodal gap. Ankyrin-B (AnkB) is enriched in the glial cytoskeleton along with F-actin at the paranodes (Ghosh et al., 2018, Trapp et al., 1989). It has been shown that AnkB is an anchoring protein which interacts with NF155 on the glial membrane and tethers it to the underlying cytoskeleton (Chang et al., 2014). Therefore, AnkB plays a critical role in stabilising the axo-glial junction at the paranode.

Cell adhesion molecules

At the paranode, the glial paranodal loops form septate-like junctions with the axonal membrane creating the axo-glial junction. The proteins involved in the axo-glial junction are NF155, located on the glial membrane, which binds to Caspr and contactin on the axonal membrane (Charles et al., 2002). It has been demonstrated that NF155 is capable of clustering Nav to the nodal gap during development when NF186 is absent. Moreover, in knockout mice lacking both Caspr and NF186, there is a complete loss of Nav clustering (Amor et al., 2017). Therefore, this indicates that intact paranodal junctions are necessary for Nav clustering and operate as a second, independent mechanism to neurofascin in

nodal gap assembly. The importance of all three CAM in the formation of the axo-glial junction has been emphasised in many studies, which demonstrate genetically knocking out NF155, Caspr or contactin disrupts the paranodal junction and reduces nerve conduction velocity (Bhat et al., 2001, Boyle et al., 2001, Pillai et al., 2009). The paranodal axo-glial junction functions to restrict the diffusion of nodal components; thus, concentrating Nav at the nodal gap and Kv at the juxtaparanode and complementing the role of the paranodal cytoskeleton in acting as a barrier. In addition, the paranodal junction forms a long, narrow passage between the nodal extracellular environment and the internodal periaxonal space, which functions to reduce the diffusion of ions between the two spaces. Hence, providing high resistance to consolidate the insulating function of myelin. Disruption to the paranodal junction is extremely detrimental, resulting in a lengthening of the nodal gap and invasion of juxtaparanodal Kv to the paranode, leading to progressive neurological impairment (Rosenbluth, 2009, Chang and Rasband, 2013).

1.2.4.3 Juxtaparanodal proteins

Axonal cytoskeleton

The axonal cytoskeleton at the juxtaparanode is comparable to the cytoskeleton at the paranodes, consisting of αII-spectrin, βII-spectrin, protein 4.1B and PSD-95. Similar to its function at the paranodes, protein 4.1B has been shown to accumulate and interact with Caspr2 at the juxtaparanode, linking it to the underlying spectrin cytoskeleton (Denisenko-Nehrbass et al., 2003, Gollan et al., 2002, Horresh et al., 2010). Moreover, in protein 4.1B null mice, there is a loss of Kv1.2 and a reduction in Caspr2 and transient axonal glycoprotein 1 (TAG-1) immunofluorescence staining. Hence, this implicates the importance of protein 4.1B in compartmentalising CAM and Kv along the axonal membrane at the juxtaparanode (Pinatel and Faivre-Sarrailh, 2021). PSD-95 has been found to be localised at the juxtaparanodes in mammalian myelinated nerves where it binds to Kv1 and Caspr2 (Rasband et al., 2002). Caspr2 contains a PDZ binding domain, thus it is speculated that PSD-95 may act as a scaffolding protein alongside protein 4.1B, to link Caspr2 and Kv to the cytoskeleton (reviewed by (Bhat, 2003, Pinatel and Faivre-Sarrailh, 2021)).

Voltage gated ion channels

Kv1.1 and Kv1.2, associated with Kvβ2 auxiliary subunits, are enriched on the axonal membrane at the juxtaparanode, located below the myelin sheath. These channels

belong to the delayed rectifier *Shaker*-type potassium channels that function to promote membrane repolarisation. Additionally, due to the enrichment of Kv at juxtaparanodes, it is believed that they maintain the internodal resting potential. The localisation of Kv at the juxtaparanodes is maintained by the presence of intact axo-glial junctions and the underlying cytoskeleton at the paranodes (for reviews see (Bhat, 2003, Pinatel and Faivre-Sarrailh, 2021, Rasband and Trimmer, 2001)). Rasband and colleagues (1998) showed that in demyelinating PNS axons, Kv diffuse laterally, invading the paranode and nodal gap, resulting in disruption to conduction. Thereby, this reinforces the importance of localisation of Kv at the juxtaparanode for the functioning of saltatory conduction.

During development, Kv1.1/Kv1.2 initially cluster at the nodal gap before being rapidly redistributed, first to the paranode and then to the juxtaparanode (Rasband et al., 1998). The axo-glial interaction mediated by the CAM is responsible for clustering Kv1 to the juxtaparanode. Following formation of the paranodal junction, protein 4.1B links Kv to the spectrin cytoskeleton via their interactions with Caspr2, thus stabilizing the axo-glial junction (Poliak et al., 1999, Denisenko-Nehrbass et al., 2003).

Cell adhesion molecules

The CAM at the juxtaparanode form a complex between the axonal and glial membrane. This junction consists of Caspr2 and TAG-1 (also called contactin2) on the axonal membrane interacting with TAG-1 on the glial membrane (Traka et al., 2003). These CAM are analogous to the paranodal CAM, Caspr and contactin. Therefore, suggesting that the function of these proteins is comparable to those at the paranode, mediating crucial axo-glial interactions. It is believed that the clustering of Kv at the juxtaparanodes depends on the interactions mediated between Caspr2 and TAG-1 (Pinatel and Faivre-Sarrailh, 2021). Furthermore, it has been demonstrated that in TAG-1 knockout mice, Caspr2 and Kv fail to localise to the juxtaparanode. Therefore, this strongly suggests that TAG-1 plays a vital role in the enrichment of Caspr2 and Kv to the axonal membrane at the juxtaparanode (Traka et al., 2003). Equivalent to its function at the paranode, protein 4.1B binds to Caspr2 and anchors it to the cytoskeleton (Denisenko-Nehrbass et al., 2003); thereby, stabilizing the axo-glial junction at the juxtaparanode. Additionally, the transmembrane receptor ADAM22 is enriched on the axonal membrane and is thought to play a role in the assembly of the juxtaparanode. ADAM22 interacts with Kv and the clustering of these proteins is dependent on the axo-glial interactions mediated by Caspr2 and TAG-1

(Pinatel and Faivre-Sarrailh, 2021). Moreover, ADAM22 has been found to recruit PSD-95 to the juxtaparanode (Ogawa et al., 2010). Lastly, Connexin29 has been found to be expressed by Schwann cells, in the inner most layer of myelin, adjacent to the internodal axolemma (Li et al., 2002). Connexins are intercellular channels that function by exchanging ions and metabolites, thereby participating in cell-to-cell communication. It is hypothesised that myelin plays an electrically active role through K^+ recycling, mediated by Connexin29, contributing to faster axonal repolarisation and conduction velocity (reviewed by (Cisterna et al., 2019)).

1.2.5 Neuromuscular junction

The distal portion of motor axons forms a synapse with skeletal muscle fibres, forming the NMJ. It is responsible for communicating signals which control vital processes, such as voluntary body movements and breathing [see review by (Lepore et al., 2019)]. The NMJ is composed of the presynaptic nerve terminal, the synaptic cleft, the postsynaptic membrane (end plate), non-myelinating pSC and capping cells called kranocytes (Court et al., 2008) (as illustrated in Figure 1.7). For the purpose of this thesis, I will focus on the presynaptic elements: the motor nerve terminal, pSC and kranocytes.

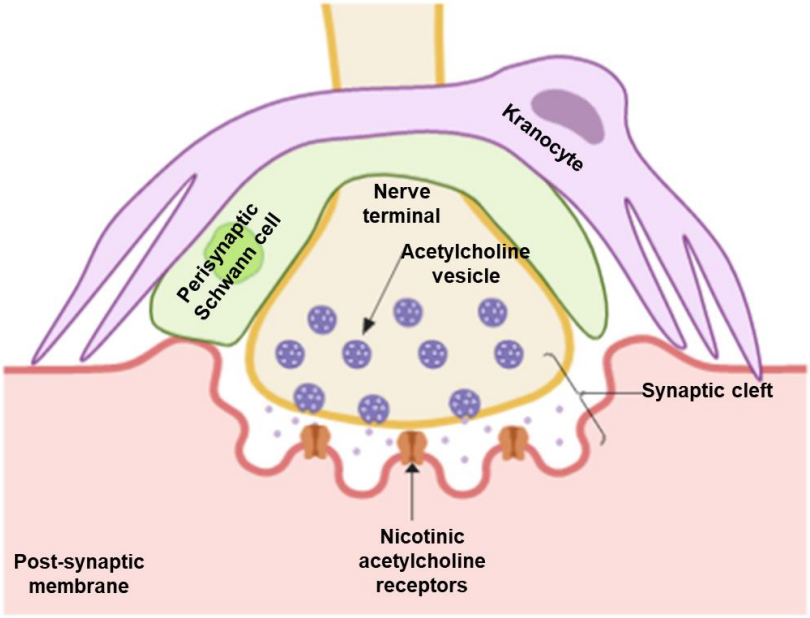

Figure 1.7: Labelled diagram of the neuromuscular junction. The nerve terminal is the most distal part of the nerve which makes a synapse with the motor endplate. The terminal is capped by kranocytes and the non-myelinating perisynaptic Schwann cell. The signal that is carried by the axon, crosses the synaptic cleft by release of acetylcholine vesicles. Acetylcholine binds to nicotinic receptors which are located on the post-synaptic membrane. Together, this structure is referred to as the neuromuscular junction. Created using BioRender.

1.2.5.1 Motor nerve terminal

The motor nerve terminal is the axonal membrane which forms a synapse with the muscle endplate. Neurofilament, an axonal cytoskeletal protein, is located in the abjunctional portion of the terminal along with mitochondria and other organelles. At the surface of the nerve terminal are high concentrations of synaptic vesicles containing acetylcholine (ACh). Additionally, the extracellular membrane is rich in an array of gangliosides and can be targeted by autoantibodies causing pathophysiological effects (reviewed by (Plomp and Willison, 2009)). Upon depolarisation of the nerve terminal, ACh is released from the synaptic vesicles and travels across the synaptic cleft where it binds to nicotinic acetylcholine receptors (nAChR) that are concentrated on the postsynaptic membrane (illustrated in Figure 1.7). Binding of ACh causes the influx of Na+ into the end plate, initiating the end-plate potential, leading to muscle contraction. Following the activity of ACh on the postsynaptic membrane, it is broken down by ACh esterase located in the synaptic cleft. Neurotransmitters can then be recycled by the nerve terminal (Nishimune and Shigemoto, 2018). In addition to neurotransmitter recycling, motor nerve terminals have also been shown to endocytose AGAbs (Fewou et al., 2012, Cunningham et al., 2016) and toxins, such as tetanus (Matteoli et al., 1996), which may contribute to their pathological effects. The motor nerve terminal can be visualised using bungarotoxin (BTx), a toxin which binds to the post-synaptic nAChR on the postsynaptic membrane.

1.2.5.2 Perisynaptic Schwann cells

As mentioned previously, pSC are non-myelinating terminal Schwann cells which cap the axon at the presynaptic nerve terminal (Figure 1.7 and Figure 1.8). There is an average of ~1.7 pSC per NMJ in both human and mice (Alhindi et al., 2021). It is believed that pSC are involved in many functions at the synapse, such as formation, maintenance, remodelling and regeneration. Initially, pSC play an essential role during development of the NMJ as they promote synaptic growth, maturation, and maintenance (reviewed by (Ko and Robitaille, 2015)). Studies have demonstrated that pSC are not necessary for short-term maintenance but are crucial for the long-term maintenance of the NMJ in amphibians (Reddy et al., 2003). However, results in mice contradict these findings as targeted ablation of pSC had no significant impact on axon morphology or function and the NMJ had recovered from pSC injury by 3 weeks (Hastings et al., 2020). Moreover, there is evidence which indicates that pSC are also involved in NMJ activity. They express several

surface receptors, including ACh receptors, and are believed to participate in the transmission of information between motor axons and muscles, thereby having an active role in modulation of NMJ activity [reviewed by (Ioghen et al., 2020)]. Following injury to the nerve, pSC dedifferentiate into a repair phenotype where they become phagocytic, removing axonal and myelin debris at degenerating terminals (Arthur-Farraj et al., 2012, Cunningham et al., 2020). This then clears the way for the regenerating axon. Additionally, they produce processes which direct axonal sprouts from innervated endplates to reinnervate denervated endplates by creating a bridge (Boyd and Gordon, 2003, Ioghen et al., 2020). Furthermore, it has been shown that AGAbs can bind to pSC and damage motor nerve terminals in a complement-mediated MFS mouse model. Hence, implicating pSC as potential targets to autoantibodies contributing to distal nerve failure found in GBS (Halstead et al., 2004, Halstead et al., 2005).

1.2.5.3 Kranocytes

A fourth cell type has been described at the NMJ as a fibroblast-like capping cell, termed the kranocyte. During postnatal development, kranocytes become restricted to the endplate where they lie outwith the basal lamina and cap the pSC as demonstrated in Figure 1.8. Immunocytochemical profiling of kranocytes found that they express neuregulin. The function of these cells has still to be determined; however, the expression of neuregulin suggests they may be involved in signalling of cellular processes, such as cell growth and differentiation, at the NMJ. Additionally, they were found to express GM1 ganglioside and hence, this may give insight into other functions of kranocytes (see ganglioside function in section 1.3.4). Following nerve injury or paralysis in adults, kranocytes selectively proliferate and spread even prior to terminal Schwann cell sprouting. Therefore, indicating that they may be involved in maintenance and repair of NMJs (Court et al., 2008).

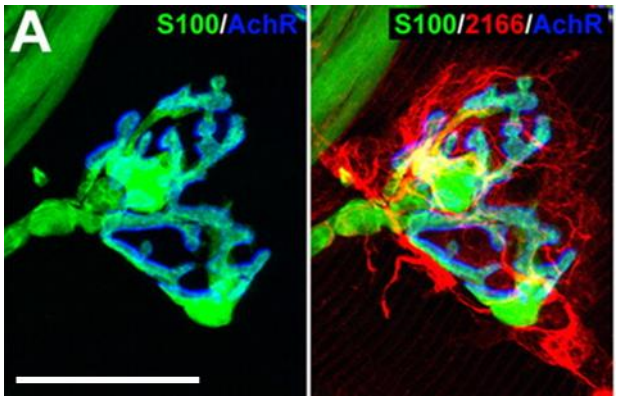

Figure 1.8: A fibroblast-like capping cell at the neuromuscular junction. A) Triangularis sterni muscle endplate stained for S100 (green), to identify perisynaptic Schwann cells, which overlie endplate acetylcholine receptors (blue). B) Superimposition of 2166 (red; labels kranocytes) demonstrates that kranocytes are fibroblast-like capping cells at the NMJ. Taken with permission from (Court et al., 2008).

1.3 Gangliosides

As mentioned previously, autoantibodies directed towards gangliosides expressed in the nervous system are implicated in the pathogenesis of GBS. This section will give an overview of gangliosides.

In 1942, Ernst Klenk was the first person to isolate gangliosides, a type of glycosphingolipid, from the human brain (Klenk, 1942, Schnaar, 2019). Gangliosides are glycosphingolipids which contain one or more sialic acid residues (Robert et al., 2011). They are expressed on plasma membranes ubiquitously throughout the body but are highly concentrated within the nervous system, contributing 10-12% of the total lipid content (de Chaves and Sipione, 2010). There are different kinds of gangliosides, determined by their structure, two of which are simple and complex gangliosides, and these are expressed at varying levels throughout the body (Robert et al., 2011).

1.3.1 Nomenclature

The ganglioside nomenclature which is used widely across the field was introduced by Svennerholm (1994). The shorthand nomenclature for gangliosides is the letter “G” followed by the letter “M” (mono-), “D” (di-), or “T” (tri-), which refers to the total number of sialic acid (N-acetylneuraminic acid; NeuAc) groups which belong to the ganglioside. Additionally, gangliosides are classed into four series (0-, a-, b-, and c-series)

which are named depending on the number of NeuAc groups attached to the internal galactose: 0=0; a=1; b=2; c=3 (Svennerholm, 1994).

1.3.2 Ganglioside synthesis

Ceramide, the backbone structure of gangliosides, is synthesised in the endoplasmic reticulum before being transported to the Golgi apparatus. The synthesis of gangliosides is a multi-step process, involving the addition of saccharide residues, which takes place in the Golgi apparatus. Firstly, glucose is added to the ceramide core by glucosyltransferase (Glc-T) resulting in the formation of glucosylceramide (GlcCer). Lactosylceramide (LacCer), from which most gangliosides are synthesised from, is produced from GlcCer by the addition of a galactose group by galactosyltransferase (Gal-TI). The sialyation (addition of sialic acid) of LacCer by GM3 synthase (or α2-3 sialyltransferase; S-TI) results in the formation of the simple ganglioside, GM3. GD3 and GT3 are then formed from GM3 and GD3, respectively, by the sequential addition of NeuAc by GD3 synthase (or α2-8 sialyltransferase; S-TII) or GT3 synthase (or α2-8 sialyltransferase; S-TIII). The simple gangliosides then function as precursors for the formation of complex gangliosides; 0-series gangliosides are produced from LacCer, GM3 forms the a-series gangliosides, GD3 is the precursor for b-series gangliosides, and GT3 forms the basis of the c-series gangliosides. Complex gangliosides are produced by the addition of N-acetylgalactosamine (GalNAc), galactose, and NeuAc, catalysed by either β1-4 N-acetylgalactosaminyltransferase (GalNAc-transferase; GalNAc-T), β1-3 galactosyltransferase (Gal-TII), α2-3 sialyltransferase (S-TIV) or α2-8 sialyltransferase (S-TV). The ganglioside synthesis pathway is outlined in Figure 1.9, of particular importance to this thesis are the complex gangliosides which are outlined by the red broken line. Once formed, the gangliosides are transported via vesicular transport to the outer leaflet of the plasma membrane where they reside within lipid rafts [reviewed by (Ledeen and Wu, 2018, Robert et al., 2011, Schnaar, 2019).

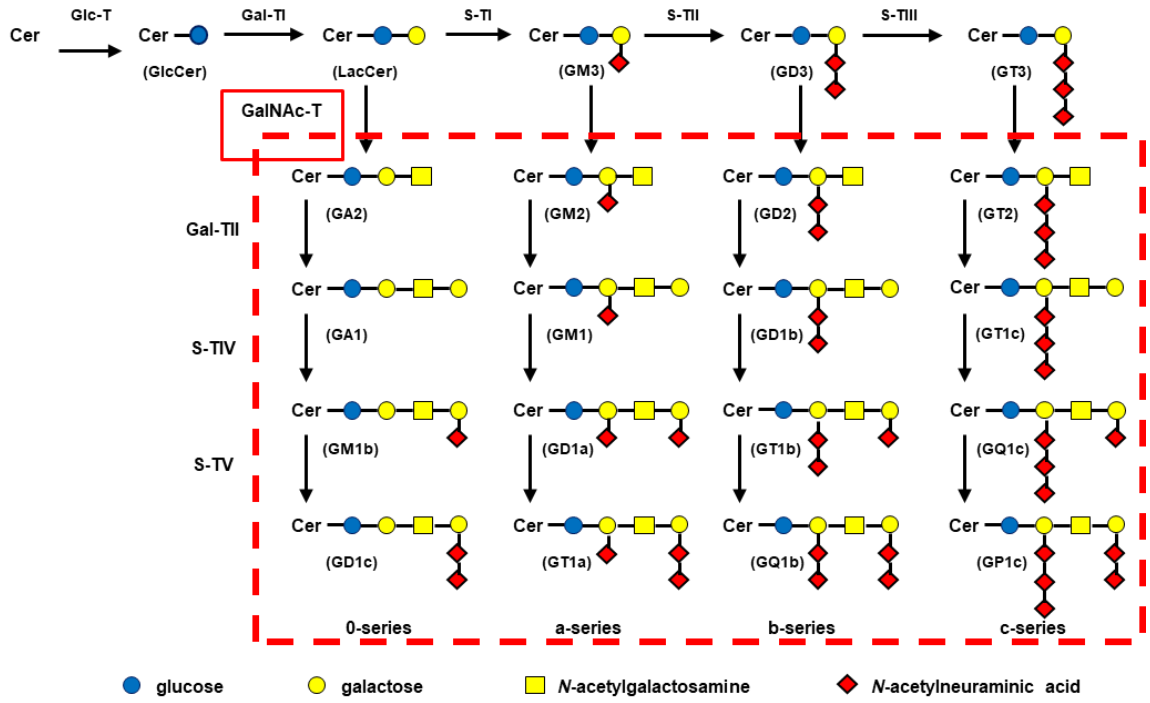

Figure 1.9: Ganglioside biosynthesis pathway. GalNAc transferase (GalNAc-T) is the enzyme responsible for producing complex gangliosides (outlined by the broken red line). Gangliosides consist of a ceramide backbone, glucose, galactose, *N*-acetylgalactosamine, and *N*-acetylneuraminic acid molecules.

1.3.3 Ganglioside location

Gangliosides are found in the outer leaflet of the plasma membrane where they form lipid rafts, rich in sphingolipids and cholesterol. The hydrophobic and lipophilic GlcCer group of the ganglioside is inserted in the membrane, and the remaining hydrophilic glycan core extends outwards into the surrounding aqueous milieu. They are expressed ubiquitously throughout the body but are highly concentrated within the nervous system (Schnaar, 2019). It has been found that the expression level of gangliosides alters throughout brain development. Initially, the simple gangliosides, GM3 and GD3, are expressed at higher levels in the embryonic rat brain (Yu et al., 1988). During post-natal brain development, the expression levels of GM3 and GD3 are reduced, and the predominant gangliosides located in the adult rat brain, accounting for 97% of gangliosides, are GM1, GD1b, GD1a and GT1b; thought to be due to the high activity of GalNAc-T (Dicesare and Dain, 1971). The exact location of GM1 ganglioside is of relevance to this thesis. Cholera toxin, which has a specificity for binding GM1 ganglioside, has been found to bind to both nerve terminals and the nodal gap at the NoR (Ganser et al., 1983, Hansson et al., 1977). Antibodies to GM1 bound strongly to the paranodal loops of dorsal

roots in wild type mice (Susuki et al., 2007a), and to the Schwann cell membrane of peripheral nerves (Sheikh et al., 1999). Furthermore, GM1 has been found to be enriched in peripheral motor nerve myelin but not in sensory nerves (Ogawa-Goto et al., 1992). Therefore, GM1 is enriched on both the neuronal and glial membrane of mouse motor nerves.

1.3.4 Ganglioside function

The genetic knockout of specific glycosyltransferase genes using transgenic mice has revealed the function of downstream gangliosides in the biosynthesis pathway. Transgenic mice that are deficient in GalNAc-T (and therefore, complex gangliosides), appear grossly normal until ~6 months of age when they develop an age-dependent neurodegenerative phenotype; characterised by weakness, ataxia, degeneration and demyelination (Takamiya et al., 1996, Chiavegatto et al., 2000). Additionally, it has been shown that GalNAc-T knockout mice have a reduced nerve conduction velocity compared to wild type mice, indicating the involvement of complex gangliosides in neural transmission (Takamiya et al., 1996). Knocking out GD3 synthase and preventing the expression of b- and c-series gangliosides, results in mice with an impaired regenerative ability (Kawai et al., 2001, Okada et al., 2002). Additionally, there is evidence which suggests that the simple ganglioside, GD3, is involved in neurogenesis and the long-term maintenance of neural stem cells (Wang et al., 2014).

Within lipid rafts, gangliosides play a role in cell-cell recognition, adhesion, membrane trafficking, cytoskeletal organisation and signal transduction (de Chaves and Sipione, 2010, Robert et al., 2011). The function of gangliosides is very broad due to the gangliosides both inserting into the membrane and extending outwards into the external environment, giving them dual properties. Within the nervous system, complex gangliosides have been shown to be involved in neuronal functions, such as neuronal transmission and the structural maintenance of the nervous system, notably at the NoR [reviewed by (Schnaar, 2019, McGonigal and Willison, 2021)].

1.4 Complement mediated injury in GBS

Despite the beneficial effects of complement in the immune system, there are cases when activation of the complement pathway can result in harmful effects to self-cells.

Complement has been found to be involved in both the injury and recovery phases of GBS, with evidence demonstrating a dual role of being both advantageous and harmful. Primarily, complement deposits have been found to be deposited on axonal and glial membranes in patients with AMAN and AIDP, respectively (Hafer-Macko et al., 1996a, Hafer-Macko et al., 1996b). An AGAb-mediated mouse model demonstrated the formation of membrane attack complex (MAC) pores in the membrane (Halstead et al., 2004). The formation of MAC results in the uncontrolled influx of ions into the cell (Acosta et al., 1996), resulting in swelling and cell lysis (Mayer, 1972). The influx of calcium ions activates the calcium-dependent protease, calpain, leading to the destruction of neuronal structural proteins. Additionally, the calcium influx results in the rapid release of ACh from the synapse (O'Hanlon et al., 2003). On the other hand, there is evidence which shows that complement activates macrophages which aid in the recovery process by phagocytosing axonal and myelin debris, clearing the way for regeneration (Dailey et al., 1998). Due to the pathogenic role of complement in GBS, the complement cascade has become of significant interest as a therapeutic target over recent years.

1.4.1 The complement pathway

The complement pathway plays a part in both the innate and the adaptive immune system, consisting of over 30 different proteins. These proteins circulate in the body in an inactive state, until they become activated either directly (by pathogens) or indirectly (by pathogen-bound antibody), which results in the sequential activation of proteins via an enzyme cascade. The primary roles of complement were traditionally considered to be opsonization of microbial pathogens to aid phagocytosis and to lyse susceptible organisms. However, it is now known that the complement system is involved in activating an inflammatory response and regulating tolerance to self-antigens. There are three different pathways through which complement can be activated: the classical pathway, the alternative pathway, and the mannose-binding lectin (MBL) pathway. Each pathway is activated by different molecules, but they converge to generate the same set of effector molecules (Illustrated in Figure 1.10) [see reviews by (Janeway Jr et al., 2001, Sarma and Ward, 2011, Walport, 2001, Sinno and Prakash, 2013)].

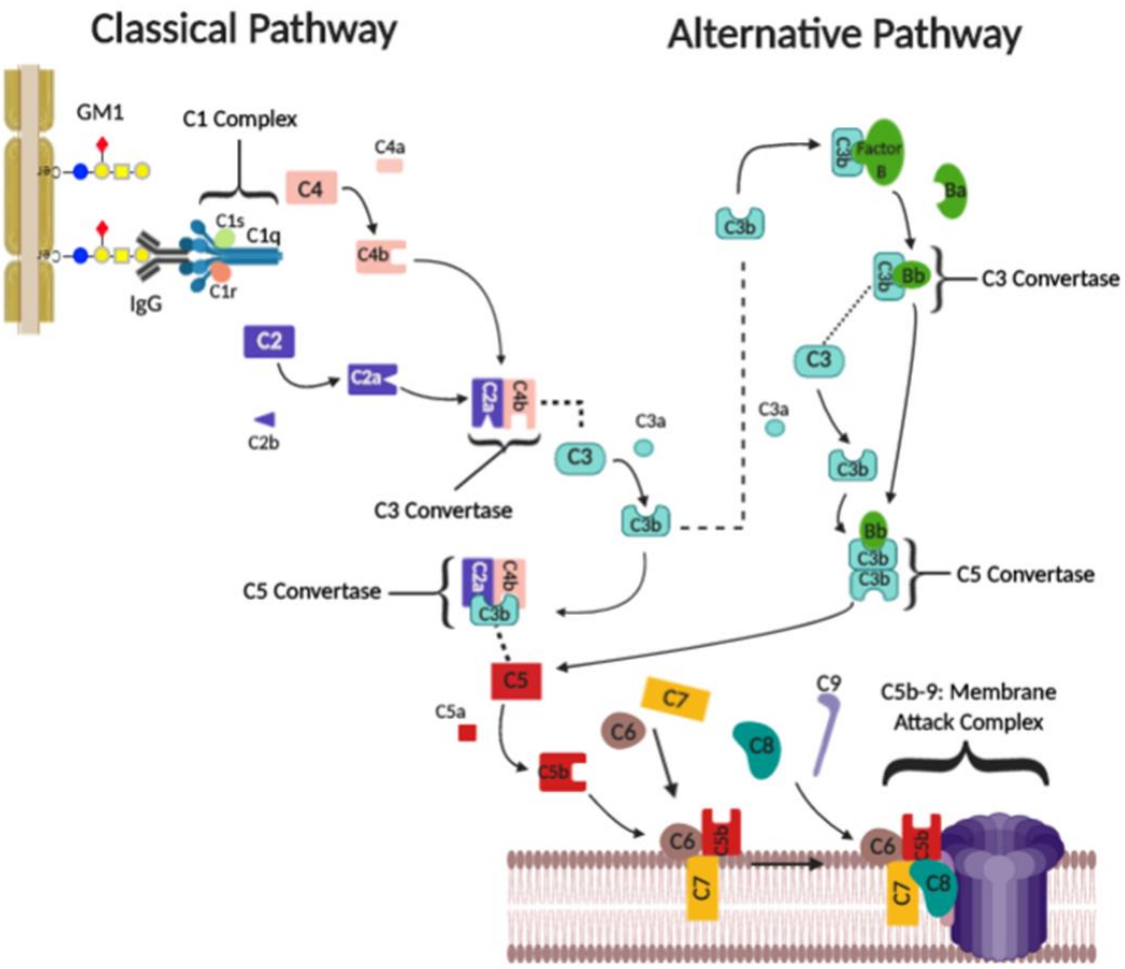

Figure 1.10: Classical and alternative complement pathway. The classical pathway is initiated by antibody binding to C1q, activating C1r and subsequently, C1s. C4 and C2 are cleaved by the activated C1s resulting in the formation of C3 convertase. C3 is cleaved and C3b binds to the C2aC4b complex forming C5 convertase. The product of C5 cleavage, C5b, is responsible for the initiation of the membrane attack complex (MAC). The spontaneous hydrolysis of C3 initiates the alternative pathway. The cleavage of factor B is triggered by the binding of C3b. Cleavage produces the Bb fragment which complexes with C3b forming C3 convertase. This causes an amplification loop resulting in the cleavage of additional C3. Some of the C3b fragments can join to the C3 convertase complex forming C5 convertase which serves to amplify the formation of the MAC pore. Diagram created using BioRender.

1.4.1.1 Nomenclature

Standardised complement nomenclature developed in 2014 is used throughout this thesis (Kemper et al., 2014). The complement pathway consists of 9 key proteins, the C1 complex, followed in succession by C4, C2, C3, C5, C6-C9, which are fragmented upon activation of the pathway (Walport, 2001). In general, the complement cleavage fragments are termed “a” or “b” depending on their relative size, with the “a” fragment being smaller than the “b” fragment. The exception to this rule is the nomenclature for C2

fragments, as C2a is larger than C2b (Bohlson et al., 2019). Primarily, the “a” component is chemotactic and initiates a local inflammatory response, especially C3a and C5a. On the other hand, the “b” fragments tend to further stimulate the proliferation of the complement cascade (Sinno and Prakash, 2013).

In the alternative pathway, the proteins which are unique to this pathway are referred to as ‘factor’ followed by a letter. The cleavage fragments are still referred to as “a” or “b”. Moreover, MBL activates the cascade in the lectin pathway and the activated enzymes are known as the mannan-binding lectin-associated serine proteases (MASP) (Janeway Jr et al., 2001, Kemper et al., 2014). The proteins which are shared between the pathways follow the same nomenclature as described above for the classical and terminal complement pathways.

1.4.1.2 Classical and lectin pathways

The classical pathway is initiated by antigen-antibody complexes to IgM and complement fixing isotypes of IgG (particularly IgG1 and IgG3), binding to the C1 complex (Lepow et al., 1963). This complex is composed of three subunits, C1q, C1r and C1s, where the letters refer to their order of elution from ion exchange chromatography (Kemper et al., 2014, Lepow et al., 1963). Aggregated immunoglobulins are recognized by C1q which results in the activation of C1r. Once activated, C1r cleaves the C1s subunit which then activates and cleaves both C4 and C2. These proteins are cleaved into fragments of C4a and C4b, and C2a and C2b, respectively. C2a and C4b then form a complex referred to as C3 convertase, as C2a contains an enzymatic site which is responsible for the cleavage of C3. The fragments produced from C3 cleavage are the anaphylactic C3a fragment, and C3b fragment, which binds to the C2aC4b complex to form C5 convertase. In turn, this produces C5a, an anaphylatoxin, and C5b, which initiates the terminal complement pathway (Atkinson et al., 2019, Janeway Jr et al., 2001, Sarma and Ward, 2011). Illustrated in Figure 1.10.

The lectin pathway is initiated by MBL and ficolins that bind to oligosaccharides on pathogenic microorganisms, resulting in the activation of the complement cascade. Upon activation, MASP-1 and MASP-2 cleave C4 and C2. Once cleaved, the pathway proceeds in the same way as descried above. (Atkinson et al., 2019, Wallis et al., 2010).

1.4.1.3 Alternative pathway

The third pathway in the complement system is the alternative pathway, which is rapidly acting and functions to amplify the classical and lectin pathway activation (Janeway Jr et al., 2001). Activation of this pathway is via an antibody-independent route; hydrolysis of the C3 thioester bond spontaneously activates the pathway. Alternatively, it can be activated by surface components of microorganisms (Atkinson et al., 2019). Spontaneous hydrolysis of C3 results in the production of the C3a and C3b fragments. C3b then binds to factor B, triggering a conformational change resulting in factor B being cleaved, producing Ba and Bb. The latter protein, Bb, then binds to C3b forming C3 convertase, cleaving additional C3, resulting in C3a and C3b. This enhances the complement response produced by the classical and lectin pathways. Additionally, the excess C3b binds to the C3bBb complex to form C5 convertase; again, functioning to amplify the cleavage of C5 and enhance the terminal complement pathway (see Figure 1.10) (Atkinson et al., 2019, Thurman and Holers, 2006).

1.4.1.4 Membrane attack complex

The most important step of the complement pathway is the terminal complement pathway which involves the assembly of proteins to form MAC. All three pathways, described above, converge on the formation of C3 convertase. C3, which is cleaved by C3 convertase, is the most abundant complement protein in plasma (Porter and Reid, 1979). Once cleaved, C3b forms a complex with C2aC4b, producing C5 convertase. As described above, the cleavage of C5 results in the production of C5a and C5b fragments. This is the final enzymatic step of the pathway and the first step in the formation of MAC. In stepwise formation, C5b forms a complex with C6 and C7, which initiates a conformational change enabling the complex to insert into the lipid bilayer. Once inserted into the cell membrane, this allows C8 to bind to the membrane-associated complex. Multiple copies of C9 are recruited and polymerised, resulting in the formation of a transmembrane pore (illustrated in Figure 1.10). The pore created by MAC disrupts ionic homeostasis, destruction of protein gradients, and eventually results in the lysis of the pathogen [reviewed by (Atkinson et al., 2019, Janeway Jr et al., 2001, Sarma and Ward, 2011)].

The function of each component of the classical, lectin and alternative pathway is explained in Table 1.2.

1.4.1.5 Endogenous complement inhibitors

Due to the amplification effect of the complement cascade, notably at the critical C3 step, it is essential that the cascade is closely regulated. In humans, there is a group of structurally, functionally, and genetically related membrane-associated proteins that are termed the *regulators of complement activation* (RCA). These include decay accelerating factor (DAF), membrane cofactor protein (MCP), complement receptor type 1 (CR1) and factor H. DAF functions to accelerate the decay of C3 and C5 convertases by inhibiting C2 from binding to cell-bound C4b, and factor B from binding to cell-bound C3b. The other RCA proteins (MCP, CR1 and factor H) all display 'cofactor activity'. These proteins bind to C3b or C4b to promote their enzymatic degradation by a plasma serine protease called factor I, that catalyses the cleavage of C3b, into iC3b and C3dg, and C4b, into C4c and C4d, to reduce the formation of C3 convertase. In addition to the RCA proteins, CD59 is expressed in humans which regulates the formation of MAC by preventing C9 from binding to the C5b/C6/C7/C8 complex. There are notable differences between species in the expression of complement regulatory proteins, of importance are those between humans and mice. The expression of DAF and CD59 genes are duplicated in mice (DAF1, DAF2, CD59a, and CD59b); DAF1 and CD59a are expressed broadly whereas DAF2 and CD59b are restricted to the testis. Despite this, they are orthologous to human DAF and CD59. In addition, mice express a unique transmembrane protein known as complement receptor-1 related gene/protein Y (Crry) that is functionally homologous to human MCP and DAF [reviewed by (Atkinson et al., 2019)](Kim and Song, 2006). The function of these regulatory proteins is displayed in Table 1.2.

Component	Function
Classical Pathway (CP)	
C1q	Subunit of C1 complex. Binds to IgM, complement fixing IgG, and ligands on apoptotic cells to initiate CP activation
C1r	Subunit of C1 complex. Cleaves C1s
C1s	Subunit of C1 complex. Activated by C1r. Cleaves C4 and C2.
C4	Cleaved by C1s to form C4b. Component of C3 and C5 convertases in both the CP and LP. An opsonin.
C2	Cleaved by C1s to form C2a; enzymatic components of C3 and C5 convertases in the CP and LP.
Lectin Pathway (LP)	
MBL	Binds to oligosaccharides on pathogenic microorganisms to activate the LP.
MASP-1	Enzyme which cleaves C2, but not C4.
MASP-2	Enzyme which cleaves C2 and C4.
Ficolins 1-3	Recognises and binds to glycans to activate LP.
Alternative Pathway (AP)	
C3	Cleaved by C3 convertases to form C3b and C3a. C3b is part of the AP C3 convertase, and a component of C5 convertase in all pathways. C3a is an anaphylatoxin.
Factor B (FB)	Binds to C3b. Cleaved to form Bb; enzymatic component of the AP C3 and C5 convertases.
Membrane Attack Complex (MAC)	
C5	Cleaved by C5 convertases to form C5b and C5a. C5b initiates MAC formation. C5a is an anaphylatoxin.
C6 & C7	Component of MAC. Binds membranes.
C8	Component of MAC. Initiates pore formation
C9	Component of MAC. Polymerizes to form lytic pores
Regulatory Proteins	
Decay accelerating factor (DAF; humans / DAF1; mice)	In CP-inhibits C2 from binding to C4b. In AP-inhibits FB from binding to C3b. Accelerate decay of C3 and C5 convertases.
Membrane cofactor protein (MCP), complement receptor type 1 (CR1) and factor H (human)	Cofactor proteins. Binds to cell-bound C3b or C4b to promoted degradation by factor I.
Factor I (human)	Catalyses the cleavage of C3b and C4b when bound to a cofactor protein.
Complement receptor-1 related gene/protein y (Crry; mice)	Homologous in function to human MCP and DAF
CD59 (humans) / CD59a (mice)	Inhibits C9 from binding. Regulates MAC assembly and cell lysis

Table 1.2: Function of complement components [modified from (Atkinson et al., 2019)].

1.5 Calpain mediated injury in GBS

The involvement of calpain in the pathogenesis of GBS was first speculated by O'Hanlon and colleagues (2001). The authors hypothesised that the formation of MAC resulted in an influx of calcium ions, thereby activating calpain and resulting in the cleavage of cytoskeletal proteins. They went on to confirm this hypothesis, showing that both depletion of extracellular calcium and application of an exogenous calpain inhibitor preserved the integrity of the axon at the nerve terminal in an AGAb and complement mediated *ex vivo* injury model (O'Hanlon et al., 2003). Additionally, it has also been shown that calpain mediated injury at the distal NoR, in a similar *ex vivo* injury model, causes the loss of nodal protein staining, such as Nav clustering, as demonstrated in Figure 1.11 (McGonigal et al., 2010). The involvement of calpain in complement-mediated pathogenesis is now widely accepted.

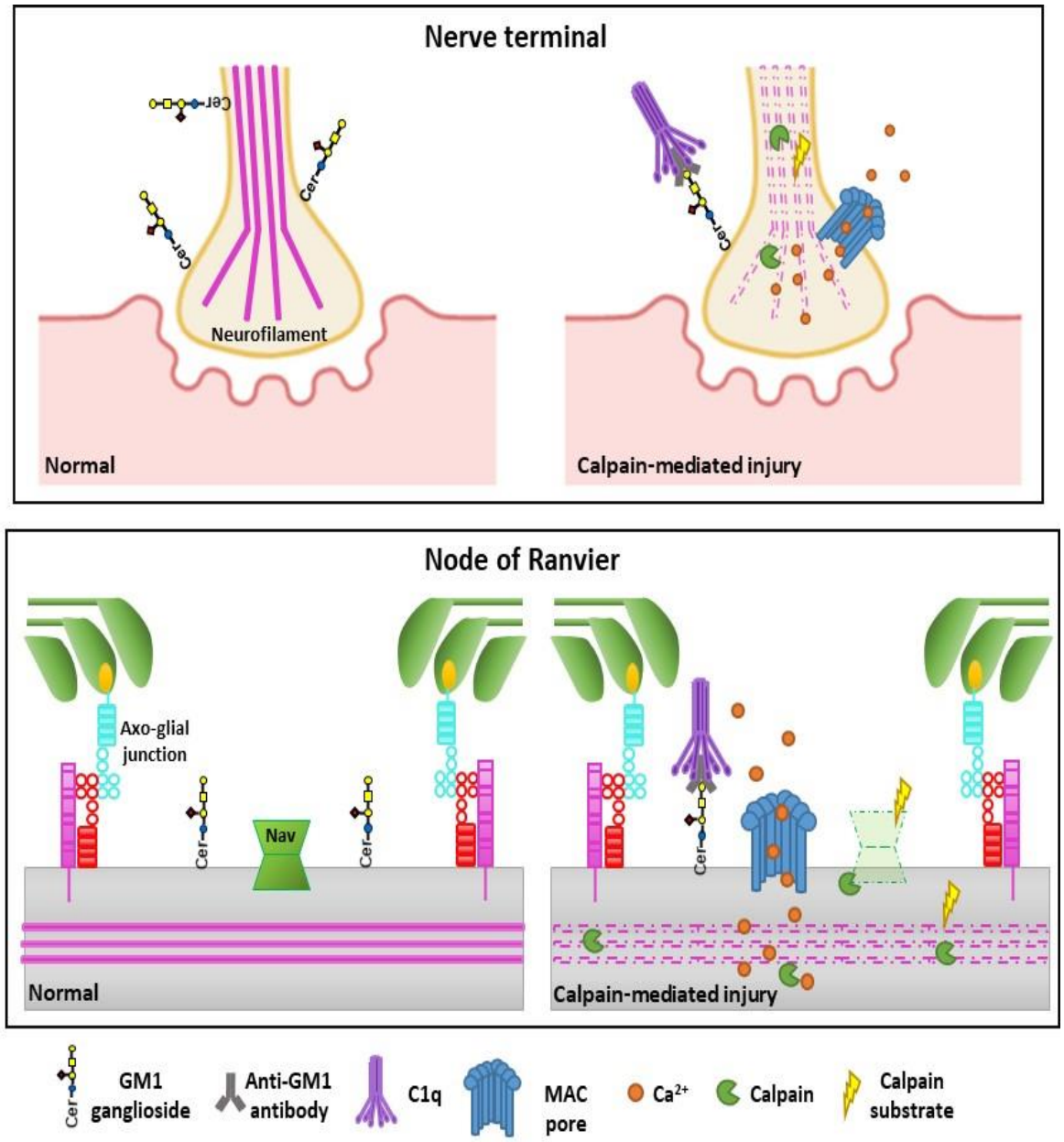

Figure 1.11: Calpain-mediated injury at the nerve terminal and NoR in models of GBS. Binding of anti-ganglioside antibody results in the activation of the complement pathway. Formation of membrane attack complex (MAC) pores in the membrane causes the uncontrolled influx of ions, such as calcium ions (Ca^{2+}). High concentrations of Ca^{2+} activate calpain, resulting in cleavage of neurofilament at the nerve terminal, and of voltage-gated sodium channels (Nav) at the node of Ranvier.

1.5.1 Calpain

Calpain is a protein which belongs to the family of cysteine proteases. They are expressed ubiquitously and are dependent on calcium for activation. Inactive calpains reside in the cytoplasm of cells until they are activated by an increase in intracellular calcium levels. Once activated, they translocate to phospholipid membranes and degrade substrate proteins. They have many physiological roles but play a particularly important role in

programmed cell death (Cheng et al., 2018). There are over a dozen calpains which have now been discovered but the most documented calpains are μ-calpain and m-calpain. As reviewed by Goll, et al. (2003), μ- and m-calpain were given their names as they respectively require micromolar or millimolar concentrations of calcium to be activated *in vitro*. Due to the high concentration of calcium required to activate m-calpain, it has been speculated that this may only be encountered under pathologic conditions and may therefore, represent a pathologic isoform (Geddes and Saatman, 2010). Calpastatin is an endogenous calpain inhibitor which specifically inhibits the proteolytic activity of μ- and m-calpains without inhibiting any other proteases (Goll et al., 2003).

1.5.2 Calpain substrates

As mentioned above, once calpain is activated it proteolyzes substrate proteins. Although this role is necessary for programmed cell death, dysfunction of calpain can be detrimental to the cell and as a result, calpain has been linked to many pathological conditions, including peripheral neuropathies. Calpain is known to have an array of protein substrates, of particular importance to this thesis are the substrates which are present in the myelinated axon. Primarily, cytoskeletal proteins located in the cytoplasm of both axons and Schwann cells, such as spectrin and actin, are known calpain substrates (reviewed by (Ma et al., 2013)). Additionally, neurofilament – the most abundant cytoskeletal protein - is also a known calpain substrate (Kamakura et al., 1983). Calpain-mediated injury has been found to be responsible for the loss of cytoskeletal proteins (including neurofilament) and synaptic degeneration during Wallerian degeneration (Ma et al., 2013). Furthermore, ankyrin, protein 4.1B and PSD95, which are essential anchoring proteins that tether proteins to the underlying cytoskeleton, can also be proteolyzed by calpain (Boivin et al., 1990, Lu et al., 2000). In addition to cytoskeletal substrates, other proteins located at the NoR such as Nav have been shown to be proteolyzed by calpain (von Reyn et al., 2009). Calpains are also linked to the mis-localisation of nodal and paranodal proteins, such as Nav1.6 and Caspr (McGonigal et al., 2010). This could be due to direct cleavage of the proteins by calpain, or it has been suggested that this could be a causal effect of calpain proteolyzing the underlying cytoskeleton.

1.6 Clinical trials

Due to the discovery of the involvement of AGAbs and complement in the pathogenesis of GBS (Ilyas et al., 1988, Koski et al., 1987), it prompted the investigation of more targeted treatment strategies. In 2008, thirty years after the first effective treatment of GBS was documented, Halstead and colleagues demonstrated that treatment with a C5 complement inhibitor, Eculizumab, protected mice from AGAb-mediated neuropathy (Halstead et al., 2008). As a result, Eculizumab was then taken to clinical trial. Unfortunately, due to the potential side-effects of Eculizumab (vulnerability to contracting meningitis), the recruitment of patients was too small to determine an effect (Davidson et al., 2017). A larger scale clinical trial was performed in Japan using the same protocol developed by Willison and colleagues (Misawa et al., 2018, Misawa and Suichi, 2020). The results from the trial suggested that IVIg treatment combined with Eculizumab improves the outcome of patients with severe GBS. However, further work is required to determine whether this treatment will be introduced to all GBS patients. Furthermore, another study performed by McGonigal et al., (2016) demonstrated the protection of axonal structural proteins at the nerve terminal following treatment with an inhibitor of an early component of the classical complement pathway, C1q. Since, this drug has progressed from Phase1b to Phase2 of clinical trial, with preliminary data demonstrating efficacy (Islam et al., 2020).

1.6.1 C2 complement inhibitor

As stated in full in section 1.9, one of the aims of my thesis was to assess the effects of complement inhibition in an *in vivo* peripheral neuropathy mouse model in collaboration with Argenx. The inhibitor which was investigated in this thesis inhibits the complement protein C2, an early complement protein. The C2 inhibitor, ARGX-117, acts by binding to the S2 domain of C2 and preventing interaction with C4b (Van de Walle et al., 2020). Binding of the inhibitor to C2 occurs in circulation and is then released in the endosomes of endothelial cells by endocytosis. Here, C2 is then taken up by lysosomes to be degraded and ARGX-117 can be recycled to the circulation enabling it to bind additional free C2. The ‘sweeping’ properties of this antibody is due to a mutation in its Fc region which causes optimal binding of C2 at physiological plasma pH and calcium concentration, but reduced binding of C2 to the inhibitor at a lower pH and lower concentrations of

calcium, typically found in endosomes, therefore encouraging dissociation of C2. This property translates to an extended serum half-life of up to 2 weeks and so it is an attractive therapeutic for treating complement-mediated immune diseases (Van de Walle et al., 2020).

1.7 Animal models of GBS

The use of animal models to further our understanding of disease pathogenesis is essential. Various animal model of GBS have advanced the field of research dramatically. Early animal models of AIDP suggested that T-cells and macrophages were involved in pathogenesis. However, increasing evidence was published which demonstrated the involvement of autoantibody-dependent pathomechanisms in GBS, diverting the interest away from T cell-dependent mechanisms. Some of these animal models will be discussed in more detail below.

1.7.1 Models of AIDP

1.7.1.1 Experimental allergic neuritis

The pathogenesis of AIDP is less established compared to AMAN. This is in part due to the limited availability of suitable animal models to study the downstream pathways involved; additionally, all the antigenic targets responsible for the development of AIDP have yet to be discovered. Nevertheless, the closest animal model to resemble AIDP is experimental allergic neuritis (EAN), developed by Waksman and Adams (1955). They immunised rabbits with peripheral nerve tissue in Freund's adjuvant and two weeks later, animals developed weakness and ataxia, reaching disease nadir at 3 days. Additionally, rabbits developed respiratory impairment in the advanced stages of the disease and were found to have albuminocytological dissociation in the CSF. Upon histological examination, lesions were present in nerve roots, spinal ganglia, and peripheral nerves, consisting of infiltration of lymphocytes, segmental demyelination, and varying degrees of axonal degeneration. Therefore, given the similarities of clinical presentation and pathology with GBS, they concluded that EAN was the first experimental model to closely resemble demyelinating GBS and could be used to study pathogenic mechanisms.

Following on from the development of EAN, many studies were performed to try and determine the antigenic target responsible for inducing EAN and therefore, AIDP. Initially, it was found that peripheral myelin neurotogenic P2 peptide was able to induce EAN (Brostoff et al., 1977); furthermore, EAN could also be induced by peripheral myelin proteins, such as myelin P0 and peripheral myelin protein 22 (Milner et al., 1987, Gabriel et al., 1998). Serum antibodies to peripheral nerve myelin proteins have been found in patients with AIDP; however, their contribution to pathology is poorly understood (Gabriel et al., 2000, Kwa et al., 2001). The first model of EAN using a myelin glycolipid as the target molecule was described by Saida and colleagues (1979). They immunised rabbits with Gal-C, a major glycolipid component of myelin in the PNS, resulting functionally in conduction block, and pathologically in demyelinating lesions with macrophage infiltration. They later confirmed that anti-Gal-C antibodies were responsible for the resulting pathogenesis by demonstrating that rats inoculated with anti-Gal-C serum from rabbits, exhibited demyelinating lesions at the paranodes of sciatic nerves with acute conduction block (Saida et al., 1982). In addition, anti-Gal-C antibody titres were elevated in the sera of rabbits with EAN induced by whole PNS tissue (Saida et al., 1977); therefore, they concluded that anti-Gal-C antibodies may play a role in the pathogenesis of EAN. It was later shown that GBS patients with a preceding *Mycoplasma pneumonia* infection commonly had anti-Gal-C antibodies present in their sera and so it was suggested that Gal-C may be an important myelin target involved in the pathogenesis (Kusunoki et al., 1995). More recently, there has been evidence to suggest that the antigenic targets might be located at the NoR in EAN. Research by Lonigro and Devaux (2009) demonstrated that Nav, neurofascin and gliomedin were all disrupted in a model of EAN, induced in the Lewis rat by inoculation with peripheral myelin, prior to the onset of demyelination. The injury to the nodal gap was accompanied with conduction deficits. Taken together, two conclusions can be drawn from these results: 1) the antigenic target may be located at the nodal gap/paranode in EAN and AIDP; 2) disruption to the NoR causes early conduction failure occurring before demyelination and axonal degeneration. Subsequently, Devaux et al, (2012) published evidence indicating that some AIDP patients have IgG antibodies against gliomedin, NF186 and contactin, thus suggesting a possible role for these antibodies in the pathogenesis of AIDP.

Parallel to determining the antigenic target, studies were ongoing to establish the mechanisms involved in the pathogenesis of EAN. In 1984, Linington and colleagues

demonstrated that EAN could be induced in the Lewis rat following the adoptive transfer of T-cells (Linington et al., 1984); therefore, it was considered that cell-mediated immunity was responsible for the pathology in EAN and AIDP. In addition, the role of the complement pathway in EAN was later studied (Vriesendorp et al., 1995). Results indicated that complement functions to recruit macrophages into the endoneurium where they work together to opsonize myelin for phagocytosis.

Unfortunately, the use of EAN as an animal model has not identified the antigenic targets involved in AIDP. Moreover, with the increasing evidence published regarding the role of autoantibodies and complement in the pathogenesis of GBS, research has diverted away from T cell-mediated mechanisms. As such, EAN is not suitable for all approaches to modelling AIDP as it is unable to model AGAb-mediated injury.

1.7.2 Models of AMAN

The first animal study to implicate AGAbs in the pathogenesis of GBS was carried out by Nagai and colleagues (Nagai et al., 1976). They discovered that rabbits, immunised with GM1, developed a rigid/spastic paralysis. Unfortunately, they did not investigate the pathological symptoms of these rabbits; however, this was the first animal model to show neurological signs following GM1-immunisation. The pathological effect of anti-GM1 antibodies was later described in a similar rabbit model (Thomas et al., 1991). It was discovered that antibody deposits were commonly present at the nodal gap, but in some cases could be seen overlying the paranode and internode in peripheral nerves. Additionally, this resulted in impaired nerve conduction and mild signs of axonal degeneration with no signs of segmental demyelination. Therefore, it was concluded that anti-GM1 antibodies may exert their effect at the NoR in the peripheral nerve, resulting in peripheral neuropathy (Thomas et al., 1991).

Following the demonstration of molecular mimicry between LOS on the outer surface of *C. jejuni* and the terminal tetrasaccharide of GM1; Yuki and colleagues went on to confirm the hypothesis that molecular mimicry and anti-GM1 antibodies are involved in the pathogenesis of AMAN (Yuki et al., 2001). Primarily, they sensitised rabbits with a bovine brain ganglioside (BBG) mixture (containing GM1, GD1a, GD1b and GT1b), and they discovered that limb weakness progressed for 4-13 days after onset, resulting in flaccid

paresis. All diseased rabbits developed high titres of anti-GM1 antibodies with high affinity antibodies only present at the onset of the disease. Therefore, they hypothesised that anti-GM1 antibodies were essential for the development of the disease (Yuki et al., 2001). Subsequently, they immunised rabbits with isolated GM1, resulting in rabbits producing anti-GM1 antibodies and developing acute flaccid paralysis. Pathological examination of the peripheral nerves revealed predominant axonal degeneration and infiltration of macrophages to the periaxonal space with the absence of demyelination (Yuki et al., 2001, Susuki et al., 2003). Furthermore, they demonstrated that anti-GM1 antibodies were strongly bound to motor nerve axons, at both the nodal gap and internodal axolemma; therefore, providing an explanation for the link between anti-GM1 antibodies in AMAN patients and the development of a motor axonal neuropathy. Due to the similar pathological and clinical features in BBG-immunised rabbits and AMAN, they concluded that this model of experimental motor axonal neuropathy could be used to model AMAN and study the molecular pathogenesis (Yuki et al., 2001). Following on from this study, they then sensitised rabbits with *C. jejuni* LOS isolated from an AMAN patient (Yuki et al., 2004). All rabbits developed flaccid paralysis and were found to have anti-GM1 IgG antibodies. The pathological findings were comparable to that demonstrated previously by immunising with isolated GM1 and to AMAN pathology. Taken together, these studies were fundamental in confirming that molecular mimicry, between GM1 and *C. jejuni* LOS, is responsible for the resulting pathogenesis of AMAN.

Susuki and colleagues then investigated anti-GM1 antibody-mediated injury at the NoR of peripheral nerves (Susuki et al., 2007b). They described the binding of IgG antibodies and corresponding C3 complement deposits at the NoR in the spinal anterior roots of rabbits. Analysis of Nav staining highlighted that Nav were absent at lengthened nodal gaps with complement deposition. Additionally, they found that Caspr dimers were also significantly altered when MAC deposits extended to paranodes with subsequent paranodal detachment. However, if complement deposits were restricted to the nodal gap, both Nav and Caspr dimer staining were preserved, as demonstrated in Figure 1.12. Furthermore, the nodal cytoskeleton and Schwann cell microvilli were also disrupted. Complement deposits were predominantly found in the acute progressive phase of the disease and decreased significantly at the late recovery phase, therefore suggesting that complement plays a pathogenic role in initial nodal disruption (Susuki et al., 2007b). In a subsequent study it was demonstrated that Nav were protected following application of a

complement inhibitor, confirming the involvement of complement in the pathogenesis (Phongsisay et al., 2008). Therefore, these studies strongly indicated that AGAbs could bind to and disrupt the NoR.

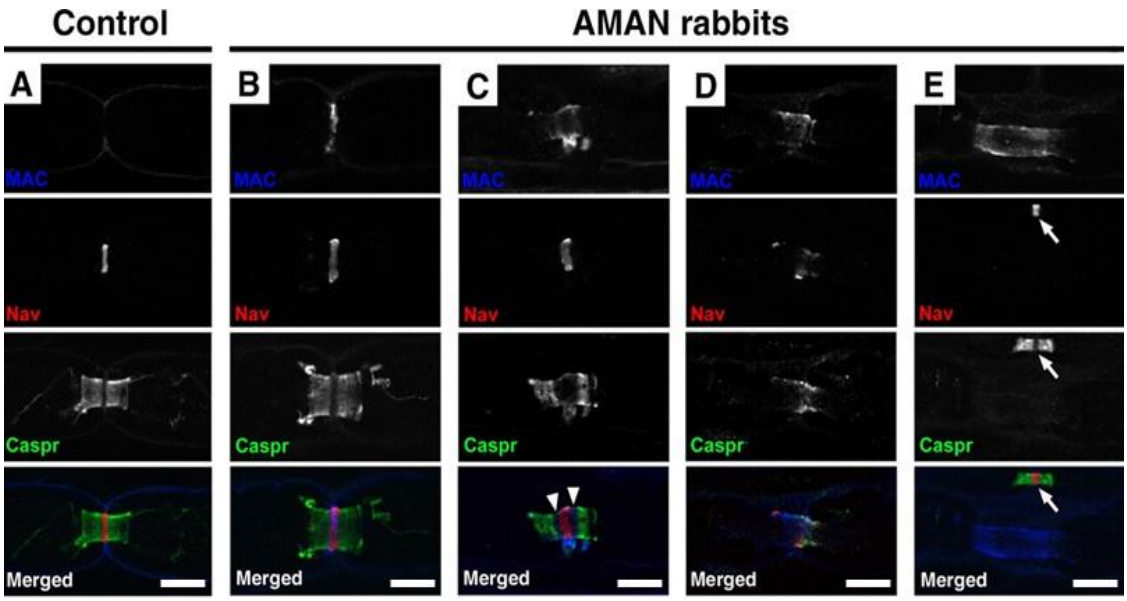

Figure 1.12: Complement deposition at the NoR results in disruption to the nodal gap and paranodes. Illustrative images of longitudinal sections of ventral roots, immunostained with antibodies to MAC (blue), Nav (red), and Caspr (green). A) Staining from control rabbit demonstrates Nav clusters at the nodal gap and Caspr dimers present at the paranode. (B-E) Varying stages of injury to the node of Ranvier in AMAN rabbits are illustrated. B) When MAC deposits are restricted to the nodes, Nav and Caspr dimers remain intact. C) MAC deposits extend to the paranodes resulting in an increased gap between Caspr dimer staining compared to control. Nav staining is unaffected, but gaps are present between Nav and Caspr staining (white arrow heads). D) MAC lesion extends to the juxtaparanode and causes disruption to Nav and Caspr dimer staining. E) MAC lesion present overlying the nodal gap and adjacent paranodes and internodes. As a result, Nav and Caspr dimer staining are absent, whereas staining is preserved in an adjacent fibre with no complement deposits present (white arrow). Scale bar = 10 µm. Modified with permission from (Susuki et al., 2007b).

It was later shown that anti-GM1 antibodies can also exert neuropathogenic effects at the motor nerve terminal in an *ex vivo* mouse model (Greenshields et al., 2009). Here, they demonstrated that both human and mouse anti-GM1 antibodies bind to nerve terminals under specific conditions, activating the complement pathway resulting in the loss of neurofilament staining. Subsequently, this manifested in conduction block as determined by electrophysiological recordings. Following on from these studies, an *in vivo* axonal mouse model was developed (McGonigal et al., 2016). Mice treated with anti-GM1 IgG antibody and normal human serum (NHS), as a source of complement, presented with a respiratory phenotype. Immunoanalysis identified complement deposits at the distal

motor nerve terminal and consequently, axonal integrity was significantly disrupted, as indicated by a loss of neurofilament staining, with no evidence of macrophage infiltration. Additionally, they found that the clinical and neuropathological effects were attenuated following inhibition of the initiating protein of the complement cascade, C1q (McGonigal et al., 2016). It has since been demonstrated in a similar mouse model of axonal injury, that the pSC become phagocytic and clear axonal debris without the recruitment of phagocytic immune cells to the injury site (Cunningham et al., 2020). This study does not rule out the possibility of immune cells being recruited to more proximal injury sites; however, it implies that clearance of debris from the nerve terminal occurs independently to external immune cell recruitment, allowing for rapid clearance and regeneration of the axon.

In addition to anti-GM1 antibodies, AMAN is characterised by the presence of serum anti-GD1a antibodies (Ho et al., 1999, Yuki et al., 1992). It is hypothesised that molecular mimicry is responsible for the induction of anti-GD1a antibodies. Despite the growing evidence implicating AGAbs and complement in the pathogenesis of GBS, there was limited evidence which demonstrated a pathogenic role of anti-GD1a antibodies in AMAN. This was because there was no animal model available to investigate the effects of anti-GD1a antibody-mediated injury; attributable to the poor immunogenicity of GD1a and the accessibility of AGAb being able to bind to the membrane. However, Goodfellow and colleagues overcame these issues by cloning anti-GD1a antibodies from *GalNAc-T* deficient mice (*GalNAc-T*$^{-/-}$, expressing only GM3, GD3, and GT3) immunised with *C. jejuni* strains expressing LOS structures identical to GD1a (Goodfellow et al., 2005). The binding affinity of GD1a was compared in wild type mice (normal GD1a expression), *GD3s*$^{-/-}$ mice (overexpress GD1a), and *GalNAc-T*$^{-/-}$ (no GD1a) at the NMJ, and the subsequent neuropathological effects of GD1a binding was assessed in *ex vivo* diaphragm preparations. It was shown that GD1a levels were highest in *GD3s*$^{-/-}$ mice compared to wild type, resulting in higher levels of complement and significant loss of neurofilament, whereas wild type mice appeared to be relatively resistant to anti-GD1a-mediated injury. In *GalNAc-T*$^{-/-}$ mice, no antibody or complement deposits were present and neurofilament remained intact at the NMJ, due to GD1a being absent in these mice. Additionally, the effects of anti-GD1a IgG-positive sera from AMAN patients was investigated and it was demonstrated that they produce the same pathological effects at the NMJ as mouse anti-GD1a antibodies. Overall, this study demonstrated that anti-GD1a antibodies can induce

axonal pathology at the motor nerve terminal and this model could be used to study GD1a-mediated axonal neuropathy (Goodfellow et al., 2005). Furthermore, the difference in antibody levels and subsequent injury in wild type and *GD3s*$^{-/-}$ mice has greater implications relating to the human disease. It suggests that individuals may vary in ganglioside composition; therefore, AGAb binding, and the resulting neuropathological effects may vary from person-to-person.

Further studies, using the same animal model, demonstrated that anti-GD1a antibody deposits were also prominent at the distal NoR (McGonigal et al., 2010). Antibody deposits were also found at more proximal sites, such as nerve bundles, but at a decreased intensity compared to the distal NoR. This was hypothesised to be because the BNB is less protective at the distal NoR and so they are exposed to circulating factors, whereas the BNB is relatively impermeable at proximal nerve bundles. Additionally, McGonigal and colleagues demonstrated that anti-GD1a antibody binding resulted in the formation of MAC, predominantly at distal NoR and small nerve fibres (McGonigal et al., 2010). Formation of MAC pores resulted in the disruption to nodal proteins, such as Nav1.6, AnkG, Caspr and neurofascin. The loss of Nav1.6 staining was found to be calpain-mediated, as application of an exogenous calpain inhibitor protected immunostaining. Furthermore, it was shown that injured NoR were electrically unexcitable, even when structural integrity was preserved following calpain inhibition. Therefore, these results strongly suggest that formation of MAC pores and the disruption to ionic homeostasis is critical in mediating axonal conduction block (McGonigal et al., 2010). Overall, these studies were instrumental in providing pathological evidence of anti-GD1a antibody-mediated axonal injury and the pivotal downstream role of complement and calpain in mediating disorganisation to both the nerve terminal and NoR. Furthermore, they highlighted the vulnerability of distal nerves to autoimmune attack in AMAN.

Our understanding of AMAN pathogenesis is owed to the development of various anti-GM1 and anti-GD1a mediated animal models; it is now widely recognised that AGAbs activate the complement pathway resulting in the development of axonal GBS. However, it is unclear why motor axons are primarily affected in AMAN. Despite the association between GM1 antibodies and AMAN, thought to be due to the enrichment of GM1 gangliosides located on motor axons; it is known that GM1 is also expressed in myelin and sensory axons too. Furthermore, AIDP patients with a preceding *C. jejuni* infection also

have anti-GM1 antibodies present in their sera. Therefore, this suggests that anti-GM1 antibody can bind and cause injury to both the axon and the myelin sheath. The implications of this evidence could suggest that dichotomisation of GBS pathogenesis is more complicated than initially thought. Consequently, this is an on-going discussion within the research field (Uncini et al., 2013).

1.7.3 Models of AMSAN

Anti-GD1b antibodies are commonly present in patients diagnosed with AMSAN and so are believed to play a role in the pathogenesis (Pan et al., 2001). This hypothesis is strongly supported by the fact that GD1b gangliosides have been shown to be enriched in both motor nerves and in primary sensory neurons in rabbits and humans (Kusunoki et al., 1993, Kusunoki et al., 1996, Susuki et al., 2012). Furthermore, rabbits inoculated with purified GD1b develop sensory ataxia; axonal degeneration is found in the dorsal column of the spinal cord, in the dorsal root, and in the sciatic nerve with an absence of demyelinating lesions (Kusunoki et al., 1999, Kusunoki et al., 1996). There is no sign of cell infiltration in the affected areas however, the rabbits had high anti-GD1b antibody titre. It was later demonstrated that anti-GD1b antibodies caused complement-mediated disruption to the NoR (Susuki et al., 2012). This was accompanied with the presence of periaxonal macrophages in the dorsal roots, a characteristic of the acute phase in ventral roots from AMAN (Hafer-Macko et al., 1996a) and AMSAN patients (Griffin et al., 1996). Therefore, it was concluded that anti-GD1b-mediated damage to the sensory neurons was responsible for the pathogenesis in this model, with predominant damage to the NoR. This animal model, experimental sensory neuropathy, closely identifies with AMSAN pathogenesis and can be used to study the pathophysiological mechanisms of AGAb-mediated neuropathy.

1.7.4 Models of MFS

In the early 1990s, it was discovered that MFS patients commonly have anti-GQ1b antibodies present in their sera, but the pathophysiological relevance of these antibodies were not determined until almost a decade later. Following clinical electrophysiological evidence which implicated the involvement of the NMJ in MFS, initial studies investigated the effect of anti-GQ1b antibodies binding to mouse NMJ in *ex vivo* diaphragm preparations. Both human and mouse anti-GQ1b antibodies were found to induce a rapid

quantal release of ACh which resulted in neuromuscular conduction block, similar to the effects of α-latrotoxin. Immunohistological analysis of paralysed tissue revealed that complement deposits were found at the NMJ (Goodyear et al., 1999, Plomp et al., 1999). It was later shown that complement activation following anti-GQ1b antibody binding, resulted in the destruction of neurofilament at the motor nerve terminals via a calpain-mediated pathway (O'Hanlon et al., 2003, O'Hanlon et al., 2001). Furthermore, anti-GQ1b antibodies were also found to target pSC, resulting in MAC deposition and consequently, pSC death (Halstead et al., 2005, Halstead et al., 2004). Taken together, these studies highlighted the importance of the NMJ as a vulnerable injury site that can result in electrophysiological defects and the causal effect of complement activation on nerve injury.

An *in vivo* mouse model of MFS was developed through intraperitoneal injection of anti-GQ1b antibody and NHS (Halstead et al., 2008). In this model, anti-GQ1b antibody and complement-mediated injury resulted in transmission block at the diaphragm NMJ (due to the proximity of the intraperitoneal antibody and complement injections) which resulted in respiratory paralysis, measured by whole-body plethysmography (WBP). This *in vivo* model was fundamental in demonstrating the effect of complement inhibition in attenuating both structural (see Figure 1.13) and functional damage at the nerve terminal (Halstead et al., 2008, McGonigal et al., 2016). As a result, both the C1q inhibitor and Eculizumab (C5b-9 inhibitor) have progressed to clinical trial stages as new potential therapeutics to treat GBS.

The *ex vivo* and *in vivo* mouse models of MFS, mediated by anti-GQ1b antibody, were indispensable in demonstrating the involvement of complement and calpain-mediated injury in GBS pathogenesis. As a result, the complement pathway is now the focus of ongoing therapeutic strategies.

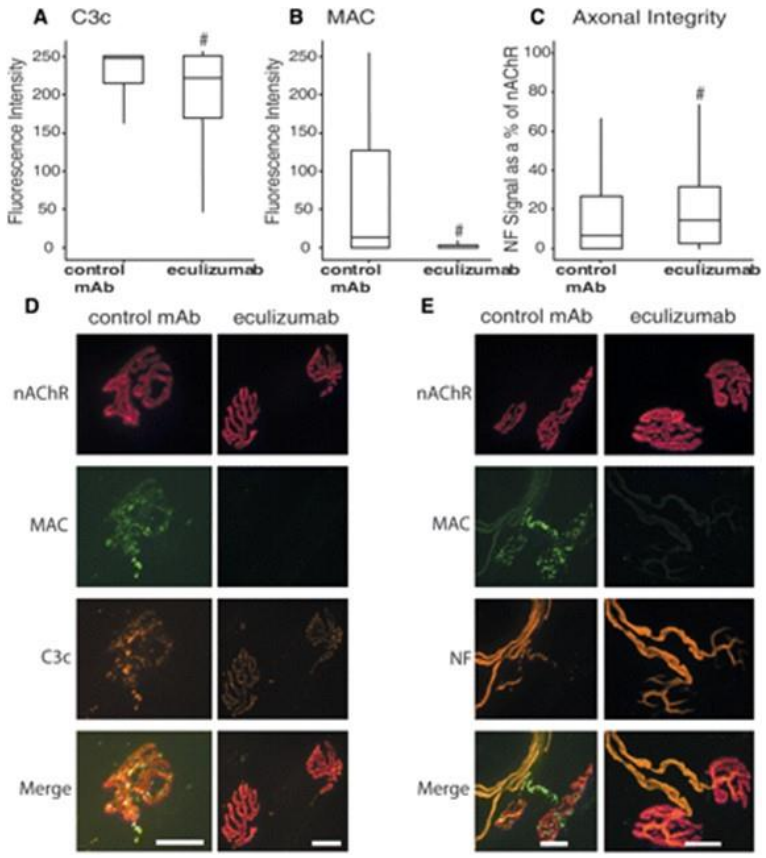

Figure 1.13: Inhibition of MAC by eculizumab attenuates structural damage at the nerve terminal. Mice were passively immunised with anti-GQ1b antibody, followed by normal human serum and eculizumab or control monoclonal antibody (mAb). A) C3c deposition is significantly reduced at neuromuscular junctions (NMJ) of eculizumab-treated mice compared with control. B) MAC deposits are not present at the NMJ following eculizumab treatment. C) The intensity of neurofilament (NF) is significantly higher at NMJs in eculizumab-treated mice compared with control. D) Representative images showing MAC (green) and C3c (orange) overlying the nerve terminal (nAChR, red). E) Illustrative images showing MAC (green) and NF staining (orange) at the nerve terminal. Scale bars = 20 µm. Taken with permission from (Halstead et al., 2008).

1.7.5 Naturally occurring models

Over and above the experimental animal models of GBS, there have been numerous reported cases of spontaneous conditions which share similar pathology to GBS; they present with acute ascending paralysis and are associated with polyradiculoneuropathies. The most documented and recognised conditions are those reported in chickens (Stevens et al., 1981) and dogs (Cummings and Haas, 1972, Rupp, 2016).

1.8 Complex ganglioside rescue mice

Molecular mimicry between human ganglioside GM1 and *C. jejuni* LOS is believed to mediate GBS pathogenesis (Yuki et al., 2004). There is a significant association between

AMAN and anti-GM1 antibodies (Yuki et al., 1990), however, autoantibodies to GM1 ganglioside are also present in sera from AIDP patients with a preceding *C. jejuni* infection (Rees et al., 1995a). It is unknown whether the pathological phenotype mediated by anti-GM1 antibodies arises from injury to the axonal or glial membrane (or both) in AMAN and AIDP. This is because GM1 is expressed on both axonal and glial membranes in wild type mice (Gong et al., 2002, Sheikh et al., 1999, Susuki et al., 2007b); therefore, current animal models are unable to differentiate between primary injury and the consequences of cell-specific membrane injury. To address this issue, we generated transgenic mice that had restricted expression of complex gangliosides, and thus GM1, to either the axonal or glial membrane (Yao et al., 2014); allowing us to anatomically segregate axonal and glial GM1 and investigate the downstream consequences of site-specific autoimmune injury. Expression of GalNAc-T, the enzyme responsible to produce complex gangliosides, was driven by either a neuronal promoter (Thy1.1, analogous to the previously published NFL promoter (Yao et al., 2014)) or a glial promoter (PLP). These mice were then crossed with *GalNAc-T*$^{-/-}$ mice, restricting expression of GM1 to axonal (*GalNAc-T*$^{-/-}$*-Tg(neuronal)*) or glial membranes (*GalNAc-T*$^{-/-}$*-Tg(glial)*), respectively; in contrast to wild type mice that express GM1 on both membranes (Figure 1.14).

The generation of these mice has given further insight into the function of gangliosides within the nervous system. It was previously demonstrated that mice deficient in GalNAc-T appear grossly normal up until 6 months where they present with an age-dependent neurodegenerative phenotype, characterised by weakness, ataxia, motor deficits, nerve degeneration and demyelination (Chiavegatto et al., 2000, Sheikh et al., 1999, Takamiya et al., 1996). Yao and colleagues established that the rescue of complex gangliosides in neurons, by the selective reintroduction of GalNAc-T activity, prevented the age-dependent neurodegenerative phenotype; however, *GalNAc-T*$^{-/-}$*-Tg(glial)* mice exhibited the same phenotype as *GalNAc-T*$^{-/-}$ mice (Yao et al., 2014). Thus, it was concluded that complex ganglioside expression in neurons, but not glia, is essential in maintaining nervous system integrity. In addition, nodal abnormalities are present at 6 months in *GalNAc-T*$^{-/-}$*-Tg(neuronal)* and *GalNAc-T*$^{-/-}$*-Tg(glial)* mice, highlighting the importance of complex ganglioside expression within lipid rafts on both membranes at the NoR (reviewed by (McGonigal and Willison, 2021)). Nevertheless, assessment of nodal organisation at 4-6 weeks of age in *GalNAc-T*$^{-/-}$*-Tg(neuronal)* and *GalNAc-T*$^{-/-}$*-Tg(glial)* mice was comparable to that of wild type mice. However, there was evidence of early-

stage nodal disruption in *GalNAc-T$^{-/-}$-Tg(glial)* mice, therefore it was suggested that these mice should not be used beyond 4-6 weeks of age in experimental studies when investigating autoimmune injury (McGonigal and Willison, 2021). Overall, these transgenic mice are invaluable tools to study the downstream consequences of antibody binding selectively to axonal or glial membranes at the NoR.

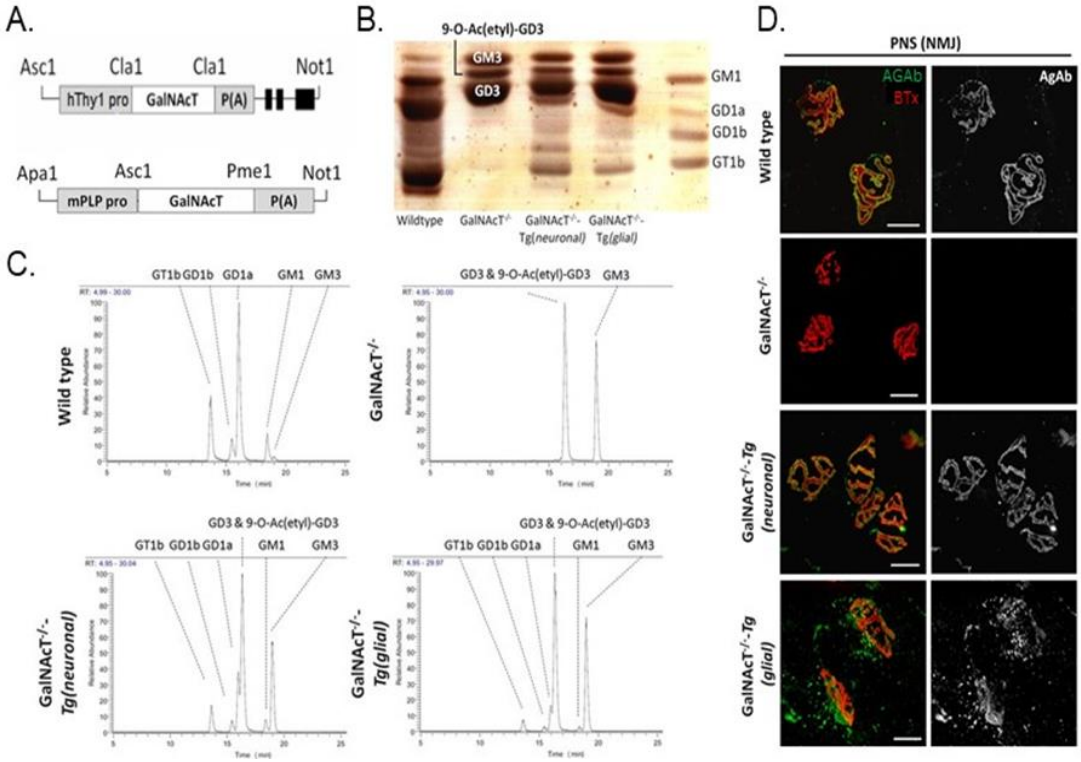

Figure 1.14: Restricted expression of complex gangliosides in *GalNAc-T$^{-/-}$-Tg(neuronal)* and *GalNAc-T$^{-/-}$-Tg(glial)* mice. A) GalNAc transferase driven by Thy1 or PLP promoter to restrict expression to axonal or glial membranes, respectively. B) TLC of extracts from brain demonstrate complex gangliosides are absent in *GalNAc-T$^{-/-}$* mice but are restored in *GalNAc-T$^{-/-}$-Tg(neuronal)* and *GalNAc-T$^{-/-}$-Tg(glial)* mice. C) Mass spectrometry confirms TLC results – complex gangliosides have been successfully restored in *GalNAc-T$^{-/-}$-Tg(neuronal)* and *GalNAc-T$^{-/-}$-Tg(glial)* mice. D) Fluorescent images demonstrate anti-ganglioside antibody (AGAb; green) on the axolemma in wild type and *GalNAc-T$^{-/-}$-Tg(neuronal)* mice overlying the endplate, identified by bungarotoxin (BTx; red). In contrast, AGAb is present overlying the perisynaptic Schwann cells at the neuromuscular junction (NMJ) in *GalNAc-T$^{-/-}$-Tg(glial)* mice. AGAb staining is absent in *GalNAc-T$^{-/-}$* mice. Modified with permission from (Yao et al., 2014).

Since the generation of the ganglioside rescue mice, an acute axonal model, representative of AMAN, has been generated by McGonigal and colleagues (McGonigal et al., 2016). In this model, *GalNAc-T$^{-/-}$-Tg(neuronal)* mice were used to target the axonal membrane with an anti-GM1 mAb. Consequently, this resulted in the loss of axonal integrity at the NMJ which was attenuated following complement inhibition (McGonigal

et al., 2016). The aim of this thesis was to develop the counterpart demyelinating model by exclusively targeting the glial membrane in *GalNAc-T$^{-/-}$-Tg(glial)* mice and compare the resulting injury at the distal NoR with the currently unknown nodal phenotype in *GalNAc-T$^{-/-}$-Tg(neuronal)* mice.

1.9 Hypothesis and aims of thesis

The pathogenesis of AIDP and secondary bystander axonal injury are poorly understood due to the limited availability of suitable animal models, in comparison to the established mechanisms involved in primary axonal degeneration in AMAN. Both primary and secondary axonal degeneration are associated with a poor prognosis in GBS (Altmann et al., 2020, Martín-Aguilar et al., 2020); thus, understanding the diverse degenerative mechanisms is essential to develop targeted treatments to improve long-term prognosis.

The antigenic target(s) that mediate AIDP have yet to be discovered however, results from patient autopsy studies have demonstrated the presence of complement deposits on Schwann cell (glial) membranes (Hafer-Macko et al., 1996b), suggesting that the antigenic target may be located on this membrane. Molecular mimicry between human ganglioside GM1 and *C. jejuni* LOS is believed to mediate GBS pathogenesis (Yuki et al., 2004). Although there is a significant association between AMAN and anti-GM1 antibodies (Yuki et al., 1990), autoantibodies to GM1 ganglioside are also present in sera from AIDP patients with a preceding *C. jejuni* infection (Rees et al., 1995a). It is unknown whether the pathological phenotype mediated by anti-GM1 antibodies arises from injury to the axonal or glial membrane (or both) in AMAN and AIDP. Current animal models are unable to differentiate between primary injury and the consequences of cell-specific membrane injury because GM1 is expressed on both axonal and glial membranes in wild type mice (Gong et al., 2002, Sheikh et al., 1999, Susuki et al., 2007b). Hence, the overall aim of this thesis was to develop animal models of peripheral neuropathy to investigate the consequences of axonal and glial-directed anti-GM1 antibody attack.

It has previously been demonstrated that wild type mice (on a C57BL/6 background) are not suitable for passive immunisation injury due to AGAbs being sequestered by global ganglioside expression (Cunningham et al., 2016). Moreover, as GM1 is expressed on both axonal and glial membranes in wild type mice, it is not possible to distinguish whether the

resulting pathological phenotype arises from injury to one or other, or both membranes. To overcome this issue, we generated transgenic mice with exclusive expression of complex gangliosides (including GM1) to either axonal (*GalNAc-T$^{-/-}$-Tg(neuronal)*) or glial membranes (*GalNAc-T$^{-/-}$-Tg(glial)*), allowing us to selectively target each membrane independently. Cunningham established that AGAb sequestration did not occur in the neuronal or glial ganglioside rescue mice (Cunningham et al., 2016); thus, corroborating their use to model peripheral nerve injury models over wild type mice.

An *in vivo* axonal mouse model of AMAN has been established in *GalNAc-T$^{-/-}$-Tg(neuronal)* mice (McGonigal et al., 2016). It was demonstrated that passive immunisation with anti-GM1 antibody resulted in complement-mediated injury to the axonal membrane, presenting as a loss of axonal integrity at the distal motor nerve terminal. Anti-GM1-mediated injury to the axolemma at the NoR has yet to be established in *GalNAc-T$^{-/-}$-Tg(neuronal)* mice. Currently, there are no AGAb-mediated animal models which exclusively target the glial membrane and thus, the pathogenesis of demyelination is not clearly defined. In addition, establishing a demyelinating animal model is critical to determine the downstream mechanisms which lead to secondary axonal degeneration. Therefore, the aim of this thesis was to develop a demyelinating model by exclusively targeting the glial membrane in *GalNAc-T$^{-/-}$-Tg(glial)* mice and compare the resulting injury at the distal NoR with the currently unknown nodal phenotype in *GalNAc-T$^{-/-}$-Tg(neuronal)* mice. Moreover, AIDP has a predominantly demyelinating phenotype, however, secondary 'bystander' injury can occur to the axon through unknown mechanisms (Asbury et al., 1969, Feasby et al., 1993). By exclusively targeting the glial membrane in *GalNAc-T$^{-/-}$-Tg(glial)* mice, independently of the axonal membrane, this provides the opportunity to investigate the secondary consequences to the axon. Hence, axon integrity was then assessed following targeted injury to the glial membrane in *GalNAc-T$^{-/-}$-Tg(glial)* mice.

Complement inhibition has been demonstrated to be protective in animal models of AMAN (McGonigal et al., 2016, Phongsisay et al., 2008). However, it has yet to be established whether inhibition of complement would prevent the resulting phenotype in the demyelinating variant. Thus, following the characterisation of the newly developed anti-GM1 mAb-mediated paranodal demyelinating injury model, it was investigated whether complement inhibition attenuated injury to the glial membrane.

On the basis of this background, my hypotheses were:

- The binding capability of anti-GM1 ligands would differ between the different mouse genotypes based on accessibility of GM1 on the plasma membrane. In addition, the staining pattern of bound anti-GM1 ligand would differ between strains of mice, depending on what membrane(s) GM1 is expressed on.
- Wild type mice would be resistant to injury following passive immunisation with anti-GM1 mAb. On the other hand, *GalNAc-T$^{-/-}$-Tg(neuronal)* and *GalNAc-T$^{-/-}$-Tg(glial)* mice would be suitable models to investigate the contribution of nodal membrane injury in GBS. It was hypothesised that the resulting injury at the NMJ and NoR would differ depending on whether the axonal (*GalNAc-T$^{-/-}$-Tg(neuronal)*) or glial *GalNAc-T$^{-/-}$-Tg(glial)*) membrane was selectively targeted.
- Exclusive injury to the glial membrane in *GalNAc-T$^{-/-}$-Tg(glial)* mice would induce 'bystander' injury to the axon, resulting in secondary axonal degeneration.
- Injury to the glial membrane would be attenuated following complement inhibition in *GalNAc-T$^{-/-}$-Tg(glial)* mice.

Based on these hypotheses, my aims were:

- Assess the binding pattern of different anti-GM1 ligands in wild type, *GD3s$^{-/-}$, GalNAc-T$^{-/-}$-Tg(neuronal), GalNAc-T$^{-/-}$-Tg(glial)* and *GalNAc-T$^{-/-}$* mice and select a single anti-GM1 antibody that binds to both the axonal and glial membrane.
- Investigate the consequences of anti-GM1 antibody-mediated injury when both membranes are targeted *in vivo* in wild type mice and to compare this to the injury produced when the axonal or glial membranes are targeted independently in *GalNAc-T$^{-/-}$-Tg(neuronal)* and *GalNAc-T$^{-/-}$-Tg(glial)* mice, respectively.
- Determine whether there are secondary effects to the integrity of the axon following targeted injury to the glial membrane in *GalNAc-T$^{-/-}$-Tg(glial)* mice.
- Investigate the effects of complement inhibition in an acute anti-GM1 mAb mediated injury model in *GalNAc-T$^{-/-}$-Tg(glial)* mice.

2 Methods

2.1 Materials

2.1.1 Antibodies

The commonly used primary and secondary antibodies are illustrated in Table 2.1 and Table 2.2, respectively. The tables highlight the host, isotype, dilution, and manufacturer of each antibody.

Table 2.1: Details of primary antibodies used.

Antibody	Host	Isotype	Dilution		Manufacturer
			Sections	Whole-mount TS	
Neurofilament heavy (NFH; SMI 31)	Mouse	IgG1	1:1500	1:1000	Biolegend (*California, USA*)
Myelin basic protein (MBP)	Rat	IgG	1:500	1:500	BioRad (*California, USA*)
MAC C5b-9	Mouse	IgG2a	1:50	1:40	Dako (*Glostrup, Denmark*)
FITC conjugated human C3c complement	Rabbit	IgG	1:300	1:300	Dako (*Glostrup, Denmark*)
FITC conjugated human C1q complement	Rabbit	IgG	/	1:100	Dako (*Glostrup, Denmark*)
pan-Nav	Mouse	IgG1	1:100	1:100	Sigma-Aldrich (*Missouri, USA*)
Caspr	Rabbit	IgG	1:1000	1:500	Gifted from E. Peles (*Rehovot, Israel*)
pan-neurofascin	Rabbit	IgG	1:750	/	Gifted from Professor P. Brophy (*Edinburgh, UK*)
Ankyrin B	Mouse	IgG2a	1:800	1:200	Neuromab; Antibodies Inc (*California, USA*)
Ankyrin G	Mouse	IgG1	1:100	/	Invitrogen (*California, USA*)
Kv1.1	Rabbit	IgG	1:200	/	Alomone Labs (*Jerusalem, Israel*)
Caspase 3 Active	Rabbit	IgG	1:100	/	R&D systems (*Minnesota, USA*)

Table 2.2: Details of secondary antibodies used.

Antibody	Host	Isotype	Fluorophore	Dilution		Manufacturer
				Sections	Whole-mount TS	
Mouse IgG	Goat	IgG1/ IgG2a/ IgG3	Alexa Fluor 488, 555 or 647	1:500	1:500	Invitrogen (*California, USA*)
Mouse IgG	Goat	IgG2a/IgG2b /IgG3	Alexa Fluor 488/TRITC/Cy5	1:300	1:200	Southern Biotech (*Alabama, USA*)
Rat IgG	Goat	IgG	Alexa Fluor 488 or 555	1:1000	1:500	Invitrogen (*California, USA*)
Rabbit IgG	Goat	IgG	Alexa Fluor 488, 555, or 647	1:500	1:500	Invitrogen (*California, USA*)
Human IgM	Goat	IgM (µ chain)	Alexa Fluor 488	1:500	/	Invitrogen (*California, USA*)
Mouse IgG (for ELISA)	Goat	IgG2b/IgG3	HRP conjugated	1:3000		Invitrogen (*California, USA*)
Human IgM (for ELISA)	Goat	IgM	HRP conjugated	1:3000		Invitrogen (*California, USA*)

2.1.2 Buffers

A 10x stock solution of phosphate buffered saline (PBS), was prepared as follows: 1400 mM NaCl, 18 mM KH_2PO_4, 27 mM KCl, 100 mM Na_2HPO_4 made up to 1L in distilled water (dH_2O). 10x PBS was used at a 1 in 10 dilution to give 1x PBS working buffer.

Ringer's solution is an isotonic solution which mimics a physiological solution, used to keep tissue alive *ex vivo.* A 10x stock solution was prepared containing the following salts: 116 mM NaCl, 4.5 mM KCl, 1 mM $MgCl_2$, 1 mM NaH_2PO_4, 23 mM $NaHCO_3$, 11 mM glucose and made up to 1L in deionised water (dH_2O). For use, 10x Ringer's was diluted 1 in 10 and bubbled in medical oxygen for 10 minutes before adding 2 mM $CaCl_2$ (1:500), producing 1x Ringer's solution.

All buffers were prepared and used at pH 7.3.

2.1.3 Commonly used reagents

The following reagents were used routinely:

- GM1 ganglioside, stock concentration of 1 mg/ml (*Sigma-Aldrich, Missouri, USA*)
- Alpha-bungarotoxin (BTx) – Alexa Fluor 488, 555, 647 conjugates (*Invitrogen; California, USA*)
- Cholera toxin subunit B (CTB) – Alexa Fluor 488 conjugate (*Invitrogen; California, USA*)
- Normal goat serum (NGS), heat inactivated at 60℃ for 30 minutes (*Sigma-Aldrich; Missouri, USA*)
- Normal human serum was taken from a single donor and serum stored at -80℃
- Bovine serum albumin (BSA; *Sigma-Aldrich; Missouri, USA*)
- Citifluor antifade mounting medium (*Citifluor; Canterbury, UK*)
- Vectashield antifade mounting medium with DAPI (*Vector laboratories, California, USA*)
- Tissue Tek optical cutting temperature compound (OCT; *Tissue-Tek®; Netherlands)*
- Triton X-100 (*Sigma-Aldrich; Missouri, USA*)
- DMEM/F12 Media (1X Gibco; *Thermo Fisher Scientific; Massachusetts, USA*)
- Foetal calf serum (FCS; *Invitrogen; California, USA*)
- 4% paraformaldehyde (PFA; 20g CH_2O added to 500 mL 1x PBS and heated on a hotplate to 60-70℃. Whilst stirring, 1 M NaOH was added until solution turned clear. Aliquoted and stored at -20℃ until required)
- 0.1 M glycine ($C_2H_5NO_2$; dissolved in 1x PBS)
- 30% sucrose ($C_{12}H_{22}O_{11}$; dissolved in 1x PBS)

2.1.4 Human C2 complement inhibitor

Bro-2 is an anti-C2 IgG4 antibody which acts by binding to the S2 domain of C2 and preventing interaction with C4b. The C2 inhibitor, Bro-2, is analogous to the previously published anti-C2 IgG1 humanised antibody, ARGX-117 (Van de Walle et al., 2020). Unlike ARGX-117, Bro-2 does not carry the mutation in its Fc region; thus, Bro-2 is unable to dissociate from C2 in the endosome and be recycled into the circulation, reducing the half-life of the antibody. Despite this, both antibodies are the same and have the same mechanism of action. The inhibitor only binds to human C2 and does not inhibit the mouse complement pathway. Bro-2 was used for *ex vivo* studies and ARGX-117 was used to perform the *in vivo* complement inhibition studies. Argenx (*Netherlands*), supplied Bro-

2 at a stock concentration of 4.2 mg/ml and an isotype control (IgG4), stock concentration of 3.6 mg/ml. Additionally, Argenx supplied ARGX-117 at a stock concentration of 128 mg/ml and an isotype control (IgG1), stock concentration of 36 mg/ml. All were stored at -20℃ until required.

For *ex vivo* studies, Bro-2 and IgG4 isotype control were used at 100 or 200 µg/ml when assessing the integrity of the nerve terminal and NoR, respectively in our injury models. The concentration of ARGX-117 and IgG1 isotype control used for *in vivo* studies was 200 mg/kg.

2.2 Mice

Five different strains of mice were used throughout this thesis, and they are referred to as wild type*, GD3s$^{-/-}$ GalNAc-T$^{-/-}$, GalNAc-T$^{-/-}$-Tg(neuronal)* and *GalNAc-T$^{-/-}$-Tg(glial)* mice. All mice were on a C57Bl/6 background.

GD3s$^{-/-}$ mice are deficient in GD3 synthase, therefore they do not express b- or c-series gangliosides. As a consequence, these mice overexpress a-series gangliosides (Okada et al., 2002).

GalNAc-T$^{-/-}$ mice were generated and supplied by Furukawa and colleagues. These mice have a disrupted β1,4-*N*-acetylgalactosaminyltransferase gene, which is responsible for the biosynthesis of complex gangliosides (Takamiya et al., 1996). Therefore, these mice do not express complex gangliosides.

The *GalNAc-T$^{-/-}$-Tg(neuronal)* and *GalNAc-T$^{-/-}$-Tg(glial)* mice have been described previously (Yao et al., 2014, McGonigal et al., 2016). In brief, mice that express the full-length cDNA encoding GalNAc-T under the control of either the Thy1.2 promoter or the proteolipid protein (PLP) promoter, were crossed with *GalNAc-T$^{-/-}$* mice, restricting expression of complex gangliosides to axonal (*GalNAc-T$^{-/-}$-Tg(neuronal)*) or glial membranes (*GalNAc-T$^{-/-}$-Tg(glial)*), respectively. *GalNAc-T$^{-/-}$-Tg(neuronal)* and *GalNAc-T$^{-/-}$-Tg(glial)* mice were then crossed with fluorescent adult B6.Cg-Tg mice that expressed intracytosolic cyan fluorescent protein (CFP) in their peripheral motor and sensory axons (Thy1-CFP).

Genotyping was done by polymerase chain reaction and phenotyping of ear-punches to confirm inheritance of transgenes. All genotyping was performed by Dr Denggao Yao.

All mice used in *in vivo* experiments were 4-5 weeks old; for *ex vivo* experiments, mice were aged between 4-6 weeks of age. *GalNAc-T$^{-/-}$-Tg(glial)* mice present with an age dependent phenotype (Yao et al., 2014), and so to avoid this interfering with the results, mice were used at a young age when *GalNAc-T$^{-/-}$-Tg(glial)* mice appear structurally normal at the NoR (McGonigal and Willison, 2021). Male and female mice, ranging from 10-18 g, were used during experiments. All mice were housed with a light/dark cycle of 12h/12h and they had unlimited access to food and water. Animals were killed with a rising concentration of CO_2 and cervical dislocation was then performed to confirm death. All experiments complied with the United Kingdom Home Office Guidelines.

2.3 Production of anti-GM1 antibody

2.3.1 Hybridoma cell lines

The mouse monoclonal anti-GM1 antibodies, DG1 and DG2, were produced by fusing the splenocytes from GM1 lipopolysaccharide immunized ganglioside deficient *GalNAc-T$^{-/-}$* mice with a myeloma cell line, creating a hybridoma (G Meehan, 2015, thesis). Immunization protocols are described previously (Goodyear et al., 1999, Bowes et al., 2002). Additionally, a human anti-GM1 IgM mAb, named BO3, was cloned from peripheral blood lymphocytes from a patient with MMN and fused with a mouse myeloma cell line, previously described in detail by (Willison et al., 1994).

Cell line stocks were frozen down in DMEM/F12 media, containing 20% heat inactivated FCS and 10% dimethyl sulfoxide (DMSO), and stored in liquid nitrogen. The anti-GM1 mAb, DG2, was selected to use in all experiments.

2.3.2 Monoclonal antibody production

For antibody production, cells were removed from liquid nitrogen and thawed briefly before being added to 10 ml of pre-heated (32°C) growth media (DMEM/F12 media with 5% FCS, 1% penicillin/streptomycin solution (100x*, Sigma-Aldrich; Missouri, USA*) and 0.1% Fungin (*InvivoGen; Toulouse, France*)). The cells were then spun down at 300 *g* in a

Biofuge Primo Centrifuge (*Thermo Fisher Scientific; Massachusetts, USA*) for 5 minutes. The DMSO contaminated media was discarded, and the pellet of cells were re-suspended in 5 ml of pre-heated media. The re-suspended cells were split between two T75 vented cell culture flasks (*Corning; New York, USA*) containing 35 ml pre-heated growth media. Cells were left to grow in an incubator at 37℃ with 5% CO_2. Once confluent, cells were split and transferred into T150 vented cell culture flasks (*Corning; New York, USA*) containing 110 ml pre-heated media.

To collect antibody from the supernatant, the cell suspension was removed from the T150 flask and transferred into 50 ml Falcon tubes. Suspension was centrifuged at 300 *g* and the supernatant was collected and stored at -20℃ until purification. Cells were re-suspended in fresh media warmed to 32℃ and transferred back into T150 flasks. Flasks were topped up with 100 ml of media and placed back into the incubator. Cells were split approximately two times a week or more frequently if cells became too confluent.

The BO3 supernatant was concentrated using a 250 ml Vivacell pressure sample concentration device (*Sartorius Stedim Biotech; Germany*). Meanwhile, DG1 and DG2 were purified as explained below.

2.3.3 Antibody purification

The frozen supernatants were defrosted overnight and then filtered through 180 µm filter paper (*GE Healthcare, Little Chalfont, UK*) to remove particulate matter. Filtered supernatant was dialysed overnight in 10x volume binding buffer (0.2 M NaH_2PO_4 $2H_20$, 0.2 M Na_2HPO_4) at 4℃. The supernatant was then filtered through a 0.22 µm membrane and stored at 4℃. Binding buffer and 0.1 M glycine were also filter sterilised prior to use.

A HiTrap Protein G HP column *(GE Healthcare, Little Chalfont, UK)* was used. Protein G has a high affinity for IgG antibodies, so antibody in the supernatant binds to the protein, meanwhile the growth media flows through the column and is eventually discarded as waste material. The column was washed with 10x column volume binding buffer prior to loading the supernatant to equilibrate the column to pH 7.4. Flow through was collected and stored at 4℃ until confirmation of successful antibody purification. Once the supernatant had been loaded, the column was washed with binding buffer and 10x 5 ml wash samples were collected. To elute the antibody, elution buffer (0.1 M glycine-HCl pH

2.7) was loaded into the column and 10x 5 ml elutions were collected in bijoux bottles containing the required volume of neutralising buffer (TRIS-HCl pH 9.0). Following antibody elution, the column was washed through with 25 ml binding buffer, then 25 ml of 20% filter sterile EtOH before being stored at 4℃.

The protein concentration of the wash and elution aliquots were determined using a DS-11 Series spectrophotometer (*DeNovix; Delaware, USA*) and the concentrated elution aliquots were pooled together for buffer exchange. The pooled antibody was dialysed overnight at 4℃ in 10x volume of PBS. Binding of the purified antibody to GM1 ganglioside was confirmed by performing an ELISA (see section 2.7). Antibodies were aliquoted and stored at -80℃ until required for experiments. For *in vivo* experiments, aliquots were only freeze-thawed once to reduce the risk of introducing contamination.

2.4 Nerve-muscle preparations

2.4.1 Diaphragm dissection

The *in vivo* procedure used throughout this thesis involves the delivery of anti-GM1 mAb and complement to the peritoneal cavity (see section 2.6.1). Due to the proximity of the diaphragm to the site of injection, this results in intra-diaphragmatic nerve and nerve terminal injury (Halstead et al., 2008). Therefore, the diaphragm was dissected at the end of the *in vivo* experiment and immunofluorescence analysis was performed. Additionally, diaphragm sections were required to trial staining protocols, perform complement assays and to perform *in vitro* dose-response studies.

Mice were culled with a rising concentration of CO_2 followed by a secondary measure (cervical dislocation); they were then pinned supine and an incision was made up the midline of the body to expose the ribcage and abdomen. The peritoneum was opened, and the viscera were moved downwards, exposing the diaphragm. Once the diaphragm was exposed, it was either: cut away from the ribcage, severing the blood vessels, snap frozen and stored at -80℃ for unfixed immunofluorescence staining; or the diaphragm was removed with ribs bordering the edge, so the diaphragm could be pinned out flat on Sylgard to be fixed in 4% PFA or 2.5% glutaraldehyde for immunofluorescence or ultrastructure analysis.

2.4.2 Diaphragm sectioning

The diaphragm muscle is a relatively thick muscle which can be sectioned; maximising the number of staining protocols used per mouse. OCT was applied to a chuck and left to freeze before using a freezing cryostat (*Bright Instruments, Cambridge, UK*), to create a longitudinal flat surface. Unfixed diaphragm was thawed and then mounted flat onto OCT surface and left to freeze. Tissue was cut at -24℃ into 15, 10, and 8 µm longitudinal sections and collected onto 3-aminopropyltriethoxysilane (APES) coated slides. For fixed diaphragm, a small drop of OCT was applied to the diaphragm and mounted flat onto frozen OCT and left to freeze. Fixed diaphragm was cut into 15 or 10 µm longitudinal sections and collected on APES coated slides. All slides were left to dry at room temperature (RT) for an hour before being stored at -20℃ until further use.

2.4.3 Triangularis sterni *ex vivo* preparations

The triangularis sterni (TS) muscle was selected for use in *ex vivo* experiments because it is extremely advantageous for investigating nerve terminals and distal nerves, as it is highly innervated by the third, fourth and fifth intercostal nerves. The muscle, which is located on the inner surface of the ribcage, is also very thin and flat and so can be used for whole-mount preparations. Finally, the preparation can be kept 'alive' in an oxygenated physiological solution for several hours, preserving morphology and structure, making it an ideal muscle for *ex vivo* studies (McArdle et al., 1981).

The method used for TS dissection was modified from (Kerschensteiner et al., 2008). In brief, the ribcage was removed from the mouse and pinned out flat, ventral side-up, in a Sylgard-lined dish containing oxygenated Ringer's solution. The pectoral muscles and loose connective tissue were removed. The ribcage was then turned dorsal side-up, and remnants of thymus and diaphragm were removed. The dorsal segments of the ribs were trimmed to the cartilage-bone transition, and the ribcage was cut in half at the sternum. The preparations were pinned out flat in small Sylgard-lined dishes and maintained in Ringer's. Each mouse provides two TS preparations, allowing for one preparation to receive treatment/injury and the other half to serve as a biological uninjured control. At this stage, the *ex vivo* preparations were used to study the effects of complement inhibition on axonal integrity at the nerve terminal, and the integrity of axo-glial proteins at the NoR (see section 2.7.2). After completion of the experiment and the tissue being

fixed in 4% PFA as per the protocol for diaphragm, the muscle was carefully detached from the ribs and intercostal muscles. The muscle was peeled away from the ribcage and cut using fine scissors. Once detached from the ribcage, the muscle was cleaned by removing any fat and connective tissue. Tissue was then frozen down and stored at -80℃ until immunofluorescence staining was performed.

2.4.4 Sciatic nerve preparations

The sciatic nerve is the largest nerve trunk in mammals and consists of both motor and sensory axons. It was used to compare the staining between different anti-GM1 ligands. To dissect the sciatic nerve, mice were culled with a rising concentration of CO_2 followed by a secondary measure and pinned out dorsal side up. An incision was made through the skin overlying the pelvis and the upper thigh muscles were cleared away, revealing a pocket containing the sciatic nerve. The nerve was tied off with a piece of thread distally, at the branch point of the nerve, and proximally, adjacent to the spinal cord, and carefully removed. The sciatic nerve was then pinned out flat (through the string) in a sylgard-coated dish containing Ringer's solution and was desheathed, to remove the outer epineurium, by using the needle of a 0.3 ml insulin syringe. At this stage, the desheathed sciatic nerve preparation was used for anti-GM1 binding studies explained in section 2.5.

2.4.5 Sciatic nerve sectioning

Fixed sciatic nerve was placed flat in a small plastic mould and OCT was added. The preparation was frozen and stored at -80℃ until required for sectioning. To section the sciatic nerve, the block of OCT and sciatic nerve was trimmed to remove the excess OCT. OCT was applied to a chuck and the block of OCT containing sciatic nerve was placed on top and left to freeze in the cryostat. Longitudinal sections of 15 µm were cut and collected on APES coated slides. Slides were left to dry for 2-hours at RT before being stored at -20℃ until immunofluorescence staining was performed.

2.5 Antibody binding characterisation studies

Initial anti-GM1 antibody binding characterisation studies were performed in sciatic nerves to select a single anti-GM1 ligand which could bind to both axonal and glial membranes. Sciatic nerves were dissected from wild type, *GD3s*$^{-/-}$, *GalNAc-T*$^{-/-}$, *GalNAc-T*$^{-/-}$

-*Tg(neuronal)* and *GalNAc-T*$^{-/-}$*-Tg(glial)* mice, as described previously (see section 2.4.4) and maintained in Ringer's solution. The nerves were carefully desheathed before applying 100 µg/ml of DG1, DG2 or BO3 or Alexa Fluor™ 488 conjugated CTB (1/250), prepared in Ringer's, for 2 hours at 4℃. They were then washed in Ringer's solution before applying the relevant secondary antibodies for 1 hour at 4℃. As CTB is conjugated, it was left to incubate for 3 hours in total. After washing in Ringer's, the nerves were fixed in 4% PFA for 20 minutes at 4℃. Following fixation, the nerves were washed in PBS, then 0.1M glycine, followed by PBS again for 10 minutes each. They were then snap frozen in OCT and sectioned as explained in section 2.4.5.

The sectioned sciatic nerves were then permeabilised for 10 minutes in EtOH at -20℃. Following washes in PBS, the nerves were incubated in mouse anti-pan-Nav (pNav; 1/100) and rabbit anti-Caspr (1/500) made up in 0.1% Triton X-100 and 3% NGS, overnight at 4℃. Nerves were then washed in PBS before being incubated in either Alexa Fluor™ 488 anti-mouse IgG2b (1/300), Alexa Fluor™ 488 anti-mouse IgG3 (1/500) or Alexa Fluor™ 488 anti-human IgM (1/500) to identify DG1, DG2 or BO3, respectively, along with Alexa Fluor™ 555 anti-mouse IgG1 (1/500) and Alexa Fluor™ 647 anti-rabbit IgG (1/500) for 2 hours at RT. As CTB is primary conjugated, it was incubated in pNav and Caspr secondaries only. Secondary antibodies were prepared in PBS and 3% NGS. The nerves were washed in PBS before applying citifluor and a coverslip and sealing the slide with nail varnish.

2.6 *In vivo* procedures

2.6.1 Acute injury model

All experiments complied with United Kingdom Home Office guidelines. The *in vivo* model used here is based on an injury model established by (Halstead et al., 2008), as illustrated in Figure 2.1. Wild type*, GalNAc-T*$^{-/-}$*-Tg(neuronal)* and *GalNAc-T*$^{-/-}$*-Tg(glial)* 4-week-old mice, weighing 10-18 g, were handled prior to being put on procedure, and then habituated to WBP chambers (*Electro-Medical Measurement systems (EMMS); Hampshire, UK*) for 1 hour (see below). The following day, a 20-minute baseline recording was taken before mice were injected intraperitoneally (IP) with 50 mg/kg of anti-GM1 mAb (known as DG2), or the equivalent volume of PBS for control groups. As a source of

complement, 30 µl/g of NHS was then administered IP 16 hours later. WBP was performed from 3.5 hours – 5.5 hours post injury. At 6 hours post injury, mice were asphyxiated with a rising concentration of CO_2 followed by a secondary measure. A blood sample was taken for ELISA and complement assay, and the diaphragm was harvested. The blood was spun down at 10,000 *g* for 10 minutes at 4℃, the supernatant was collected and stored at -80℃ until use. Half of the diaphragm was snap frozen and stored at -80℃ for immunofluorescence analysis. The remaining half was halved again, and the two pieces of diaphragm were pinned out flat on Sylgard. One piece was fixed in 4% PFA for 1 hour at 4℃ for immunofluorescence analysis, and the other piece was placed in 2.5% glutaraldehyde and stored at 4℃ for ultrastructure analysis. Following fixation in 4% PFA, the diaphragm was unpinned and washed in PBS, then 0.1 M glycine to reduce autofluorescence, followed by PBS again for 10 minutes each. The diaphragm was then left in cryoprotectant, 30% sucrose, overnight at 4℃. The following morning, the diaphragm was snap frozen and stored at -80℃ until required for immunostaining. A power analysis was performed using G*Power software (3.0.10). The required sample size for 80% power assuming a 5% significance level was determined to be an n of four for each injury group.

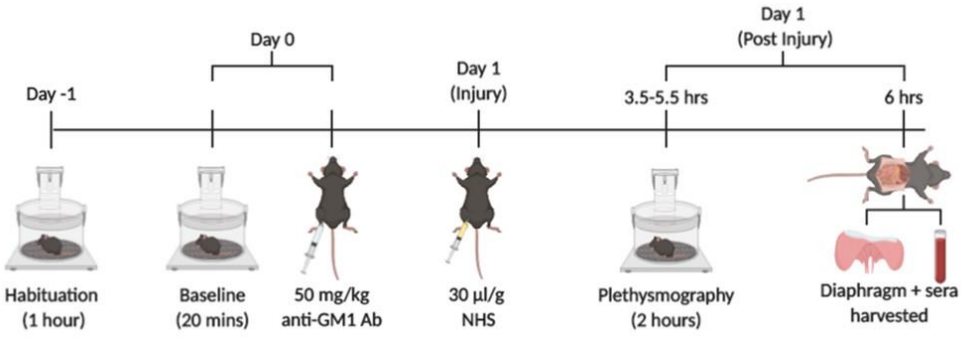

Figure 2.1: Acute *in vivo* injury model performed in wild type, *GalNAc-T$^{-/-}$-Tg(neuronal)* and *GalNAc-T$^{-/-}$-Tg(glial)* mice.

2.6.2 Extended injury model

To determine whether secondary axonal degeneration occurs following injury to the glial membrane, the *in vivo* injury model was extended and performed in *GalNAc-T$^{-/-}$-Tg(glial),* 4-week-old mice. The details of the *in vivo* experiment are detailed in the schematic in Figure 2.2. The same protocol was followed as was described for the acute injury model (2.6.1) except mice were survived until 24 hours post NHS injection. A 20-minute WBP

recording was performed at 6, 12 and 24 hours to monitor respiratory function. At 24 hours post NHS injection, mice were culled with a rising concentration of CO_2 followed by a secondary measure, a blood sample was taken for ELISA, and the diaphragm was harvested for immunofluorescence analysis. The blood was spun down at 10,000 *g* for 10 minutes at 4℃, the supernatant was collected and stored at -80℃ until use. Half of the diaphragm was snap frozen and stored at -80℃ and the remaining half was pinned out flat on Sylgard and fixed in 4% PFA for 1 hour at 4℃. Following fixation, the diaphragm was processed as described previously (2.6.1).

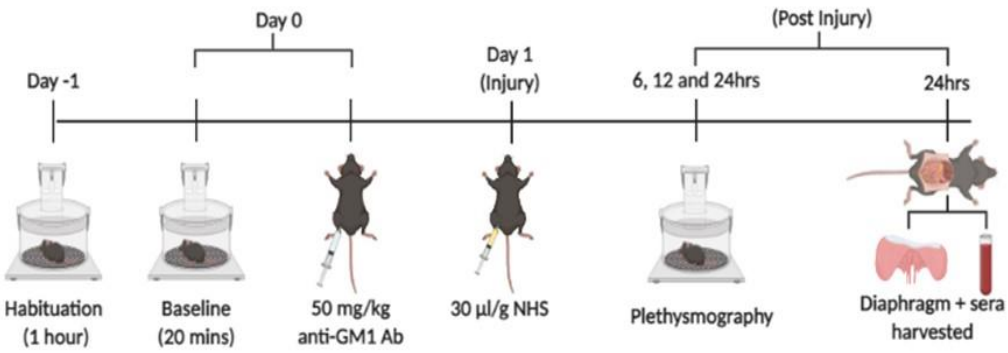

Figure 2.2: Extended *in vivo* injury model performed in *GalNAc-T$^{-/-}$-Tg(glial)* mice.

2.6.3 Whole-body plethysmography

As previously explained, the *in vivo* models detailed above target the diaphragm. The diaphragm is the main inspiratory muscle in the body and its function can be measured using WBP. This is a non-invasive method which can be used to measure and assess respiratory function in small animals. The main outputs of WBP are tidal volume (TV), the normal volume of air which is displaced during inhalation and exhalation, and respiratory rate (RR), the number of breaths per minute (Lim et al., 2014). In this injury model, a respiratory phenotype presents due to paralysis of the intra-diaphragmatic nerve and can be identified by a reduction in TV, measured by WBP (Halstead et al., 2008, McGonigal et al., 2016). Furthermore, mice present with a pinched wasp-like abdomen, indicative of diaphragm paralysis, and so the phenotype can be monitored physically throughout the experiment.

Prior to the start of the experiment, the WBP chambers were calibrated according to the manufacturer's instructions (*EMMS; Hampshire, UK*). Mice were habituated to the WBP chambers for 1 hour, at least 8 hours prior to taking a baseline recording. Before every

recording, mice were left to acclimatise to the chambers for at least 15 minutes. A 20-minute baseline recording was taken before anti-GM1 mAb injection. For the acute injury model (2.6.1), a 2-hour recording was taken between 3.5-5.5 post NHS injection, but for the extended injury model (2.6.2) a 20-minute recording was taken at 6, 12 and 24 hours post NHS delivery. All recordings were performed using eDaq software (version 1.9.4). Each data output from the eDaq software represent an average from 25 accepted breaths; considered as a TV over 0.01 ml. When determining the TV and RR at each time point, data was collected as an average of the last 25 data outputs.

2.7 Inhibition of human C2 complement

2.7.1 *In* vitro: Inhibitor dose-response study

Diaphragm was harvested from naïve *GalNAc-T$^{-/-}$-Tg(neuronal)* mice and sectioned as described previously (2.4.1). Tissue was blocked for 30 minutes in 10% NGS prepared in Ringer's solution. Mouse anti-GM1 mAb was then prepared at a concentration of 10 µg/ml in Ringer's solution and applied to the tissue for 2 hours at 4°C in a humidifying chamber, meanwhile the negative control received Ringer's solution only. Following antibody incubation, tissue was washed in Ringer's. A stock solution of C2 inhibitor (Bro-2), or the IgG4 isotype control was prepared in Ringer's medium at a concentration of 2.5 µg/ml and a 5-fold serial dilution was performed giving a concentration range of 0.004 µg/ml – 2.5 µg/ml. Once the inhibitor had been diluted out, 4% NHS (as a source of complement) was added to each dilution and left for 10 minutes, prior to applying the solution to the tissue. The positive and negative controls received 4% NHS in Ringer's only. The solutions were applied to the tissue for 2 hours at RT in a humidifying chamber. The sections were then washed before FITC conjugated anti-human C3c complement (1/300), Cy5 anti-mouse IgG3 (1/300) and Alexa Fluor™ 555 conjugated α-BTx (1/750) were prepared in PBS and applied to the tissue for 3 hours at RT to identify complement, anti-GM1 mAb and BTx, respectively. After antibody incubation, the tissue was washed and mounted in citifluor.

2.7.2 *Ex vivo*: Effect of human C2 complement inhibition

Based on the results from the *in vitro* dose-response and preliminary experiments, 100 µg/ml of Bro-2 was determined to be the optimal dose that successfully inhibited

complement in our acute *ex vivo* injury model when assessing the integrity of the nerve terminal. The *ex vivo* model used here is adapted from Halstead et al. (2008). Working solutions of 100 µg/ml Bro-2 (or 100 µg/ml IgG4 isotype control) and 40% NHS were prepared in Ringer's. Solutions were left for 10 minutes before adding 100 µg/ml anti-GM1 mAb. Control tissue received 40% NHS in Ringer's. Working solutions were added to the TS from *GalNAc-T$^{-/-}$-Tg(neuronal)* mice and left for 1 hour at 32℃ in a humidifying chamber.

As characterisation of the anti-GM1 mAb mediated injury in *GalNAc-T$^{-/-}$-Tg(glial)* mice showed that there was no change in axonal integrity at the nerve terminal in the acute *in vivo* injury model, it was therefore decided to focus on the integrity of the NoR in these mice in order to minimise the number of animals used in this experiment to comply with the 3Rs (NC3Rs). It has previously been shown *ex vivo,* that injury to the distal NoR occurs following 4 hours incubation in AGAb and complement (McGonigal et al., 2010). Initial experiments revealed that 200 µg/ml of Bro-2 was required to inhibit complement in this 4-hour *ex vivo* injury model. To investigate axo-glial integrity at the distal NoR, working solutions (prepared as described previously) were added to the TS from both *GalNAc-T$^{-/-}$-Tg(neuronal)* and *GalNAc-T$^{-/-}$-Tg(glial)* mice and left to incubate for 4 hours at 32℃ in a humidifying chamber.

Following antibody and complement incubation, the TS was washed 3x in cold Ringer's prior to being fixed in 4% PFA for 20 minutes at 4℃. The TS was then washed for 10 minutes in PBS, 0.1 M glycine and then PBS again at RT. The muscle was carefully cut away from the intercostal muscles, snap frozen and stored at -80℃ until required for immunofluorescence staining.

2.7.3 *In vivo:* Effect of human C2 complement inhibition

The acute *in vivo* model used here, outlined in Figure 2.3, is adapted from the acute *in vivo* model described in section 2.6.1. *GalNAc-T$^{-/-}$-Tg(glial)* mice, aged 4-6 weeks, weighing 10-18 g, were handled prior to being put on procedure, and then habituated to the WBP chambers for 1 hour. The following day, a 20-minute baseline recording was taken before mice were injected IP with 50 mg/kg of anti-GM1 mAb. The following morning, mice received 200 mg/kg of ARGX-117 or 200 mg/kg of IgG1 isotype control,

administered intravenously (IV). Ten minutes later, 30 µl/g of NHS was delivered IP as a source of complement. WBP was performed from 3.5 hours – 5.5 hours post injury. Heterozygous litter mates were used as naïve controls, receiving PBS instead of antibody and complement. At 6 hours post injury, mice were asphyxiated with a rising concentration of CO_2 followed by a secondary measure. A blood sample was taken for ELISA and the diaphragm was harvested for immunofluorescence analysis. The blood was spun down at 10,000 *g* for 10 minutes at 4℃, the supernatant was collected and stored at -80℃ until use. Half of the diaphragm was snap frozen and stored at -80℃, the remaining half was fixed in 4% PFA for 1 hour at 4℃ before being washed for 10 minutes in PBS, followed by 0.1 M glycine and then PBS again at RT. The fixed diaphragm was then left in cryoprotectant, 30% sucrose, overnight at 4℃. The following morning, the fixed diaphragm was snap frozen and stored at -80℃ until required for immunofluorescence staining. All experiments complied with United Kingdom Home Office guidelines.

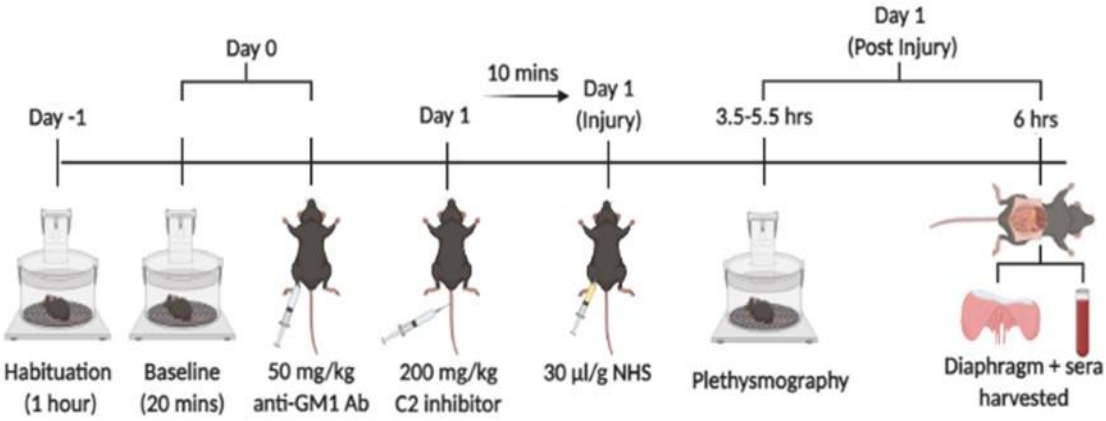

Figure 2.3: Acute *in vivo* injury model performed to assess the effects of C2 inhibition in *GalNAc-T$^{-/-}$-Tg(glial)* mice.

2.8 Enzyme-linked immunosorbent assay (ELISA)

ELISAs were performed to confirm the presence of anti-GM1 mAb in the mouse sera from *in vivo* experiments, or to check purified anti-GM1 mAb against GM1 ganglioside. Immulon 2HB 96 well plates (*Thermo Fisher Scientific; Massachusetts, USA*) were coated with 2 µg/ml GM1 ganglioside. Plates were blocked with 2% BSA-PBS for 1 hour at 4℃. After blocking, mouse serum or purified elution samples were prepared at 1/50 in 0.1% BSA-PBS and added to the ELISA plate; they were left to incubate overnight at 4℃. An aliquot of anti-GM1 mAb of known concentration was used as a positive control (10 µg/ml in 0.1% BSA-PBS). Plates were washed in cold PBS before the relevant HRP

conjugated secondary antibody (prepared in 0.1% BSA and PBS) was added and left to incubate for 1 hour at 4℃: goat anti-mouse IgG3-HRP conjugated (1/3000); goat anti-mouse IgG2b-HRP conjugated (1/3000); goat anti-human IgM-HRP conjugated (1/3000). Following 4 washes in chilled PBS, substrate solution (14 ml 0.1 M $C_6H_8O_7$, 16 ml 0.2 M Na_2HPO_4, 30 ml dH_2O, one 15 mg O-Phenylenediamine tablet, 20 µl 30% H_2O_2), prepared immediately before use, was added for 15 minutes in the dark at RT. To stop the reaction, 4N (2 M) H_2SO_4 was added. The plate was read on a TECAN Sunrise spectrophotometer (*Männedorf, Switzerland*) at an absorbance of 492 nm using Magellan software.

2.9 Topical complement assay

To confirm that the NHS IP injection had been delivered successfully, a topical complement assay was performed using the sera taken from the mice at the end of the acute *in vivo* experiment (2.6.1). The complement assay was carried out on diaphragm sections harvested from naïve *GalNAc-T$^{-/-}$-Tg(neuronal)* or *GalNAc-T$^{-/-}$-Tg(glial)* mice following asphyxiation with a rising concentration of CO_2. Once harvested, the diaphragm was snap frozen and stored at -80℃ until required. The diaphragm was sectioned at 10 µm and collected onto APES coated slides before being stored at -20℃ until further use. The sera samples from the acute *in vivo* experiment were prepared at a 1/2 dilution in Ringer's solution, prepared immediately prior to use. As control mice received NHS only, the addition of a complement-fixing antibody had to be added to the sera and Ringer's solution to activate the complement pathway. The antibody which was selected was CGM3 - binds to disialylated gangliosides: GQ1b and GD3- as it is an IgM subtype and so would not interfere with the IgG3 antibody used to detect the anti-GM1 mAb (Bullens et al., 2002, Goodyear et al., 1999). The final concentration of CGM3 in the sera and Ringer's solution was 50 µg/ml. Sera was then added to the diaphragm and left to incubate for two hours at RT. Following incubation, the slides were washed in Ringer's solution. The diaphragm was then incubated in FITC conjugated anti-human C3c (1/300), Cy5 anti-mouse IgG3 (1/300), Alexa Fluor™ 555 α-BTx (1/750) and 3% NGS, prepared in PBS, to confirm the presence of complement and antibody deposits at the NMJ (identified by BTx), respectively. The slides were then viewed on a Zeiss Axio Imager Z1, and positive observation of C3c deposits confirmed successful *in vivo* delivery of complement. Mice with negative sera, shown by negative immunofluorescence staining in this assay, were excluded from further analysis.

2.10 Immunofluorescence staining

2.10.1 Staining of triangularis sterni from *ex vivo* experiments

Following *ex vivo* injury with anti-GM1 mAb and complement (as described in section 2.7.2), fixed TS was snap frozen and stored at -80℃ until required. For all immunofluorescence analysis, whole-mount TS preparations were used. The TS was halved post-fixation so that two-marker studies could be performed per mouse. Prior to staining, the TS was placed in PBS to thaw. Unless stated otherwise, antibody solutions were made up in PBS and 3% NGS and were incubated on an ELMI RM-2M Intelli Mixer (*VitaScience*). Following secondary antibody incubations, the TS was washed in PBS, before mounting on slides using citifluor and coverslipped. To identify the NMJ and distal nerves, α-BTx (488 or 555 conjugated) and rat anti-myelin basic protein (MBP) were used throughout.

To confirm that the complement pathway had been activated by anti-GM1 mAb, the TS was incubated in rat anti-MBP (1/500) overnight at 4℃. The following morning the TS was washed in PBS before being incubated in Alexa Fluor™ 555 conjugated α-BTx (1/500), Alexa Fluor™ 555 anti-rat IgG (1/500), FITC conjugated anti-human C1q (1/100) and Cy5 anti-mouse IgG3 (1/500) overnight at 4℃. In addition, to confirm the complement pathway had been inhibited, C3c or MAC were stained for. When assessing C3c, anti-human C3c complement FITC (1/300) was applied to the secondary antibody solution and left to incubate for 2 hours at RT. To investigate the presence of MAC, TS was permeabilised in EtOH (for 10 minutes at -20℃) and then incubated overnight at 4℃ in mouse anti-MAC C5b-9 (1/40). The TS was washed in PBS then incubated in Alexa Fluor™ 488 anti-mouse IgG2a (1/500) for 2 hours at RT.

To assess axon integrity at the nerve terminal following complement inhibition in *GalNAc-T$^{-/-}$-Tg(neuronal)* mice, the TS prep was permeabilised in EtOH for 20 minutes at -20℃ and then washed thoroughly in PBS. The TS was then incubated overnight at 4℃ in SMI 31, mouse anti-NFH antibody (1/1000), prepared in 0.5% Triton X-100 in PBS. The following morning, the TS was washed prior to being incubated in Alexa Fluor™ 647 anti-mouse IgG1 (1/500) for 3 hours at 4℃. To assess the presence of Nav at the NoR, the TS was permeabilised in EtOH for 10 minutes at -20℃ and then washed thoroughly in PBS.

Following permeabilization, the TS was incubated overnight at 4℃ in mouse anti-pan-Nav (pNav; 1/100), prepared in 0.5% Triton X-100 and 3% NGS. The next morning, the TS was washed before incubating in Alexa Fluor™ 647 anti-mouse IgG1 (1/500) for 2 hours at RT.

The integrity of the axo-glial junction following complement inhibition was assessed in *GalNAc-T$^{-/-}$-Tg(glial)* mice by staining for AnkB and Caspr. The TS was permeabilised in ethanol for 10 minutes at -20℃ and then washed thoroughly in PBS. Next, the TS was incubated in mouse anti-AnkB (1/200) or rabbit anti-Caspr (1/500), prepared in 0.5% Triton X-100 and 3% NGS, overnight at 4℃. The next morning, the TS was washed before being incubated in anti-mouse IgG2a-Cy5 (1/300) or Alexa Fluor™ 647 anti-rabbit IgG (1/500) for 2 hours at RT.

2.10.2 Staining of diaphragm sections from immunised mice

The diaphragm used for immunofluorescence analysis was previously exposed to anti-GM1 mAb and NHS *in vivo.* Unless stated otherwise, primary and secondary antibodies (except anti-GM1 mAb) were prepared in PBS and 3% NGS to block non-specific binding. Alpha-BTx (488, 555 or 647 conjugated) was used throughout to label post synaptic nAchR to identify the NMJ and rat anti-MBP was used to label compact myelin, identifying the distal nerve. Following antibody incubation, tissue was washed in PBS and then mounted in citifluor.

GM1 antibody and MAC deposits were assessed at the NMJ; 8 µm sections were incubated in mouse anti-MAC C5b-9 (1/50) overnight at 4℃. Tissue was washed in PBS and Alexa Fluor™ 488 anti-mouse IgG2a (1/300), anti-mouse IgG3 TRITC (1/300) were applied for two hours at RT to identify MAC and anti-GM1 mAb, respectively. To assess complement deposition and subsequent axonal integrity at the NMJ and distal nerve, 15 µm sections were stained for the complement component, C3c and neurofilament heavy (NFH). Tissue was permeabilised with 100% ethanol (EtOH) for 10 minutes at -20℃ prior to incubation in SMI 31, mouse anti-NFH antibody (1/1500) overnight at 4℃. Tissue was washed in PBS before incubating in anti-human C3c complement FITC (1/300) and Alexa Fluor™ 647 anti-mouse IgG1 (1/600) for 2 hours at RT.

The integrity of the NoR was assessed by staining for pNav, Caspr, ankB, pan-neurofascin (pan-NFasc) and Kv1.1. Staining of pNav clusters and Caspr dimers were performed on 10

µm fresh frozen diaphragm sections. The tissue was permeabilised in EtOH for 10 minutes at -20℃ and then washed thoroughly prior to primary antibody incubation. Rabbit-anti Caspr (1/1000) was applied to the sections overnight at 4℃. Tissue was blocked in 10% NGS and 0.1% Triton X-100 for 1 hour at 4℃ prior to overnight incubation in mouse anti-pNav (1/100). The following morning, the tissue was washed and then incubated in Alexa Fluor™ 555 anti-rabbit IgG (1/500) or Alexa Fluor™ 555 anti-mouse IgG1 (1/500) for 2 hours at RT. When staining for pNav, antibodies were prepared in 10% NGS and PBS. Fixed diaphragm sections of 10 µm were used to assess AnkB at the paranode, pan-NFasc at the NoR and Kv1.1 at the juxtaparanode. Tissue was permeabilised in EtOH for 10 minutes at -20℃ and then washed thoroughly in PBS. Fixed diaphragm was incubated in mouse anti-AnkB (1/800), rabbit anti-pan-NFasc (1/750) or rabbit Kv1.1 (1/200), prepared in 0.5% Triton X-100 and 3% NGS, overnight at 4℃. Tissue was then washed in PBS before applying Alexa Fluor™ 647 anti-mouse IgG2a (1/300) or Alexa Fluor™ 647 anti-rabbit IgG (1/500) for 2 hours at RT.

2.11 Microscopy

All imaging was performed using a Zeiss Axio Z1 Imager with Apotome attachment, or a Zeiss LSM 880 confocal microscope and captured with Zen blue edition (version 6.1.7) or Zen black edition software (version 2.3), respectively. Each mouse was analysed in duplicate or triplicate for each antibody stain. All tissue was coded prior to imaging. The exposure time for each channel were set prior to imaging the slides and they were kept consistent throughout.

2.11.1 Fluorescent microscopy

A Zeiss Axio Z1 imager, with the apotome attachment removed, was used to image diaphragm tissue from the *in vivo* models and sciatic nerve from the anti-GM1 binding studies. When investigating the NMJ in diaphragm sections following anti-GM1 mAb and complement-mediated injury, 15 single slice snaps per section were taken using a 40x oil objective. A minimum of 70 NMJs were captured and analysed for each mouse. When assessing the integrity of the distal nerve and NoR in diaphragm sections following anti-GM1 mAb and complement-mediated injury, every distal nerve identified by MBP and BTx staining were imaged in each piece of diaphragm. At least 20 distal nerves were assessed

per treatment group. To assess anti-GM1 binding in sciatic nerve, 5 images were captured and 5 independent NoR were analysed. Z-stacks, with a 0.4 µm interval, were used to capture distal nerves and NoR in diaphragm and sciatic nerve sections using a 63x oil objective.

When imaging whole-mount TS from *ex vivo* experiments, images were taken on a Zeiss Axio Z1 imager with the apotome attachment in. For assessing the integrity of the nerve terminal following human C2 complement inhibition in *GalNAc-T$^{-/-}$-Tg(neuronal)* mice, a 40x oil objective was used to capture single slice snaps of NMJs. Images were only captured of superficial NMJs to reduce any anomalies that may be present due to antibody penetration issues in deep NMJs. A minimum of 25 NMJs were captured and analysed for each piece of tissue. To investigate the integrity of the distal NoR in *GalNAc-T$^{-/-}$-Tg(neuronal)* and *GalNAc-T$^{-/-}$-Tg(glial)* mice following human C2 complement inhibition, every distal nerve identified by MBP and BTx staining was imaged in each TS. Z-stacks, with a 0.4 µm interval, were taken using a 63x oil objective; a minimum of 12 distal nerves were captured per piece of tissue.

2.11.2 Confocal Microscopy

A Zeiss LSM 880 confocal microscope was used to image the diaphragm sections from the *in vitro* dose response assay, outlined in section 2.7.1. A 40x water objective was used to capture 15 single slice snaps per tissue. A minimum of 50 NMJs were imaged per mouse.

2.12 Immunofluorescence analysis

2.12.1 Intensity analysis

The fluorescence intensity of GM1 ligands at the NoR was performed on sectioned sciatic nerve (see section 2.5) and quantified using Fiji software (*ImageJ, version 2.0.0*). Images were converted to 8-bit grey-scale and the channels were split. Nav and Caspr were used as markers to identify the nodal gap and paranodes, respectively and only NoR with both markers present were analysed. Using the line tool, a length of 8 µm (width 1 µm) was drawn across the NoR, ensuring that the middle of the line was located overlying pNav at the nodal gap. The mean intensity of anti-GM1 ligand, pNav and Caspr at each distance along the NoR was measured at 5 independent NoR for each ligand and genotype. The

intensity of the nodal (pNav) and paranodal (Caspr) markers were then plotted alongside the mean intensity of the anti-GM1 ligand to assess the binding patterns of each ligand in the different strains of mice.

The fluorescence intensity of anti-GM1 mAb, C3c, MAC, and neurofilament at the NMJ of diaphragm sections (from the *in vivo* study detailed in section 2.6.1) were quantified using Fiji software (*ImageJ, version 2.0.0*). Due to antibody and complement binding beyond the BTx labelled NMJ, most likely binding to pSC, staining surrounding the BTx (a circle with a diameter of between 15-25 µm) was considered when quantifying intensity. Images were opened in Fiji, converted to 8-bit grey-scale, and the channels were split. There was high background in anti-GM1 mAb, C3c and MAC images, therefore, the 'subtract background' process in Fiji was performed on these channels. The threshold for BTx and neurofilament were set between 50-255 pixels. A region of interest (ROI), with an area of 200-650 μm^2 (depending on the size of the NMJ), was drawn around the BTx staining, using the oval tool, and overlaid on to the channel containing anti-GM1 mAb, C3c, MAC or neurofilament. The mean intensity grey value overlying the ROI was measured, generating a pixel value between 0 and 255. Results were plotted on Tukey box and whisker plots (see Appendix 8.1).

MBP intensity at the distal internode, defined as the most distal 'section' of MBP staining extending from the nerve terminal, was calculated using Fiji software. A line width of 10 was selected and a 10 µm line was drawn along the distal internode, extending from the BTx staining. The resulting intensity was then plotted for each distal internode and outliers were removed using ROUT analysis. Following the removal of outliers, the average intensity for each treatment group was calculated and plotted so that statistics could be performed.

To quantify fluorescent intensity at the NMJ of diaphragm sections from the *in vitro* dose response assay (described in 2.7.1), the intensity of anti-GM1 mAb and complement overlying BTx was measured using Fiji software. This quantification was performed using macros, explained previously by (O'Hanlon et al., 2001), that were modified by Dr Madeleine Cunningham. The threshold for the BTx channel was set between 50–255 pixels and ROI selected. Only BTx staining of 10-1000 particles in size and circularity between 0.00-1.00 were selected as an ROI. This ROI was then overlaid on to the channel

containing anti-GM1 mAb or complement and the mean intensity grey value overlying the nerve terminal was determined. This then generated a pixel value between 0 and 255 and was plotted as arbitrary units.

2.12.2 Occupancy analysis

Observational presence/absence analysis was performed using Zen blue software (version 3.0). For NMJ analysis, the presence of detected anti-GM1 mAb and complement deposits surrounding the nerve terminal were assessed, to consider all components of the NMJ. Using the 'circle' tool on Zen, a circle with a diameter of between 15-25 µm (depending on the size of NMJ), was drawn around the BTx staining to include the surrounding NMJ. If there were anti-GM1 mAb or complement deposits detected in the highlighted area, then it was classified as present, if there were no deposits detected then they were classified as absent. The percentage of NMJs with positive anti-GM1 mAb and complement deposits for each treatment group were then calculated. Axonal integrity was assessed by the presence of the axonal structural protein, neurofilament, overlying the NMJ. The percentage of NMJs that were occupied with neurofilament staining was determined for each treatment group. The presence of anti-GM1 mAb, complement and neurofilament at the distal internode and distal NoR, considered together as the distal nerve, were also evaluated. The distal NoR was defined, by a gap in the MBP staining, as the first adjacent gap to the distal internode. If anti-GM1 mAb or complement deposits were detected overlying the distal internode and/or NoR, then this was considered as positive. For each treatment group, the percentage of distal nerves with antibody and/or complement deposits were calculated. Subsequently, the presence of neurofilament staining at the most distal internode and NoR was assessed and the percentage of distal nerves with neurofilament were determined for each treatment group.

To assess the integrity of axo-glial proteins at the NoR, occupancy analysis was performed. In this context, dimer was used throughout the thesis to describe the presence of axo-glial proteins at both paranodes/juxtaparanodes at the NoR. When characterizing the injury at the NoR in Chapter 4 and 5, scoring for presence and normality of nodal protein clustering (pNav), or paranodal/juxtaparanodal dimer formation (AnkB, Caspr, Kv1.1) was split into three categories: 1. Present; 2. Abnormal; or 3. Absent. If staining was present and appeared normal, then it was classified as category

1, present (Figure 2.4). If the nodal protein cluster or dimer was present, but the staining was either fragmented or the staining appeared elongated (as illustrated in Figure 2.4), then it was classified as abnormal. If there was only a paranodal/juxtaparanodal hemi-dimer present, or the paranodal/juxtaparanodal dimer or nodal protein cluster was completely gone then it was classified as absent, as demonstrated in Figure 2.4. In addition, I also investigated the presence of pan-NFasc at the distal NoR; however, as this protein binds to both NF186 at the nodal gap and NF155 at the paranode, analysis of this protein was more complicated. Firstly, the condition of the full pan-NFasc protein was considered and was categorised as either normal, abnormal or absent. Normal pan-NFasc staining was defined as both nodal and paranodal pan-NFasc being present and normal; if both nodal and paranodal pan-NFasc were present but the staining appeared punctate or elongated, then it was categorised as abnormal; lastly, if nodal and/or paranodal pan-NFasc were absent, or only a paranodal pan-NFasc hemi-dimer was present, then the staining was classed as absent. The schematic diagram in Figure 2.4 illustrates each category. Secondly, the percentage of distal NoR with either nodal pan-NFasc clustering or paranodal pan-NFasc dimers were assessed separately. Distal NoR were identified by a gap in the MBP staining and the presence of a nodal marker or complement/antibody deposition. When assessing the presence of dimers at the paranodes and juxtaparnodes, distal nerves with absent staining were only included in the final analysis if this coincided with complement or anti-GM1 mAb deposits on the distal nerve.

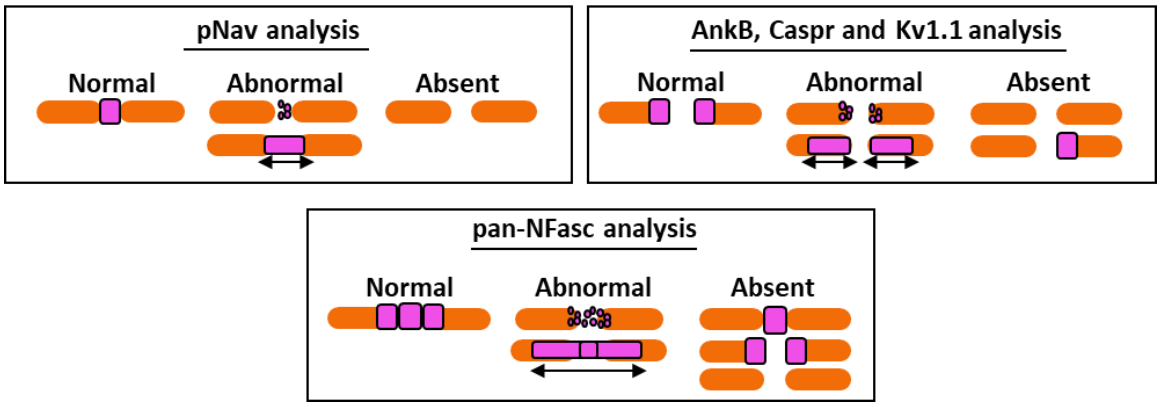

Figure 2.4: Schematic diagram illustrating scoring of nodal, paranodal and juxtaparanodal markers at the node of Ranvier.

Whilst performing occupancy analysis at the distal NoR various measurements were performed using the 'line' tool in Zeiss blue software. The length between the MBP gap and between paranodal dimers were determined. Furthermore, the span (length between

outer edge of each dimer) or full length of present paranodal dimer staining was measured.

2.13 Electron microscopy

Electron microscopy was performed by Jennifer Barrie (MSc).

2.13.1 Reagents and buffers

Listed below are the reagents and buffers used during ultrastructural analysis:

- 2% PFA (10g CH_2O added to 500 mL 1x PBS and heated on a hotplate to 60-70℃. Whilst stirring, 1 M NaOH was added until solution turned clear)
- 2.5% Glutaraldehyde (prepared in 0.08 M sodium cacodylate buffer)
- Araldite resin embedding medium (Araldite CY212 and dodecenyl succinic anhydride hardener were mixed and heated at 60℃ until liquid. DMP 30 accelerator (2,4,6-tris dimethylaminomethyl phenol) and Di-butylphthalate plasticiser were added in fume-hood and mixed on a stirrer for 1 hour (all sourced from *Agar Scientific; Essex, UK*))
- 1% osmium tetroxide (OsO_4; *Agar Scientific; Essex, UK*)
- Propylene oxide (C_3H_6O; *Agar Scientific; Essex, UK*)
- Uranyl acetate ($C_4H_6O_6U$; *Agar Scientific; Essex, UK*)
- Lead citrate ($Pb(NO_3)_2$, $Na_3C_6H_5O_7$, NaOH dissolved in 1L dH_2O)
- 0.08 M sodium cacodylate buffer ($NaO_2As(CH_3)_2$ prepared in 1L dH_2O)
- Isotonic sodium cacodylate buffer ($NaO_2As(CH_3)_2$, NaCl, $CaCl_2$, and $MgCl_2$ dissolved in 1L dH_2O)

2.13.2 Tissue processing

To assess the ultrastructure of the NMJ following anti-GM1 mAb and complement-mediated injury, *GalNAc-T$^{-/-}$-Tg(neuronal)* mice were vascularly perfused with 2% PFA plus 2.5% glutaraldehyde in PBS. Following perfusion, the diaphragm was removed and immersed in the same fixative for 1 hour at RT before being processed. When investigating the effects to NoR ultrastructure following anti-GM1 mAb-mediated injury in *GalNAc-T$^{-/-}$-Tg(neuronal)* and *GalNAc-T$^{-/-}$-Tg(glial)* mice, the diaphragm was harvested at

the end of the *in vivo* experiment (detailed in section 2.6.1) and immersion fixed in 2.5% glutaraldehyde for 1 hour at RT. The diaphragm was then unpinned and stored in 2.5% glutaraldehyde at 4℃ until tissue processing was performed.

Fixed tissue was cut into squares no larger than 2 mm^3 around estimated locations of NMJ and distal nerves. Post-fixation and dehydration were performed using a bottle rotator in a fume-hood as follows:

1) Isotonic sodium cacodylate buffer for 30 mins
2) 2 hours in 1% osmium tetroxide
3) Isotonic sodium cacodylate buffer for 30 mins
4) 20 mins in 50% EtOH
5) 20 mins in 70% EtOH
6) 20 mins in 80% EtOH
7) 20 mins in 90% EtOH
8) 2x 30 mins in 100% EtOH
9) 2x 30 mins in propylene oxide
10) Overnight in 1:1 complete araldite/propylene oxide
11) Overnight in 3:1 complete araldite/propylene oxide
12) Lids were removed to allow the propylene oxide to evaporate

The tissue was then embedded in araldite embedding medium and cured/polymerised for 48 hours at 65℃.

2.13.3 Sectioning and staining

Once the tissue was processed, semi-thin sections of 1 µm were cut and transferred to a bubble of water on a slide, to flatten the sections. Slides were then dried on a hot plate before being stained with a solution consisting of 1% methylene blue, 1% azur II, and 1% sodium tetraborate, performed on a hot plate to enhance staining. Once the outer edge of the stain turned greenish, the slides were washed in dH_2O, dried and cover slipped. Semi-thin sections were then observed on a Zeiss, Axiostar Plus light microscope to determine the precise location to cut for ultrathin sections.

Ultrathin sections of 70 nm were cut and collected on copper grids (200 mesh) immersed in water. They were then placed on filter paper to allow the excess water to be drained. Once dried, the grids were stained with uranyl acetate and then lead citrate, for 15 minutes each at RT. Grids were then viewed on a JEOL 1200 EXII Transmission Electron Microscope.

2.14 Experimental design

The experimental design applied to the acute *in vivo* injury model (section 2.6.1) was based on the 'random block design' technique which has been explained previously (Aguilar-Nascimento, 2005). This experimental design assures more balance between animals and minimizes variation. One of the aims of my experiment was to investigate the injury output in 3 different strains of mice when treated with either AGAb and complement or complement only. Therefore, it was decided to 'block' the mice into three subgroups based on the different strains of mice - wild type*, GalNAc-T$^{-/-}$-Tg(neuronal)* or *GalNAc-T$^{-/-}$-Tg(glial).* Within each subgroup, mice were paired together to control for: age, weight, and where possible, sex. Using an online random team generator, mice within a pair, were then randomly assigned to either the control (complement only) or injury (anti-GM1 mAb and complement) treatment groups. With this technique, the variability within blocks is less than the variability between blocks allowing for a better estimate of treatment effects. Each block was also separated by time; the advantage of this is that it provides a way of building reproducibility into an experiment by replicating in time.

Prior to performing immunofluorescence analysis in all experiments, the tissue was coded by an independent individual and the user was blinded until analysis was completed.

2.15 Statistical Analysis

Graphs were prepared in GraphPad Prism 6 and statistical tests were performed using this software. A significance value of $p < 0.05$ was used.

Data was found to be normally distributed by performing Shapiro-Wilk test and so parametric tests were used throughout. When analysing WBP data, a repeated measures two-way ANOVA test was performed to assess whether there was a difference within

each treatment group between the baseline TV/RR and the subsequent TV/RR at each timepoint post injury. To determine whether there were any differences between treatment groups, a regular two-way ANOVA with Tukey's multiple comparisons test was carried out. A linear regression model and/or correlation test was performed on xy plots to investigate the relationship between two variables. The statistical test used for each figure is detailed in the figure legends.

To display presence/absence and occupancy data, scatter plots with bars or grouped bar charts were used. The error bars represent the standard error of the mean (SEM) for each treatment group. An unpaired t-test or one-way ANOVA were performed to test for significant differences between treatment groups on scatter plots; and a two-way ANOVA with Tukey's multiple comparisons test was used on grouped bar charts to determine whether there were any significant differences between the different treatment groups. Non-parametric data are displayed as Tukey box and whisker plots, as these plots are beneficial to illustrate the distribution of data. Outliers were removed using ROUT analysis. The mean intensity value from each individual animal was plotted for each treatment group and they were found to be from a Gaussian distribution, as determined by performing a Shapiro-Wilk test. Therefore, a one-way ANOVA with Tukey's multiple comparisons test was performed on the mean values.

3 Differential binding patterns of anti-GM1 ligands

3.1 Introduction

GBS is considered as a 'nodopathy' due to the prevalent pathogenesis at the NoR demonstrated by autopsy studies and animal models (Uncini et al., 2013, Hafer-Macko et al., 1996a, Susuki et al., 2007b, Griffin et al., 1996, McGonigal et al., 2010). Thus, understanding the pathophysiological contribution of nodal membrane injury in GBS is vital to further our understanding of disease pathogenesis. Evidence from serology studies and animal models indicates that autoantibodies directed towards gangliosides, such as GM1, are responsible for the pathogenesis of GBS (Willison, 2018, Yuki et al., 2001, Yuki et al., 1990). However, current AGAb-mediated animal models are not able to differentiate between axonal and glial membrane injury at the NoR because GM1 is expressed in both neural membranes in wild type mice (Guyton, 1947, Sheikh et al., 1999, Susuki et al., 2007a). Therefore, it is unknown whether the resulting injury is a consequence of antibody binding-effector pathway mediated injury to the axonal membrane, the glial membrane, or a combination of targeting and injury to both membranes.

To address this mechanistic impasse, we generated transgenic mice with exclusive expression of complex gangliosides, notably GM1, to either the axonal (*GalNAc-T$^{-/-}$-Tg(neuronal)*) or glial membrane (*GalNAc-T$^{-/-}$-Tg(glial)*) (Yao et al., 2014), allowing us to target each membrane independently with an anti-GM1 antibody. The aim thereafter was to characterise the downstream mechanisms involved in anti-GM1 mAb-mediated injury, focussing on the distal motor nerve as a highly vulnerable and tractable site. Thus, the aim of this chapter was to initially select a single anti-GM1 mAb that could bind both the axonal and glial membranes to investigate the consequences of targeting each neural membrane independently in our *GalNAc-T$^{-/-}$-Tg(neuronal)* and *GalNAc-T$^{-/-}$-Tg(glial)* mice and compare this with the effects of when both membranes are targeted in wild type mice. CTB is a toxin with known mono-specificity for GM1 ganglioside (Holmgren et al., 1973) and therefore, was used as a positive control and compared to the binding patterns of the anti-GM1 mAbs available for study.

Four different anti-GM1 ligands were assessed:

- **CTB**: a toxin with high selective specificity and affinity for GM1
- **DG1**: an anti-GM1 IgG mouse mAb
- **DG2**: an anti-GM1 IgG mouse mAb
- **BO3**: an anti-GM1 IgM human mAb

The binding of each GM1 ligand was compared between:

- **Wild type mice**: that express GM1 on both neural membranes
- ***GD3s*$^{-/-}$ mice**: that overexpress GM1 on axonal and glial membranes
- ***GalNAc-T*$^{-/-}$*-Tg(neuronal)* mice**: that express GM1 only on axonal membranes
- ***GalNAc-T*$^{-/-}$*-Tg(glial)* mice**: that express GM1 only on glial membranes
- ***GalNAc-T*$^{-/-}$ mice**: that do not express any GM1

3.2 Results

The purpose of this chapter was to compare and select a single anti-GM1 mAb that bound live tissue and bound to GM1 on both the axonal and glial membrane at the NoR. De-sheathed sciatic nerves were incubated with either CTB, DG1, DG2 or BO3 and binding was compared in wild type, *GD3s*$^{-/-}$, *GalNAc-T*$^{-/-}$*-Tg(neuronal), GalNAc-T*$^{-/-}$*-Tg(glial),* and *GalNAc-T*$^{-/-}$ mice. *GalNAc-T*$^{-/-}$ mice were used as a negative control throughout this chapter as they do not express GM1 ganglioside and should therefore demonstrate GM1 specificity.

First, an ELISA was performed to confirm the mAbs (DG1, DG2 and BO3) bind to GM1. Then, intensity analysis was performed on sectioned sciatic nerve to determine the intensity of each GM1 ligand at the NoR. Nav and Caspr were used as markers to identify the nodal gap and paranodes, respectively. A length of 8 µm was measured across the NoR and the intensity of the anti-GM1 ligand was plotted alongside the intensity of pNav and Caspr to illustrate the binding pattern of the ligand (as illustrated by Figure 3.1). On the graphs, 0 µm represents the nodal gap and (+/-) 1-4 µm represents the paranodes.

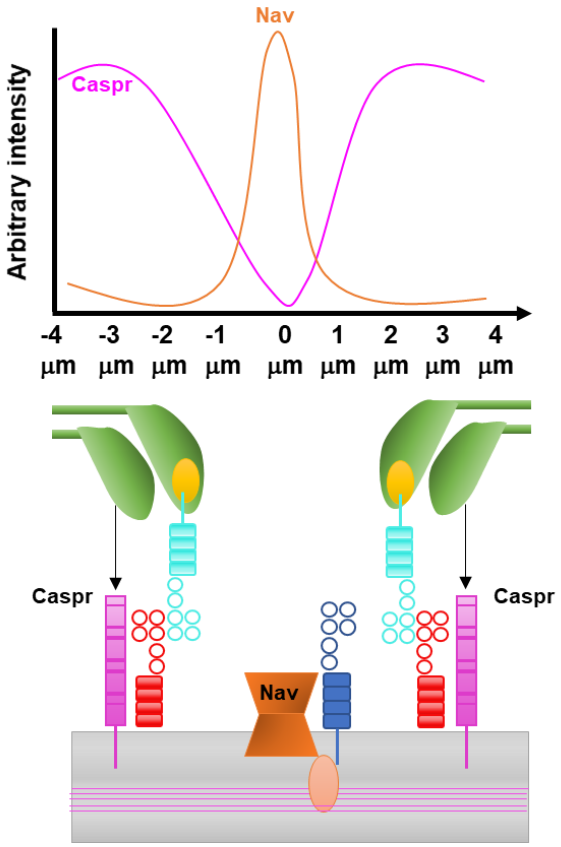

Figure 3.1: Schematic diagram detailing method of intensity analysis at the node of Ranvier. Method modified from (Lonigro and Devaux, 2009)

3.2.1 Confirmation of binding of anti-GM1 monoclonal antibodies to GM1 in ELISA

Prior to assessing the binding capabilities of the GM1 ligands in live tissue, it was first confirmed that each mAb (DG1, DG2 and BO3) bound to GM1 in ELISA, as has been previously reported (Paterson et al., 1995, Townson et al., 2007). The results in Figure 3.2 demonstrate that DG1, DG2 and BO3 bound to GM1 in ELISA as represented by positive optical density (OD) values of 0.68 $\pm$ 0.15, 0.68 $\pm$ 0.04 and 0.83 $\pm$ 0.05 AU, respectively. There were no significant differences between the OD values of the mAbs. The OD values of each anti-GM1 mAb was significantly higher compared to the OD values of their respective secondary antibody only OD values ($p<0.001$). Therefore, providing confirmation that DG1, DG2 and BO3 bind GM1 in ELISA.

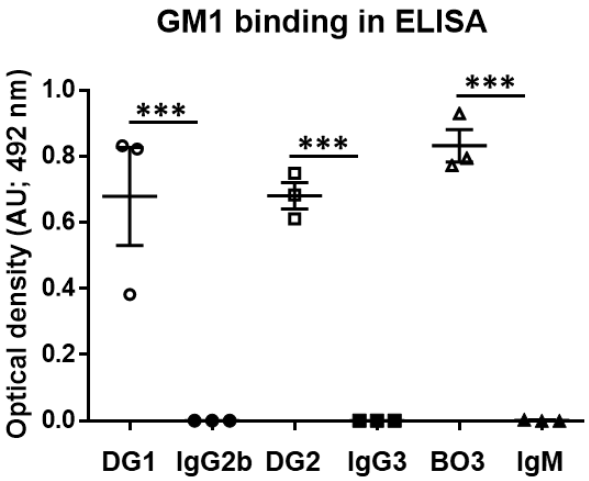

Figure 3.2: Binding of DG1, DG2 and BO3 monoclonal antibodies to GM1 in ELISA. An ELISA plate was coated with 2 µg/ml GM1 ganglioside and 20 µg/ml of monoclonal antibodies (mAbs), DG1, DG2 and BO3, were applied overnight at 4℃. Horseradish peroxidase (HRP) conjugated secondary antibodies were used to detect DG1, DG2 and BO3. Secondary antibody only wells were incubated in 0.1% bovine serum albumin-phosphate buffered saline (BSA-PBS) overnight at 4℃ before applying HRP conjugated secondary antibodies. The ELISA plate was read on a spectrophotometer at 492 nm and the results demonstrate that DG1, DG2 and BO3 successfully bound to GM1 on the ELISA plate. There were no significant differences between the optical density (OD) values of the mAbs. The OD value was significantly higher in DG1, DG2 and BO3 compared to their respective secondary antibody only OD values (***=p<0.001). Results represent average ± SEM. n=3/group. One-way ANOVA performed to test for statistical significance.

3.2.2 Assessment of cholera toxin subunit B binding in sciatic nerve

CTB is a toxin with known mono-specificity for GM1 ganglioside (Holmgren et al., 1973) and so was used as a positive control to assess GM1 expression in the transgenic mice. In wild type mice, CTB staining was predominantly detected at the nodal gap, co-localising with pNav staining, and bound diffusely at the paranodes where it overlay Caspr dimers; illustrated by the graph and representative images in Figure 3.3A. The graph in Figure 3.3B demonstrates that the intensity of detected CTB deposits in *GD3s*$^{-/-}$ mice appeared comparable at both the nodal gap and the paranodes. This is represented in the images with CTB detected overlying both pNav clusters and Caspr dimers. In *GalNAc-T*$^{-/-}$*-Tg(neuronal)* mice, the intensity of CTB at the NoR followed a similar pattern to that demonstrated in wild type mice (Figure 3.3C). The representative images in Figure 3.3C demonstrate CTB binding strongly at the nodal gap with staining extending into the paranodes in *GalNAc-T*$^{-/-}$*-Tg(neuronal)* mice. The binding pattern of CTB in *GalNAc-T*$^{-/-}$*-Tg(glial)* mice differed to all other genotypes (Figure 3.3D). Illustrative images show CTB

deposits absent from the nodal gap but present surrounding the Caspr dimers at the paranode, suggesting CTB was binding to GM1 present on the paranodal loops in *GalNAc-T$^{-/-}$-Tg(glial)* mice. As illustrated by the graph, the CTB staining in *GalNAc-T$^{-/-}$-Tg(glial)* mice was not symmetrical at the paranodes and appeared commonly overlying one Caspr dimer, for unknown reasons as discussed below. The graph and representative images in Figure 3.3E demonstrate that CTB was absent from the NoR in *GalNAc-T$^{-/-}$* mice, indicating that CTB was only binding to GM1.

Overall, these results suggest that CTB binds to GM1 on both axonal and glial membranes and confirms the successful reintroduction of GM1 selectively to either the axonal or glial membrane in the *GalNAc-T$^{-/-}$-Tg(neuronal)* and *GalNAc-T$^{-/-}$-Tg(glial)* mice, respectively.

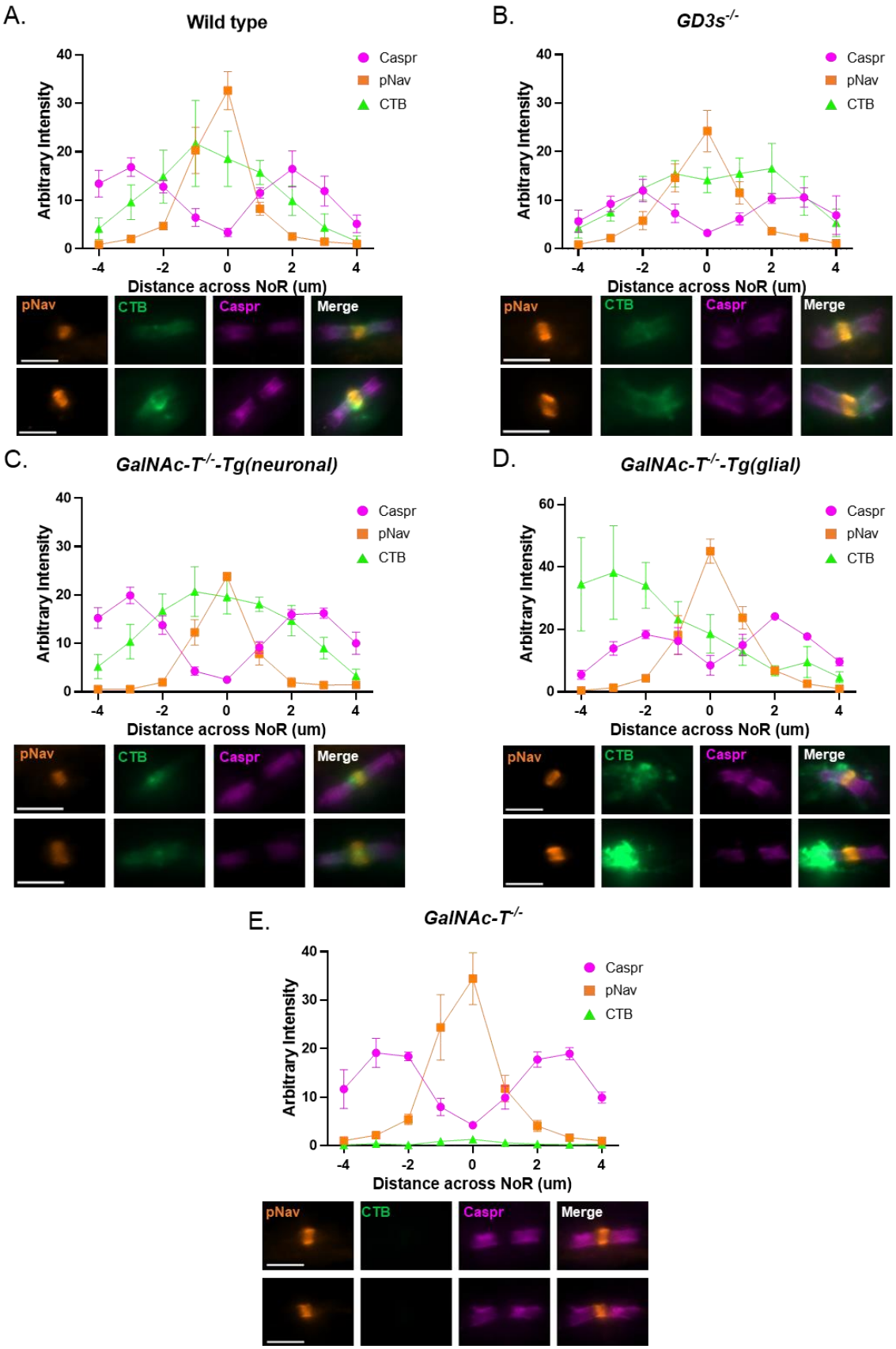
A.
Wild type
B.
GD3s-/-
C.
GalNAc-T-/--Tg(neuronal)
D.
GalNAc-T-/--Tg(glial)
E.
GalNAc-T-/-
Caspr
pNav
CTB
Arbitrary Intensity
Distance across NoR (um)
pNav
CTB
Caspr
Merge

Figure 3.3: Cholera toxin subunit B binding in sciatic nerve. (See previous page) The sciatic nerve was harvested from wild type, *GD3s*$^{-/-}$, *GalNAc-T*$^{-/-}$*-Tg(neuronal), GalNAc-T*$^{-/-}$*-Tg(glial)* and *GalNAc-T*$^{-/-}$ mice and de-sheathed before incubating in 50 µg/ml cholera toxin subunit B (CTB) for 3 hours at 4℃. Following fixation in 4% paraformaldehyde, the sciatic nerve was sectioned, and immunofluorescence analysis was performed to assess the binding pattern of CTB at the node of Ranvier (NoR). To identify the nodal gap and paranodes, pNav and Caspr were studied, respectively. A length of 8µm across the NoR was measured, with 0 µm marking the nodal gap and (+/-) 1-4 representing the paranodes. The intensity of CTB, Caspr and pNav at 5 independent NoR was plotted for each genotype. A-C) The graphs demonstrate CTB intensity present at the nodal gap and decreasing over the paranodes. Illustrative images show CTB (green) deposited at the nodal gap (identified by pNav, orange) and diffusely at the paranodes (identified by Caspr dimers, magenta) in wild type (A), *GD3s*$^{-/-}$(B), and *GalNAc-T*$^{-/-}$*-Tg(neuronal)* mice (C). D) CTB intensity was predominantly present overlying one paranode. The fluorescent images show CTB deposits strongly overlying one Caspr dimer but absent from the nodal gap. E) The intensity of CTB in *GalNAc-T*$^{-/-}$ mice was very low across the NoR. These results are confirmed by the images which show CTB was absent from the NoR. Results represented as average ± SEM. n=5 NoR/genotype. Scale bar = 5 µm.

3.2.3 Assessment of DG1 binding in sciatic nerve

DG1 is a mouse monoclonal IgG antibody with affinity to GM1 (Townson et al., 2007). It has previously been demonstrated that DG1 is unable to bind live wild type tissue due to the presence of interactions present in the glycolipid raft (Greenshields et al., 2009). However, it has yet to be determined whether DG1 is capable of binding GM1 when expression is restricted to axonal or glial membranes in the *GalNAc-T*$^{-/-}$*-Tg(neuronal)* and *GalNAc-T*$^{-/-}$*-Tg(glial)* mice described herein. Furthermore, the ability of DG1 to bind the NoR has not yet been formally assessed as previous work has focussed on the pre-synaptic motor nerve terminal (Greenshields et al., 2009). The results in Figure 3.4A and Figure 3.4D demonstrate that DG1 did not bind at the NoR in wild type nor *GalNAc-T*$^{-/-}$*-Tg(glial)* mice, as shown by the low intensity values and the absence of DG1 deposits at the NoR in the illustrative images. DG1 deposits were also absent from the NoR in *GalNAc-T*$^{-/-}$*-Tg(neuronal)* mice, despite the slight spike in intensity at the nodal gap, likely due to background staining (Figure 3.4C). When GM1 was overexpressed in *GD3s*$^{-/-}$ mice, the intensity of DG1 was elevated at the nodal gap (Figure 3.4B). This corresponded to weak DG1 deposits at the nodal gap which co-localised with and extended outwith pNav clusters in the images in Figure 3.4B. As expected, DG1 was absent from *GalNAc-T*$^{-/-}$ mice as illustrated by the low intensity values and absent deposits from the NoR in the representative images.

In summary, these results demonstrate that DG1 is unable to bind GM1 in wild type nodal tissue. Furthermore, restricted expression of GM1 to the axonal (*GalNAc-T*$^{-/-}$-*Tg(neuronal)*) or glial (*GalNAc-T*$^{-/-}$-*Tg(glial)*) membranes does not enable DG1 binding. Nonetheless, DG1 successfully bound the nodal gap when GM1 expression was increased and *cis*-interacting *b-series* gangliosides were eliminated in *GD3s*$^{-/-}$ mice.

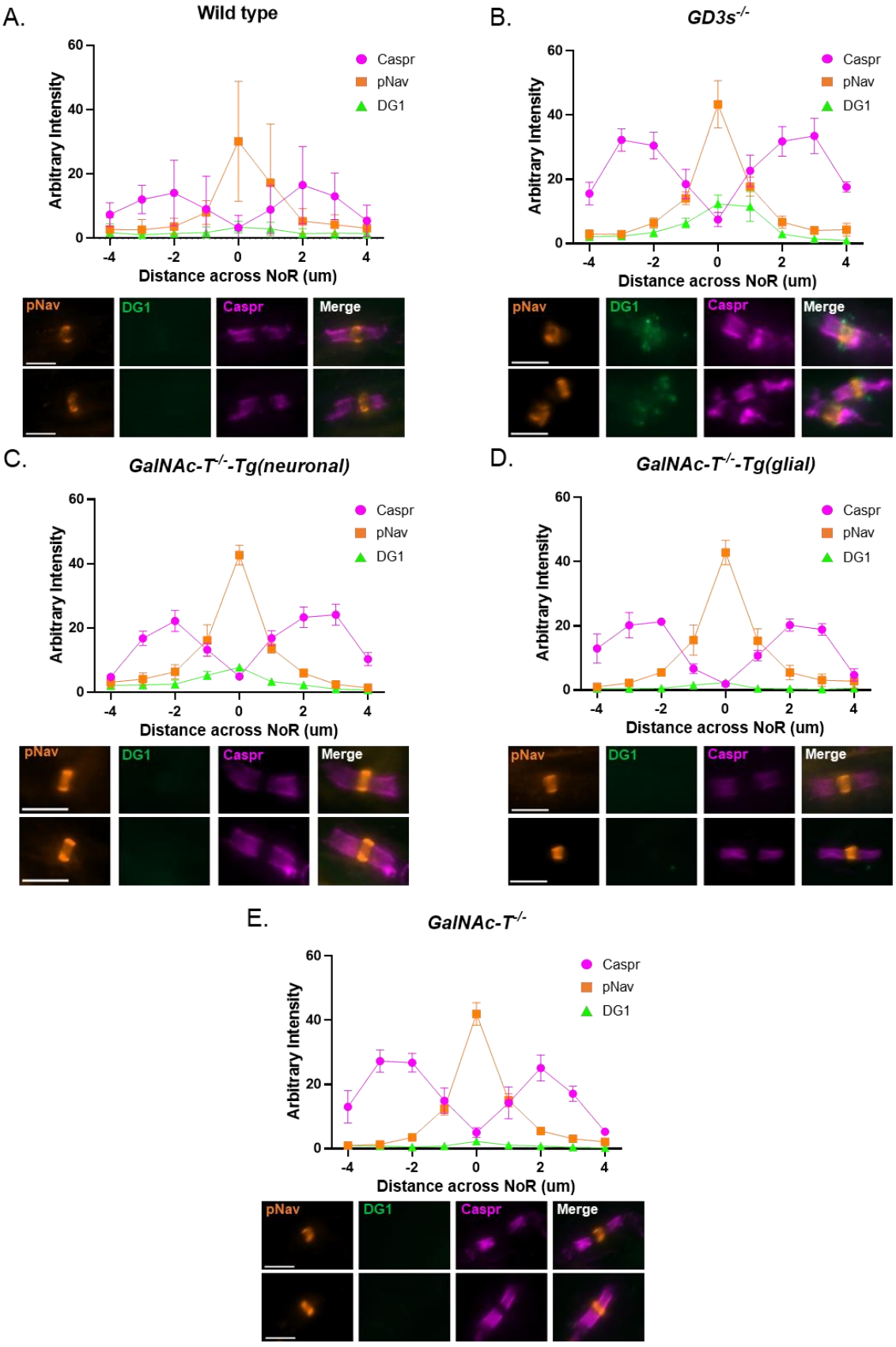
A.
Wild type
B.
GD3s-/-
C.
GalNAc-T-/--Tg(neuronal)
D.
GalNAc-T-/--Tg(glial)
E.
GalNAc-T-/-
Caspr
pNav
DG1
Arbitrary Intensity
Distance across NoR (um)
pNav
DG1
Caspr
Merge

Figure 3.4: DG1 binding in sciatic nerve. (See previous page) The sciatic nerve was harvested from wild type, *GD3s*$^{-/-}$, *GalNAc-T*$^{-/-}$*-Tg(neuronal), GalNAc-T*$^{-/-}$*-Tg(glial)* and *GalNAc-T*$^{-/-}$ mice and de-sheathed before incubating in 100 µg/ml DG1 for 2 hours at 4°C. Following fixation in 4% paraformaldehyde, the sciatic nerve was sectioned, and immunofluorescence analysis was performed to assess the binding pattern of DG1 at the node of Ranvier (NoR). To identify the nodal gap and paranodes, pNav and Caspr were studied, respectively. A length of 8µm across the NoR was measured, with 0 µm marking the nodal gap and (+/-) 1-4 representing the paranodes. The intensity of DG1, Caspr and pNav at 5 independent NoR was plotted for each genotype. A) DG1 deposits were absent from the NoR in wild type mice as demonstrated graphically and illustratively by the fluorescent images. B) The intensity of DG1 was increased slightly at the nodal gap, demonstrated graphically; corresponding to weak DG1 deposits (green) at the nodal gap (identified by pNav, orange) and absent from the paranodes (delineated by Caspr dimers, magenta) in the fluorescent images. C-E) DG1 did not bind to the NoR in *GalNAc-T*$^{-/-}$*-Tg(neuronal)* (C), *GalNAc-T*$^{-/-}$*-Tg(glial)* (D), nor *GalNAc-T*$^{-/-}$ (E) mice as the intensity of DG1 was low across the NoR. These results are confirmed by the representative images which show an absence of DG1 deposits at pNav clusters (orange) and Caspr dimers (magenta). Results represented as average ± SEM. n=5 NoR/genotype. Scale bar = 5 µm.

3.2.4 Assessment of DG2 binding in sciatic nerve

Previous studies have established that the mouse anti-GM1 IgG3 mAb, DG2, binds to GM1 in ELISA and live tissue and can exert neuropathological effects (Greenshields et al., 2009). Additionally, this DG2 anti-GM1 mAb has been used to generate an *ex vivo* axonal injury model in *GalNAc-T*$^{-/-}$*-Tg(neuronal)* mice, further supporting the ability of DG2 to bind GM1 in live tissue and activate the downstream complement pathway (McGonigal et al., 2016). Therefore, the binding of DG2 in wild type and *GalNAc-T*$^{-/-}$*-Tg(glial)* mice was assessed in this dichotomised context to determine whether it could bind to GM1 on either or both axonal and glial membranes. The results in Figure 3.5A demonstrates that DG2 intensity increased markedly at the nodal gap, corresponding to an increase in pNav intensity, in wild type mice. The representative images confirm this as they show DG2 deposited at the nodal gap but absent from the paranodes, delineated by immunofluorescence staining for Caspr dimers. DG2 was strongly present at both the nodal gap and the paranodes in *GD3s*$^{-/-}$ mice; illustrated by both the graph and representative images in Figure 3.5B. The binding pattern of DG2 in *GalNAc-T*$^{-/-}$*-Tg(neuronal)* mice was comparable to wild type mice; there was an increase in DG2 intensity at the nodal gap (Figure 3.5C). The illustrative images show DG2 co-localising with pNav clusters at the nodal gap and absent from the paranodes. DG2 intensity was comparable across the NoR in *GalNAc-T*$^{-/-}$*-Tg(glial)* mice, indicating that DG2 was detected at both the nodal gap and the paranodes (Figure 3.5D). However, the

representative images demonstrate DG2 overlying the Caspr dimers but absent at the nodal gap, strongly suggesting that DG2 is only binding to the glial membrane. In *GalNAc-T*$^{-/-}$ mice, DG2 intensity was low across the NoR, signifying an absence of DG2 as highlighted by the illustrative images in Figure 3.5E.

In conclusion, DG2 strongly and selectively bound to GM1 on both axonal and glial membranes in wild type, *GD3s*$^{-/-}$, *GalNAc-T*$^{-/-}$*-Tg(neuronal)*, and *GalNAc-T*$^{-/-}$*-Tg(glial)* mice.

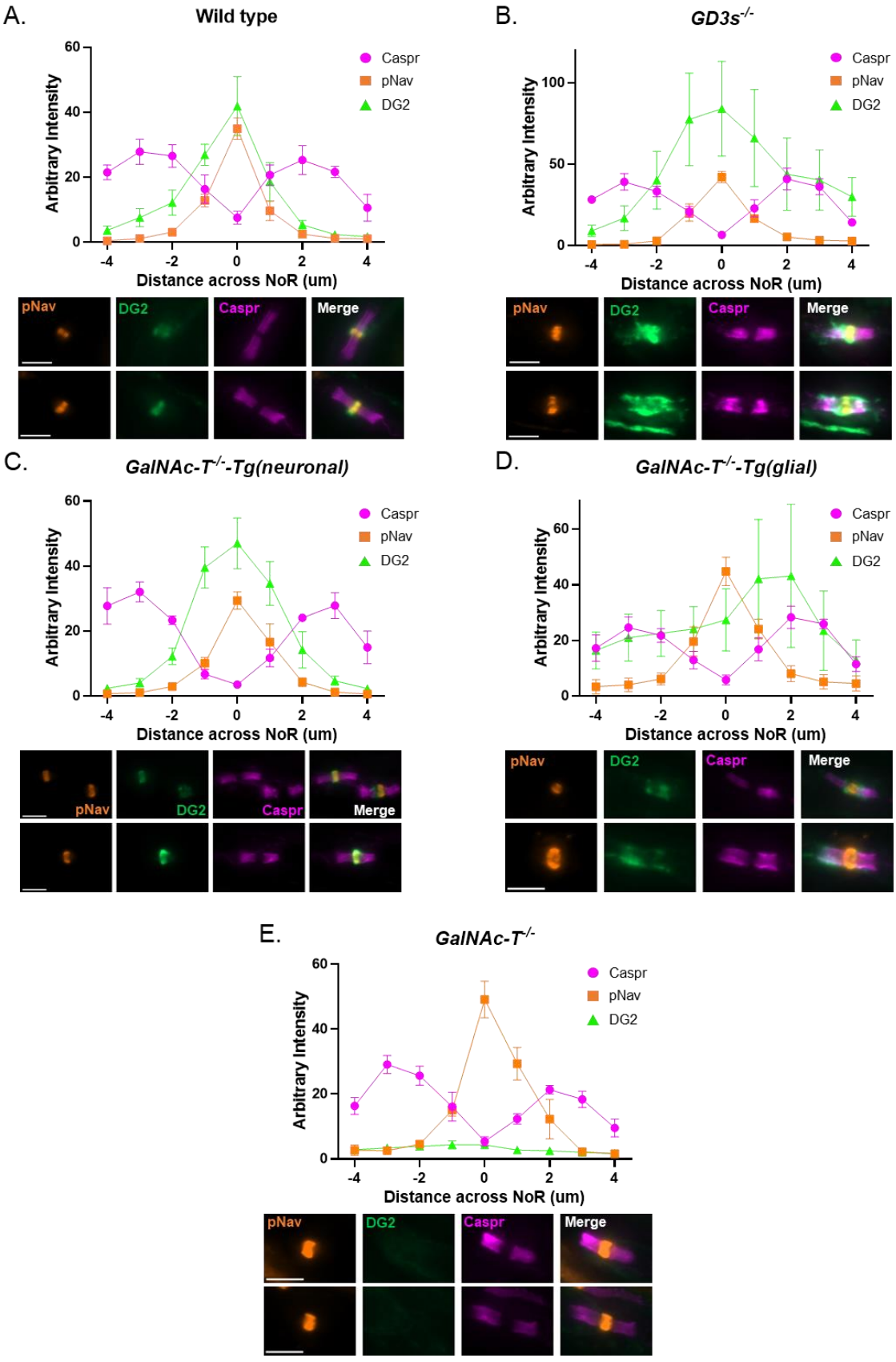
A.
Wild type
Caspr
pNav
DG2
Arbitrary Intensity
Distance across NoR (um)
pNav
DG2
Caspr
Merge
B.
GD3s-/-
C.
GalNAc-T-/--Tg(neuronal)
D.
GalNAc-T-/--Tg(glial)
E.
GalNAc-T-/-

Figure 3.5: DG2 binding in sciatic nerve. (See previous page) The sciatic nerve was harvested from wild type, *GD3s*$^{-/-}$, *GalNAc-T*$^{-/-}$*-Tg(neuronal), GalNAc-T*$^{-/-}$*-Tg(glial)* and *GalNAc-T*$^{-/-}$ mice. The sciatic nerve was de-sheathed and then incubated in 100 µg/ml DG2 for 2 hours at 4℃. Following fixation in 4% paraformaldehyde, the sciatic nerve was sectioned, and immunofluorescence analysis was performed to assess the binding pattern of DG2 at the node of Ranvier (NoR). To identify the nodal gap and paranodes, pNav and Caspr were studied, respectively. A length of 8µm across the NoR was measured, with 0 µm marking the nodal gap and (+/-) 1-4 representing the paranodes. The intensity of DG2, Caspr and pNav at 5 independent NoR was plotted for each genotype. A+C) DG2 deposits were predominantly present at the nodal gap in wild type (A) and *GalNAc-T*$^{-/-}$*-Tg(neuronal)* mice (C), as demonstrated graphically and illustratively with DG2 deposits (green) at the nodal gap (identified by pNav clusters, orange) and absent from the paranodes (Caspr dimers, magenta). B) DG2 intensity was detected across the NoR and was prominent at the nodal gap in *GD3s*$^{-/-}$ mice. Representative images show strong DG2 binding at the nodal gap (pNav clusters) and overlying Caspr dimers. D) DG2 intensity was consistently elevated along the NoR in *GalNAc-T*$^{-/-}$*-Tg(glial)* mice. Illustrative images show DG2 deposits at the paranodes but absent from the nodal gap. E) DG2 was absent from the NoR as shown graphically and illustratively in *GalNAc-T*$^{-/-}$ mice. Results represented as average ± SEM. n=5 NoR/genotype. Scale bar = 5 µm.

3.2.5 Assessment of BO3 binding in sciatic nerve

BO3 is a human anti-GM1 IgM mAb that was derived from an MMN patient (O'Hanlon et al., 1998, Paterson et al., 1995, Willison et al., 1994). The binding properties of BO3 have been studied previously and it was determined that BO3 bound to small fibres in the dorsal root and to nerve bundles in diaphragm sections (O'Hanlon et al., 1998). Additionally, this staining could be blocked by pre-incubation with CTB; therefore, the authors of this study concluded that BO3 had at least some CTB-like features. Thus, BO3 binding in sciatic nerve was assessed and compared among genotypes. Despite the ability of BO3 to bind GM1 in ELISA, BO3 was absent from the NoR in wild type, *GalNAc-T*$^{-/-}$*-Tg(neuronal)* and *GalNAc-T*$^{-/-}$*-Tg(glial)* mice and was comparable to *GalNAc-T*$^{-/-}$ mice (Figure 3.6). Additionally, the increased expression of GM1 in *GD3s*$^{-/-}$ mice had no effect on the ability of BO3 to bind GM1.

Therefore, these results indicate that BO3 was unable to bind GM1 in live tissue under these experimental conditions.

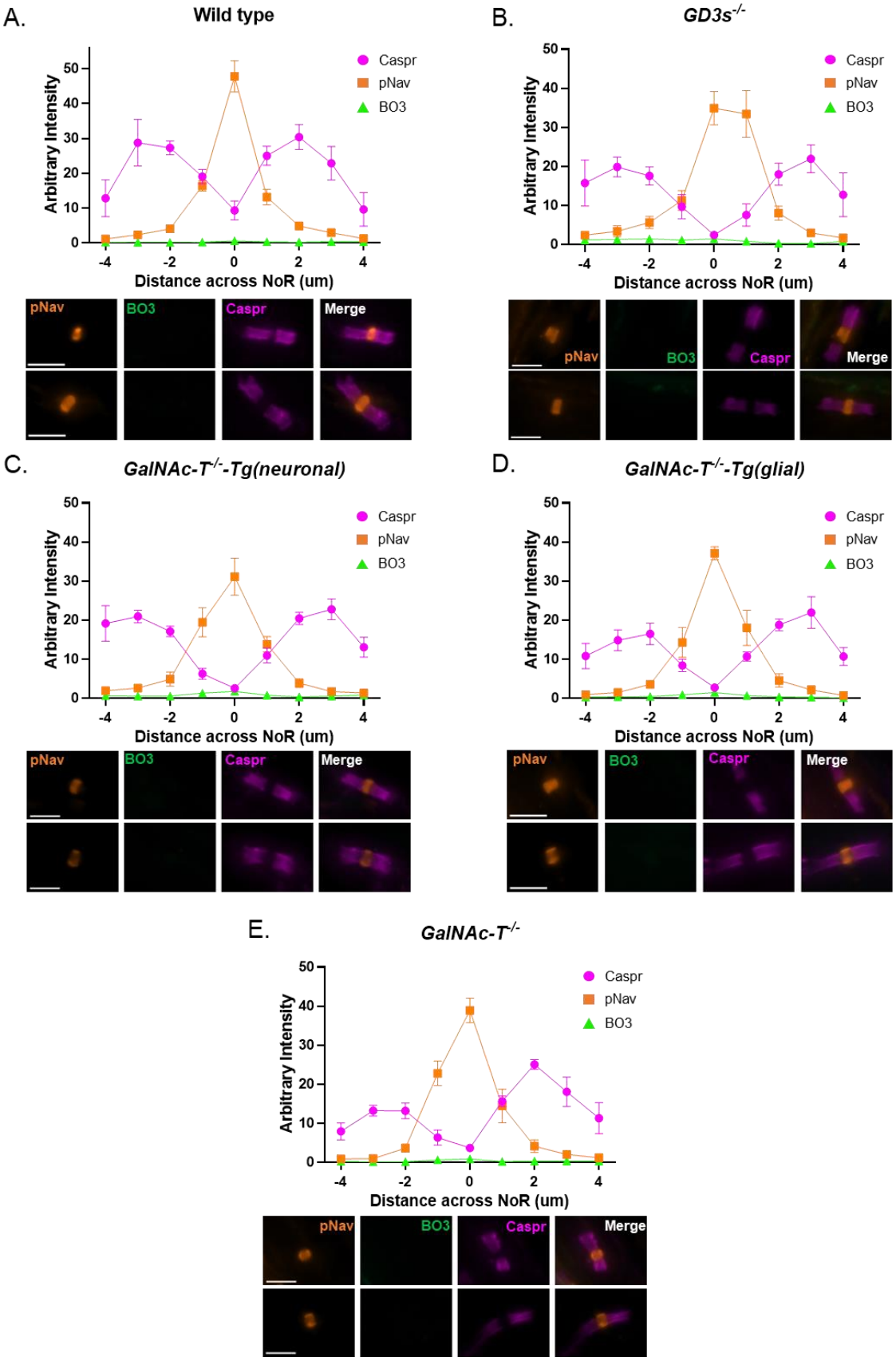
A.
Wild type
B.
GD3s-/-
C.
GalNAc-T-/--Tg(neuronal)
D.
GalNAc-T-/--Tg(glial)
E.
GalNAc-T-/-
Caspr
pNav
BO3
Arbitrary Intensity
Distance across NoR (um)
pNav
BO3
Caspr
Merge

Figure 3.6: BO3 binding in sciatic nerve. (See previous page) The sciatic nerve was harvested from wild type, *GD3s*$^{-/-}$, *GalNAc-T*$^{-/-}$*-Tg(neuronal), GalNAc-T*$^{-/-}$*-Tg(glial)* and *GalNAc-T*$^{-/-}$ mice. The sciatic nerve was de-sheathed and then incubated in 100 µg/ml BO3 for 2 hours at 4℃. Following fixation in 4% paraformaldehyde, the sciatic nerve was sectioned, and immunofluorescence analysis was performed to assess the binding pattern of BO3 at the node of Ranvier (NoR). To identify the nodal gap and paranodes, pNav and Caspr were studied, respectively. A length of 8µm across the NoR was measured, with 0 µm marking the nodal gap and (+/-) 1-4 representing the paranodes. The intensity of BO3, Caspr and pNav at 5 independent NoR was plotted for each genotype. A-E) BO3 was absent from the NoR in all genotypes as demonstrated graphically, by low intensity and illustratively, by absent deposits at pNav clusters (orange) and Caspr dimers (magenta). Results represented as average ± SEM. n=5 NoR/genotype. Scale bar = 5 µm.

3.3 Summary

In summary, these results highlight DG2 as the most suitable of the tested antibody ligands for binding to GM1 on axonal and glial membranes in wild type, *GalNAc-T*$^{-/-}$*-Tg(neuronal)* and *GalNAc-T*$^{-/-}$*-Tg(glial)* mice. Therefore, DG2 was selected as the anti-GM1 mAb to use in further experiments to investigate the downstream pathways involved in anti-GM1 mAb-mediated injury.

3.4 Discussion

It is well established that CTB has a high affinity and selectivity for GM1 ganglioside (Holmgren et al., 1975, Holmgren et al., 1973, Turnbull et al., 2004). Therefore, CTB was used as a positive control and compared to the binding patterns of the anti-GM1 mAbs available for study. The CTB staining revealed variability in apparent GM1 distribution on the membrane between the different genotypes. In wild type and *GD3s*$^{-/-}$ mice, CTB bound predominantly to the nodal gap with staining spreading uniformly into the paranodes. From the images, we are unable to differentiate whether antibody is binding to the axonal membrane or to the glial membrane at the paranodes. There was some weak staining present surrounding the pNav clusters and Caspr dimers in wild type and *GD3s*$^{-/-}$ mice, signifying that this may be binding to the glial membrane. On the other hand, in *GalNAc-T*$^{-/-}$*-Tg(neuronal)* mice, CTB staining at the nodal gap and paranodes was contained within the pNav cluster and Caspr dimer staining, suggesting this may be binding to the axolemmal membrane. The binding pattern of CTB in *GalNAc-T*$^{-/-}$*-Tg(glial)* mice was surprising as it appeared asymmetrical. Although CTB was clearly binding to the glial membrane at the paranodes (as shown by deposits surrounding Caspr dimers),

deposits were predominantly present surrounding one Caspr dimer and not the other Caspr dimer. It is possible that this is due to disproportionate expression of GM1 at the paranodes in *GalNAc-T$^{-/-}$-Tg(glial)* mice. Or alternatively, it could indicate that ganglioside expression differs at different locations along the nerve. However, DG2 binding at the glial paranodes was balanced on each side of the nodal gap in *GalNAc-T$^{-/-}$-Tg(glial)* mice, therefore strongly suggesting that GM1 expression is symmetrical. A possible explanation for the imbalanced binding of CTB at the paranodes could be due to the strong intensity of fluorescence at one paranode, masking weaker fluorescence at the other paranode. Furthermore, there were some examples in the images where CTB deposits were present at both paranodes in *GalNAc-T$^{-/-}$-Tg(glial)* mice but only one Caspr dimer was present and therefore these nodes could not be included in analysis. This indicates that the asymmetrical staining may be a result of tissue sectioning with one hemi-dimer beyond the plane of section. Nonetheless, these results confirm exclusive expression of GM1 on axonal and glial membranes in *GalNAc-T$^{-/-}$-Tg(neuronal)* and *GalNAc-T$^{-/-}$-Tg(glial)* mice, respectively.

Despite all mAbs binding GM1 in ELISA, the results of this chapter demonstrate that DG2 was the only mAb studied here capable of binding the NoR in wild type, *GD3s$^{-/-}$*, *GalNAc-T$^{-/-}$-Tg(neuronal)* and *GalNAc-T$^{-/-}$-Tg(glial)* mice. DG2 bound predominantly to the nodal gap in wild type mice but appeared to be absent from the paranodes. It is possible that the strong DG2 intensity at the nodal gap in wild type mice could be masking the fluorescence present at the paranode, giving the impression that binding is not occurring at this location. Additionally, this could be due to GM1 being more accessible on the axonal membrane at the nodal gap than at the paranode. This is supported by the binding pattern present in *GD3s$^{-/-}$* mice which demonstrated DG2 binding to both the nodal gap and to the paranodes, with staining extending outwith the Caspr dimers, indicating DG2 is binding to the glial membrane. A possible explanation for this could be because GD1b and GT1b are not expressed in *GD3s$^{-/-}$* mice. It has previously been demonstrated that GM1 interacts with GD1a within lipid rafts, masking the binding epitope of GM1 for some AGAbs (Greenshields et al., 2009). Thus, it is possible that GM1 can interact with other gangliosides present on the membrane, such as GD1b and GT1b, and therefore, this inhibitory interaction is removed in *GD3s$^{-/-}$* mice allowing DG2 to freely bind GM1 on the paranodes. Nonetheless, the demonstration of DG2 staining extending beyond the Caspr dimers in *GD3s$^{-/-}$* mice confirms that GM1 is expressed in glial membranes when wild type

GalNAc-T is expressed. This is important as it validates that GM1 is normally expressed in glial membranes and that the reintroduction of gangliosides to the glial membrane in *GalNAc-T$^{-/-}$-Tg(glial)* mice does not result in ectopic expression of GM1. The binding of DG2 to the nodal gap in *GalNAc-T$^{-/-}$-Tg(neuronal)* mice and to the paranodes in *GalNAc-T$^{-/-}$-Tg(glial)* mice further corroborates the successful reintroduction of gangliosides to either the axonal or glial membrane, respectively. Taken together, this validates the use of *GalNAc-T$^{-/-}$-Tg(neuronal)* and *GalNAc-T$^{-/-}$-Tg(glial)* mice to segregate the respective injury to the axonal and glial membrane mediated by anti-GM1 mAb and indicates that the resulting pathology will be physiologically relevant.

Greenshields and colleagues have previously demonstrated the inability of DG1 and other human mAbs derived from MMN patients (SM1 and DO1) to bind wild type live tissue (Greenshields et al., 2009). It was established that these antibodies were unable to bind GM1 on the membrane as the binding epitope was masked by GD1a. This was demonstrated by successful binding of DG1, SM1 and DO1 following pre-treatment with neuraminidase to cleave the terminal sialic acid residue of GD1a, thereby producing *de-novo* GM1 and thus, increasing the density of GM1 in the membrane. BO3 was derived from an MMN patient in the same cohort as SM1 and DO1 (Willison et al., 1994); thus, it is possible that BO3 will have similar binding properties to these antibodies. Despite DG1 and BO3 binding to GM1 in ELISA, I demonstrated that DG1 and BO3 are also unable to bind GM1 in live tissue when expression is restricted to axonal or glial membranes in *GalNAc-T$^{-/-}$-Tg(neuronal)* and *GalNAc-T$^{-/-}$-Tg(glial)* mice, respectively. As already mentioned, it has been determined that DG1 is unable to bind live tissue, likely due to an inhibitory effect with GD1a or *b-series* gangliosides (Greenshields et al., 2009). To determine whether the masking effect of GD1a is interfering with BO3 binding to GM1, the membrane could be pre-treated with neuraminidase to remove all GD1a from the membrane. Surprisingly, DG1 bound to the nodal gap of *GD3s$^{-/-}$* mice but BO3 did not. These mice lack any *b-series* gangliosides resulting in a build-up of GD3, consequently leading to overexpression of *a-series* gangliosides, such as GM1 and GD1a. Therefore, this increased expression could result in GM1 being more accessible to DG1 on the membrane. Furthermore, this suggests that GM1 also interacts with *b-series* gangliosides, like GD1b and GT1b, and hence, the lack of these gangliosides in *GD3s$^{-/-}$* mice removes the inhibitory effect, allowing DG1 to bind GM1. A possible explanation of the inability of BO3 to bind GM1 in *GD3$^{-/-}$* mice is due to the overexpression of GD1a in these mice in

comparison to wild type mice, which could result in GM1 being masked. Additionally, there is evidence to suggest that pathogenic AGAbs can be cleared from the circulation via receptor-dependent internalisation, whilst non-pathogenic AGAbs are left to circulate for longer (Cunningham et al., 2016). BO3 was derived from an MMN patient (Paterson et al., 1995) and hence, it is possible that this antibody was unable to bind and so was present in the sera of the patient, therefore rendering the antibody non-pathogenic. Overall, these results support that the reintroduction of GM1 to either axonal (*GalNAc-T$^{-/-}$-Tg(neuronal)*) or glial membranes (*GalNAc-T$^{-/-}$-Tg(glial)*) is closely representative to GM1 expression in wild type mice and does not alter the glycolipid environment.

Overall, the results of this chapter highlight how the variation in ganglioside composition between different strains of mice can alter the ability of anti-GM1 mAb to bind. An example is DG1 binding to *GD3s$^{-/-}$* mice which overexpress GM1 ganglioside, but not to *GalNAc-T$^{-/-}$-Tg(neuronal)* or *GalNAc-T$^{-/-}$-Tg(glial)* mice that have restricted expression of GM1 to axonal and glial membranes, respectively. It is possible that ganglioside expression in humans varies between individuals. This has ramifications to human disease as it could provide an explanation of why binding of AGAb and the resulting neuropathological effects may differ between individuals.

The results presented in this chapter confirm that *GalNAc-T$^{-/-}$-Tg(neuronal)* and *GalNAc-T$^{-/-}$-Tg(glial)* mice can be used to differentiate between anti-GM1-mediated injury to each neural membrane. In conclusion, DG2 was selected as the anti-GM1 mAb to use in further experiments to characterise targeted anti-GM1 mAb-mediated injury to axonal or glial membranes in *GalNAc-T$^{-/-}$-Tg(neuronal)* and *GalNAc-T$^{-/-}$-Tg(glial)* mice, respectively.

4 Selective injury to axonal or glial membranes

4.1 Introduction

It is well established that AMAN is associated with a serological response directed towards gangliosides, notably GM1 on the motor axolemma (Naik et al., 2017, Willison and Yuki, 2002). However, AIDP patients with a preceding *C. jejuni* infection also have anti-GM1 antibodies present in their sera (Rees et al., 1995a). GM1 is expressed in both axonal and glial membranes in wild type mice (Gong et al., 2002, Sheikh et al., 1999, Susuki et al., 2007b); thus, providing an explanation for the presence of anti-GM1 antibodies in both the axonal and demyelinating variants of GBS. It is currently unknown whether the pathological phenotype mediated by anti-GM1 antibodies arises from injury to the axonal or glial membrane (or both) in AMAN and AIDP. As GM1 is expressed in both membranes, current animal models are unable to differentiate between primary injury and the consequences of cell-specific membrane injury. The aim of this chapter was to anatomically segregate axonal and glial GM1 and develop animal models to study the downstream mechanisms involved, following selective injury to each neural membrane.

Herein, transgenic mice were studied which only express complex gangliosides on either axonal (*GalNAc-T$^{-/-}$-Tg(neuronal)* mice) or glial membranes (*GalNAc-T$^{-/-}$-Tg(glial)* mice) (Yao et al., 2014), allowing each membrane to be independently targeted using the same anti-GM1 mAb. An acute axonal model, representative of AMAN, has been generated previously by McGonigal and colleagues by specifically targeting the axonal membrane with an anti-GM1 mAb in *GalNAc-T$^{-/-}$-Tg(neuronal)* mice (McGonigal et al., 2016). Using the same anti-GM1 mAb, the aim was to develop the counterpart paranodal demyelinating model by exclusively targeting the glial membrane in *GalNAc-T$^{-/-}$-Tg(glial)* mice. Herein, I characterise the injury output at the NMJ and the distal NoR following selective injury to axonal or glial membranes with a single anti-GM1 mAb, and compare the injury to when GM1 is expressed in both neural membranes in wild type mice.

The anti-GM1 mAb mediated injury model was adapted from a previously established axonal murine injury model by Halstead et al. (2008). Only distal motor NMJs and the most distal NoR were considered during analysis. This site restriction arises because distal nerves are highly vulnerable to antibody-mediated injury as they lie outwith the

protection of the BNB and so are exposed to circulating factors (Brown and Snow, 1991). It has been demonstrated, in a similar injury model, that injury does not occur to nerve bundles due to the presence of the BNB (McGonigal et al., 2010); although, injury may occur in nerve roots which similarly reside outwith a prominent blood nerve barrier. Due to the proximity of the diaphragm to the intraperitoneal site of antibody and complement injections, this results in prominent intra-diaphragmatic nerve and nerve terminal injury (Halstead et al., 2008). The function of the diaphragm can be measured as an indication of injury output in our model by using WBP. This is a non-invasive method which can be used to measure TV and RR in small animals (Lim et al., 2014).

In this chapter, I first describe the clinical phenotype as manifested by changes in respiratory function of wild type, *GalNAc-T$^{-/-}$-Tg(neuronal)* and *GalNAc-T$^{-/-}$-Tg(glial)* mice following intraperitoneal administration of anti-GM1 mAb and NHS, as a source of complement. Subsequently, I performed immunofluorescence analysis to assess the effects of complement-mediated injury to cytoskeletal structural proteins at the NMJ and distal NoR and to axo-glial adhesion molecules at the NoR. Finally, the ultrastructure of the NMJ and NoR was explored in *GalNAc-T$^{-/-}$-Tg(neuronal)* and *GalNAc-T$^{-/-}$-Tg(glial)* mice following selective injury to axonal or glial membranes, respectively.

4.2 Results

Wild type*, GalNAc-T$^{-/-}$-Tg(neuronal)* and *GalNAc-T$^{-/-}$-Tg(glial)* mice were injected intraperitoneally with either anti-GM1 mAb and complement (injury group) or PBS and complement (control group). WBP was performed to monitor respiratory function. At the end of the experiment (6 hours post NHS injection), the diaphragm was harvested for associated immunofluorescence or ultrastructure analysis, and the sera collected to perform an ELISA and topical complement assay. The results from this analysis are described in detail below.

4.2.1 Confirmation of anti-GM1 antibody and complement in sera of mice

To determine whether the passive immunisations were successful, a blood sample was taken from each mouse at the end of the *in vivo* experiment to investigate whether anti-GM1 mAb and complement were present in the circulation of wild type, *GalNAc-T$^{-/-}$-*

Tg(neuronal) and *GalNAc-T$^{-/-}$-Tg(glial)* mice, by performing an ELISA and a topical complement assay, respectively.

Figure 4.1A presents the results from the ELISA, illustrating the mean OD values for each individual mouse. The results show that injured *GalNAc-T$^{-/-}$-Tg(neuronal)* mice have a mean OD value of 1.33 $\pm$ 0.07 AU which was significantly higher than 0.21 $\pm$ 0.09 AU of *GalNAc-T$^{-/-}$-Tg(neuronal)* control mice ($p<0.001$). Likewise, the OD value of injured *GalNAc-T$^{-/-}$-Tg(glial)* mice was 1.29 $\pm$ 0.11 AU which was significantly higher compared *GalNAc-T$^{-/-}$-Tg(glial)* control mice ($p<0.001$). The mean OD values of injured *GalNAc-T$^{-/-}$-Tg(neuronal)* and injured *GalNAc-T$^{-/-}$-Tg(glial)* mice were higher than the mean OD value of the GM1 positive control; therefore, indicating the presence of anti-GM1 mAb in the sera of all mice. There were no mice which had to be excluded from the injured *GalNAc-T$^{-/-}$-Tg(neuronal)* or injured *GalNAc-T$^{-/-}$-Tg(glial)* groups due to the absence of anti-GM1 mAb in the sera. In contrast, the OD value of injured wild type mice does not follow the same trend. The mean OD value of injured wild type mice was 0.08 $\pm$ 0.04 AU which was significantly lower compared to both *GalNAc-T$^{-/-}$-Tg(neuronal)* and *GalNAc-T$^{-/-}$-Tg(glial)* injured mice ($p=<0.001$). There was no significant difference between the mean OD values of injured wild type mice and control wild type mice. As GM1 is expressed in other tissues in wild type mice, it is predicted that the antibody is being sequestered and binding elsewhere (Cunningham et al., 2016).

To assess whether the NHS injection was successfully delivered and that anti-GM1 mAb had subsequently activated the complement pathway, a topical complement assay was performed. The graph in Figure 4.1B shows the number of mice who had positive or negative complement deposits in the assay. As control mice received NHS only, the addition of CGM3 (an AGAb) had to be administered to the assay to activate the complement pathway in control mice. From the results we can see that complement was found to be activated by anti-GM1 mAb (injured group) or CGM3 (control group) in all wild type mice, indicating successful delivery of NHS to the circulation (Figure 4.1B). Sera from 2 control and 2 injured *GalNAc-T$^{-/-}$-Tg(neuronal)* mice were negative for complement. Complement was also absent from the sera of 2 injured and 2 control *GalNAc-T$^{-/-}$-Tg(glial)* mice. All mice with negative C3c deposits in the assay and therefore, no evidence of complement present in their sera, were removed from analysis.

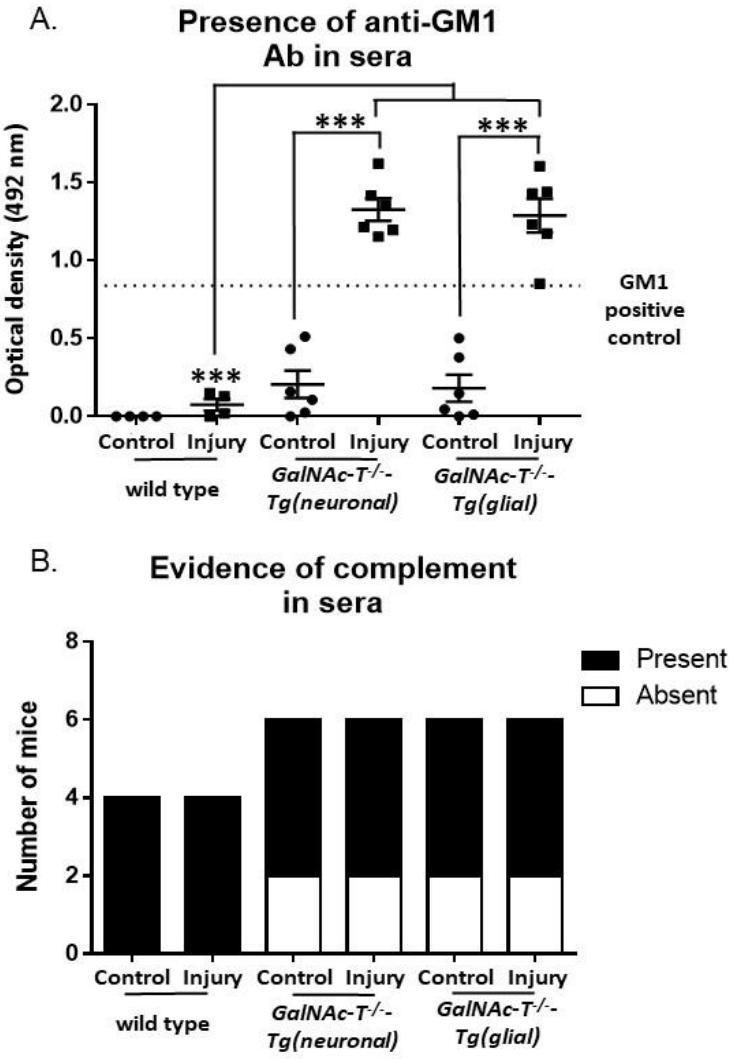

Figure 4.1: Confirmation of anti-GM1 mAb and complement in the sera of mice. Wild type, *GalNAc-T$^{-/-}$-Tg(neuronal)* and *GalNAc-T$^{-/-}$-Tg(glial)* mice were injected intraperitoneally (IP) with 50 mg/kg anti-GM1 mAb, followed 16 hours later with 30 µl/g normal human serum (NHS), delivered IP. Control mice received PBS and NHS. A blood sample was collected 6 hours post NHS injection; an ELISA and topical complement assay were performed using the sera to confirm the presence of anti-GM1 mAb and complement, respectively. A) Injured *GalNAc-T$^{-/-}$-Tg(neuronal)* and injured *GalNAc-T$^{-/-}$-Tg(glial)* mice had significantly higher optical density (OD) values compared to their respective controls (***=p<0.001). Wild type injured mice had significantly lower OD values compared to *GalNAc-T$^{-/-}$-Tg(neuronal)* and *GalNAc-T$^{-/-}$-Tg(glial)* injured mice (***=p<0.001). Results represent mean ±SEM. A two-way ANOVA with Tukey's multiple comparisons test was performed to test for statistical significance. B) Complement was detected by immunofluorescence staining for the early complement component, C3c. Two mice from each treatment group in *GalNAc-T$^{-/-}$-Tg(neuronal)* and *GalNAc-T$^{-/-}$-Tg(glial)* mice had negative immunofluorescence staining for C3c and were removed from analysis. n=4 wild type mice; n=6 for *GalNAc-T$^{-/-}$-Tg(neuronal)* and *GalNAc-T$^{-/-}$-Tg(glial)* mice.

4.2.2 Respiratory phenotype of mice

A baseline WBP recording was taken prior to injection of anti-GM1 mAb to determine the normal TV and RR for each animal. Respiratory function was then monitored between 225-315 minutes post NHS injection, referred to as post injury, to assess the changes in TV and RR.

4.2.2.1 Change in tidal volume post injury

To assess the change in TV, the average TV at 15-minute intervals was determined. Figure 4.2 illustrates the TV of wild type, *GalNAc-T$^{-/-}$-Tg(neuronal),* and *GalNAc-T$^{-/-}$-Tg(glial)* mice, as a percentage of the baseline TV between 225-315 minutes post injury (MPI). Each genotype is separated into separate graphs, but all treatment groups were considered in the one data set when performing statistical analysis. The TV in control wild type mice was elevated above baseline at every time point, although not significantly. On the other hand, the TV in injured wild type mice was significantly reduced at 255-315 MPI compared to baseline ($p<0.05$ at 225-285 and 315 MPI; $p<0.01$ at 300 MPI). In *GalNAc-T$^{-/-}$-Tg(neuronal)* control mice, the TV was comparable to baseline at all time points except at 285 MPI when it was significantly reduced to 78 $\pm$ 7% ($p<0.05$). The TV in *GalNAc-T$^{-/-}$-Tg(neuronal)* injured mice was severely affected; the TV was significantly reduced at every time point compared to baseline ($p<0.001$). In *GalNAc-T$^{-/-}$-Tg(glial)* control mice, the TV was elevated above baseline at every timepoint, differing significantly at 225, 255 and 285 MPI ($p<0.001$; $p<0.01$; $p<0.05$, respectively). The TV of injured *GalNAc-T$^{-/-}$-Tg(glial)* mice was significantly reduced in comparison to baseline at 240-315 MPI ($p<0.05$ at 240 and 270 MPI; $p<0.01$ at 300 and 315 MPI; $p<0.001$ at 255 and 285 MPI). In addition, the TV of injured *GalNAc-T$^{-/-}$-Tg(glial)* mice was significantly reduced to control at 225, 255 and 285 MPI ($p<0.01$ at 225 and 285 MPI; $p<0.001$ at 255 MPI). Overall, these results demonstrate that injured mice present with a significant reduction in TV.

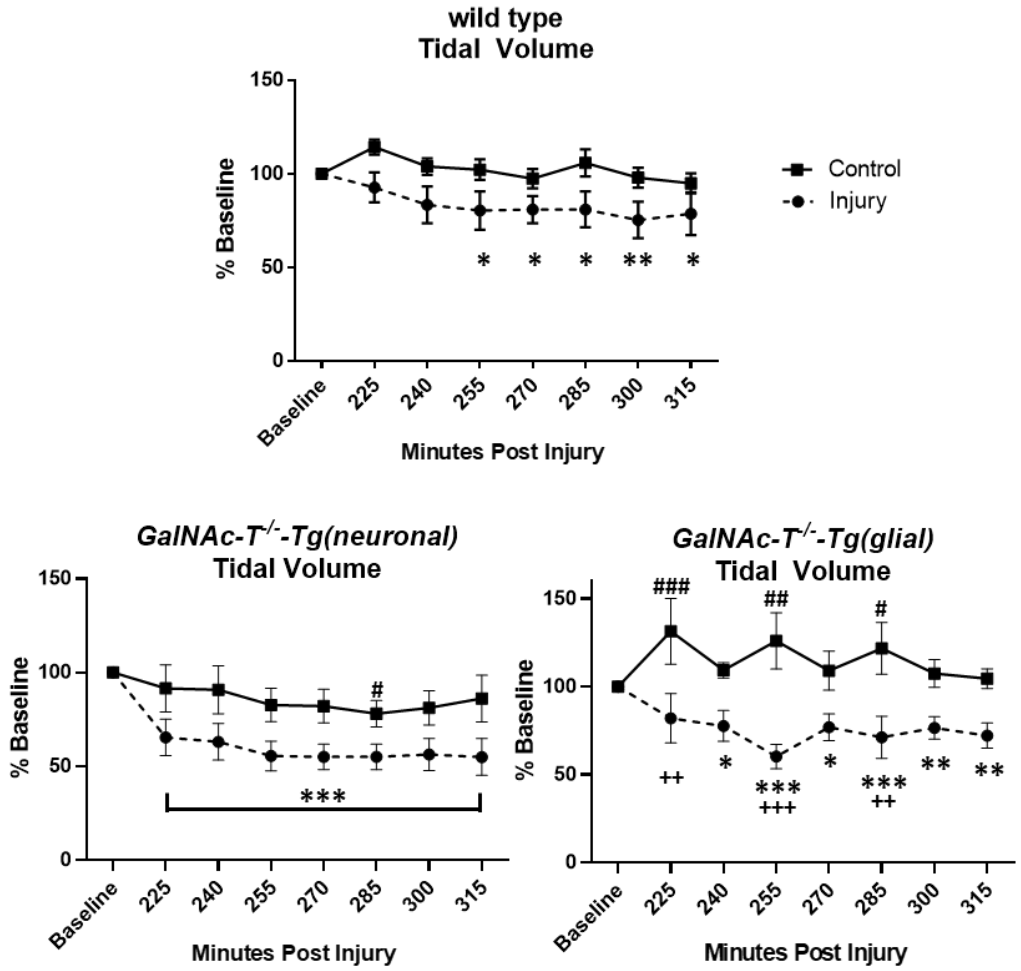

Figure 4.2: Assessment of tidal volume over time. A baseline whole-body plethysmography (WBP) recording was taken prior to an intraperitoneal (IP) injection of 50 mg/kg of anti-GM1 mAb, followed 16 hours later with an IP injection of 30 µl/g normal human serum (NHS), in wild type, *GalNAc-T$^{-/-}$-Tg(neuronal)* and *GalNAc-T$^{-/-}$-Tg(glial)* mice. Control mice received PBS and NHS. A WBP recording was then taken 225-315 minutes post NHS injection, to monitor the tidal volume (TV). There was no significant difference in the TV of control wild type mice at any time point compared to baseline. The TV in injured wild type mice was significantly reduced from 255-315 minutes post injury (MPI) compared to baseline (*=p<0.05; **=p<0.01). The TV of *GalNAc-T$^{-/-}$-Tg(neuronal)* control mice was significantly reduced compared to baseline at 285 MPI (#=p<0.05). In injured *GalNAc-T$^{-/-}$-Tg(neuronal)* mice, the TV was significantly lower than baseline at each time point (***=p<0.001). Similarly, the TV was significantly reduced at every time point in injured *GalNAc-T$^{-/-}$-Tg(glial)* mice compared to baseline, except at 225 MPI (*=p<0.05; **=p<0.01; ***=p<0.001). The TV of *GalNAc-T$^{-/-}$-Tg(glial)* control mice was significantly elevated in comparison to baseline (#=p<0.05; ##=p<0.01; ###=p<0.001) and injured *GalNAc-T$^{-/-}$-Tg(glial)* mice (++=p<0.01; +++=p<0.001) at 225, 255 and 285 MPI. Statistical significance was tested by performing a repeated measures two-way ANOVA with Dunnett's multiple comparisons test to compare the TV at each time point with the baseline TV, within in each treatment group. A regular two-way ANOVA with Sidak's multiple comparisons test was performed to test for statistical significance between control and injured groups at each time point. ***** = injured mice compared to baseline; **#** = control mice compared to baseline. **+** = injured mice compared to control mice. Results represented as the average ± SEM, n=4/genotype/treatment.

4.2.2.2 Change in respiratory rate post injury

Next, the change in RR over the 2-hour recording was investigated by averaging the RR at 15-minute intervals. Figure 4.3 illustrates the RR of wild type, *GalNAc-T$^{-/-}$-Tg(neuronal),* and *GalNAc-T$^{-/-}$-Tg(glial)* mice, as a percentage of the baseline RR between 225-315 MPI. Each genotype is separated into separate graphs for ease of reading; however, all treatment groups were considered in the one data set for statistical analysis. The RR of wild type control mice was comparable to baseline throughout. Although the RR of injured wild type mice was elevated above baseline and control at each time point, this did not differ significantly at any time point. The RR of control and injured *GalNAc-T$^{-/-}$-Tg(neuronal)* mice was comparable to each other throughout the recording. In comparison to baseline, the RR of control and injured *GalNAc-T$^{-/-}$-Tg(neuronal)* mice was elevated at every time point, although not significantly. In contrast to all other treatment groups, the RR of *GalNAc-T$^{-/-}$-Tg(glial)* control mice was reduced at every time point compared to baseline, reaching significance at 255, 285, 300 and 315 MPI ($p<0.05$ at 255, 285 and 315 MPI; $p<0.01$ at 300 MPI). The RR of injured *GalNAc-T$^{-/-}$-Tg(glial)* mice was extremely variable, rising and falling at each consecutive time point, although the RR did not differ significantly to baseline at any time point. Nevertheless, the RR of injured *GalNAc-T$^{-/-}$-Tg(glial)* mice was significantly elevated at 255 MPI in comparison to control ($p<0.05$).

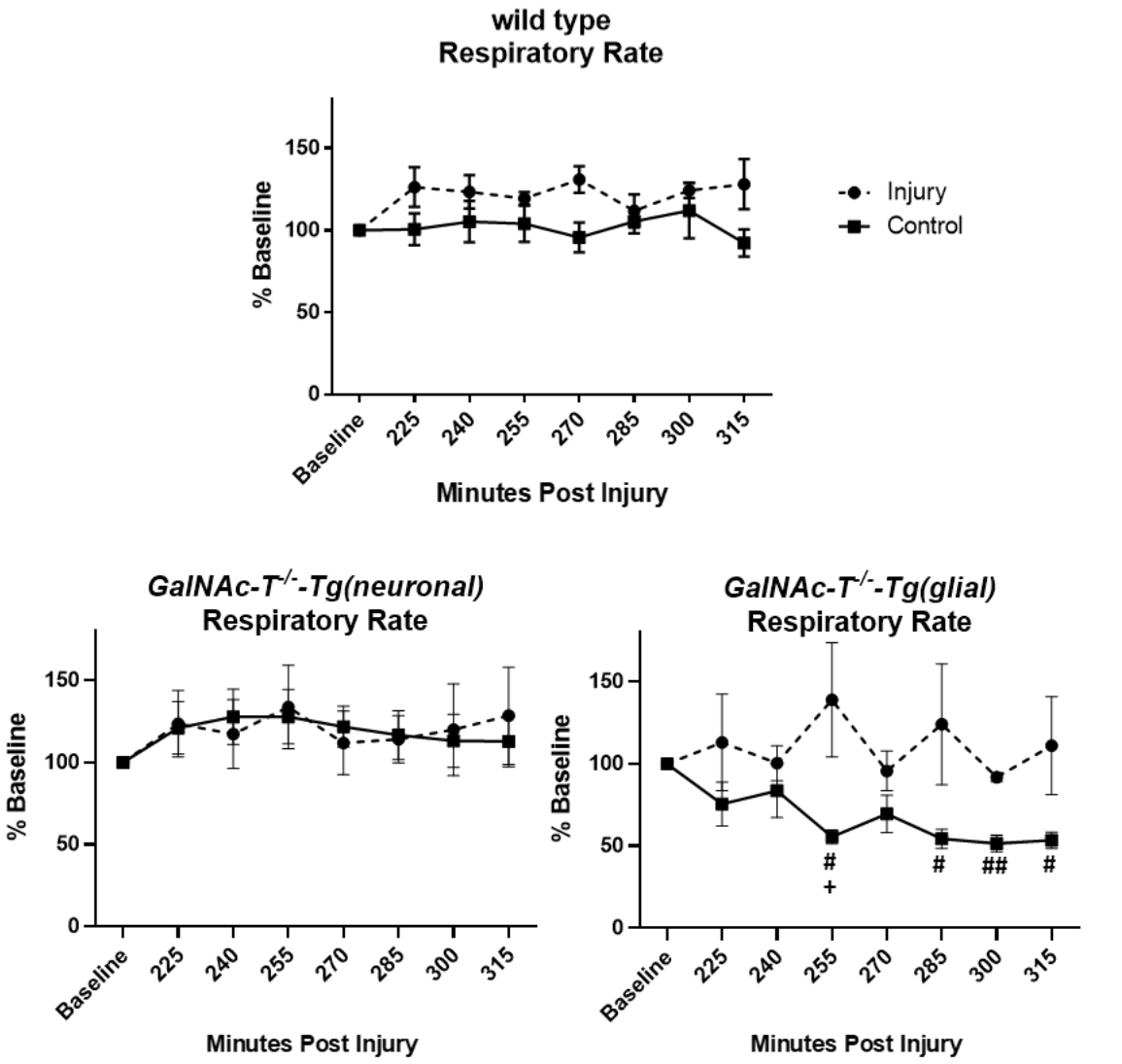

Figure 4.3: Assessment of respiratory rate over time. To determine the baseline respiratory rate (RR), whole-body plethysmography (WBP) was performed prior to intraperitoneal (IP) injection of 50 mg/kg of anti-GM1 mAb. Sixteen hours later, 30 µl/g normal human serum (NHS) was delivered IP, in wild type, *GalNAc-T$^{-/-}$-Tg(neuronal)* and *GalNAc-T$^{-/-}$-Tg(glial)* mice. Control mice received PBS and NHS. A WBP recording was then taken 225-315 minutes post NHS injection, to monitor the change in RR following injury. The RR in injured wild type mice was elevated compared to control at each time point, although not significantly. The RR of control wild type mice was comparable to baseline at each time point. The RR of control and injured *GalNAc-T$^{-/-}$-Tg(neuronal)* mice did not differ at any time point to baseline nor to each other. The RR of control *GalNAc-T$^{-/-}$-Tg(glial)* mice was significantly reduced compared to baseline at 255, 285, 300 and 315-minutes post injury (#=p<0.05; ##=p<0.01). In injured *GalNAc-T$^{-/-}$-Tg(glial)* mice, the RR was elevated above baseline at 255, 285 and 315 MPI, although not significantly. Statistical significance was tested by performing a repeated measures two-way ANOVA with Dunnett's multiple comparisons test to compare the RR at each time point with the baseline RR, within each treatment group. A regular two-way ANOVA with Sidak's multiple comparisons test was performed to test for statistical significance between control and injured groups at each time point. **#** = control mice compared to baseline. + = injured mice compared to control. Results represented as the average ± SEM, n=4/genotype/treatment.

4.2.2.3 Respiratory flow charts

The representative flow charts in Figure 4.4 illustrate the TV and RR results discussed above (Figure 4.2 and Figure 4.3, respectively). They show a noticeable reduction in volume in injured *GalNAc-T$^{-/-}$-Tg(neuronal)* mice at 5-hours compared to baseline and control, which was accompanied with an increased rate of flow. The flow charts also demonstrate an increased RR in injured wild type and injured *GalNAc-T$^{-/-}$-Tg(glial)* mice compared to baseline and their respective controls, paired with a subtle reduction in TV. Additionally, there is a decreased rate of flow at 5 hours in *GalNAc-T$^{-/-}$-Tg(glial)* control mice in comparison to baseline which explains the significant reduction in RR, detailed in Figure 4.3.

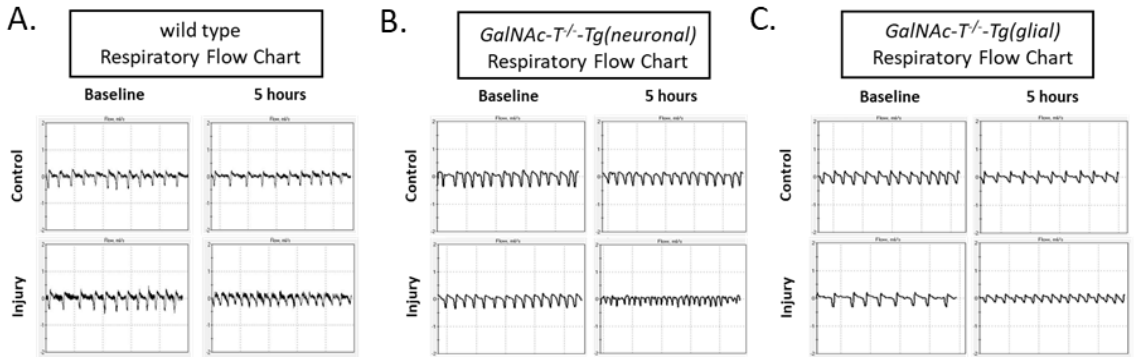

Figure 4.4: Representative respiratory flow charts. Wild type, *GalNAc-T$^{-/-}$-Tg(neuronal)* and *GalNAc-T$^{-/-}$-Tg(glial)* mice were injected intraperitoneally (IP) with 50 mg/kg anti-GM1 mAb, followed 16 hours later with 30 ul/g normal human serum (NHS), delivered IP. Control mice received PBS and NHS. Representative flow charts at baseline and 5-hours post injury for each treatment group are shown. A) There is an increased rate of flow in injured wild type mice at 5 hours in comparison to baseline and control. B) There is a noticeable reduction in volume in injured *GalNAc-T$^{-/-}$-Tg(neuronal)* mice at 5-hours post injury paired with an increased rate of flow. C) Control *GalNAc-T$^{-/-}$-Tg(glial)* mice present with a decreased rate of flow at 5 hours compared to baseline. There is a subtle decrease in TV in injured *GalNAc-T$^{-/-}$-Tg(glial)* mice accompanied with an increased rate of flow.

4.2.3 Observed phenotype

During the *in vivo* experiment, the behaviour and phenotype of each mouse was assessed. It was noted that injured mice commonly presented with abnormally rapid breathing, termed tachypnoea. Some injured mice also displayed signs of piloerection (erection of hair), pinned back ears, and a reluctance to move once placed in the WBP chambers. On occasion, control mice also presented with tachypnoea. In contrast to injury mice, control mice would be more active during the recording and would groom

and forage. Injured wild type, *GalNAc-T$^{-/-}$-Tg(neuronal)* and *GalNAc-T$^{-/-}$-Tg(glial)* mice all presented with tachypnoea, however, only in injured *GalNAc-T$^{-/-}$-Tg(neuronal)* mice was the phenotype accompanied with a pinched wasp-like abdomen, indicative of diaphragm paralysis (Figure 4.5).

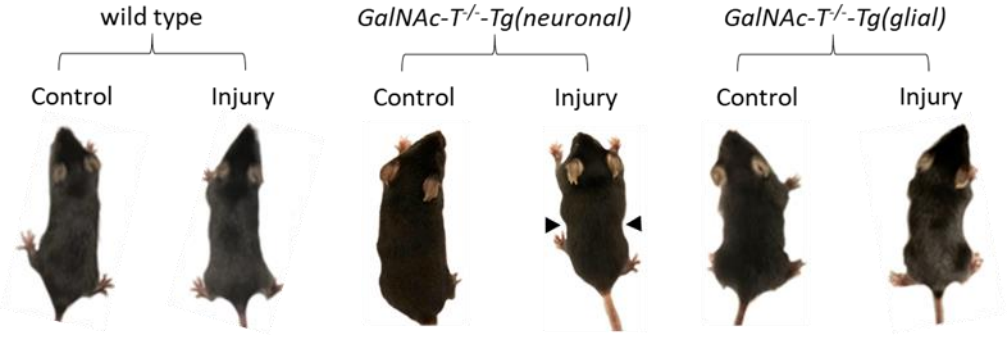

Figure 4.5: Observed phenotype of mice at 5-hours post injury. Wild type, *GalNAc-T$^{-/-}$-Tg(neuronal)* and *GalNAc-T$^{-/-}$-Tg(glial)* mice were injected intraperitoneally (IP) with 50 mg/kg anti-GM1 mAb followed 16 hours later with an IP injection of 30 µl/g normal human serum (NHS). Control mice received PBS and NHS. The phenotypes of all mice at 5-hours post injury were observed. Black arrow heads indicate a pinched wasp-like abdomen in injured *GalNAc-T$^{-/-}$-Tg(neuronal)* mice caused by diaphragm paralysis.

4.2.4 Anti-GM1 antibody and complement deposition at the NMJ

The results from the intensity analysis at the NMJ were inconclusive, partly because the mean intensity values were all very low and so it was difficult to pull apart differences between groups (see Appendix 8.1). Therefore, it was decided that subjective presence/absence analysis would be more informative. Figure 4.6 illustrates the total number of NMJs with anti-GM1 mAb, C3c and MAC deposits (displayed as a percentage).

Results indicate that anti-GM1 mAb deposits were detected at 73 $\pm$ 7 % of NMJs in injured *GalNAc-T$^{-/-}$-Tg(neuronal)* mice which was significantly higher compared to all other treatment groups ($p=<0.001$; Figure 4.6). In contrast, 26 $\pm$ 5% of NMJs had positive anti-GM1 mAb deposits in injured *GalNAc-T$^{-/-}$-Tg(glial)* mice. Although significantly lower compared to injured *GalNAc-T$^{-/-}$-Tg(neuronal)* mice, this was significantly higher compared to *GalNAc-T$^{-/-}$-Tg(glial)* control mice and injured wild type mice ($p=<0.01$). Surprisingly, only 5 $\pm$ 2% of NMJs had anti-GM1 mAb deposits in injured wild type mice and this was comparable to control mice. This data corroborates the ELISA results which were discussed previously (section4.2.1). Anti-GM1 mAb deposits were absent from all control groups, as expected. Representative images illustrate the differential binding

pattern of anti-GM1 mAb in *GalNAc-T$^{-/-}$-Tg(neuronal)* and *GalNAc-T$^{-/-}$-Tg(glial)* mice. In injured *GalNAc-T$^{-/-}$-Tg(neuronal)* mice, anti-GM1 mAb deposits were directly overlying the NMJ, identified by BTx. On the other hand, anti-GM1 mAb was deposited surrounding the NMJ in injured *GalNAc-T$^{-/-}$-Tg(glial)* mice, likely binding to pSC.

Figure 4.6B shows that C3c deposits were detected at 54 ± 15% and 43 ± 8% of NMJs in injured *GalNAc-T$^{-/-}$-Tg(neuronal)* and injured *GalNAc-T$^{-/-}$-Tg(glial)* mice, respectively, which was significantly higher compared to their respective controls (p=<0.01 *GalNAc-T$^{-/-}$-Tg(neuronal)* control; p=<0.05 *GalNAc-T$^{-/-}$-Tg(glial)* control). The percentage of NMJs with C3c deposits was comparable in control and injured wild type mice. There were significantly fewer NMJs with C3c deposits in injured wild type mice compared to injured *GalNAc-T$^{-/-}$-Tg(neuronal)* mice (p=<0.05). Illustrative images show C3c present overlying the NMJ in injured *GalNAc-T$^{-/-}$-Tg(neuronal)* mice. In contrast, C3c is deposited surrounding the NMJ in injured *GalNAc-T$^{-/-}$-Tg(glial)* mice. As anticipated, C3c deposits were absent from NMJs in injured wild type mice and all control mice.

The deposition of MAC at the NMJ followed the same trend which was found for both anti-GM1 mAb and C3c deposition. MAC deposits were detected at 52 ± 17% of NMJs in injured *GalNAc-T$^{-/-}$-Tg(neuronal)* mice, which was significantly higher compared to control mice (p=<0.01; Figure 4.6C). There were significantly fewer NMJs with MAC deposits in injured wild type mice compared to injured *GalNAc-T$^{-/-}$-Tg(neuronal)* mice. Injured *GalNAc-T$^{-/-}$-Tg(glial)* mice had MAC deposits present at 29 ± 6% of NMJs, but this did not differ significantly to control. There were low levels of MAC deposition found in all control mice which corresponded with the C3c results, likely due to non-specific activation. Representative images demonstrate MAC deposits overlying the NMJ in injured *GalNAc-T$^{-/-}$-Tg(neuronal)* mice, whereas MAC deposits were present surrounding the NMJ in injured *GalNAc-T$^{-/-}$-Tg(glial)* mice, likely binding to non-myelinating pSC. MAC deposits were absent from injured wild type NMJs and all control mice.

In summary, anti-GM1 mAb and complement deposits were detected at the NMJ in both *GalNAc-T$^{-/-}$-Tg(neuronal)* and *GalNAc-T$^{-/-}$-Tg(glial)* injured mice, but not to a significant degree in injured wild type mice or controls.

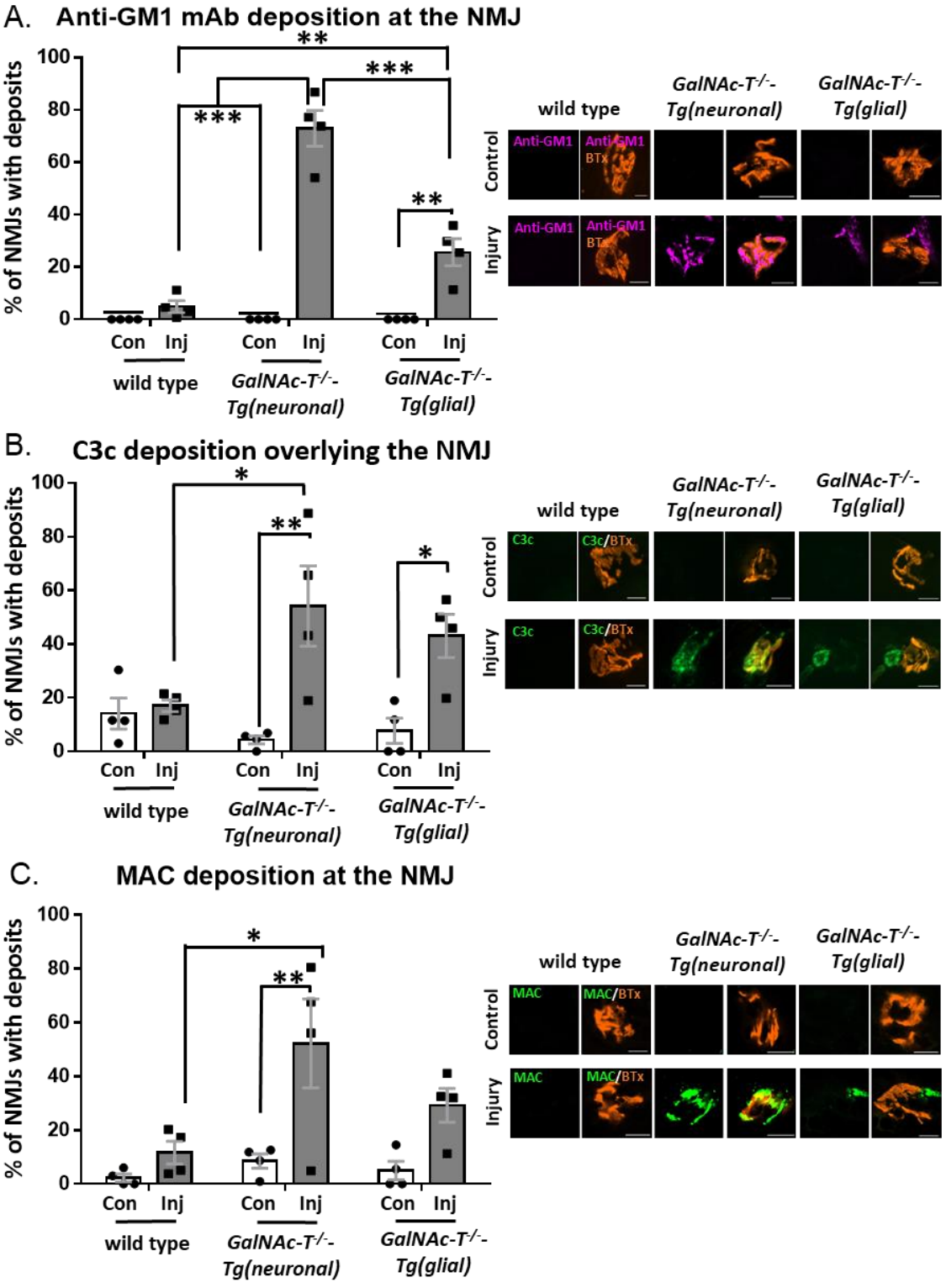
A. Anti-GM1 mAb deposition at the NMJ
% of NMJs with deposits
Con Inj Con Inj Con Inj
wild type
GalNAc-T-/- Tg(neuronal)
GalNAc-T-/- Tg(glial)
wild type
GalNAc-T-/- Tg(neuronal)
GalNAc-T-/- Tg(glial)
Control
Injury
Anti-GM1
Anti-GM1 BTx
B. C3c deposition overlying the NMJ
% of NMJs with deposits
Con Inj Con Inj Con Inj
wild type
GalNAc-T-/- Tg(neuronal)
GalNAc-T-/- Tg(glial)
wild type
GalNAc-T-/- Tg(neuronal)
GalNAc-T-/- Tg(glial)
Control
Injury
C3c
C3c/BTx
C. MAC deposition at the NMJ
% of NMJs with deposits
Con Inj Con Inj Con Inj
wild type
GalNAc-T-/- Tg(neuronal)
GalNAc-T-/- Tg(glial)
wild type
GalNAc-T-/- Tg(neuronal)
GalNAc-T-/- Tg(glial)
Control
Injury
MAC
MAC/BTx

Figure 4.6: Assessment of antibody and complement deposition at the NMJ. (Figure on previous page) Diaphragm was harvested from wild type*, GalNAc-T$^{-/-}$-Tg(neuronal)* and *GalNAc-T$^{-/-}$-Tg(glial)* mice following anti-GM1 mAb and complement mediated *in vivo* injury and immunofluorescence analysis was performed. The percentage of neuromuscular junctions (NMJs) with anti-GM1 mAb, C3c and membrane attack complex (MAC) deposits were determined. A) There were significantly more NMJs with anti-GM1 mAb deposits in injured *GalNAc-T$^{-/-}$-Tg(neuronal)* mice compared to all other groups (***=p<0.001). There were significantly more NMJs with anti-GM1 mAb deposits in injured *GalNAc-T$^{-/-}$-Tg(glial)* mice compared to control mice and wild type injured mice(**p=<0.01). The percentage of anti-GM1 mAb deposits in injured wild type mice did not differ significantly compared to control. Representative images show anti-GM1 mAb (magenta) overlying the NMJ (identified by bungarotoxin (BTx), orange) in injured *GalNAc-T$^{-/-}$-Tg(neuronal)* mice and surrounding the nerve terminal in injured *GalNAc-T$^{-/-}$-Tg(glial)* mice. B) C3c was deposited at an increased number of NMJs in injured *GalNAc-T$^{-/-}$-Tg(neuronal)* and injured *GalNAc-T$^{-/-}$-Tg(glial)* mice compared to their respective controls (**=p<0.01; *=p<0.05). There were significantly less NMJs with C3c deposits in injured wild type mice compared to injured *GalNAc-T$^{-/-}$-Tg(neuronal)* mice (*=p<0.05). The percentage of NMJs with C3c deposits was comparable in control and injured wild type mice. Representative images show C3c complement (green) overlying the NMJ (BTx, orange) in injured *GalNAc-T$^{-/-}$-Tg(neuronal)* mice and surrounding the NMJ in injured *GalNAc-T$^{-/-}$-Tg(glial)* mice. C) MAC deposits were present at an increased number of NMJs in injured *GalNAc-T$^{-/-}$-Tg(neuronal)* mice compared to control (**=p<0.01) and injured wild type mice (*=p<0.05). Injured wild type mice and injured *GalNAc-T$^{-/-}$-Tg(glial)* mice did not differ significantly compared to their respective controls. Illustrative images demonstrate MAC (green) deposits overlying the NMJ in injured *GalNAc-T$^{-/-}$-Tg(neuronal)* mice and surrounding the NMJ in injured *GalNAc-T$^{-/-}$-Tg(glial)* mice. Scale bar=10 µm. Statistical significance tested by performing two-way ANOVA with Tukey's multiple comparisons test. Results represent mean ±SEM. n=4/genotype/treatment.

4.2.5 Axonal integrity at the NMJ

The axonal structural protein, neurofilament, is cleaved by calpain following MAC pore formation (Kamakura et al., 1983, O'Hanlon et al., 2003). Therefore, axonal integrity following complement mediated injury was assessed by studying the presence of NFH. Figure 4.7A illustrates that the percentage of NMJs that were occupied with NFH did not differ between wild type control (66 ± 2%) and injury (72 ± 8%) groups, nor between *GalNAc-T$^{-/-}$-Tg(glial)* control (73 ± 5%) and injury (68 ± 5%) groups. There was a significant reduction in occupied NMJs in injured *GalNAc-T$^{-/-}$-Tg(neuronal)* mice to 42 ± 14%, compared to 81 ± 1% of occupied NMJs in control mice (p<0.05). Representative images demonstrate C3c deposits at the NMJ in *GalNAc-T$^{-/-}$-Tg(neuronal)* injured mice, corresponding to a loss of NFH (Figure 4.7B). Contrastingly, in injured *GalNAc-T$^{-/-}$-Tg(glial)* mice, NFH was still occupying the NMJ even when C3c deposits were present surrounding the NMJ.

In conclusion, injury to the axonal membrane in *GalNAc-T$^{-/-}$-Tg(neuronal)* mice results in significant disruption to axon integrity at the NMJ, measured by a loss of neurofilament.

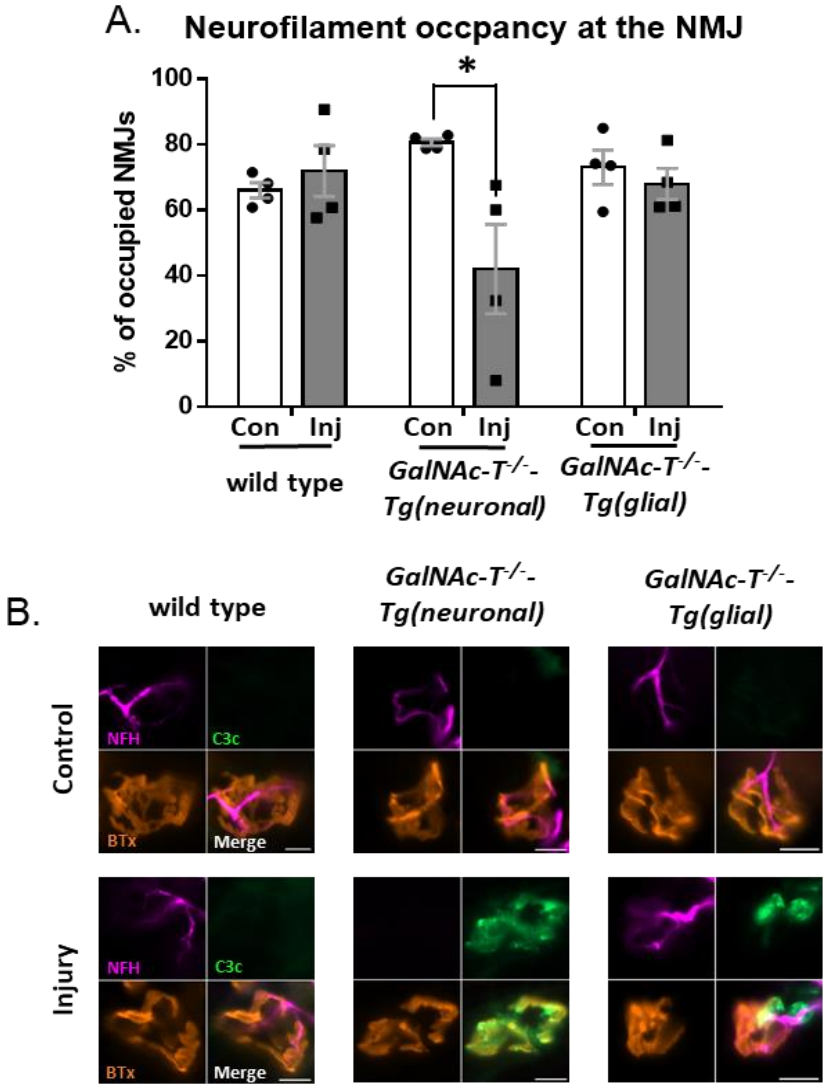

Figure 4.7: Assessment of axon integrity at the NMJ. Immunofluorescence analysis was performed on fresh frozen diaphragm from wild type, *GalNAc-T$^{-/-}$-Tg(neuronal)* and *GalNAc-T$^{-/-}$-Tg(glial)* mice who received 50 mg/kg of anti-GM1 mAb, intraperitoneally (IP). Sixteen hours later, 30 µl/g normal human serum (NHS) was delivered IP; control mice received PBS and NHS. Axon integrity at the neuromuscular junction (NMJ) was assessed by the presence of the axonal structural protein, neurofilament heavy (NFH). A) NFH occupancy was significantly reduced in injured *GalNAc-T$^{-/-}$-Tg(neuronal)* mice compared to control (*=$p<0.05$). There were no significant differences in NFH occupancy between control and injured groups in wild type and *GalNAc-T$^{-/-}$-Tg(glial)* mice. B) Illustrative images show NFH (magenta) occupying the NMJ, identified by bungarotoxin (BTx, orange) in injured *GalNAc-T$^{-/-}$-Tg(glial)* mice, despite the presence of complement deposits (green) surrounding the NMJ. In contrast, complement deposits were present overlying the NMJ (BTx, orange) in injured *GalNAc-T$^{-/-}$-Tg(neuronal)* mice and NFH staining was absent. Scale bar = 10 µm. Results represented as the average $\pm$ SEM, n=4/genotype/treatment. Statistical analysis assessed by two-way ANOVA with Tukey's multiple comparisons test.

4.2.6 Relationship between complement and neurofilament

Next, I assessed the relationship between C3c and NFH intensity at the NMJ, following anti-GM1 mAb mediated injury in *GalNAc-T$^{-/-}$-Tg(neuronal)* and *GalNAc-T$^{-/-}$-Tg(glial)* mice. Due to the low complement deposits present in injured wild type mice, they were not included in this analysis. The C3c and NFH intensities from each mouse were plotted on an xy plot and correlation analysis was performed (Figure 4.8). In *GalNAc-T$^{-/-}$-Tg(neuronal)* and *GalNAc-T$^{-/-}$-Tg(glial)* control mice, there was no clear trend identified. A very weak positive correlation was present, suggesting the two variables tend to increase together. Injured *GalNAc-T$^{-/-}$-Tg(neuronal)* mice displayed an inverse correlation between C3c and NFH intensity; when C3c intensity increased, NFH intensity decreased. In contrast, injured *GalNAc-T$^{-/-}$-Tg(glial)* mice demonstrated a weak positive correlation, which indicates that NFH intensity and C3c intensity increase together. The p value for all mice was <0.05, indicating that any correlation between C3c and NFH was not due to random sampling.

Overall, these results suggest that in injured *GalNAc-T$^{-/-}$-Tg(neuronal)* mice, the presence of C3c resulted in the loss of NFH. In contrast, when C3c was present in injured *GalNAc-T$^{-/-}$-Tg(glial)* mice, NFH appeared unaffected. These results correspond to the results demonstrated in Figure 4.7.

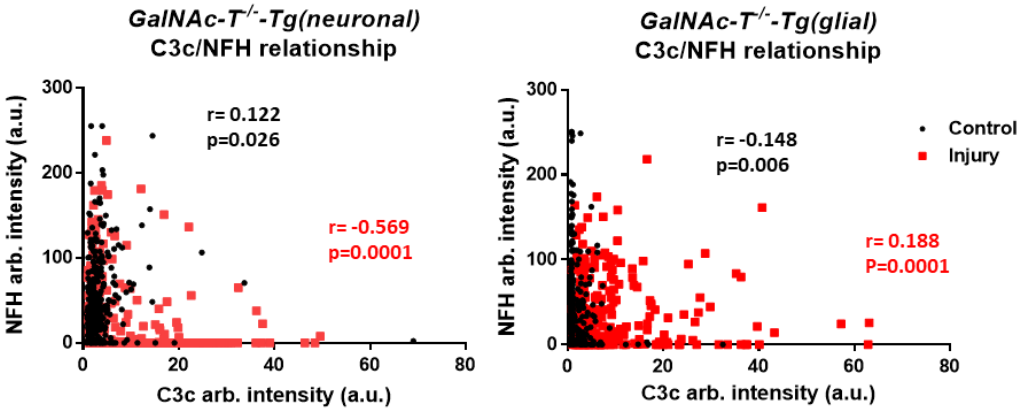

Figure 4.8: Relationship between complement and neurofilament. *GalNAc-T$^{-/-}$-Tg(neuronal)* and *GalNAc-T$^{-/-}$-Tg(glial)* mice were injected intraperitoneally (IP) with 50 mg/kg anti-GM1 mAb and 30 µl/g normal human serum (NHS); control mice received PBS and NHS. The intensity of C3c and neurofilament heavy (NFH) at the neuromuscular junction was determined and plotted on an xy plot and correlation analysis was performed to determine whether the two components are correlated in control (black) and injured (red) groups in each genotype. There was a very weak positive correlation present in both *GalNAc-T$^{-/-}$-Tg(neuronal)* and *GalNAc-T$^{-/-}$-Tg(glial)* control mice, and injured *GalNAc-T$^{-/-}$-Tg(glial)* mice. On the other hand, there was an inverse correlation between C3c and NFH in injured *GalNAc-T$^{-/-}$-Tg(neuronal)* mice. A non-parametric Spearman correlation test was performed. n=4/genotype/treatment group.

4.2.7 Anti-GM1 mAb deposition at the distal nerve

It has been shown previously that the distal nerve is vulnerable to injury as it lies outwith the protection of the BNB (Brown and Snow, 1991). Furthermore, previous AGAb and complement mediated mouse models have demonstrated that distal NoR are vulnerable to injury in these models (McGonigal et al., 2010). Therefore, I next characterised anti-GM1 mAb and complement-mediated injury at the distal nerve. First, I investigated the percentage of distal nerves with positive anti-GM1 mAb staining and compared the results between wild type, *GalNAc-T$^{-/-}$-Tg(neuronal)* and *GalNAc-T$^{-/-}$-Tg(glial)* mice. When assessing anti-GM1 mAb deposition at the distal nerve, only the distal NoR and the distal internode adjacent to the NMJ, were included in analysis (illustrated in Figure 4.9).

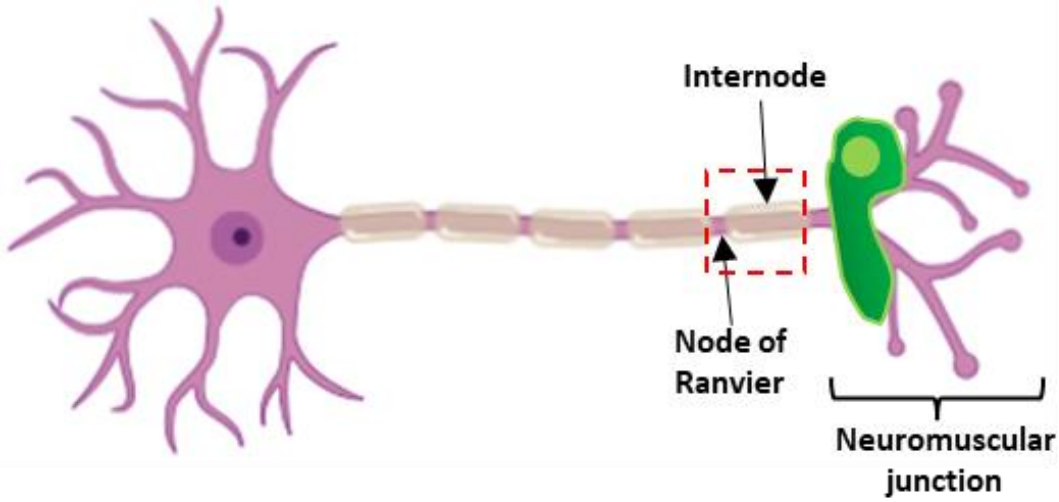

Figure 4.9: Schematic diagram illustrating distal nerve. Red box highlights the distal internode and distal node of Ranvier, adjacent to the neuromuscular junction, included in 'distal nerve' analysis. Created using BioRender.

The results illustrated in Figure 4.10A demonstrate that 90 ± 10% of distal nerves had anti-GM1 mAb deposits in injured wild type mice, which was significantly higher compared to wild type control mice and injured *GalNAc-T$^{-/-}$-Tg(neuronal)* mice ($p<0.001$; $p<0.05$, respectively). Similarly, 100 ± 0% of analysed distal nerves in injured *GalNAc-T$^{-/-}$-Tg(glial)* mice had anti-GM1 mAb deposits. This was significantly higher compared to *GalNAc-T$^{-/-}$-Tg(glial)* control mice and injured *GalNAc-T$^{-/-}$-Tg(neuronal)* mice ($p<0.001$; $p<0.01$, respectively), but not compared to injured wild type mice. Despite injured *GalNAc-T$^{-/-}$-Tg(neuronal)* mice having significantly fewer distal nerves with anti-GM1 mAb deposits compared to both injured wild type and injured *GalNAc-T$^{-/-}$-Tg(glial)* mice, there were significantly more distal nerves with anti-GM1 mAb deposits in injured *GalNAc-T$^{-/-}$-*

Tg(neuronal) mice compared to control ($p<0.001$). Anti-GM1 mAb deposits were absent from all analysed distal nerves in control mice.

It was observed that the location of anti-GM1 mAb binding differed between the genotypes of injured mice; therefore, anti-GM1 mAb staining was categorized into internodal, paranodal or nodal anti-GM1 mAb deposition. The results are presented as a percentage of the total number of distal nerves with anti-GM1 mAb deposits. Figure 4.10B shows that 89 ± 4% and 90 ± 6% of positive distal nerves in injured wild type and injured *GalNAc-T$^{-/-}$-Tg(glial)* mice, respectively, had anti-GM1 mAb deposits detected overlying the internode. This was significantly higher compared to injured *GalNAc-T$^{-/-}$-Tg(neuronal)* mice ($p<0.001$). In contrast, anti-GM1 mAb deposits were not detected at the distal internode in injured *GalNAc-T$^{-/-}$-Tg(neuronal)* mice. The trend of anti-GM1 mAb deposition at the paranode differed compared to internodal anti-GM1 mAb deposition (Figure 4.10B). Anti-GM1 mAb deposits were detected at 100 ± 0% of paranodes at positive distal nerves in injured *GalNAc-T$^{-/-}$-Tg(glial)* mice. This was significantly higher compared to injured wild type and injured *GalNAc-T$^{-/-}$-Tg(neuronal)* ($p<0.05$, $p<0.01$, respectively). Anti-GM1 mAb deposits were detected at 59 ± 12% of paranodes at positive distal nerves in injured wild type mice. In injured *GalNAc-T$^{-/-}$-Tg(neuronal)* mice, 44 ± 19% of positive distal nerves had anti-GM1 mAb deposits at the paranodes; likely due to anti-GM1 mAb binding to the axolemma at the paranode (Figure 4.10B). Injured *GalNAc-T$^{-/-}$-Tg(neuronal)* mice had anti-GM1 mAb deposits detected at nodal gaps in 81 ± 15% of positive distal nerves, which was significantly higher compared to injured wild type and injured *GalNAc-T$^{-/-}$-Tg(glial)* mice ($p<0.01$; $p<0.001$, respectively). Anti-GM1 mAb deposits were detected at 26 ± 7% and 9 ± 5% of nodal gaps at positive distal nerves in injured wild type and injured *GalNAc-T$^{-/-}$-Tg(glial)* mice, respectively. The illustrative images show the typical staining pattern found in injured mice (Figure 4.10C). In injured wild type mice, anti-GM1 mAb deposits are detected at the internode and paranode. Antibody deposits were predominantly located on the axolemma at the nodal gap in injured *GalNAc-T$^{-/-}$-Tg(neuronal)* mice. In contrast, anti-GM1 mAb deposits were located on the glial membrane at the internode and the paranodes of positive distal nerves in injured *GalNAc-T$^{-/-}$-Tg(glial)* mice.

In summary, anti-GM1 mAb deposits were detected predominantly on glial membranes at the distal NoR in injured wild type mice. On the other hand, anti-GM1 mAb deposits were

located at the nodal gap in injured *GalNAc-T$^{-/-}$-Tg(neuronal)* mice. However, in injured *GalNAc-T$^{-/-}$-Tg(glial)* mice, anti-GM1 mAb deposits were located on the myelin internode and at the paranodes. This data further corroborates that we can target the axonal and glial membranes independently by using *GalNAc-T$^{-/-}$-Tg(neuronal)* and *GalNAc-T$^{-/-}$-Tg(glial)* mice, respectively.

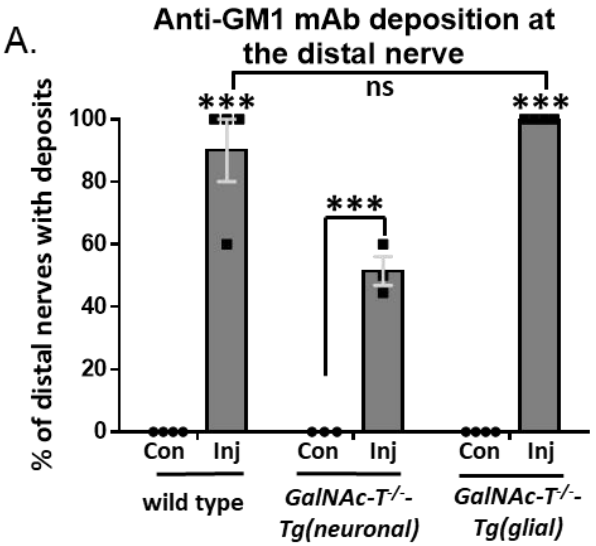
A.
Anti-GM1 mAb deposition at the distal nerve
ns
***
***
***
% of distal nerves with deposits
100
80
60
40
20
0
Con
Inj
Con
Inj
Con
Inj
wild type
GalNAc-T-/--Tg(neuronal)
GalNAc-T-/--Tg(glial)

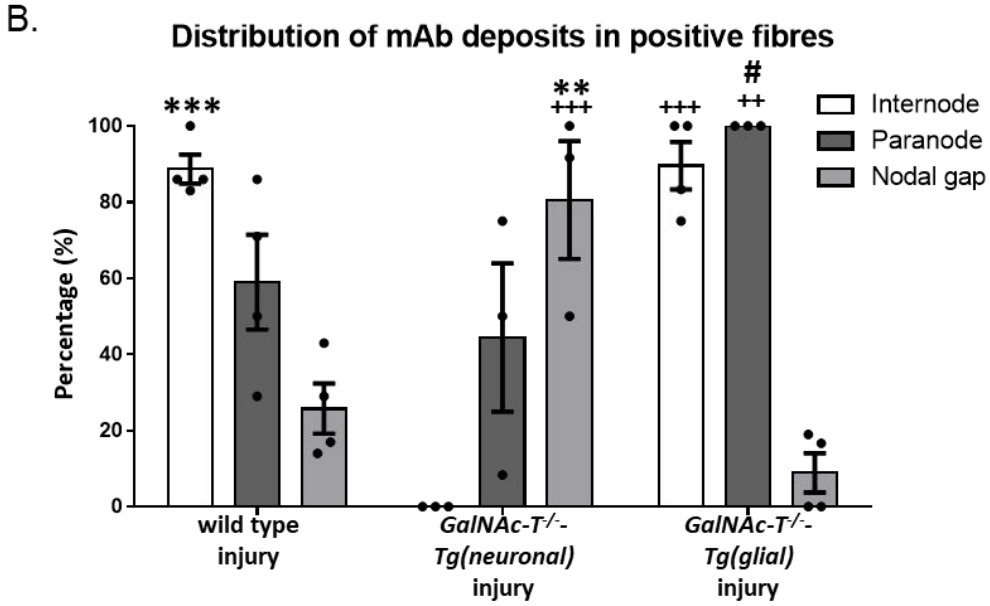
B.
Distribution of mAb deposits in positive fibres
***
**
+++
#
++
+++
Internode
Paranode
Nodal gap
Percentage (%)
100
80
60
40
20
0
wild type injury
GalNAc-T-/--Tg(neuronal) injury
GalNAc-T-/--Tg(glial) injury

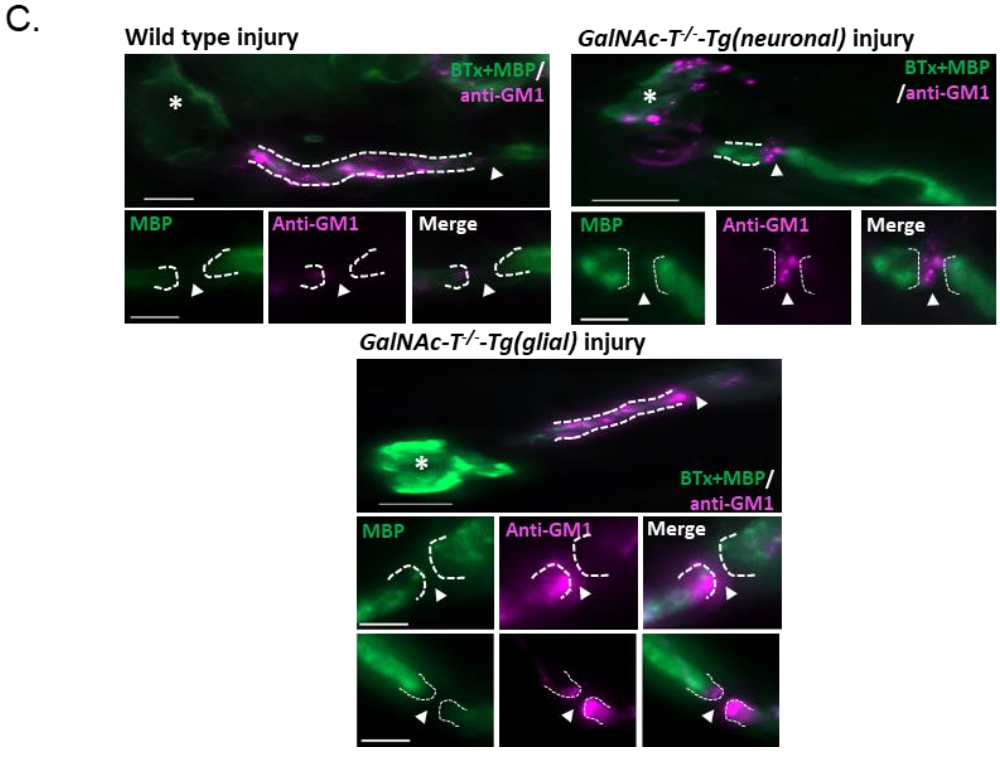
C.
Wild type injury
BTx+MBP/ anti-GM1
MBP
Anti-GM1
Merge
GalNAc-T-/--Tg(neuronal) injury
BTx+MBP /anti-GM1
MBP
Anti-GM1
Merge
GalNAc-T-/--Tg(glial) injury
BTx+MBP/ anti-GM1
MBP
Anti-GM1
Merge

Figure 4.10: Anti-GM1 mAb deposition at the distal nerve. (On previous page) Anti-GM1 mAb deposition at the distal nerve was assessed in diaphragm from wild type, *GalNAc-T$^{-/-}$-Tg(neuronal)* and *GalNAc-T$^{-/-}$-Tg(glial)* mice. Mice were injected intraperitoneally (IP) with 50 mg/kg of anti-GM1 mAb followed 16 hours later with 30 µl/g normal human serum (NHS), delivered IP; control mice received PBS and NHS. The diaphragm was harvested 6 hours post NHS injection and immunofluorescence analysis was performed. A) Anti-GM1 mAb deposits were present at significantly more distal nerves in injured mice compared to their respective controls (***=p<0.001). The percentage of distal nerves with anti-GM1 mAb deposits was significantly higher in injured wild type and injured *GalNAc-T$^{-/-}$-Tg(glial)* mice compared to injured *GalNAc-T$^{-/-}$-Tg(neuronal)* mice (***=p<0.001). B) The distribution of anti-GM1 mAb deposits in positive nerves from injured mice was assessed. The presence of anti-GM1 mAb detected at the internode was significantly higher in injured wild type and injured *GalNAc-T$^{-/-}$-Tg(glial)* mice compared to injured *GalNAc-T$^{-/-}$-Tg(neuronal)* mice (***/+++=p<0.001). There was no significant difference between the presence of anti-GM1 mAb deposits at the paranode between wild type and *GalNAc-T$^{-/-}$-Tg(neuronal)* injured mice. Anti-GM1 mAb was detected at significantly more paranodes in injured *GalNAc-T$^{-/-}$-Tg(glial)* mice compared to all other genotypes (#=p<0.05; ++=p<0.01). The presence of anti-GM1 mAb deposits at the nodal gap was significantly higher in injured *GalNAc-T$^{-/-}$-Tg(neuronal)* mice compared to injured wild type and injured *GalNAc-T$^{-/-}$-Tg(glial)* mice (**=p<0.01; +++=p<0.001). * = wild type vs *GalNAc-T$^{-/-}$-Tg(neuronal)*; # = wild type vs *GalNAc-T$^{-/-}$-Tg(glial);* + = *GalNAc-T$^{-/-}$-Tg(neuronal)* vs *GalNAc-T$^{-/-}$-Tg(glial).* C) Illustrative images show typical anti-GM1 mAb staining patterns for each injured mouse. In injured wild type mice, anti-GM1 mAb (magenta) was predominantly detected at the internode and paranode. Anti-GM1 mAb was detected at the nodal gap in injured *GalNAc-T$^{-/-}$-Tg(neuronal)* mice. On the other hand, injured *GalNAc-T$^{-/-}$-Tg(glial)* mice had anti-GM1 mAb deposits detected at the internode and the paranode. For representative images: top image illustrates the neuromuscular junction, identified by bungarotoxin (BTx, white asterisk) and distal internode (represented by broken white line) and white arrow indicates distal node of Ranvier (NoR; scale bar = 10 µm); bottom panel of images show the distal NoR enlarged. Broken white line outlines the paranode, white arrow identifies the nodal gap (scale bar = 5 µm). Significance value determined by performing a two-way ANOVA with Tukey's multiple comparisons test. Results represented as the average ± SEM, n=3 *GalNAc-T$^{-/-}$-Tg(neuronal)* mice; n=4 wild type and *GalNAc-T$^{-/-}$-Tg(glial)* mice.

4.2.8 Complement deposition at the distal nerve

Following on from assessing anti-GM1 mAb deposition at the distal nerve, I next assessed the subsequent complement deposition and determined whether the staining pattern followed the same trend as anti-GM1 mAb. The early complement component, C3c, was used as a marker of complement. Only the distal internode and distal NoR were considered when assessing complement deposition along the distal nerve (as demonstrated in Figure 4.9). Figure 4.11A shows that complement deposits were detected at 2 ± 2% and 20 ± 6% of distal nerves in control and injured wild type mice, respectively. In injured *GalNAc-T$^{-/-}$-Tg(neuronal)* mice, 19 ± 7% of distal nerves had

complement deposits compared to 3 ± 3% in control mice, although this difference was not significant. Injured *GalNAc-T$^{-/-}$-Tg(glial)* mice had the highest percentage of distal nerves with complement, as 92 ± 4% of analysed distal nerves had complement deposits compared to only 15 ± 12% in control mice. The percentage of distal nerves with complement deposits was significantly higher in injured *GalNAc-T$^{-/-}$-Tg(glial)* mice compared to all other groups ($p<0.001$).

The distal nerve was categorised into internode, paranode, and the nodal gap and the location of complement deposits along the distal nerve in injured mice was assessed. The results are presented as a percentage of the total number of distal nerves with positive complement deposits (Figure 4.11B). The percentage of distal nerves with internodal complement deposition was significantly higher in both injured wild type and injured *GalNAc-T$^{-/-}$-Tg(glial)* mice compared to injured *GalNAc-T$^{-/-}$-Tg(neuronal)* mice ($p<0.001$). Complement deposits were detected at the internode of 85 ± 9% and 90 ± 6% of positive nerves in injured wild type and injured *GalNAc-T$^{-/-}$-Tg(glial)* mice, respectively; this difference was not statistically significant. The percentage of complement positive distal nerves with paranodal deposits was significantly higher in injured *GalNAc-T$^{-/-}$-Tg(glial)* mice compared to injured *GalNAc-T$^{-/-}$-Tg(neuronal)* mice ($p<0.001$) but not to injured wild type mice. Complement deposits were present at the nodal gap in 32 ± 14% of positive distal nerves in injured wild type mice which did not differ significantly to injured *GalNAc-T$^{-/-}$-Tg(neuronal)* and injured *GalNAc-T$^{-/-}$-Tg(glial)* mice. In injured *GalNAc-T$^{-/-}$-Tg(neuronal)* mice, nodal complement deposits were present at 58 ± 20% of positive distal which was significantly higher compared to injured *GalNAc-T$^{-/-}$-Tg(glial)* mice. Illustrative images in Figure 4.11C highlight the typical complement staining pattern found in injured mice. In injured wild type mice, complement deposits are detected on both axonal and glial membranes, at the distal internode and NoR. However, in injured *GalNAc-T$^{-/-}$-Tg(neuronal)* mice complement deposits are detected on the axolemma at the nodal gap and the nodal gap appears slightly elongated. In contrast, injured *GalNAc-T$^{-/-}$-Tg(glial)* mice had complement deposits on glial membranes at the distal internode and paranode.

In summary, the location of complement deposition at the distal nerve followed a similar trend to anti-GM1 mAb deposition at the distal nerve. Complement deposits were found overlying both axonal and glial membranes in injured wild type mice. Complement

deposits were mostly located at the nodal gap of complement positive nerves in injured *GalNAc-T$^{-/-}$-Tg(neuronal)* mice. On the other hand, complement deposits were predominantly located along the internode and at the paranodes of complement positive distal nerves in injured *GalNAc-T$^{-/-}$-Tg(glial)* mice.

Due to the low levels of anti-GM1 mAb and complement deposition at the NMJ and low levels of complement deposition at the distal nerve in wild type mice, they were removed from further analysis. The presence of pNav clusters and Caspr dimers at the distal NoR in wild type mice demonstrated no significant difference between control and injured wild type mice, indicating that complement-mediated injury had not occurred (for results see Appendix 8.2).

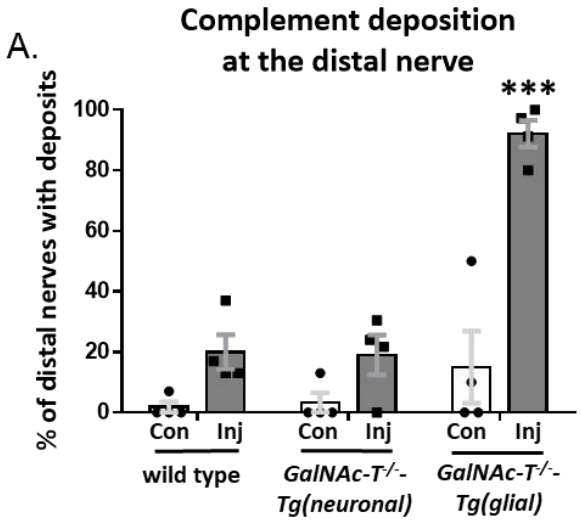
A.
Complement deposition
at the distal nerve
% of distal nerves with deposits
100
80
60
40
20
0
***
Con
Inj
Con
Inj
Con
Inj
wild type
GalNAc-T-/--
Tg(neuronal)
GalNAc-T-/--
Tg(glial)

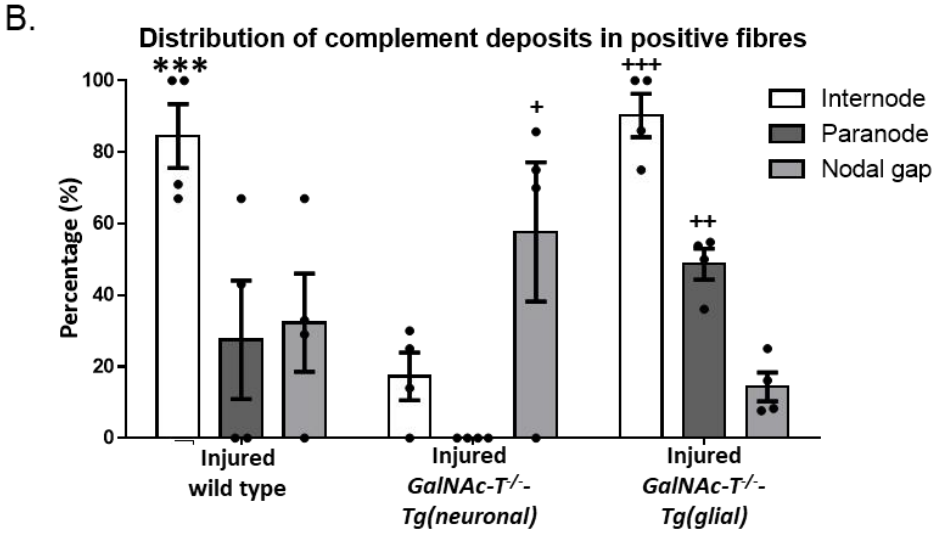
B.
Distribution of complement deposits in positive fibres
Percentage (%)
100
80
60
40
20
0
***
+
+++
++
Internode
Paranode
Nodal gap
Injured
wild type
Injured
GalNAc-T-/--
Tg(neuronal)
Injured
GalNAc-T-/--
Tg(glial)

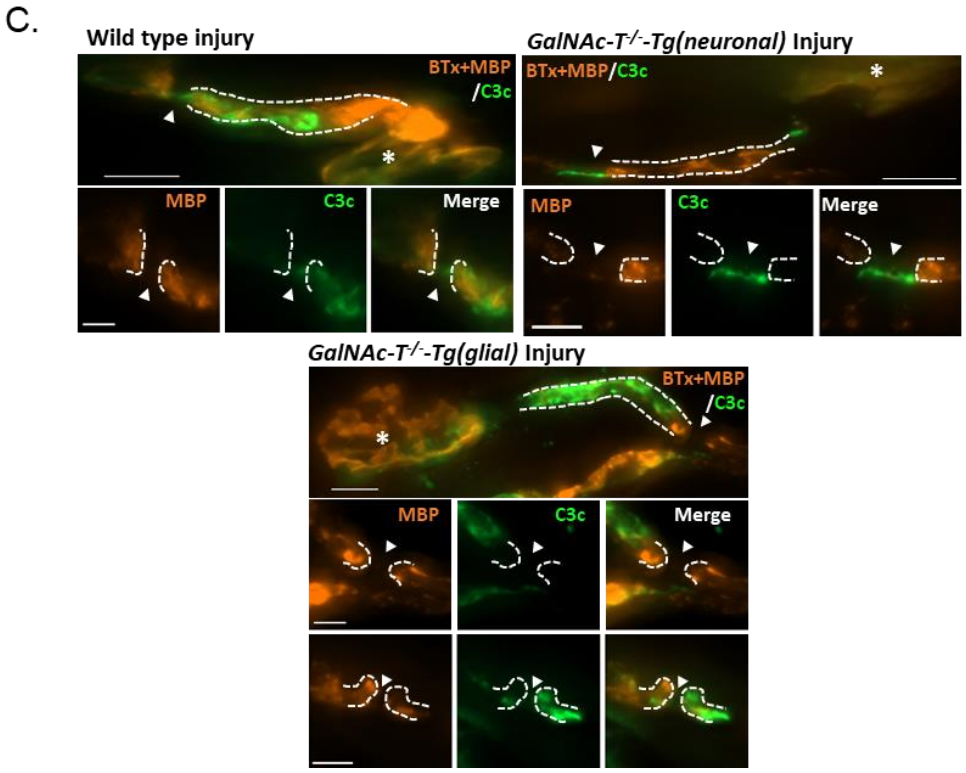
C.
Wild type injury
BTx+MBP
/C3c
MBP
C3c
Merge
GalNAc-T-/--Tg(neuronal) Injury
BTx+MBP/C3c
MBP
C3c
Merge
GalNAc-T-/--Tg(glial) Injury
BTx+MBP
/C3c
MBP
C3c
Merge

Figure 4.11: Complement deposition at the distal nerve. (See previous page) Complement deposition (C3c) at the distal nerve was assessed in fresh frozen diaphragm from wild type, *GalNAc-T$^{-/-}$-Tg(neuronal)* and *GalNAc-T$^{-/-}$-Tg(glial)* mice following anti-GM1 mAb and complement mediated injury. A) The percentage of distal nerves with C3c deposits was significantly higher in injured *GalNAc-T$^{-/-}$-Tg(glial)* mice compared to all other treatment groups (***=p<0.001). There were no significant differences in C3c deposition between control and injured wild type and *GalNAc-T$^{-/-}$-Tg(neuronal)* mice. B) The distribution of complement deposits in positive fibres was assessed in injured mice. The percentage of distal nerves with internodal deposition was significantly higher in injured wild type and injured *GalNAc-T$^{-/-}$-Tg(glial)* mice compared to injured *GalNAc-T$^{-/-}$-Tg(neuronal)* mice (***/+++=p<0.001) but did not differ significantly to each other. In injured *GalNAc-T$^{-/-}$-Tg(glial)* mice, the percentage of positive nerves with complement deposits at the paranode was significantly higher compared to injured *GalNAc-T$^{-/-}$-Tg(neuronal)* mice (++=p<0.01) but not to injured wild type mice. Complement deposits were present at significantly more nodal gaps in injured *GalNAc-T$^{-/-}$-Tg(neuronal)* mice compared to injured *GalNAc-T$^{-/-}$-Tg(glial)* mice (+=p<0.05). The presence of complement deposits at the nodal gap in injured wild type mice did not differ significantly to any other treatment group. * = wild type vs *GalNAc-T$^{-/-}$-Tg(neuronal)*; + = *GalNAc-T$^{-/-}$-Tg(neuronal)* vs *GalNAc-T$^{-/-}$-Tg(glial).* C) Representative images show typical complement staining patterns for each injured mouse. In injured wild type mice, C3c (green) was detected at the internode, paranode and the nodal gap. C3c was found deposited at the nodal gap in injured *GalNAc-T$^{-/-}$-Tg(neuronal)* mice and the nodal gap appears slightly elongated. On the other hand, injured *GalNAc-T$^{-/-}$-Tg(glial)* mice commonly had C3c deposits present at the internode and the paranode. For representative images: top image illustrates the neuromuscular junction, identified by bungarotoxin (BTx, white asterisk) and distal internode (represented by broken white line) and white arrow indicates distal node of Ranvier (NoR) (scale bar = 10 µm); bottom panel of images show the distal NoR enlarged. Broken white line outlines the paranode, white arrow identifies the node (scale bar = 5 µm). Statistical significance assessed by performing two-way ANOVA with Tukey's multiple comparisons test. Results represented as the average ± SEM, n=4/genotype/treatment.

4.2.9 Neurofilament and myelin intensity at the distal nerve

The integrity of the axon at the distal nerve was assessed by performing NFH occupancy analysis and the results are shown in Figure 4.12A. The percentage of occupied distal nerves was comparable between *GalNAc-T$^{-/-}$-Tg(neuronal)* control mice and both control and injured *GalNAc-T$^{-/-}$-Tg(glial)* mice with 88 ± 9%, 92 ± 4% and 82 ± 6% of occupied distal nerves, respectively. On the other hand, the NFH occupancy at the distal nerve was significantly reduced to 51 ± 12% in injured *GalNAc-T$^{-/-}$-Tg(neuronal)* mice compared to control. These results are illustrated in Figure 4.12C by the representative images, showing that NFH staining was often absent in injured *GalNAc-T$^{-/-}$-Tg(neuronal)* mice.

AIDP is most generally considered to be pathologically characterised by segmental demyelination (Asbury et al., 1969). Therefore, compact myelin intensity at the distal nerve was investigated to indirectly determine whether segmental demyelination was occurring following injury to the glial membrane in *GalNAc-T*$^{-/-}$*-Tg(glial)* mice. The MBP intensity in each treatment group is displayed as a Tukey box and whisker plot in Figure 4.12B. Statistical analysis was performed on the mean MBP intensity values for each individual animal. The results illustrate that control and injured *GalNAc-T*$^{-/-}$*-Tg(neuronal)* mice had comparable median MBP intensities, represented by the line in the centre of the box. On the other hand, the median MBP intensity was elevated in injured *GalNAc-T*$^{-/-}$*-Tg(glial)* mice in comparison to control. However, there were no significant differences between the mean MBP intensity of any treatment groups. Thus, it was concluded that segmental demyelination was not detectable in this injury model.

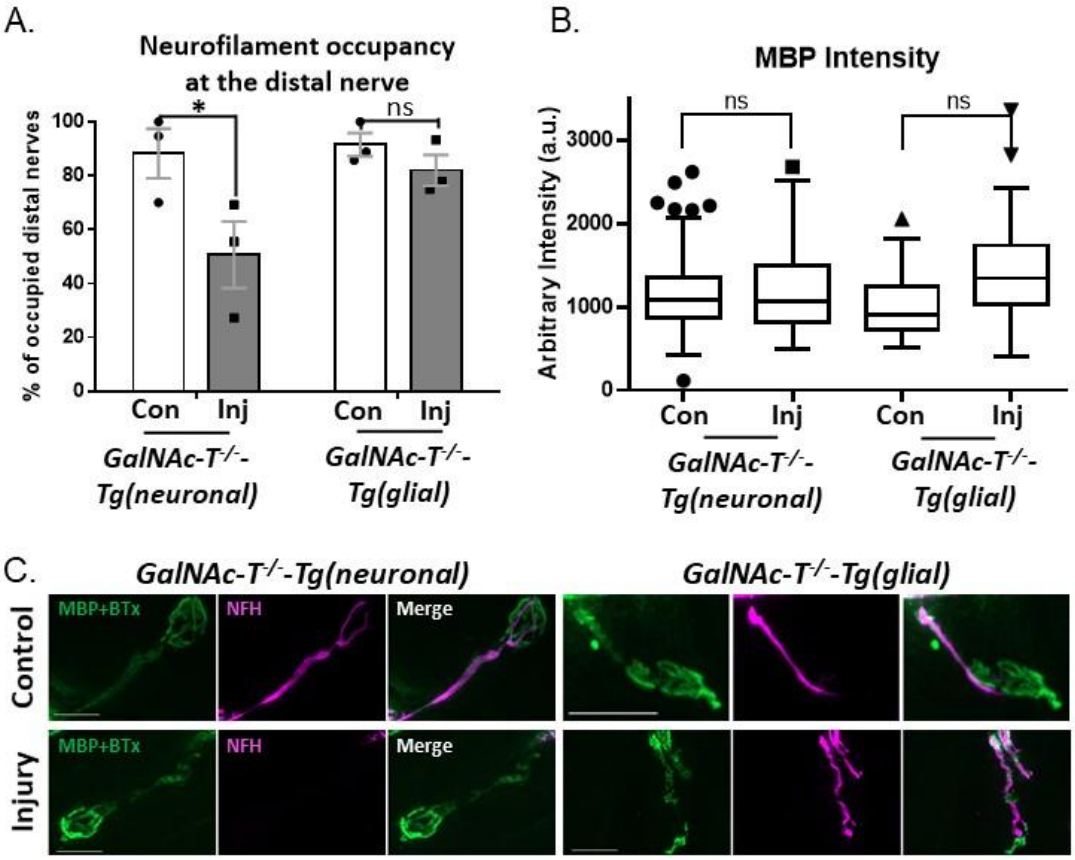

Figure 4.12: Neurofilament and MBP analysis at the distal nerve. *GalNAc-T$^{-/-}$-Tg(neuronal)* and *GalNAc-T$^{-/-}$-Tg(glial)* mice received an intraperitoneal (IP) injection of 50 mg/kg anti-GM1 mAb, followed 16 hours later with 30 µl/g normal human serum (NHS), delivered IP. Control mice received PBS and NHS. Six hours post NHS injection, the diaphragm was harvested, and associated immunofluorescence analysis was performed. A) To assess axonal integrity at the distal nerve, the axonal structural protein, neurofilament heavy (NFH) was studied in fresh frozen diaphragm sections. The percentage of occupied distal nerves was significantly reduced in injured *GalNAc-T$^{-/-}$-Tg(neuronal)* mice compared to control (*=p<0.05). There was no significant difference in NFH occupancy at the distal nerve between control and injured *GalNAc-T$^{-/-}$-Tg(glial)* mice. Results represented as the average ± SEM. B) MBP intensity was assessed to determine if segmental demyelination was occurring, and data is displayed in Tukey box and whisker plots. There were no significant differences between the mean MBP intensity amongst treatment groups. Statistics were performed on the mean intensity values. C) Illustrative images show the loss of NFH (magenta) at the distal nerve (MBP; green) in injured *GalNAc-T$^{-/-}$-Tg(neuronal)* mice but present in both control mice and injured *GalNAc-T$^{-/-}$-Tg(glial)* mice. Scale bar = 20 µm. n=3/genotype/treatment. Statistical significance assessed by performing two-way ANOVA with Tukey's multiple comparisons test.

4.2.10 Analysis of proteins at the node of Ranvier

It has been shown previously that AGAb and complement mediated injury can result in the disorganisation of nodal proteins, on both the axonal and glial membrane, at the NoR (McGonigal et al., 2010, Susuki et al., 2007b, Susuki et al., 2012). It is currently unknown whether antibody binding to the axonal membrane or to the glial membrane is responsible for this injury. Therefore, the following section evaluates the injury output at the NoR, investigating the integrity of key axo-glial proteins (illustrated in Figure 4.13), when either the axonal or glial membrane was targeted independently by using *GalNAc-T$^{-/-}$-Tg(neuronal)* and *GalNAc-T$^{-/-}$-Tg(glial)* mice, respectively.

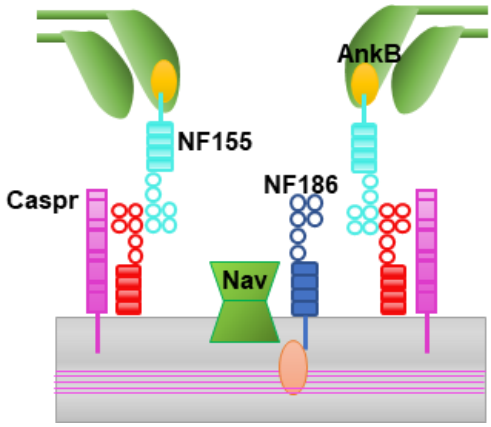

Figure 4.13: Schematic diagram of proteins of interest at the node of Ranvier.

4.2.10.1 Nav cluster analysis

Previous studies have reported that the nodal gap appears elongated in both patient autopsy and animal models of AMAN (Hafer-Macko et al., 1996a, Susuki et al., 2007b). However, in current animal models of AMAN, it has not previously been possibly to target the axonal membrane independently, and therefore, we do not know whether this injury is a result of injury to the axonal membrane, the glial membrane, or a combination of both. To determine whether the nodal gap was elongated in our injury models, the gap between the myelin sheaths at the distal NoR was measured in fixed diaphragm sections, indicated by a gap in MBP staining. Results are presented as Tukey box and whisker plots in Figure 4.14A and statistical analysis was performed on the mean gap length. The graph illustrates that the median MBP gap length was comparable in *GalNAc-T$^{-/-}$-Tg(neuronal)* control mice and both control and injured *GalNAc-T$^{-/-}$-Tg(glial)* mice, with values of 2.26, 2.35, and 2.52 µm respectively. On the other hand, the median value of injured *GalNAc-T^{-}*

$^{-/-}$*-Tg(neuronal)* mice was elongated in comparison to the other treatment groups to 3.01 µm, although the mean MBP gap did not differ significantly to control. Overall, these results suggest that injury to the axonal membrane results in an elongation of the MBP gap, representative of the nodal gap.

Following this, I assessed the presence of pNav clusters at the nodal gap, following anti-GM1 mAb and complement mediated injury. The observed pNav staining was termed as 'absent' – no pNav clusters were present; 'abnormal' – pNav was present but staining appeared punctate or elongated; or 'normal' – pNav was present and normal, as illustrated in Figure 4.14B.1. Figure 4.14B shows that normal pNav staining was present in 81 $\pm$ 6%, 80 $\pm$ 5%, and 86 $\pm$ 3% of observed nodal gaps in control *GalNAc-T$^{-/-}$-Tg(neuronal)* mice, and control and injured *GalNAc-T$^{-/-}$-Tg(glial)* mice, respectively. In contrast, normal pNav staining was significantly reduced to 47 $\pm$ 7% in injured *GalNAc-T$^{-/-}$-Tg(neuronal)* mice compared to all other treatment groups ($p<0.001$). The percentage of nodal gaps with abnormal pNav staining was comparable between control *GalNAc-T$^{-/-}$-Tg(neuronal)* mice, and control and injured *GalNAc-T$^{-/-}$-Tg(glial)* mice. Despite injured *GalNAc-T$^{-/-}$-Tg(neuronal)* mice having the highest percentage of abnormal pNav clusters, there were no significant differences between treatment groups. The percentage of nodal gaps with absent pNav clusters was significantly higher in injured *GalNAc-T$^{-/-}$-Tg(neuronal)* mice compared to all other treatment groups ($p<0.05$ compared to *GalNAc-T$^{-/-}$-Tg(neuronal)* and *GalNAc-T$^{-/-}$-Tg(glial)* control mice; $p<0.01$ compared to injured *GalNAc-T$^{-/-}$-Tg(glial)* mice). The panel of illustrative images demonstrates normal pNav clusters in *GalNAc-T$^{-/-}$-Tg(neuronal)* control mice and control and injured *GalNAc-T$^{-/-}$-Tg(glial)* mice (Figure 4.14C). On the other hand, pNav clusters are absent from the nodal gap in injured *GalNAc-T$^{-/-}$-Tg(neuronal)* mice and the nodal gap appears slightly elongated compared to all other treatment groups.

These results suggest that when the axonal membrane is targeted in *GalNAc-T$^{-/-}$-Tg(neuronal)* mice, this causes disruption to the nodal gap and nodal proteins.

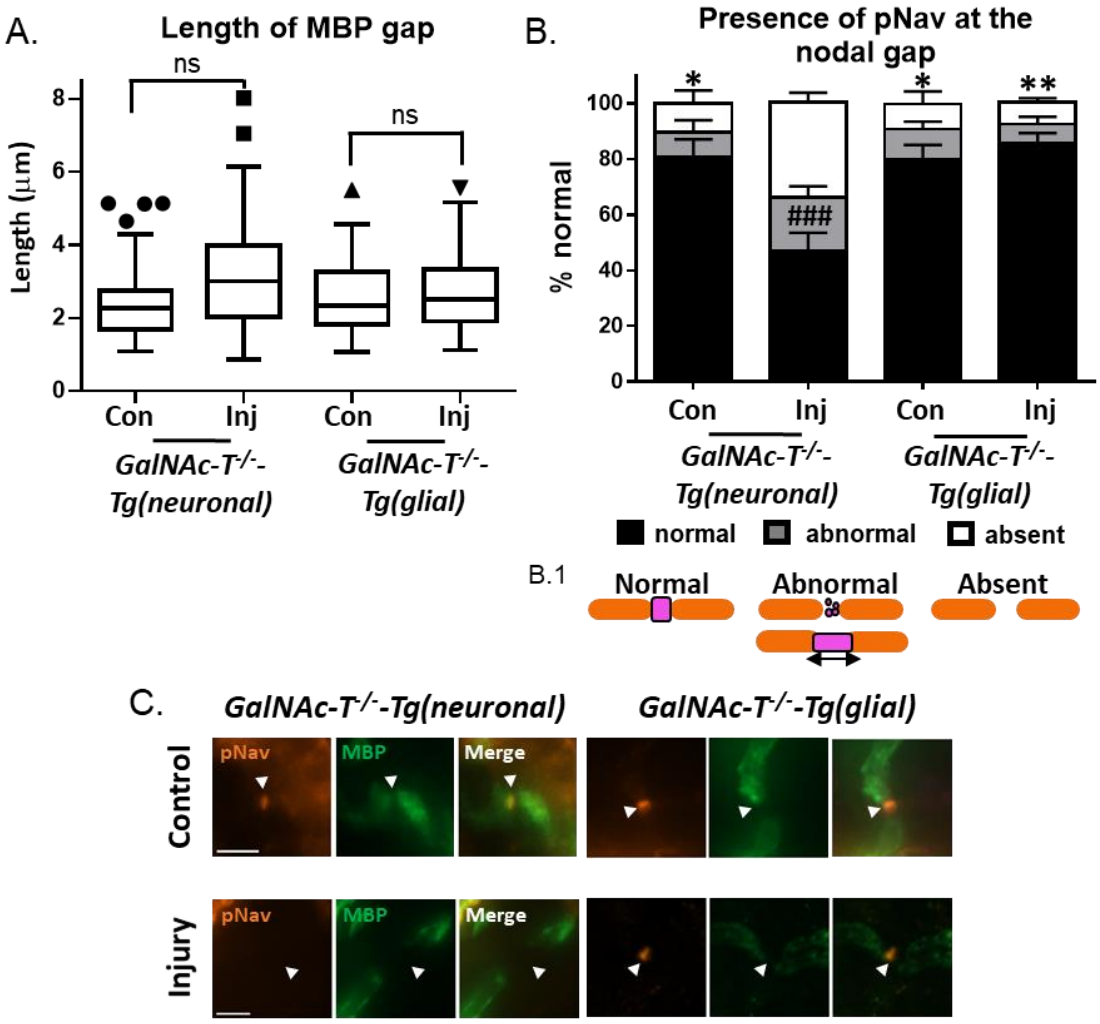

Figure 4.14: Analysis of pan-Nav at the distal nodal gap. *GalNAc-T$^{-/-}$-Tg(neuronal)* and *GalNAc-T$^{-/-}$-Tg(glial)* mice were dosed intraperitoneally (IP) with 50 mg/kg anti-GM1 mAb followed 16 hours later with 30 µl/g normal human serum (NHS), delivered IP; control mice received PBS and NHS. Diaphragm was collected for associated immunofluorescence analysis 6 hours post NHS delivery. A) The gap between myelin basic protein (MBP), indicative of the nodal gap, was measured in fixed diaphragm sections. The MBP gap appeared elongated in injured *GalNAc-T$^{-/-}$-Tg(neuronal)* mice compared to control, although not significantly. B) The percentage of distal nerves with normal pNav staining was significantly reduced in injured *GalNAc-T$^{-/-}$-Tg(neuronal)* mice compared to all treatment groups (###=p<0.001). There were no significant differences in the percentage of abnormal pNav clusters between the treatment groups. Injured *GalNAc-T$^{-/-}$-Tg(neuronal)* mice had significantly more nodal gaps with absent pNav staining compared to all treatment groups (*=p<0.05; **=p<0.01). # = compared to normal pNav staining in injured *GalNAc-T$^{-/-}$-Tg(neuronal)* mice; * = compared to absent pNav staining in injured *GalNAc-T$^{-/-}$-Tg(neuronal)* mice. B.1) Schematic diagram illustrates normal, abnormal, and absent staining. C) NoR were identified by a gap in MBP immunostaining (green) and the site of expected staining was indicated by white arrowheads. Representative images show absent pNav (orange) at the nodal gap in injured *GalNAc-T$^{-/-}$-Tg(neuronal)* mice. Scale bar = 5 µm. Two-way ANOVA with Tukey's multiple comparisons test performed to test for statistical significance. Results represented as the average ± SEM, n=4/genotype/treatment group.

4.2.10.2 Ankyrin-B analysis

AnkB is located in the paranodal cytoplasmic loops and is responsible for tethering NF155 to the underlying cytoskeleton (Chang et al., 2014). Due to the sub-membranous location, calpain sensitivity, and key functional role of AnkB at the paranodes, the integrity of this protein was assessed following anti-GM1 mAb and complement mediated injury. The presence of AnkB dimers was split into 3 categories: 'normal' – AnkB dimers were present and normal, 'abnormal' – AnkB dimers were present, but the staining appeared punctate or elongated, and 'absent' – AnkB dimers were absent, or a hemi-dimer was present (see schematic in Figure 4.15A.1). The results demonstrate that 73 ± 14%, 69 ± 5%, and 67 ± 4% of distal nerves had normal AnkB dimers in control and injured *GalNAc-T$^{-/-}$-Tg(neuronal)* mice and control *GalNAc-T$^{-/-}$-Tg(glial)* mice, respectively (Figure 4.15A). On the other hand, the presence of normal AnkB dimers was significantly reduced to 6 ± 2% in injured *GalNAc-T$^{-/-}$-Tg(glial)* mice compared to all other treatment groups ($p<0.001$). The percentage of distal paranodes with abnormal AnkB dimers did not differ significantly between treatment groups. There were significantly more distal paranodes with absent AnkB dimers in injured *GalNAc-T$^{-/-}$-Tg(glial)* mice (91 ± 4%) compared to all other treatment groups ($p<0.001$). Representative images demonstrate the presence of AnkB dimers at the paranode of control and injured *GalNAc-T$^{-/-}$-Tg(neuronal)* mice and control *GalNAc-T$^{-/-}$-Tg(glial)* mice (Figure 4.15C). In contrast, there is a loss of AnkB staining at the paranodes in injured *GalNAc-T$^{-/-}$-Tg(glial)* mice, accompanied by complement deposits overlying MBP staining.

Overall, these results demonstrate that AnkB dimers are significantly disrupted following targeted injury to the glial membrane in *GalNAc-T$^{-/-}$-Tg(glial)* mice.

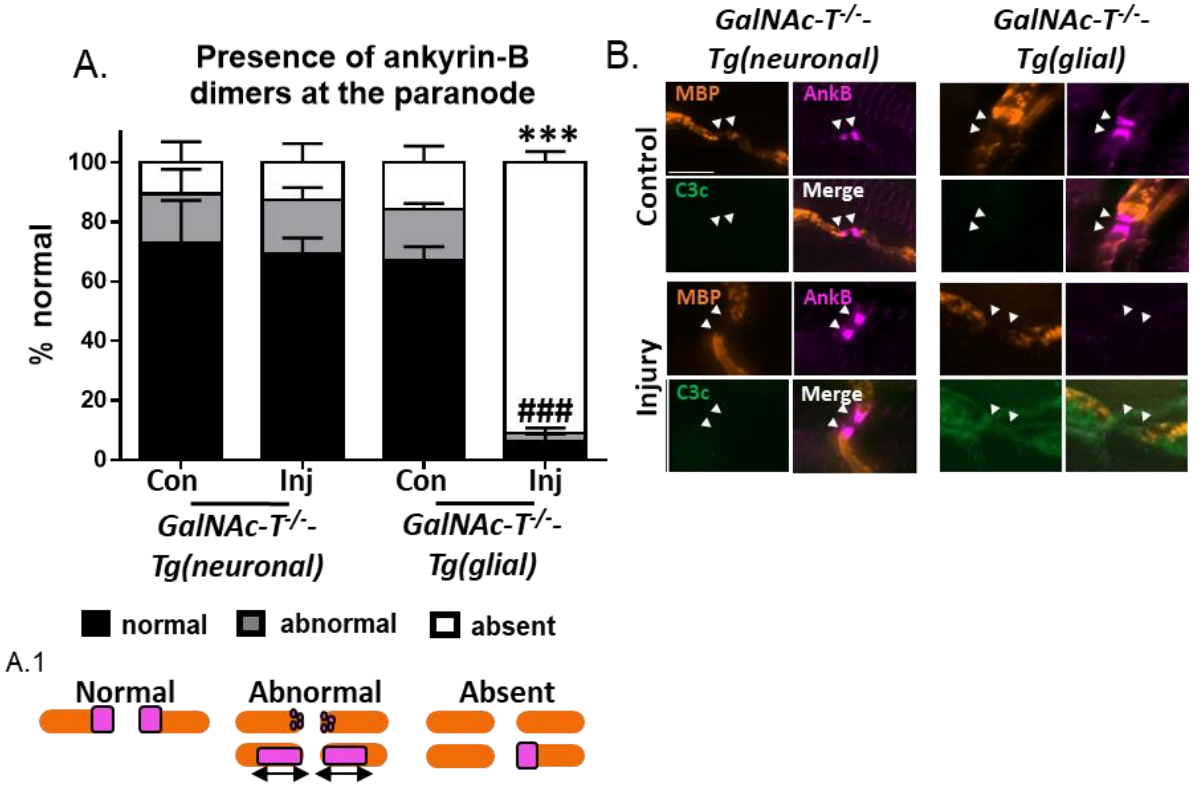

Figure 4.15: Analysis of ankyrin-B at the distal paranode. *GalNAc-T$^{-/-}$-Tg(neuronal)* and *GalNAc-T$^{-/-}$-Tg(glial)* mice were injected intraperitoneally (IP) with 50 mg/kg anti-GM1 mAb followed 16 hours later with an IP injection of 30 µl/g normal human serum (NHS); control mice received PBS and NHS. The diaphragm was harvested 6 hours post NHS injection and AnkB was assessed in fixed diaphragm sections. A.1) Schematic diagram illustrating normal, abnormal, and absent AnkB dimers. A) The presence of normal AnkB dimers at the distal paranode was significantly reduced in injured *GalNAc-T$^{-/-}$-Tg(glial)* mice compared to all other treatment groups (**###**=p<0.001). Conversely, the percentage of paranodes with absent AnkB dimer staining was significantly higher in injured *GalNAc-T$^{-/-}$-Tg(glial)* mice compared to all other treatment groups (*****=p<0.001). There was no significant difference in the presence of abnormal AnkB dimers between treatment groups. # = compared to normal AnkB dimers in injured *GalNAc-T$^{-/-}$-Tg(glial)* mice; * = compared to absent AnkB dimers in injured *GalNAc-T$^{-/-}$-Tg(glial)* mice. B) NoR were identified by a gap in myelin basic protein (MBP; orange) and the site of expected staining is indicated by white arrow heads. Representative images show AnkB dimers (magenta) present at the paranode in control and injured *GalNAc-T$^{-/-}$-Tg(neuronal)* mice and control *GalNAc-T$^{-/-}$-Tg(glial)* mice. In injured *GalNAc-T$^{-/-}$-Tg(glial)* mice, AnkB dimers are absent and complement deposits (green) can be seen along the MBP staining. Scale bar = 5 µm. Statistical analysis performed using a two-way ANOVA with Tukey's multiple comparisons test. Results represented as the average ± SEM, n=4/genotype/treatment group.

4.2.10.3 Neurofascin analysis

Neurofascin is a transmembrane protein involved in the formation and stabilisation of the NoR and comprises two major isoforms: NF186, located at the nodal gap and NF155, located at the paranodes (Sherman et al., 2005). The pan-NFasc antibody available to us binds to the extracellular domains of both NF186 and NF155, thereby identifying both isoforms of the protein. The presence of pan-NFasc immunoreactivity following direct injury to either the axonal or glial membrane was assessed. Initially, the pan-NFasc staining was categorised into 'normal' – both nodal and paranodal NFasc were present and normal; 'abnormal' – both nodal and paranodal NFasc were present but staining appeared punctate or elongated; or 'absent' – either paranodal or nodal NFasc were absent or only a paranodal hemidimer was present (see Figure 4.16A.1 for schematic). The percentage of distal NoR with normal pan-NFasc was significantly reduced to 22 $\pm$ 11% in injured *GalNAc-T$^{-/-}$-Tg(glial)* mice compared to all other treatment groups ($p<0.05$ compared to *GalNAc-T$^{-/-}$-Tg(neuronal)* injured mice; $p<0.001$ compared to both *GalNAc-T$^{-/-}$-Tg(neuronal)* and *GalNAc-T$^{-/-}$-Tg(glial)* control mice). There were fewer distal NoR with normal pan-NFasc staining in *GalNAc-T$^{-/-}$-Tg(neuronal)* injured mice compared to control, although this difference was not significant (Figure 4.16A). The percentage of distal NoR with abnormal pan-NFasc staining was comparable in all groups with 7 $\pm$ 2% and 13 $\pm$ 2% of distal NoR with abnormal pan-NFasc staining in control and injured *GalNAc-T$^{-/-}$-Tg(neuronal)* mice, and 4 $\pm$ 3% and 6 $\pm$ 4% of distal NoR in control and injured *GalNAc-T$^{-/-}$-Tg(glial)* mice, respectively. When assessing the percentage of distal NoR with absent pan-NFasc staining it was found that in injured *GalNAc-T$^{-/-}$-Tg(neuronal)* mice, there were 31 $\pm$ 7% of distal NoR with absent pan-NFasc staining, compared to 11 $\pm$ 5% in *GalNAc-T$^{-/-}$-Tg(neuronal)* control mice; however, this difference was not significant. On the other hand, in injured *GalNAc-T$^{-/-}$-Tg(glial)* mice, there were 72 $\pm$ 14% of distal NoR with absent pan-NFasc staining compared to 24 $\pm$ 3% in *GalNAc-T$^{-/-}$-Tg(glial)* control mice, and this was significantly higher compared to all other treatment groups ($p<0.01$ compared to injured *GalNAc-T$^{-/-}$-Tg(neuronal)* mice; $p<0.001$ compared to both *GalNAc-T$^{-/-}$-Tg(neuronal)* and *GalNAc-T$^{-/-}$-Tg(glial)* control mice). Following on from this, the total span of pan-NFasc staining was assessed by measuring the distance from the outer edges of each dimer (illustrated in Figure 4.16 B.1). The results are presented in a Tukey box and whisker plot and statistical analysis was performed on the mean values. The median pan-NFasc span was 4.39, 4.1, and 4.5 µm in *GalNAc-T$^{-/-}$-Tg(neuronal)* control and both control

and injured *GalNAc-T$^{-/-}$-Tg(glial)* mice. On the other hand, the median length of pan-NFasc was elongated in injured *GalNAc-T$^{-/-}$-Tg(neuronal)* mice to 5.32 µm. The mean length of pan-NFasc staining was significantly longer in injured *GalNAc-T$^{-/-}$-Tg(neuronal)* mice compared to control ($p<0.05$). These results suggest that pan-NFasc is either becoming mis-localised to the juxtaparanode in injured *GalNAc-T$^{-/-}$-Tg(neuronal)* mice or it is indicative of a lengthening of the nodal gap. The latter explanation corresponds to findings illustrated in Figure 4.14A.

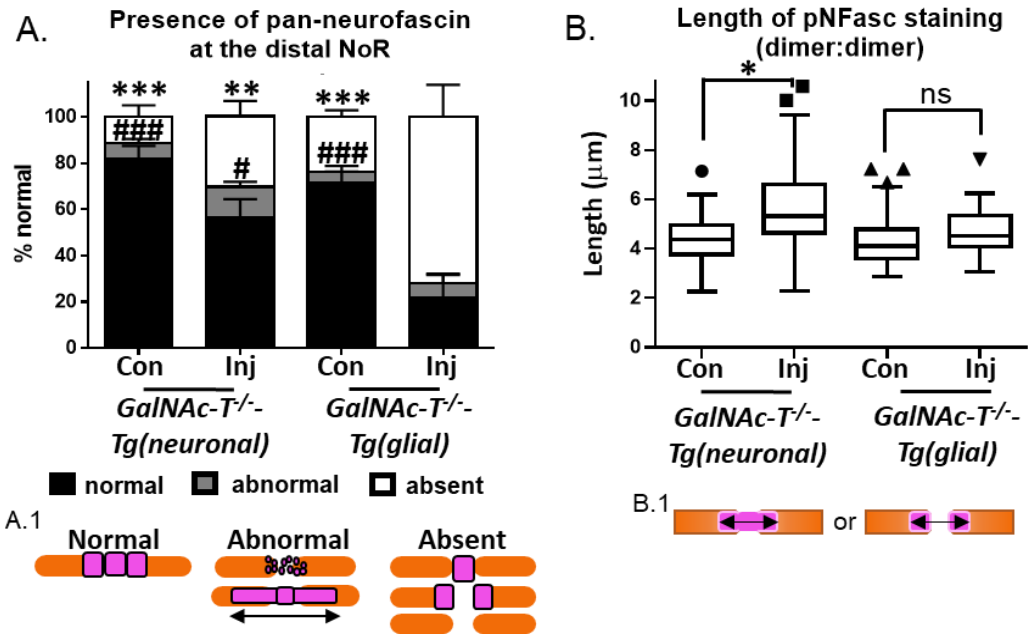

Figure 4.16: Analysis of neurofascin at the distal NoR. *GalNAc-T$^{-/-}$-Tg(neuronal)* and *GalNAc-T$^{-/-}$-Tg(glial)* mice received 50 mg/kg anti-GM1 mAb delivered intraperitoneally (IP). Sixteen hours later, 30 ul/g normal human serum (NHS) was administered IP; control mice received PBS and NHS. Diaphragm was collected for associated immunofluorescence analysis 6 hours post NHS delivery. Pan-NFasc was assessed in fixed diaphragm sections. A) The presence of normal pan-NFasc staining at the distal node of Ranvier (NoR) was significantly reduced in injured *GalNAc-T$^{-/-}$-Tg(glial)* mice compared to all groups (###=$p<0.001$; #=$p<0.05$). The percentage of distal NoR with abnormal pan-NFasc was comparable between all treatment groups. There were significantly more distal NoR with absent pan-NFasc staining in injured *GalNAc-T$^{-/-}$-Tg(glial)* mice compared to all other groups (***=$p<0.001$; **=$p<0.01$). # = compared to normal pan-NFasc staining in injured *GalNAc-T$^{-/-}$-Tg(glial)* mice; * = compared to absent pan-NFasc staining in injured *GalNAc-T$^{-/-}$-Tg(glial)* mice. A.1) Schematic diagram demonstrating normal, abnormal, and absent pan-NFasc staining. B) The mean pan-NFasc length was significantly elongated in injured *GalNAc-T$^{-/-}$-Tg(neuronal)* mice compared to control (*=$p<0.05$; n=3 injured GalNAc-T$^{-/-}$-Tg(glial) mice). B.1) Diagram illustrating the length of pan-NFasc (dimer:dimer). Statistical analysis performed using a two-way ANOVA with Tukey's multiple comparisons test. Results represented as the average ± SEM, n=4/genotype/treatment group.

Next, the percentage of distal NoR with nodal pan-NFasc staining, representative of NF186 was assessed (Figure 4.17A). The results show that the percentage of distal NoR with presumed NF186 staining in *GalNAc-T$^{-/-}$-Tg(neuronal)* and *GalNAc-T$^{-/-}$-Tg(glial)* control mice was 94 ± 4% and 88 ± 5%, respectively. In injured *GalNAc-T$^{-/-}$-Tg(neuronal)* mice, 75 ± 6% of distal NoR had NF186 present which was reduced compared to control, although not significantly. In contrast, the presence of NF186 was significantly reduced in injured *GalNAc-T$^{-/-}$-Tg(glial)* mice to 61 ± 6% in comparison to control mice ($p<0.05$). These data indicate that NF186 is mildly disrupted when both the axonal and glial membrane are injured.

Following on from this, I assessed the percentage of distal NoR with paranodal pan-NFasc present, representative of NF155 (Figure 4.17B). The percentage of nerves with presumed NF155 was comparable in both control and injured *GalNAc-T$^{-/-}$-Tg(neuronal)* mice, as 93 ± 1% and 91 ± 2% of distal NoR had paranodal dimers present, respectively. *GalNAc-T$^{-/-}$-Tg(glial)* control mice had 84 ± 2% of distal NoR with NF155 staining which was lower than both control and injured *GalNAc-T$^{-/-}$-Tg(neuronal)* mice, although not significantly. Contrastingly, the percentage of distal NoR with NF155 was significantly reduced in injured *GalNAc-T$^{-/-}$-Tg(glial)* mice to 33 ± 16%, compared to all other treatment groups ($p<0.01$ compared to injured *GalNAc-T$^{-/-}$-Tg(neuronal)* mice and *GalNAc-T$^{-/-}$-Tg(glial)* control mice; $p<0.001$ compared to *GalNAc-T$^{-/-}$-Tg(neuronal)* control mice). These results suggest that NF155 is significantly disrupted following targeted injury to the glial membrane in injured *GalNAc-T$^{-/-}$-Tg(glial)* mice.

The intensity of pan-NFasc staining spanning a 10 µm distance across the NoR was assessed from one example from each treatment group to determine whether staining at the nodal gap (single peak) or paranodal loops (two separate peaks) was evident (Figure 4.17C). In both *GalNAc-T$^{-/-}$-Tg(neuronal)* and *GalNAc-T$^{-/-}$-Tg(glial)* control mice, a uniform peak was present, stretching from -3 to 3 µm across the NoR, representative of both NF155 and NF186. In contrast, injured *GalNAc-T$^{-/-}$-Tg(neuronal)* mice presented with a decreased in intensity in the centre (0 µm) with two peaks evident on either side, suggesting NF155 dimers were present at the paranodes but NF186 was absent from the nodal gap. Injured *GalNAc-T$^{-/-}$-Tg(glial)* mice demonstrated one peak at 0 µm, delineating the presence of NF186. The arbitrary intensity was reduced at -2 µm and 2 µm, representing a loss of NF155 dimer staining from the paranodes. These findings are

illustrated by the representative images in Figure 4.17D; pan-NFasc was present overlying both the node and the paranode in *GalNAc-T$^{-/-}$-Tg(neuronal)* and *GalNAc-T$^{-/-}$-Tg(glial)* control mice at the distal NoR. Anti-GM1 mAb deposits are present at the nodal gap in injured *GalNAc-T$^{-/-}$-Tg(neuronal)* mice and the nodal gap appears slightly elongated. Both nodal and paranodal pan-NFasc is present, however the staining appears abnormal. On the other hand, paranodal pan-NFasc was absent in injured *GalNAc-T$^{-/-}$-Tg(glial)* mice but nodal pan-NFasc staining was present, coinciding with anti-GM1 mAb overlying the distal NoR.

Together these results indicate that complement mediated injury to axonal and glial membranes causes disruption to pan-NFasc at the distal NoR. Disruption to pan-NFasc appeared to be more severe when the glial membranes were targeted in *GalNAc-T$^{-/-}$-Tg(glial)* mice.

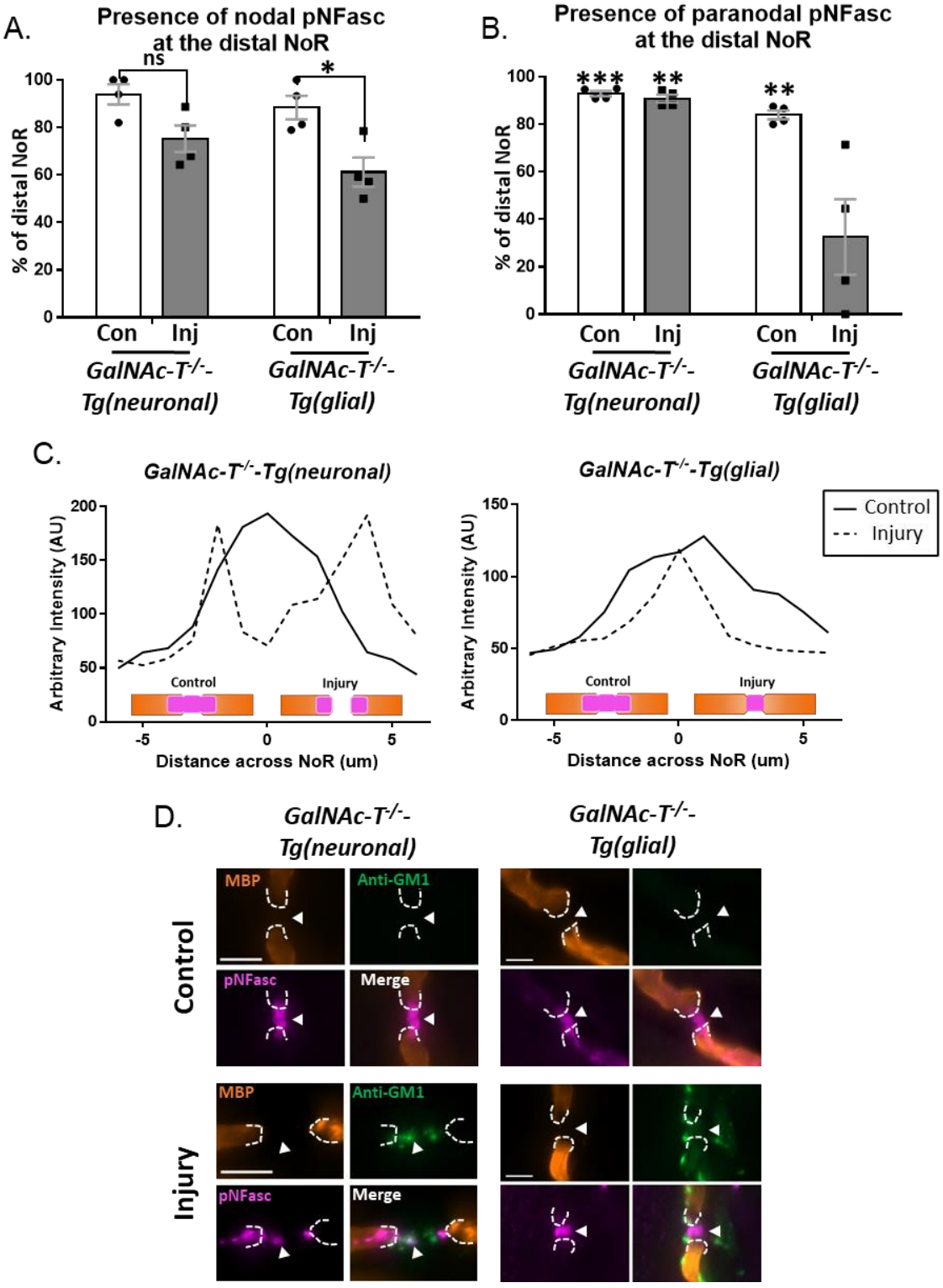
A.
Presence of nodal pNFasc at the distal NoR
ns
*
% of distal NoR
Con
Inj
GalNAc-T-/-Tg(neuronal)
GalNAc-T-/-Tg(glial)
B.
Presence of paranodal pNFasc at the distal NoR
***
**
**
% of distal NoR
Con
Inj
GalNAc-T-/-Tg(neuronal)
GalNAc-T-/-Tg(glial)
C.
GalNAc-T-/-Tg(neuronal)
GalNAc-T-/-Tg(glial)
Control
Injury
Arbitrary Intensity (AU)
Distance across NoR (um)
D.
GalNAc-T-/-Tg(neuronal)
GalNAc-T-/-Tg(glial)
Control
Injury
MBP
Anti-GM1
pNFasc
Merge

Figure 4.17: Analysis of nodal and paranodal neurofascin isoforms. (See previous page) *GalNAc-T$^{-/-}$-Tg(neuronal)* and *GalNAc-T$^{-/-}$-Tg(glial)* mice were injected intraperitoneally (IP) with 50 mg/kg of anti-GM1 mAb followed by 30 µl/g normal human serum (NHS); control mice received PBS and NHS. Diaphragm was collected for associated immunofluorescence analysis 6 hours post NHS delivery. Pan-NFasc was assessed in fixed diaphragm sections. A) Presence of nodal pan-NFasc, representative of NF186, was significantly reduced in injured *GalNAc-T$^{-/-}$-Tg(glial)* mice compared to control (*=p<0.05). B) Paranodal pan-NFasc, delineating NF155, was significantly reduced in injured *GalNAc-T$^{-/-}$-Tg(glial)* mice compared to all other treatment groups (**=p<0.01; ***=p<0.001). C) Intensity of pan-NFasc at the node was measured over a 10 µm distance. Control mice present with a uniform peak stretching from -3 to 3 µm, illustrating the presence of both NF186 and NF155. Injured *GalNAc-T$^{-/-}$-Tg(neuronal)* mice presented with two peaks, depicting NF155 at the paranodes with a loss of NF186 at the node. Injured *GalNAc-T$^{-/-}$-Tg(glial)* mice displayed one peak at 0 µm representative of NF186, NF155 was absent from the paranodes. N=1 NoR from each treatment group. D) Illustrative images demonstrate pan-NFasc (magenta) overlying both the nodal gap (white arrow) and the paranode (broken white line) in *GalNAc-T$^{-/-}$-Tg(neuronal)* and *GalNAc-T$^{-/-}$-Tg(glial)* control mice. In injured *GalNAc-T$^{-/-}$-Tg(neuronal)* mice, anti-GM1 mAb deposits (green) are present at the nodal gap and the nodal gap appears elongated; nodal and paranodal pan-NFasc are still present but appear abnormal. In injured *GalNAc-T$^{-/-}$-Tg(glial)* mice, there are anti-GM1 mAb deposits along the myelin basic protein staining; pan-NFasc is present at the node but absent from the paranode. Scale bar = 5um. Statistical analysis performed using a two-way ANOVA with Tukey's multiple comparisons test. Results represented as the average ± SEM, n=4/genotype/treatment group.

4.2.10.4 Caspr analysis

I next investigated the axo-glial protein, Caspr, which is localised in the axonal membrane at the paranode and interacts with glial NF155 (Charles et al., 2002). Caspr dimers at the paranode were categorised as 'normal', 'abnormal' or 'absent', using the same criteria as explained previously for AnkB analysis (see 4.2.10.2). Figure 4.18A demonstrates normal Caspr dimers were present in 83 ± 6% and 76 ± 16% of paranodes in both *GalNAc-T$^{-/-}$-Tg(neuronal)* and *GalNAc-T$^{-/-}$-Tg(glial)* control mice. The percentage of distal paranodes with normal Caspr dimers was lower in injured *GalNAc-T$^{-/-}$-Tg(neuronal)* mice, as only 56 ± 11% of analysed paranodes had normal Caspr staining; however, this difference was not significant. In contrast, the presence of normal Caspr dimers was significantly reduced to 5 ± 5% of distal paranodes in injured *GalNAc-T$^{-/-}$-Tg(glial)* mice compared to all other treatment groups (p<0.01 compared to injured *GalNAc-T$^{-/-}$-Tg(neuronal)* mice; p<0.001 compared to both *GalNAc-T$^{-/-}$-Tg(neuronal)* and *GalNAc-T$^{-/-}$-Tg(glial)* control mice). The percentage of paranodes with abnormal Caspr staining in injured *GalNAc-T$^{-/-}$-Tg(neuronal)* mice was higher in comparison to all other treatment groups, but this was not statistically significant. Injured *GalNAc-T$^{-/-}$-Tg(glial)* mice had 88 ± 8% of paranodes with absent Caspr

dimer staining. This was significantly higher compared to 2 ± 2%, 10 ± 6% and 7 ± 4% of paranodes with absent staining in control and injured *GalNAc-T$^{-/-}$-Tg(neuronal)* mice and control *GalNAc-T$^{-/-}$-Tg(glial)* mice, respectively ($p<0.001$). The panel of images illustrates the presence of Caspr dimers at the paranode of control mice (Figure 4.18C). Despite the presence of anti-GM1 mAb deposits at the nodal gap in injured *GalNAc-T$^{-/-}$-Tg(neuronal)* mice, Caspr dimers are present at the paranode. Conversely, Caspr dimers were absent from paranodes in injured *GalNAc-T$^{-/-}$-Tg(glial)* mice which correspond to anti-GM1 mAb deposits overlying the MBP staining along the internode and at the paranodes.

Overall, these results indicate that there is significant disruption to Caspr dimers at the distal paranode following injury to the glial membrane in *GalNAc-T$^{-/-}$-Tg(glial)* mice.

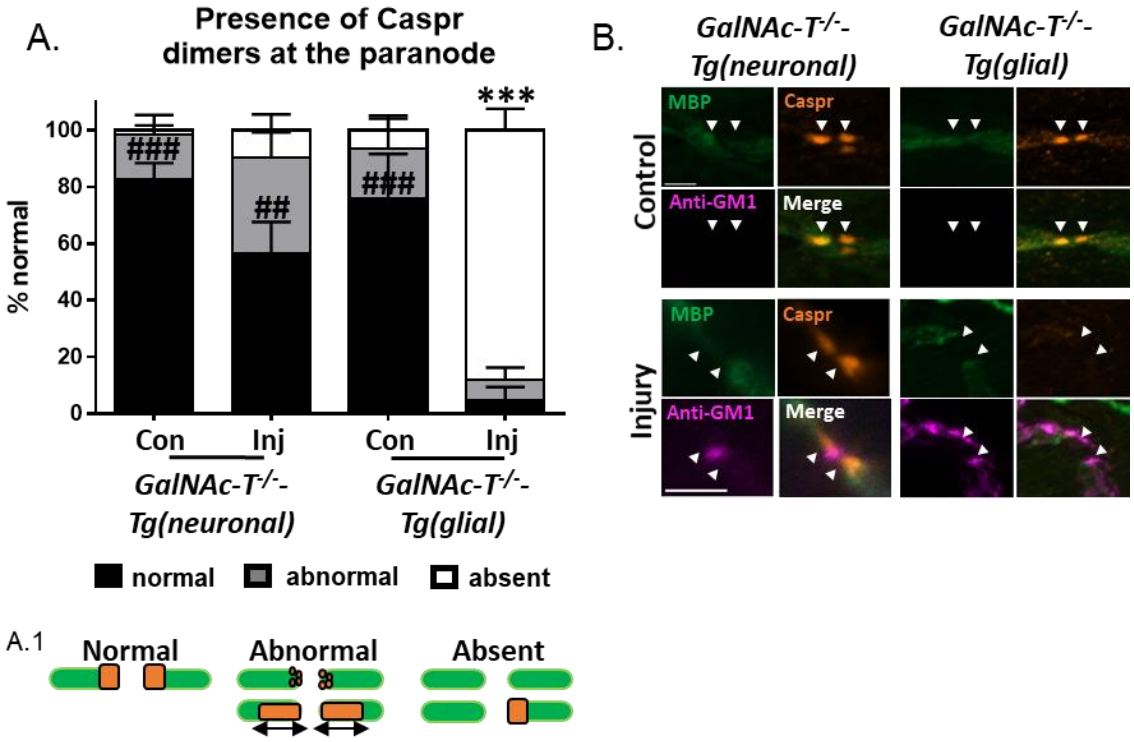

Figure 4.18: Analysis of Caspr at the distal paranode. *GalNAc-T$^{-/-}$-Tg(neuronal)* and *GalNAc-T$^{-/-}$-Tg(glial)* mice were dosed intraperitoneally (IP) with 50 mg/kg anti-GM1 Ab followed 16 hours later with an IP injection of 30 µl/g normal human serum (NHS); control mice received PBS and NHS. Diaphragm was collected for associated immunofluorescence analysis 6 hours post NHS delivery. Caspr dimers were assessed in fresh frozen diaphragm sections. A) The presence of normal Caspr dimers at the distal paranode was significantly reduced in injured *GalNAc-T$^{-/-}$-Tg(glial)* mice compared to all treatment groups (**###**=p<0.001; **##**=p<0.01). There was no significant difference in abnormal Caspr dimers between treatment groups. There were significantly more distal paranodes with absent Caspr dimer staining in injured *GalNAc-T$^{-/-}$-Tg(glial)* mice compared to all other treatment groups (*******=p<0.001). # = compared to normal Caspr dimers in injured *GalNAc-T$^{-/-}$-Tg(glial)* mice; * = compared to absent Caspr dimers in injured *GalNAc-T$^{-/-}$-Tg(glial)* mice. A.1) Schematic diagram illustrates normal, abnormal, and absent staining. B) NoR were identified by a gap in myelin basic protein immunostaining (green) and the site of expected staining indicated by white arrow heads. Illustrative images demonstrate Caspr dimers (orange) at the paranode in control and injured *GalNAc-T$^{-/-}$-Tg(neuronal)* mice, and in control *GalNAc-T$^{-/-}$-Tg(glial)* mice. In injured *GalNAc-T$^{-/-}$-Tg(glial)* mice, anti-GM1 deposits (magenta) are present and Caspr is absent from the paranodes. Scale bar=5 µm. Statistical analysis performed using a two-way ANOVA with Tukey's multiple comparisons test. Results represented as the average ± SEM, n=4/genotype/treatment group.

4.2.10.5 Kv1.1 cluster analysis

Evidence has shown that the paranode functions as a barrier to separate the juxtaparanode and the node, and that the integrity of the paranode is paramount for maintaining the localisation of key functional proteins, notably Kv to the juxtaparanode, and Nav to the nodal gap (Rosenbluth, 2009). Therefore, as it was demonstrated that the axo-glial junction was severely disrupted when the glial membrane was targeted in *GalNAc-T$^{-/-}$-Tg(glial)* mice, I assessed the consequence of this injury on Kv1.1 located at the juxtaparanode. Kv1.1 dimers were categorised as normal, abnormal, or absent as described previously (see section 4.2.10.2). The presence of normal appearing Kv1.1 dimers was reduced in injured *GalNAc-T$^{-/-}$-Tg(glial)* mice to 31 $\pm$ 6% in comparison to 74 $\pm$ 14% in control; however, this difference was not significant ($p=0.07$; Figure 4.19). The percentage of normal Kv1.1 dimers was significantly higher in *GalNAc-T$^{-/-}$-Tg(neuronal)* control mice in comparison to injured *GalNAc-T$^{-/-}$-Tg(glial)* mice ($p<0.01$). There were no significant differences in the percentage of abnormal Kv1.1 dimers between the treatment groups. Kv1.1 dimers were absent from 35 $\pm$ 10% of juxtaparanodes in injured *GalNAc-T$^{-/-}$-Tg(glial)* mice in comparison to 2 $\pm$ 1%, 4 $\pm$ 2%, and 0 $\pm$ 0% in control and injured *GalNAc-T$^{-/-}$-Tg(neuronal)* mice and control *GalNAc-T$^{-/-}$-Tg(glial)* mice, respectively. Despite this difference, it was not statistically significant.

The length between Kv1.1 dimers was investigated to determine whether the proteins were becoming mislocalised following injury to the axonal or glial membrane (Figure 4.19B). The mean gap between Kv1.1 dimers was comparable between control and injured *GalNAc-T$^{-/-}$-Tg(neuronal)* mice and control *GalNAc-T$^{-/-}$-Tg(glial)* mice (1.6 $\pm$ 0.2, 1.6 $\pm$ 0.1, 1.4 $\pm$ 0.1 µm, respectively). The mean gap between Kv1.1 dimers was elongated to 2.4 $\pm$ 0.7 µm in injured *GalNAc-T$^{-/-}$-Tg(glial)* mice but this did not differ significantly to any other treatment group.

Overall, these results indicate that Kv1.1 dimers are disrupted following injury to the glial membrane in *GalNAc-T$^{-/-}$-Tg(glial)* mice.

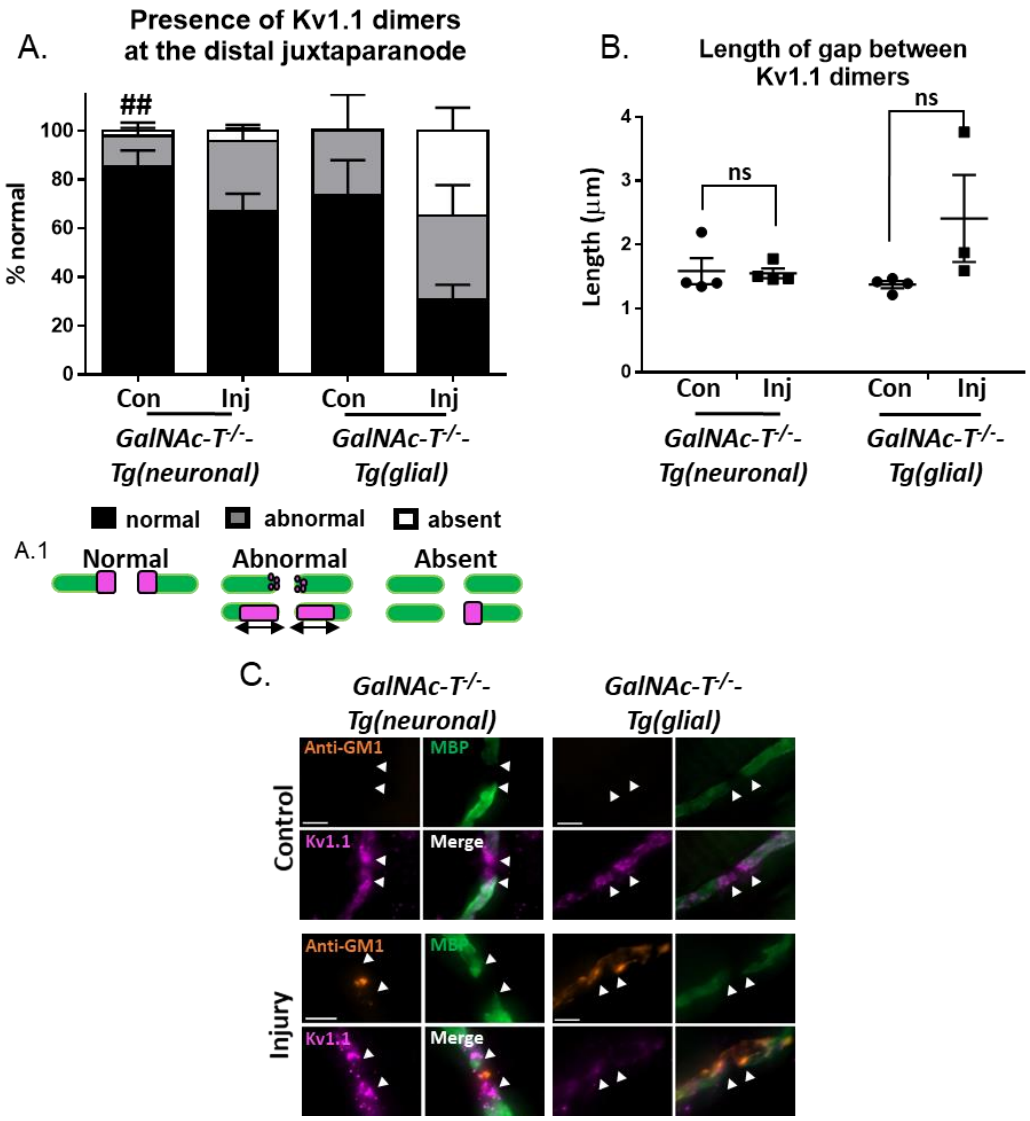

Figure 4.19: Presence of Kv1.1 channels at the juxtaparanode. *GalNAc-T$^{-/-}$-Tg(neuronal)* and *GalNAc-T$^{-/-}$-Tg(glial)* mice were injected intraperitoneally (IP) with 50 mg/kg anti-GM1 mAb followed 16 hours later with an IP injection of 30 µl/g normal human serum (NHS). Control mice received PBS and NHS. Diaphragm was harvested 6 hours post NHS injection and the presence of Kv1.1 dimers was assessed in fixed diaphragm sections. A) The presence of normal Kv1.1 dimers was significantly reduced in injured *GalNAc-T$^{-/-}$-Tg(glial)* mice compared to *GalNAc-T$^{-/-}$-Tg(neuronal)* control mice, but not to *GalNAc-T$^{-/-}$-Tg(glial)* control (##=p<0.01). There was no significant difference in the percentage of abnormal and absent Kv1.1 dimers between any treatment group. A.1) Schematic diagram illustrates normal, abnormal, and absent staining. B) The gap between Kv1.1 dimers was measured, and the mean value is plotted for each n. The mean gap between Kv1.1 dimers was elongated in injured *GalNAc-T$^{-/-}$-Tg(glial)* mice compared to all other treatment groups, although not significantly. n=3 injured *GalNAc-T$^{-/-}$-Tg(glial)* mice C) Representative images demonstrate Kv1.1 dimers (magenta) at the juxtaparanode (white arrowheads) in control and injured *GalNAc-T$^{-/-}$-Tg(neuronal)* mice and *GalNAc-T$^{-/-}$-Tg(glial)* control mice. In injured *GalNAc-T$^{-/-}$-Tg(glial)* mice, anti-GM1 mAb deposits (orange) are deposited over the myelin basic protein (green) and Kv1.1 dimers are absent from the juxtaparanode. Scale bar = 5µm. Results represented as average ± SEM. Two-way ANOVA with Tukey's multiple comparisons test performed to test for statistical significance. n=4/treatment/group.

4.2.11 Ultrastructural analysis at the NoR

Following on from the immunofluorescence analysis, the ultrastructure of the NMJ and the NoR was assessed in *GalNAc-T$^{-/-}$-Tg(neuronal)* and *GalNAc-T$^{-/-}$-Tg(glial)* mice, respectively, by performing EM (performed by Jennifer Barrie (MSc)) The electron micrographs are shown in Figure 4.20.

The ultrastructure of the NMJ was assessed in *GalNAc-T$^{-/-}$-Tg(neuronal)* mice. The NMJ of *GalNAc-T$^{-/-}$-Tg(neuronal)* control mice contains synaptic vesicles and normal appearing mitochondria (Figure 4.20A). On the other hand, synaptic vesicles are absent from the NMJ in injured *GalNAc-T$^{-/-}$-Tg(neuronal)* mice and mitochondria appears dense and vacuolated, indicative of mitochondrial damage (Figure 4.20B). Figure 4.20C demonstrates a normal NoR in injured *GalNAc-T$^{-/-}$-Tg(neuronal)* mice; paranodal loops are symmetrical across the axon, transverse bands are visible at the paranodal junctions, and the axon appears healthy. These results were not surprising as antibody and complement deposits were low at the distal nodal gap of injured *GalNAc-T$^{-/-}$-Tg(neuronal)* mice (see sections 4.2.7 and 4.2.8). The ultrastructure of the paranodes was then assessed in *GalNAc-T$^{-/-}$-Tg(glial)* mice. In *GalNAc-T$^{-/-}$-Tg(glial)* control mice, transverse bands are present at the axo-glial junction and the paranodal loops appear uniform and normal (Figure 4.20D). In contrast, there is significant disruption to the confirmation of the paranodal loops in injured *GalNAc-T$^{-/-}$-Tg(glial)* mice as demonstrated in Figure 4.20E. However, there are some paranodal loops which still form axo-glial junctions, highlighted in Figure 4.20F. Despite the disruption to the paranodes, the compact myelin appears unaffected in injured *GalNAc-T$^{-/-}$-Tg(glial)* mice.

These findings corroborate the immunofluorescence analysis results. Injury to the axonal membrane results in disruption to axonal integrity at the NMJ in *GalNAc-T$^{-/-}$-Tg(neuronal)* mice. On the other hand, injury to the glial membrane in *GalNAc-T$^{-/-}$-Tg(glial)* mice causes significant alteration to the axo-glial junctions at the NoR, leading to paranodal demyelination.

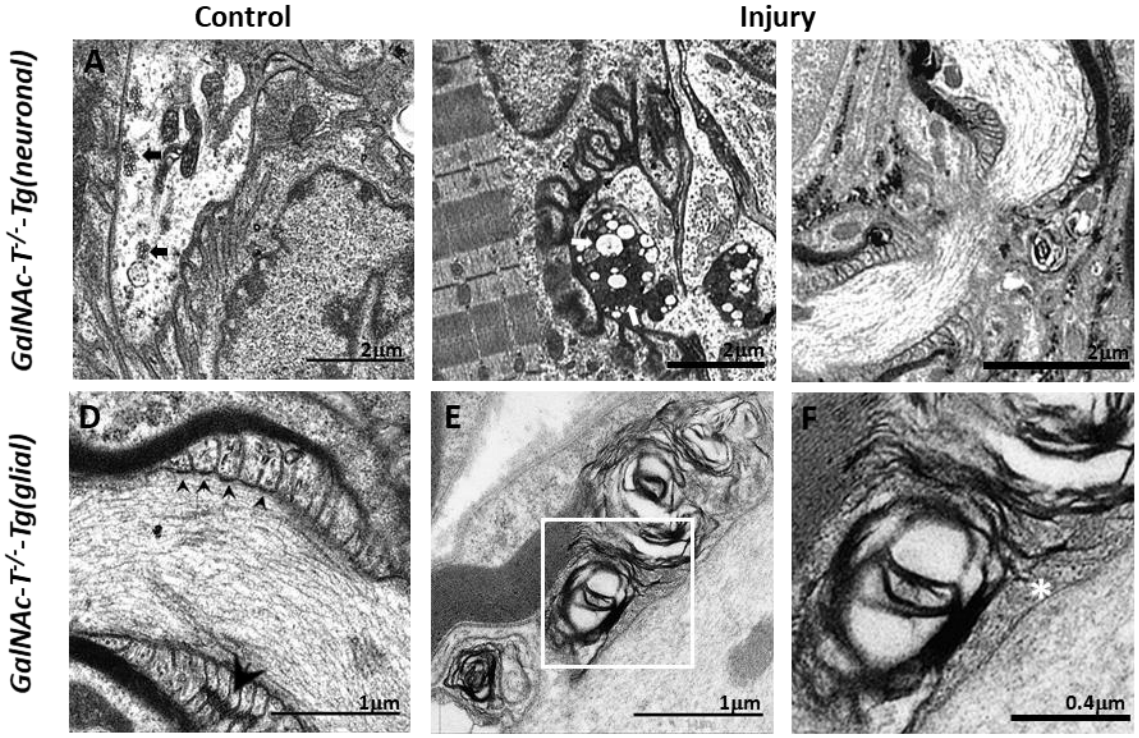

Figure 4.20: Electron micrographs of *GalNAc-T$^{-/-}$-Tg(neuronal)* and *GalNAc-T$^{-/-}$-Tg(glial)* mice. *GalNAc-T$^{-/-}$-Tg(neuronal)* and *GalNAc-T$^{-/-}$-Tg(glial)* mice were injected intraperitoneally (IP) with 50 mg/kg anti-GM1 mAb followed 16 hours later with an IP injection of 30 µl/g normal human serum (NHS). The diaphragm was harvested 6 hours post NHS injection and fixed for electron microscopy (EM) analysis. Tissue processing and image acquisition was performed by Jennifer Barrie. A) A neuromuscular junction (NMJ) from *GalNAc-T$^{-/-}$-Tg(neuronal)* control mice containing synaptic vesicles and healthy mitochondria (black arrows). B) A NMJ from injured *GalNAc-T$^{-/-}$-Tg(neuronal)* mice displaying dense or vacuolated mitochondria (white arrows). Synaptic vesicles are absent from the NMJ. C) Node of Ranvier (NoR) from injured *GalNAc-T$^{-/-}$-Tg(neuronal)* mice with no architectural disruption. D) *GalNAc-T$^{-/-}$-Tg(glial)* control paranode showing tight junctions (large arrowhead) between the paranodal loops and transverse bands (small arrowheads) at the axo-glial junction. E) Injured *GalNAc-T$^{-/-}$-Tg(glial)* paranode demonstrating disruption of the paranodal loops. F) Higher magnification of squared area in E. Some paranodal loops form axo-glial junctions (white asterisks). Scale bars illustrated on each picture.

4.3 Summary

The most important findings of this chapter are that TV was significantly reduced in all injured mice at 5-hours post injury compared to their respective baseline TV. However, only injured *GalNAc-T$^{-/-}$-Tg(neuronal)* mice presented with a pinched wasp-like abdomen demonstrating a more severe respiratory phenotype than injured wild type or injured *GalNAc-T$^{-/-}$-Tg(glial)* mice. Complement mediated injury to the axonal membrane in

GalNAc-T$^{-/-}$-Tg(neuronal) mice resulted in a significant reduction of axonal integrity at the NMJ and disruption to the NoR. In contrast, complement mediated injury to the glial membrane did not affect axon integrity acutely, but instead caused significant impairment to the axo-glial junction at the paranode, resulting in paranodal demyelination and mislocalisation of key nodal proteins.

4.4 Discussion

Current animal models of GBS, mediated by AGAbs, target both axonal and glial membranes and so the extent to which the resulting injury is due to antibody binding to the axonal or glial membrane, or to both, cannot be determined. To overcome this issue, we generated transgenic mice with exclusive expression of complex gangliosides on either axonal or glial membranes (Yao et al., 2014), therefore, allowing us to target each membrane independently with a single anti-GM1 mAb. The results of this chapter clearly demonstrate that the injury outputs differ depending on whether the axonal or glial membrane is targeted.

The *in vivo* model used in this experiment targets the myelinated distal motor nerve fibres within the diaphragm, due to the proximity of the anti-GM1 mAb and complement injection site to this muscle (Halstead et al., 2008). Therefore, WBP ideally lends itself to quantitative assessment of the functional consequence of injury by analysing the respiratory output (Goldman et al., 2005). The plethysmography results indicate that the TV was significantly reduced in all injured mice in comparison to baseline, following anti-GM1 mAb and complement-mediated injury. However, only injured *GalNAc-T$^{-/-}$-Tg(neuronal)* mice presented with a pinched wasp-like abdomen, representative of severe diaphragm paralysis. This was expected in injured *GalNAc-T$^{-/-}$-Tg(neuronal)* mice because a previous study using the same mouse model had already established that diaphragm paralysis occurs due to transmission block at the nerve terminals caused by complement (McGonigal et al., 2016). However, it was unknown what would occur when the glial membranes were targeted in *GalNAc-T$^{-/-}$-Tg(glial)* mice. A previous study demonstrated binding of AGAb at the NMJ, on both nerve terminals and pSC, resulting in subsequent complement mediated injury (Halstead et al., 2004). Despite this fact, it was unknown whether the resulting injury was a consequence of antibody binding to the nerve terminal or to pSC. Therefore, we have determined that by targeting glial membranes in *GalNAc-T^{-}*

$^{-/-}$-Tg(glial) mice, respiratory function was impaired but not as severely as the respiratory impairment in injured *GalNAc-T$^{-/-}$-Tg(neuronal)* mice. The immunofluorescence and EM analysis revealed significant disruption to the NMJ in *GalNAc-T$^{-/-}$-Tg(neuronal)* mice, whereas in *GalNAc-T$^{-/-}$-Tg(glial)* mice, there was substantial injury to the axo-glial junction at the paranodes. Therefore, the respiratory deficit in *GalNAc-T$^{-/-}$-Tg(neuronal)* mice is most likely due to MAC pore formation at the nerve terminal, causing an uncontrolled calcium influx that subsequently results in uncontrolled ACh exocytosis, eventually culminating in synaptic failure with block of synaptic transmission (O'Hanlon et al., 2003). On the other hand, the reduction in TV in *GalNAc-T$^{-/-}$-Tg(glial)* mice is possibly a consequence of detachment of the paranodal loops, causing leakage of current from the paranodal region, reducing the safety factor for impulse transmission (Uncini and Kuwabara, 2015). Although the TV was significantly reduced in injured wild type mice in comparison to baseline, the TV was not as severely reduced as *GalNAc-T$^{-/-}$-Tg(neuronal)* and *GalNAc-T$^{-/-}$-Tg(glial)* injured mice. The ELISA and immunofluorescence analysis results provide an explanation for this, as anti-GM1 mAb was not present in the sera and was deposited at a low percentage of distal nerves, therefore wild type mice were not significantly injured, as discussed below. These results were not surprising as it has previously been demonstrated that wild type mice are not suitable for passive immunisation AGAb-mediated injury due to antibody being sequestered elsewhere (Cunningham et al., 2016).

Previous AGAb and complement mediated *in vivo* mouse models have demonstrated that a reduction in TV is accompanied with a severe reduction in RR in injured mice (Halstead et al., 2008, McGonigal et al., 2016). The RR results described in this chapter did not follow the same trend. The reduced RR in previous models is likely due to an extreme injury resulting in full paralysis of the diaphragm, or the muscle becoming fatigued after prolonged breathing difficulty. There was only a severe reduction in RR found in *GalNAc-T$^{-/-}$-Tg(glial)* control mice at 255, 285, 300 and 315 MPI compared to baseline. As control mice received NHS only, then this reduction in RR was not due to antibody and complement mediated injury. A possible explanation for this could be that the baseline recording taken for *GalNAc-T$^{-/-}$-Tg(glial)* control mice was not a true representation of their normal RR; therefore, they became relaxed in subsequent recordings resulting in a reduced RR. Another explanation could be that the *GalNAc-T$^{-/-}$-Tg(glial)* control mice were less active during the plethysmography recording taken post injury compared to the

baseline recording as they further habituated to the equipment. There is evidence to suggest that motor activity and RR are positively correlated (Kabir et al., 2010); thus, reduced activity would result in a decreased RR. There is a general trend present in the data which illustrates that RR is elevated in injured mice at 300 and 315 MPI compared to their respective controls. In preliminary experiments investigating passive immunisation with a lower dose of anti-GM1 mAb and NHS, RR was increased in injured mice at 6-hours post injury (Crawford, MRes Thesis, 2017). This is comparable to my findings and can be explained by the mice initially having to increase their RR to compensate for the reduction in TV before a complete functional breakdown.

Interestingly, anti-GM1 mAb was absent from the sera of injured wild type mice and subsequently there were very low levels of complement deposition at the NMJ and distal nerve. It is established from *ex vivo* studies that anti-GM1 mAb binds to both the NMJ and distal NoR in wild type mice, resulting in complement-mediated injury (Greenshields et al., 2009)(McGonigal, unpublished data); therefore demonstrating that antibody can bind GM1 in 'live' wild type tissue and exert neuropathologic effects. Thus, implying that something is happening to the antibody in circulation to prevent it from binding *in vivo.* Cunningham et al (2016) previously established that antibody is cleared from the circulation *in vivo* in wild type mice via endocytic pathways at the NMJ, thereby explaining why anti-GM1 mAb was not detected in the sera of wild type injured mice. Furthermore, it is possible that the antibody is also sequestered in other tissues that express GM1 on their plasma membranes. As GM1 is expressed in widespread sites in wild type mice, the antibody can bind anywhere in the body that it has ready access. On the contrary, GM1 is only expressed on the targeted tissue within the nervous system in transgenic mice, and therefore, the antibody has nowhere else to bind where it could be readily sequestered. Interestingly, despite anti-GM1 mAb not being detected in the sera, antibody deposits were detected at ~90% of analysed distal nerves in injured wild type mice, whereas less than 10% of NMJs had anti-GM1 mAb deposits. Fewou et al., (2012) has previously demonstrated that AGAb is rapidly cleared from the presynaptic membrane in an *ex vivo* TS muscle preparation by endocytic pathways, but anti-GM1 mAb is not internalised by the nodal axolemmal membrane at the NoR. This is thought to be due to active endosomal trafficking pathways at the presynaptic membrane and not the NoR. Therefore, this could explain why anti-GM1 mAb was deposited along the nerve, but not at the terminal. Despite the presence of anti-GM1 mAb deposits at the distal nerve, there

was very low complement deposition at both the NMJ and the distal nerve and there was no disruption to neurofilament, Nav or Caspr. If anti-GM1 mAb is binding elsewhere in wild type mice, it is possible that complement is being sequestered. It would be interesting to perform a quantitative complement assay using the sera from the mice to compare the concentration of complement in the circulation between wild type, *GalNAc-T$^{-/-}$-Tg(neuronal)* and *GalNAc-T$^{-/-}$-Tg(glial)* mice.

When investigating anti-GM1 mAb and complement deposition in wild type, *GalNAc-T$^{-/-}$-Tg(neuronal)* and *GalNAc-T$^{-/-}$-Tg(glial)* mice, it was determined that the binding pattern differed between the strains of mice. When antibody and complement deposits were present at the distal nerve in wild type mice, they were deposited on both axonal and glial membranes. On the other hand, in *GalNAc-T$^{-/-}$-Tg(neuronal)* mice, anti-GM1 mAb and complement were commonly found deposited directly overlying the NMJ and at the nodal gap. Conversely, antibody and complement deposits were found surrounding the BTx staining in *GalNAc-T$^{-/-}$-Tg(glial)* mice and deposited at the internode and at the paranodes in distal nerves; hence, deposits were only found on glial membranes. Anti-GM1 mAb and complement were determined to be binding to pSC at the NMJ in *GalNAc-T$^{-/-}$-Tg(glial)* mice as the staining pattern was consistent with that demonstrated by Halstead and colleagues when investigating AGAb deposits at the NMJ (Halstead et al., 2004). Overall, the binding patterns of anti-GM1 mAb and complement confirm that only the axonal or glial membranes were targeted in *GalNAc-T$^{-/-}$-Tg(neuronal)* and *GalNAc-T$^{-/-}$-Tg(glial)* mice, respectively. Taken together with the low antibody and complement deposits in wild type mice, it was decided that wild type mice would be removed from further analysis.

When the axonal membrane was targeted in *GalNAc-T$^{-/-}$-Tg(neuronal)* mice, the main consequence of antibody and complement deposits overlying the nerve terminal was a severe loss of the axonal structural protein, neurofilament. This was expected because neurofilament is a calpain substrate, and it is known that the calpain-protease is activated following complement-mediated injury (O'Hanlon et al., 2003). Additionally, the electron micrographs demonstrated apparent mitochondrial damage at the NMJ. Mitochondrial injury is mediated by calcium influx and is thought to contribute to release of transmitter at the terminal (O'Hanlon et al., 2003, Calupca et al., 1999). At the NoR, injury to the axonal membrane in *GalNAc-T$^{-/-}$-Tg(neuronal)* mice resulted in disruption to the pNav

clustering at the nodal gap. As described previously, this injury model results in calpain activation (O'Hanlon et al., 2003); thus, it is likely that Nav are being proteolyzed by calpain as they are a known calpain substrate (von Reyn et al., 2009). On a similar note, it is known that spectrin and AnkG - which tether Nav to the underlying cytoskeleton - are both calpain substrates (Boivin et al., 1990). It is possible that disruption of these anchoring proteins would have a knock-on effect to the proteins which they bind to and so, Nav could be disrupted indirectly, as well as directly, by calpain. Nodal pan-NFasc, representing NF186, was reduced in injured *GalNAc-T$^{-/-}$-Tg(neuronal)* mice, although not significantly. Neurofascin is not recognised as a calpain substrate; however, NF186 is tethered to the underlying cytoskeleton via AnkG and so cleavage of this protein could result in the disorganisation of the node, explaining the reduction in nodal pan-NFasc. Additionally, NF186 is also tethered to Nav channels and so calpain mediated injury to Nav could have an indirect effect on NF186 localisation. The results from the Caspr analysis in injured *GalNAc-T$^{-/-}$-Tg(neuronal)* mice were unexpected. Due to Caspr being located on the axonal membrane at the paranode, it was expected that Caspr would be significantly disrupted following targeted injury to the axonal membrane. However, the results demonstrated that there was no significant difference in the percentage of normal Caspr dimers in injured *GalNAc-T$^{-/-}$-Tg(neuronal)* mice, even though this was reduced compared to control. It is possible that Caspr is protected from injury in *GalNAc-T$^{-/-}$-Tg(neuronal)* mice as it lies lateral to the injury sight and is offered protection by the glial paranodal loops. Furthermore, Caspr is tethered to the glial membrane through binding of NF155 (Charles et al., 2002), therefore, as the glial membrane is uninjured in *GalNAc-T$^{-/-}$-Tg(neuronal)* mice, binding of Caspr to the axo-glial junction will be preserved. There is evidence of a lengthening of the nodal gap in patient autopsy and animal models (Hafer-Macko et al., 1996a, Susuki et al., 2007b). The results described in this chapter suggest a slight elongation of the nodal gap following injury to the axonal membrane in *GalNAc-T$^{-/-}$-Tg(neuronal)* mice. This is possibly due to oedema occurring because of MAC pores in the axonal membrane. Nevertheless, the NoR appeared normal in electron micrographs in *GalNAc-T$^{-/-}$-Tg(neuronal)* mice and there was no evidence of swelling. However, it was not possible to determine whether the NoR assessed during EM analysis were located distally or proximally. It has previously been demonstrated that injury to the NoR does not occur at proximal locations due to the presence of the BNB (McGonigal et al., 2010). Therefore, complement-mediated pathology would be expected to be observed at distal nerves and

not at proximal nerves. To overcome this, NoR upstream of the NMJ could be assessed and quantitative EM analysis could be performed to determine the length of the nodal gap for example. Overall, targeted injury to the axonal membrane results in significant disruption to axonal integrity at the nerve terminal and distal NoR (summarised in Figure 4.21).

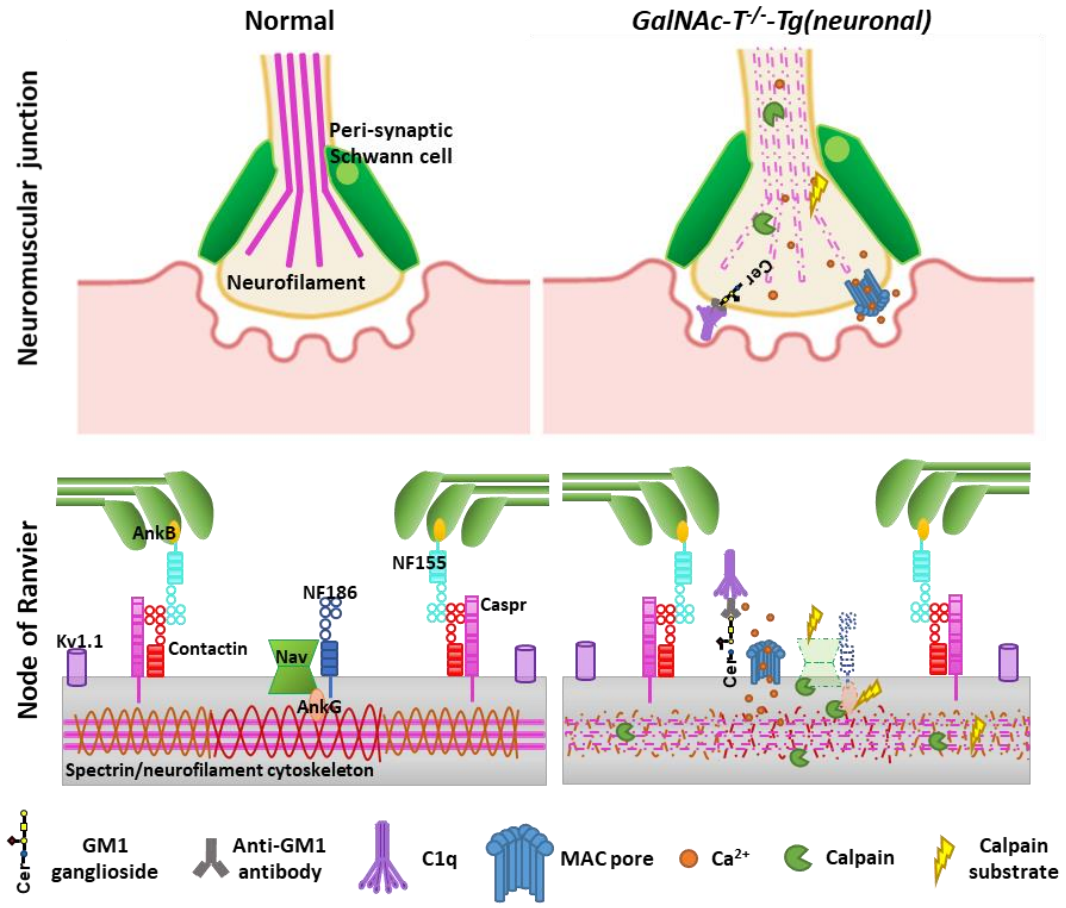

Figure 4.21: Summary diagram illustrating injury at the neuromuscular junction and node of Ranvier in *GalNAc-T-/--Tg(neuronal)* mice.

In contrast to *GalNAc-T-/--Tg(neuronal)* mice, there was no significant disruption present at the NMJ following injury to the glial membrane in *GalNAc-T-/--Tg(glial)* mice. It was hypothesised that secondary injury to the axon may occur subsequently to glial membrane injury; however, neurofilament remained intact at the NMJ in *GalNAc-T-/--Tg(glial)* mice in this acute model (Figure 4.22). These results are confirmed by the correlation analysis between C3c and NFH which demonstrated that the two components were negatively correlated in injured *GalNAc-T-/--Tg(neuronal)* mice, whereas there was a weak positive correlation between the two components in injured *GalNAc-T-/--Tg(glial)* mice. Hence, when C3c was present at the NMJ in injured *GalNAc-T-/--Tg(neuronal)* mice, this resulted in the loss of NFH, but when C3c was present in injured *GalNAc-T-/--Tg(glial)*

mice, NFH remained intact. Next, I investigated the integrity of proteins located at the distal NoR, as disruption to axo-glial proteins at this site has been demonstrated previously in animal models of AMAN (McGonigal et al., 2010, Susuki et al., 2007b). Injury to the glial membrane in *GalNAc-T$^{-/-}$-Tg(glial)* mice, resulted in significant disruption to the axo-glial junction on both the axonal and glial membrane at the paranode (Figure 4.22). The glial cytoskeletal protein, AnkB, was absent from the majority of analysed distal NoR. It is known that AnkB is a calpain substrate (Boivin et al., 1990), and so this protein is likely to have been cleaved following MAC pore formation and calcium influx. In injured *GalNAc-T$^{-/-}$-Tg(glial)* mice, paranodal pan-NFasc was significantly reduced at the paranode, which suggests that NF155 staining was lost when the glial membrane was targeted. As this protein is tethered to AnkB, then it is possible that calpain cleavage of AnkB is responsible for this disruption. Furthermore, the axo-glial protein, Caspr, which is located on the axonal membrane at the paranode and binds to its glial binding partner, NF155 (Charles et al., 2002), was also severely disrupted when the glial membrane was targeted, but not when the axonal membrane was targeted. A possible explanation for this is because AnkB tethers NF155 to the glial cytoskeleton (Ogawa et al., 2006), therefore, cleavage of AnkB could result in the detachment of NF155 from the cytoskeleton, causing the mislocalisation and subsequent disruption to Caspr and contactin localisation on the axonal membrane; consequently, leading to the paranodal loops peeling away, exposing the underlying axolemma. Surprisingly, there was also significant disruption to NF186 at the nodal gap following injury to the glial membrane. There is evidence to suggest that the paranodal junction functions as a barrier to prevent the lateral diffusion of nodal proteins (Rosenbluth, 2009); thus, the disruption to the axo-glial adhesion molecules could be causing NF186 to become mis-localised from the nodal gap. In addition, Kv1.1 channels at the juxtaparanode were also disrupted following injury to the glial membrane. The localisation of Kv1.1 at the juxtaparanode is maintained by an intact axo-glial junction at the paranode (Bhat, 2003); thereby providing an explanation for the mislocalisation of Kv1.1 following injury to the paranodes. Moreover, CAM at the juxtaparanode form a complex between the axonal and glial membrane, consisting of Caspr2 and TAG-1 on the axonal membrane interacting with TAG-1 on the glial membrane (Traka et al., 2003). It is considered that the clustering of Kv1.1 at the juxtaparanodes depends on the interactions mediated between Caspr2 and TAG-1 (Pinatel and Faivre-Sarrailh, 2021); thus, injury to the glial membrane could result in disruption to TAG-1 on

the glial membrane, destructing the axo-glial junction at the juxtaparanode, resulting in the mislocalisation of Kv1.1. To investigate the mechanisms involved in disruption to Kv1.1, it would be interesting to assess the presence of TAG-1 at the juxtaparanode. Despite the significant disruption to the NoR, the nodal gap did not appear to be elongated in *GalNAc-T$^{-/-}$-Tg(glial)* mice. As MBP is a marker of compact myelin, it is not surprising that the gap between the MBP staining at the NoR was not altered in *GalNAc-T$^{-/-}$-Tg(glial)* mice as ultrastructure analysis demonstrated that compact myelin appeared healthy in contrast to the significant disruption to the paranodal loops. Overall, these results highlight how important the axo-glial septate junctions are in maintaining the link between the glial and axonal surfaces. Injury to this site could have severe implications to the function of the NoR and health of the underlying axon and may be the initial steps which result in secondary axonal degeneration. To test this hypothesis, the injury model was extended in *GalNAc-T$^{-/-}$-Tg(glial)* mice and axonal integrity was assessed at the nerve terminal and the distal nerve. These results are detailed in Chapter 5.

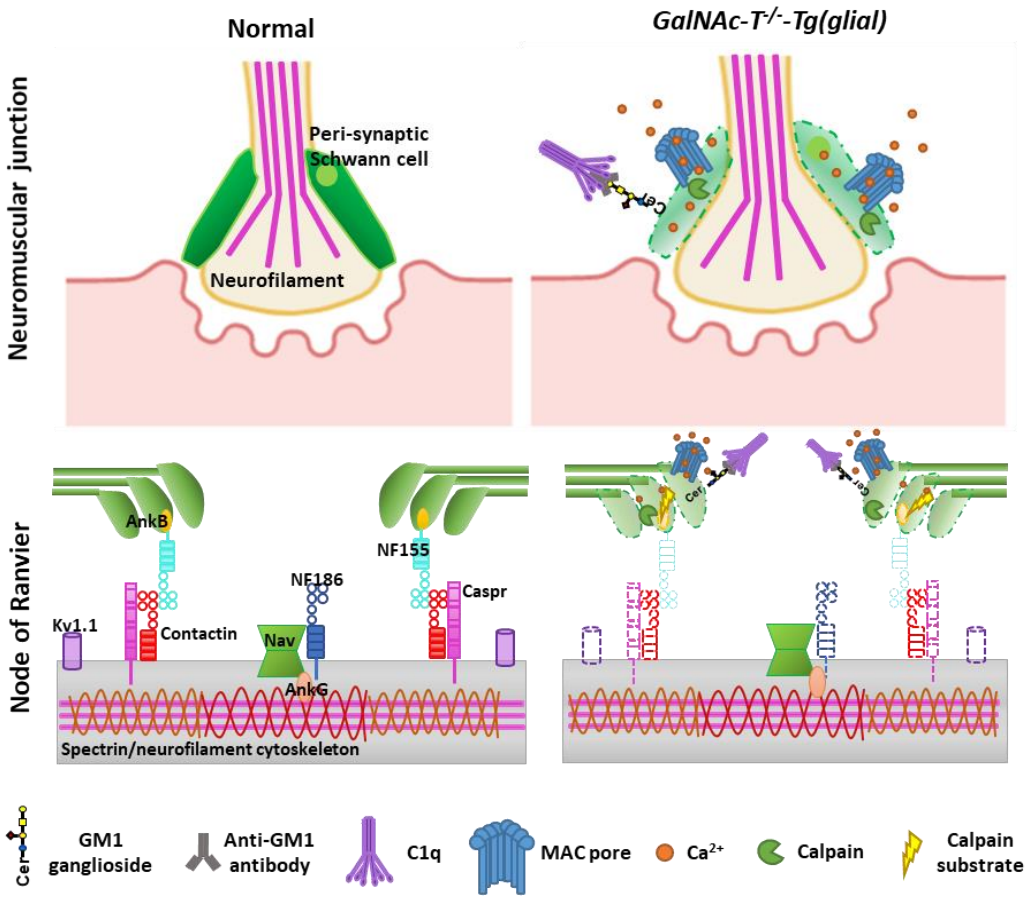

Figure 4.22: Summary schematic illustrating injury to the neuromuscular junction and node of Ranvier in *GalNAc-T$^{-/-}$-Tg(glial)* mice.

One of the key characteristics of AIDP is segmental demyelination (Haymaker and Kebnohan, 1949). As one of my aims was to establish animal models which resemble AMAN and AIDP in *GalNAc-T$^{-/-}$-Tg(neuronal)* and *GalNAc-T$^{-/-}$-Tg(glial)* mice, respectively, I determined whether segmental demyelination occurred following antibody and complement mediated injury to the glial membrane. In this acute injury model, MBP intensity was unaffected in *GalNAc-T$^{-/-}$-Tg(glial)* mice, although myelin morphology did appear abnormal. However, ultrastructure analysis revealed that compact myelin was intact and appeared normal at 6 hours post injury. On the other hand, the cytoplasmic paranodal loops were severely affected. Therefore, injury to the glial membrane in *GalNAc-T$^{-/-}$-Tg(glial)* mice at the time point studied represents a model of paranodal demyelination. Longer exposures might nevertheless induce segmental demyelination.

The results of this chapter clearly illustrate that by using *GalNAc-T$^{-/-}$-Tg(neuronal)* and *GalNAc-T$^{-/-}$-Tg(glial)* mice, the axonal and glial membranes can be selectively targeted, respectively. Hafer-Macko and colleagues have previously looked at the pattern of nodal complement deposits and highlighted the differences in patterns between AMAN and AIDP. They suggested that the responsible antigen for each variant is present in different locations of the myelinated fibre. For AMAN, they predict that the antigen is located in the nodal and internodal axolemma (Hafer-Macko et al., 1996a), whereas in AIDP, the antigen is present in the plasmalemma of Schwann cells (Hafer-Macko et al., 1996b). This is important because we have now created animal models where we can selectively target complex gangliosides, the main pathogenic antigens in GBS, on either axonal or glial membranes, thereby providing the opportunity to study the downstream mechanisms which occur in AMAN and AIDP, respectively.

In conclusion, injury to the axonal membrane causes significant damage to axonal integrity at the NMJ and disruption of nodal proteins at the NoR. In contrast, injury to the glial membrane results in significant disruption to the axo-glial adhesion molecules at the paranode, leading to paranodal demyelination.

5 Secondary effects to the axon following targeted injury to the glial membrane

5.1 Introduction

AIDP is predominantly characterised phenotypically by segmental demyelination, however secondary 'bystander' injury can occur to the axon resulting in secondary axonal degeneration (Asbury et al., 1969, Feasby et al., 1993). Axonal degeneration is associated with poor prognosis in both the axonal and demyelinating variants of GBS (Martín-Aguilar et al., 2020). Although the PNS has the capacity to regenerate, axonal regeneration is not as rapid or effective as remyelination; hence, the association with poor recovery. Understanding the pathways involved in primary and secondary axonal degeneration are imperative to develop targeted treatment strategies. The mechanisms involved in primary axonal degeneration are well established due to many accessible animal models. However, the downstream events that occur in AIDP leading to secondary axonal degeneration are currently unknown. This is due to the limited availability of animal models representative of the demyelinating variant. In addition, current models are unable to differentiate between primary injury and consequences of cell-specific membrane injury.

The paranodal demyelinating injury model in *GalNAc-T$^{-/-}$-Tg(glial)* mice is the first anti-GM1 mAb and complement-mediated demyelinating mouse model that can be used to study the disease mechanisms of AIDP. Additionally, as the glial membrane is targeted independently of the axonal membrane, it provides the opportunity to investigate the consequences to the axon following disruption to the cytoplasmic paranodal loops. Myelinating Schwann cells function in providing support and protection to the axon [reviewed by (Moss et al., 2021, Bouçanova and Chrast, 2020)]. This involves insulating the axon, establishing molecular architecture of the NoR, cytoskeletal organisation and supplying trophic and metabolic support. Thus, we hypothesised that significant injury to the cytoplasmic paranodal loops in *GalNAc-T$^{-/-}$-Tg(glial)* mice would consequently lead to secondary injury to the axon.

It has previously been demonstrated in a temporally extended *ex vivo* injury model using *GalNAc-T$^{-/-}$-Tg(glial)* mice, that there is significant disruption to axonal integrity at the

distal nerve 24-hours following injury to the glial membrane (Unpublished data). Thus, the aim of this chapter was to explore similarities in secondary effects to the axon following injury to the glial membrane in a temporally extended *in vivo* injury model in *GalNAc-T$^{-/-}$-Tg(glial)* mice.

5.2 Results

GalNAc-T$^{-/-}$-Tg(glial) mice were injected with 50 mg/kg anti-GM1 mAb followed 16 hours later with 30 µl/g NHS. Respiratory function was monitored at 6, 12 and 24-hours post injury (post NHS injection) by performing WBP. Mice were culled at 24-hours and the diaphragm was harvested to assess the integrity of axonal structural proteins at the NMJ and NoR by performing immunofluorescence analysis. An ELISA was performed on the sera taken from each mouse at the end of the experiment and it was determined that anti-GM1 mAb was present in the circulation of all injured mice (see Appendix 8.3), therefore all mice were included in analysis. The results are detailed below.

5.2.1 Change in respiratory function over 24 hours

It was previously demonstrated that *GalNAc-T$^{-/-}$-Tg(glial)* mice were found to present with a mild respiratory phenotype in Chapter 4. This was thought to be due to significant disruption to the axo-glial adhesion molecules at the paranode, hypothesised to culminate in detachment of the paranodal loops, thereby presenting as conduction block. Herein, I assessed the change in respiratory function in *GalNAc-T$^{-/-}$-Tg(glial)* mice over a 24-hour period to determine whether the respiratory phenotype recovered. A baseline WBP recording was taken prior to delivery of anti-GM1 mAb and NHS and compared to recordings from 6, 12 and 24-hours post injury. The TV and RR at each time point was assessed and is presented as scatter box plots in Figure 5.1. The TV was reduced in both control and injured mice at 6-hours post injury to 71 $\pm$ 16% and 77 $\pm$ 18% of baseline, respectively (Figure 5.1A). At 12-hours the TV had recovered and had risen above baseline to 109 $\pm$ 10% and 112 $\pm$ 10% in control and injured mice, respectively. At 24-hours, the TV had dropped slightly in the control group to 95 $\pm$ 19% of baseline, but the TV of the injured group remained above baseline at 106 $\pm$ 6%. There were no significant differences between control and injured groups at any point, nor compared to baseline at any time point. Overall, these results demonstrate that the TV was comparable between control

and injured mice at each time point and that the TV recovered following the 6-hour time point.

The RR results within each treatment group were variable as illustrated by the larger error bars (Figure 5.1B). At 6-hours post injury, the RR remained consistent with baseline for the control and injured groups with a RR of 97 $\pm$ 27% and 111 $\pm$ 35% baseline, respectively. The RR dropped in both treatment groups at 12-hours post injury to 80 $\pm$ 23% of baseline in control and 92 $\pm$ 28% of baseline in the injured group. At 24-hours, the RR had increased in the control group to 117 $\pm$ 23% of baseline. On the other hand, the RR of injured mice was 88 $\pm$ 20% of baseline, comparable to the RR at 12-hours post injury. There were no significant differences between control and injury at any time point, nor compared to baseline. In summary, the results are too variable to draw any conclusions, but the average RR was comparable between control and injury groups.

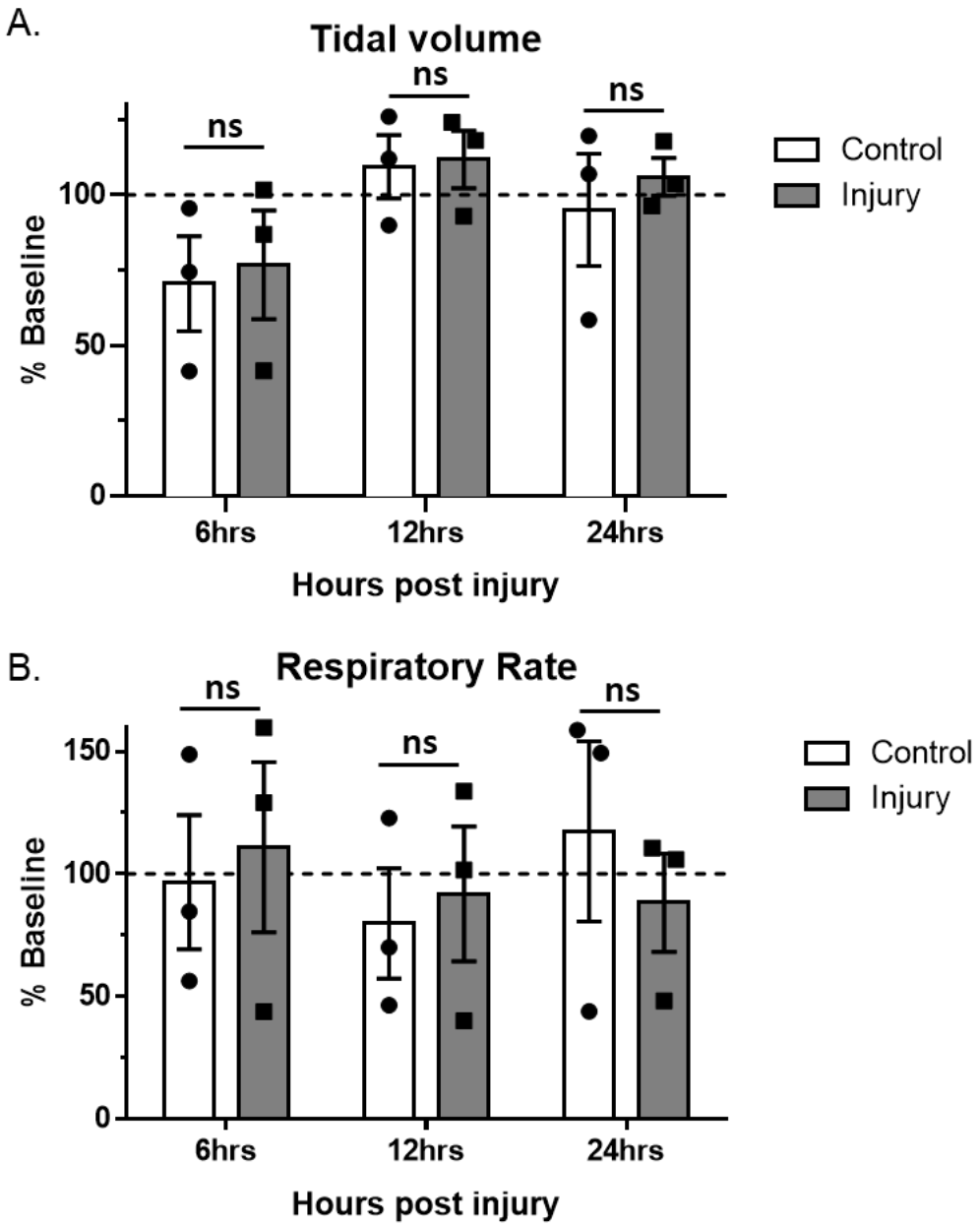

Figure 5.1: Assessment of respiratory function in extended injury model in *GalNAc-T$^{-/-}$-Tg(glial)* mice. A baseline WBP recording was taken prior to *GalNAc-T$^{-/-}$-Tg(glial)* mice receiving an intraperitoneal (IP) injection of 50 mg/kg anti-GM1 mAb followed 16 hours later with 30 µl/g normal human serum (NHS) IP. Control mice received PBS and NHS. Respiratory function was monitored 6, 12 and 24-hours post injury (post NHS injection) and the TV and RR at each time point was assessed and plotted as a percentage of the baseline (broken line). A+B) The TV and RR were comparable between control and injury groups at each time point. There were no significant differences between control and injury at any time point, nor compared to baseline. A repeated measures two-way ANOVA was performed to test for significance between baseline and post injury value. Regular two-way ANOVA was performed to determine significance between treatment groups at each time point. Results represented as the average ± SEM. n=3/treatment.

5.2.2 Anti-GM1 mAb and complement deposition at the distal nerve

Prior to studying the integrity of the axon, the presence of anti-GM1 mAb and complement was assessed at the distal nerve to ensure that the complement pathway had been activated. The distal nerve was defined as the first myelin internode and NoR adjacent to the NMJ. Anti-GM1 mAb deposits were detected at 96 $\pm$ 2% of distal nerves in the injured group in comparison to the control group that had no anti-GM1 mAb deposits detected (Figure 5.2A). Statistics were unable to be performed as it was only an n=2 in the injured group, however there was a clear difference between the control and injured groups. The representative images demonstrate anti-GM1 mAb deposited along the distal internode in injured mice but absent from control mice. Next, the early complement component, C3c, was studied to determine whether the complement pathway had been activated by anti-GM1 mAb. The results in Figure 5.2B demonstrate that C3c deposits were absent from the control group, as expected. On the other hand, C3c deposits were detected at 76 $\pm$ 19% of distal nerves in the injured group which was significantly higher in comparison to control ($p<0.05$). The illustrative images show C3c deposited overlying the distal internode and deposited around the NMJ in the injured group. No complement deposits are present in the control group.

Overall, these results demonstrate that anti-GM1 mAb bound to the glial membrane at the distal nerve, activating the complement pathway.

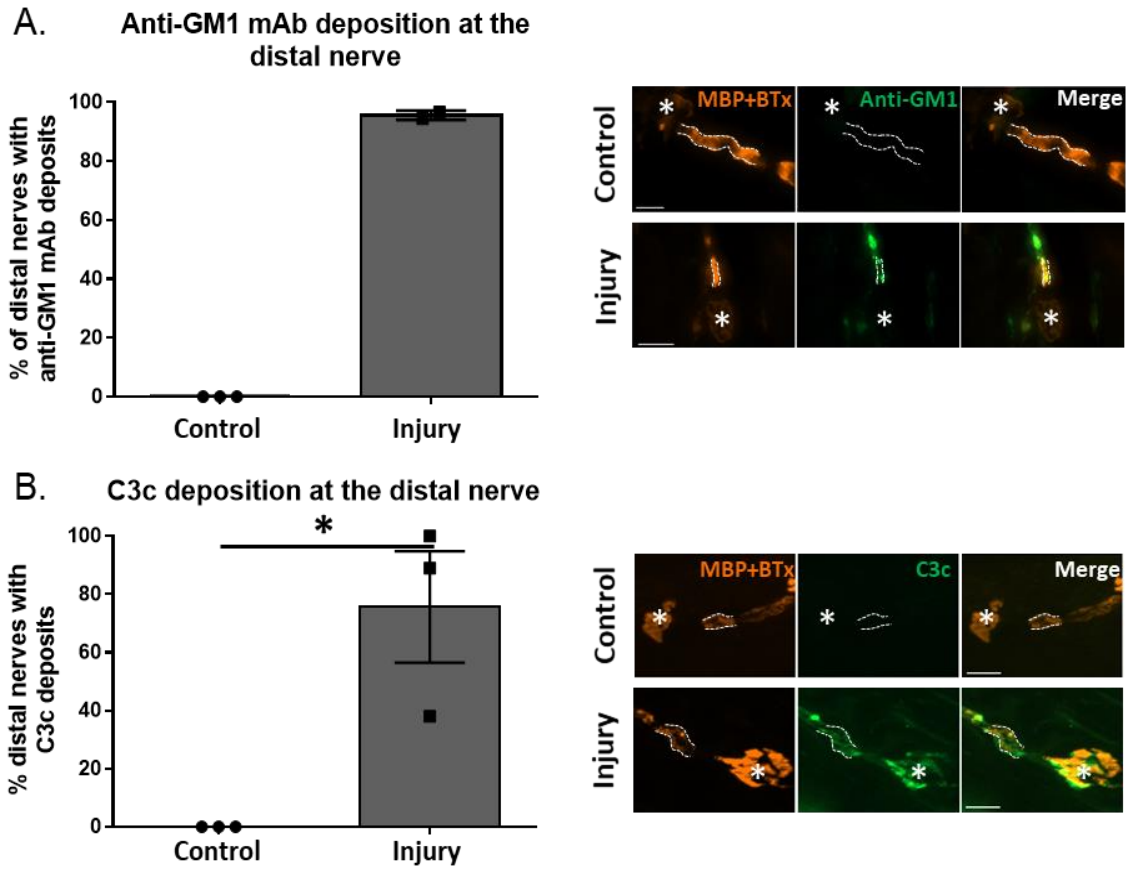

Figure 5.2: Deposition of anti-GM1 mAb and complement at the distal nerve. *GalNAc-T$^{-/-}$-Tg(glial)* mice were injected intraperitoneally (IP) with 50 mg/kg anti-GM1 mAb followed 16 hours later with 30 µl/g normal human serum (NHS) delivered IP. Control mice received PBS and NHS. The diaphragm was harvested 24-hours post NHS delivery and immunofluorescence analysis was performed. A) Anti-GM1 mAb deposition at the distal nerve was studied in fixed diaphragm sections. As expected, no anti-GM1 mAb deposits were present in the control group but anti-GM1 mAb deposits were present at most distal nerves in the injured group. Images demonstrate anti-GM1 mAb (green) deposits along the distal internode (MBP; orange, broken white line) in the injured group but absent from the control group. Bungarotoxin (BTx; orange, white asterisks) was used to identify the neuromuscular junction (NMJ). Results represented as average ± SD. n=3 control; n=2 injury. B) C3c deposition at the distal nerve was studied in fresh diaphragm sections. C3c deposits were present at significantly more distal nerves in the injured group compared to control (*=$p<0.05$). Illustrative images show C3c deposits (green) overlying the distal internode (MBP; orange, white broken line) and surrounding the NMJ (BTx; orange, white asterisks) in the injured group but absent from control. n=3/treatment. Results represented as average ± SEM. Unpaired t-test was performed to test for statistical significance.

5.2.3 Axonal integrity at the distal nerve

I next investigated the integrity of the axonal cytoskeleton by staining for the structural protein, neurofilament. First, occupancy analysis was performed to determine the percentage of nerve terminals, distal internodes, and distal nodal gaps, occupied with neurofilament. The results in Figure 5.3A illustrate that 72 ± 8% of nerve terminals were occupied with neurofilament in the control group. The percentage of nerve terminals occupied with neurofilament was reduced to 42 ± 19 % in injured mice, although this did not differ significantly from control. The percentage of distal internodes with neurofilament staining was comparable between control (99 ± 1%) and injured (87 ± 3%) groups. Neurofilament occupancy at the nodal gap was reduced in injured mice to 21 ± 13% in comparison to 62 ± 12% in control, however this difference was not significant ($p=0.07$). Next, the fluorescent intensity of neurofilament at the nodal gap was assessed and the mean intensity values were plotted in Figure 5.3B. The results show that the mean NFH intensity at the nodal gap was 1127 ± 72 AU in control mice. The mean NFH intensity at the nodal gap was significantly reduced in injured mice to 585 ± 129 AU ($p<0.05$). The illustrative images in Figure 5.3C show neurofilament present overlying the nerve terminal, distal internode, and distal nodal gap in control mice. In injured mice, neurofilament is present overlying the nerve terminal and distal internode but is absent from the distal nodal gap.

In summary, these results indicate that neurofilament appears to be significantly disrupted at the distal nodal gap, 24-hours following injury to the glial membrane; suggesting that there could be secondary damage to the underlying axonal cytoskeleton at the NoR.

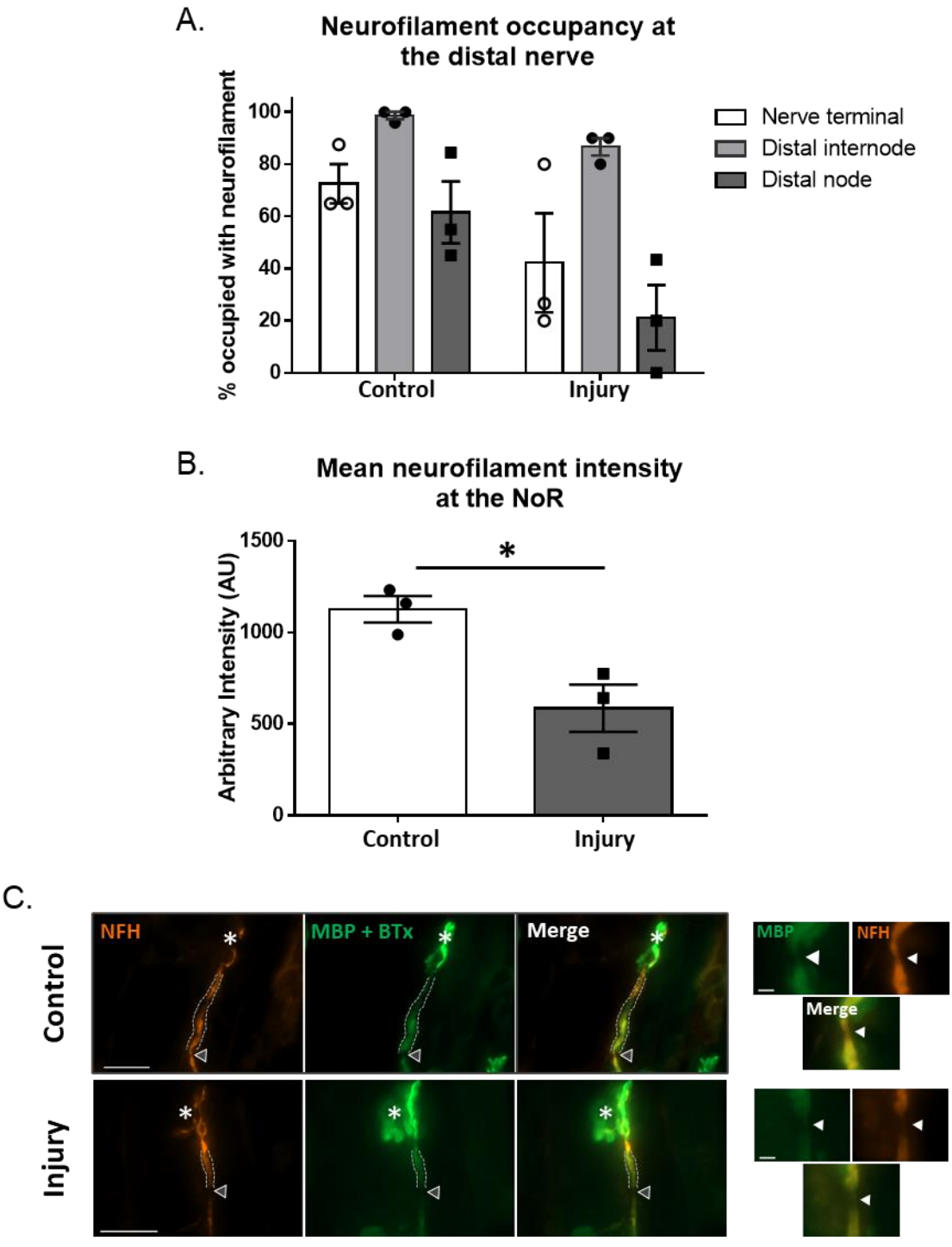
A.
Neurofilament occupancy at the distal nerve
% occupied with neurofilament
100
80
60
40
20
0
Control
Injury
Nerve terminal
Distal internode
Distal node
B.
Mean neurofilament intensity at the NoR
Arbitrary Intensity (AU)
1500
1000
500
0
*
Control
Injury
C.
Control
Injury
NFH
MBP + BTx
Merge
MBP
NFH
Merge

Figure 5.3: Assessment of neurofilament at the distal nerve. (See previous page). *GalNAc-T$^{-/-}$-Tg(glial)* mice received 50 mg/kg anti-GM1 mAb intraperitoneally (IP) followed 16 hours later with an IP injection of 30 µl/g normal human serum (NHS). Control mice received PBS and NHS. Diaphragm was harvested 24-hours post NHS delivery and immunofluorescence analysis was performed on fixed diaphragm sections. Neurofilament heavy (NFH) was studied to determine the integrity of the underlying axonal cytoskeleton at the distal nerve. A) The distal nerve was categorized into the nerve terminal, distal internode, and distal nodal gap and the percentage occupied with NFH was calculated. The percentage of occupied distal internodes was comparable between control and injured groups. There was a reduction in the percentage of occupied nerve terminals and distal nodal gaps in the injured group in comparison to control, but this did not differ significantly. Two-way ANOVA with Bonferroni's multiple comparisons test. B) The intensity of NFH staining overlying the nodal gap was assessed and the mean intensity is plotted for each treatment group. There was a significant reduction in NFH intensity at the distal nodal gap in injured mice in comparison to control mice (*=$p<0.05$). Significance tested by performing an unpaired student's t-test. C) Representative images demonstrate NFH (orange) occupying the nerve terminal (identified by BTx; green, white asterisks), distal internode (identified by MBP; green, outlined with light grey broken line) and distal nodal gap (white outlined arrowhead) in control mice. In injured mice, NFH is occupying the nerve terminal and distal internode but is absent from the distal nodal gap. Scale bar = 20 µm. Images on right hand side show the distal node of Ranvier enlarged (scale bar = 2 µm), clearly demonstrating absent NFH at the nodal gap (white arrowhead). Results represent average $\pm$ SEM. n=3/treatment.

5.2.4 Caspase 3 positivity in perisynaptic Schwann cells

It has previously been demonstrated that AGAb and complement-mediated injury to pSC results in the uptake of ethidium homodimer, indicative of lytic cell death (Halstead et al., 2004). The authors hypothesised that death of the pSC would leave the denuded nerve terminals vulnerable to injury under inflammatory or stress conditions. Following the discovery of reduced neurofilament occupancy at the nerve terminal in injured *GalNAc-T$^{-/-}$-Tg(glial)* mice, I next determined whether targeting pSC with an anti-GM1 mAb resulted in caspase 3-mediated apoptosis. The percentage of cleaved caspase 3 positive pSC (identified by DAPI nuclei overlying the NMJ) was studied to determine whether the pSC were apoptotic following anti-GM1 mAb-mediated injury to the glial membrane. The results in Figure 5.4 demonstrate that 30 $\pm$ 5% of NMJs had caspase 3 positive pSC in the control group. In the injured group, 64 $\pm$ 1% of NMJs had caspase 3 positive pSC, which was significantly higher in comparison to control ($p<0.01$). The illustrative images show caspase 3 deposits overlying DAPI nuclei at the NMJ with anti-GM1 mAb deposits in the injured group. In the control group, one example demonstrates the absence of caspase 3 and anti-GM1 mAb deposits but the second example illustrates a representative image of

positive caspase 3 staining in control mice. The caspase 3 staining does not appear as intense or punctate in control mice in comparison to injured mice, however no intensity analysis was performed and so this cannot be confirmed.

In summary, these results suggest that pSC become apoptotic following anti-GM1 mAb-mediated injury to the glial membrane and confirm that the pSC are injured.

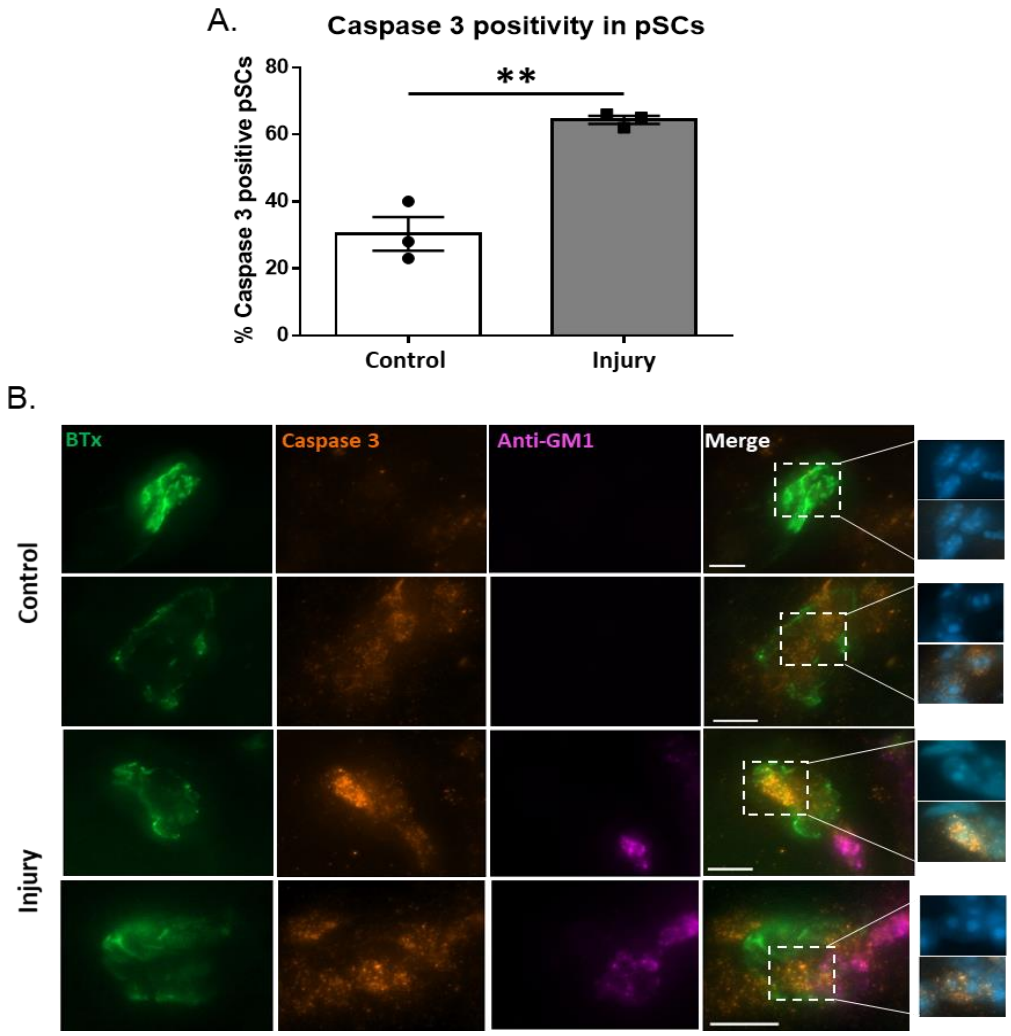

Figure 5.4: Quantification of caspase 3 positive perisynaptic Schwann cells. *GalNAc-T$^{-/-}$-Tg(glial)* mice received 50 mg/kg anti-GM1 mAb intraperitoneally (IP). Sixteen hours later, an IP injection of 30 µl/g normal human serum (NHS) was administered. Control mice received PBS and NHS. The diaphragm was harvested 24-hours post injury and immunofluorescence analysis was performed on fresh frozen diaphragm sections. The presence of caspase 3 positive perisynaptic Schwann cells (pSC; identified by DAPI nuclei overlying the neuromuscular junction (NMJ)) was determined to confirm pSC injury. A) There were significantly more caspase 3 positive pSC in the injured group compared to control (**=p<0.01). B) Representative images demonstrate a positive and negative example in control mice. In the positive example, caspase 3 deposits (orange) are present within cell nuclei (identified by DAPI, blue) at the NMJ. In injured mice, caspase 3 deposits are detected within cell nuclei blue and anti-GM1 mAb (magenta) are detected at the NMJ (identified by BTx; green). Scale bar = 10 µm. Results represented as average ± SEM. Statistical analysis determined by performing an unpaired t-test. n=3/treatment.

5.2.5 Analysis of Nav clusters at the distal nodal gap

Next, the integrity of the axon at the NoR following injury to the glial membrane was investigated. First, the presence of pNav clusters at the nodal gap was assessed. To establish the condition of pNav clusters, the staining was categorized into normal (pNav is present and staining is normal); abnormal (pNav clusters present but staining is punctate or elongated); or absent (pNav is absent), as illustrated in Figure 5.5.

Figure 5.5: Categorization of staining at the distal nodal gap.

The results in Figure 5.6A demonstrate that normal pNav clusters were present at 70 ± 7% of nodal gaps in the control group. The presence of normal pNav clusters was significantly reduced to 23 ± 6% in the injured group ($p<0.001$). There was no significant difference between the presence of abnormal pNav clusters in control (32 ± 7%) and injured (42 ± 6%) groups. The percentage of nodal gaps with absent pNav clusters was significantly higher in the injured group (36 ± 1%) in comparison to control (0 ± 0%; $p<0.01$). The illustrative images in Figure 5.6B show pNav present at the nodal gap of control mice but absent from the nodal gap in injured mice. Complement deposits are present overlying the paranode and myelin internode in the injury group.

These results indicate that axonal integrity is significantly disrupted at the nodal gap, as demonstrated by a loss of pNav clusters, 24-hours after injury to the glial membrane in *GalNAc-T$^{-/-}$-Tg(glial)* mice.

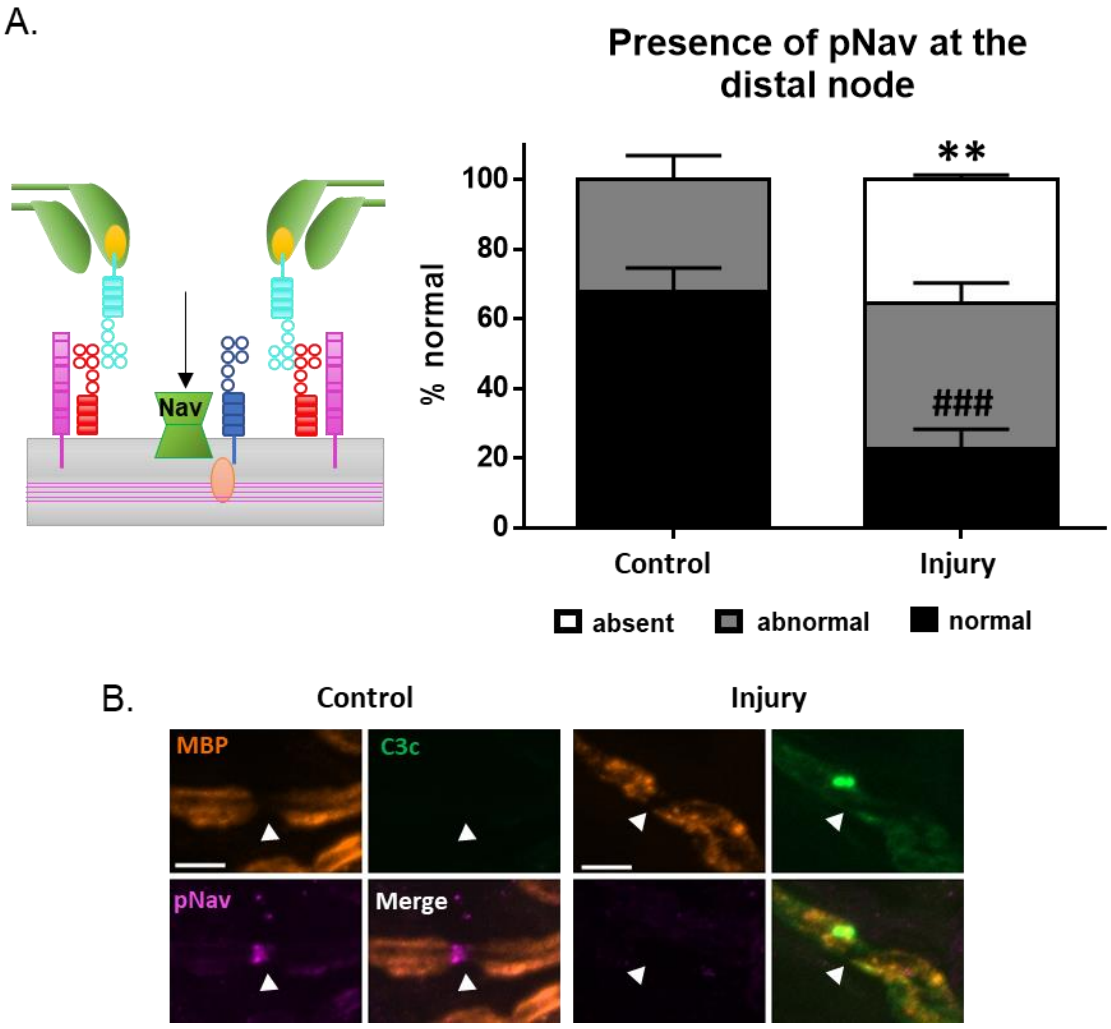

Figure 5.6: Presence of Nav channels at the distal nodal gap. *GalNAc-T$^{-/-}$-Tg(glial)* mice were injected intraperitoneally (IP) with 50 mg/kg anti-GM1 mAb followed 16 hours later with an IP injection of 30 µl/g normal human serum (NHS). Control mice received PBS and NHS. The diaphragm was harvested 24-hours post NHS delivery and immunofluorescence analysis was performed. A) The integrity of pNav clusters at the distal nodal gap (illustrated by the schematic) was assessed in fresh frozen diaphragm sections. The presence of normal appearing pNav clusters was significantly reduced in the injured group compared to control (###=p<0.001). There was no significant difference between the percentage of abnormal pNav clusters in the control and injured groups. The percentage of nodal gaps with absent pNav clusters was significantly increased in the injured group compared to control (**=p<0.01). B) Images demonstrate pNav (magenta) present at the nodal gal (white arrowhead) of control mice. C3c deposits (green) are present overlying the distal internode (MBP; orange) and there is a loss of pNav clusters at the nodal gap. Scale bar = 5 µm. Results represented as average ± SEM. A two-way ANOVA with Tukey's multiple comparisons test was performed to determine statistical significance. * = significant difference between absent pNav. # = significant difference between normal appearing pNav. n=3/treatment.

5.2.6 Assessment of ankyrin-G at the distal nodal gap

Following the discovery that pNav clusters were significantly reduced in the injured group, I next investigated the presence of AnkG, the anchoring protein in the axonal cytoplasm at the nodal gap ((Rasband and Peles, 2020): illustrated by the schematic in Figure 5.7A). The appearance of AnkG was categorized into normal, abnormal or absent, as illustrated previously for pNav analysis (Figure 5.5). The results in Figure 5.7A demonstrate normal appearing AnkG clusters were present at 74 $\pm$ 9% of nodal gaps in the control group. The presence of normal AnkG clusters was significantly reduced to 21 $\pm$ 9% in the injured group ($p<0.01$). The appearance of abnormal AnkG clusters was higher in the injured group (31 $\pm$ 8%) compared to control (17 $\pm$ 6%), although not significantly. Only 9 $\pm$ 4% of nodal gaps had absent AnkG clusters in the control group. The percentage of nodal gaps with absent AnkG staining was significantly higher in the injured group (48 $\pm$ 8%; $p<0.05$). The representative images demonstrate AnkG present at the nodal gap of control mice (Figure 5.7B). Contrastingly, AnkG is absent from the nodal gap in injured mice and complement deposits are present overlying the paranode and myelin internode.

In summary, these results demonstrate that the axonal cytoskeleton at the distal NoR is significantly disrupted following injury to the glial membrane in this extended injury model.

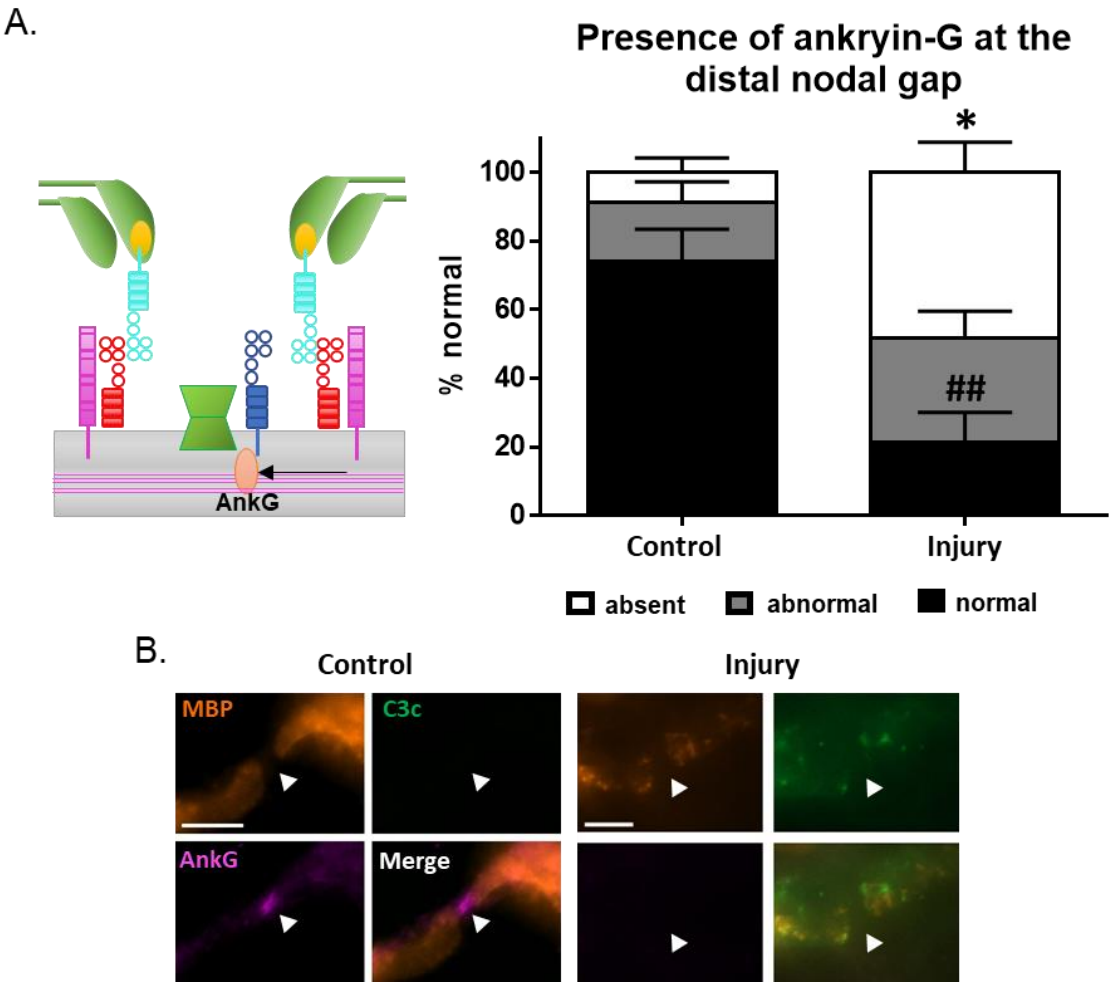

Figure 5.7: Presence of ankyrin-G at the distal nodal gap. *GalNAc-T$^{-/-}$-Tg(glial)* mice were injected intraperitoneally (IP) with 50 mg/kg anti-GM1 mAb followed 16 hours later with 30 µl/g normal human serum (NHS) delivered IP. Control mice received PBS and NHS. Twenty-four hours after NHS delivery, the diaphragm was harvested, and immunofluorescence analysis was performed. A) The integrity of ankyrin-G (AnkG) at the distal nodal gap was assessed in fresh frozen diaphragm sections. The presence of normal appearing AnkG staining was significantly reduced in the injured group compared to control (##=$p<0.01$). There was no significant difference in the appearance of abnormal AnkG staining. AnkG was absent from significantly more distal nodal gaps in the injured group compared to control (*=$p<0.05$). B) Illustrative images demonstrate AnkG (magenta) present at the nodal gap (white arrowhead) in control mice. C3c deposits (green) are present overlying the myelin internode (MBP; orange) in injured mice and there is a loss of AnkG staining. Scale bar = 5 µm. Results represented as average ± SEM. Two-way ANOVA with Tukey's multiple comparisons test was performed to determine statistical significance. n=3/treatment.

5.2.7 Ankyrin-B analysis at the distal paranode

I previously demonstrated that there was significant disruption to AnkB dimers at the distal NoR following complement-mediated injury to the glial membrane at 6-hours (4.2.10.2). AnkB is a known calpain substrate (Boivin et al., 1990), thus it was hypothesised that AnkB was being cleaved following activation of calpain. Therefore, it was anticipated that AnkB dimers would still be absent 24-hours post injury. To investigate this, the presence of AnkB dimers at the distal paranode was assessed (see schematic in Figure 5.9A). The condition of AnkB staining was categorised, as illustrated in Figure 5.8, into normal (dimers were present and staining was normal), abnormal (dimers were present but staining was punctate or nodal gap was elongated), or absent (dimers were absent or only a hemi-dimer was present).

Figure 5.8: Categorization of staining at the distal paranode.

The results in Figure 5.9A demonstrate that 74 ± 2 % of distal paranodes had normal AnkB dimer staining in control mice. The presence of normal AnkB dimer staining was significantly reduced to 11 ± 6% in injured mice in comparison to control ($p<0.001$). There was no significant difference between the percentage of distal paranodes with abnormal AnkB dimer staining in control (17 ± 1%) and injured (11 ± 6%) groups. Only 9 ± 2% of distal paranodes had absent AnkB dimer staining in control mice, however the percentage of absent paranodes was significantly higher in the injured group with 78 ± 11% of distal paranodes having absent AnkB dimer staining ($p<0.001$).

In summary, these results confirm that AnkB dimers are still significantly disrupted 24-hours following injury to the glial membrane.

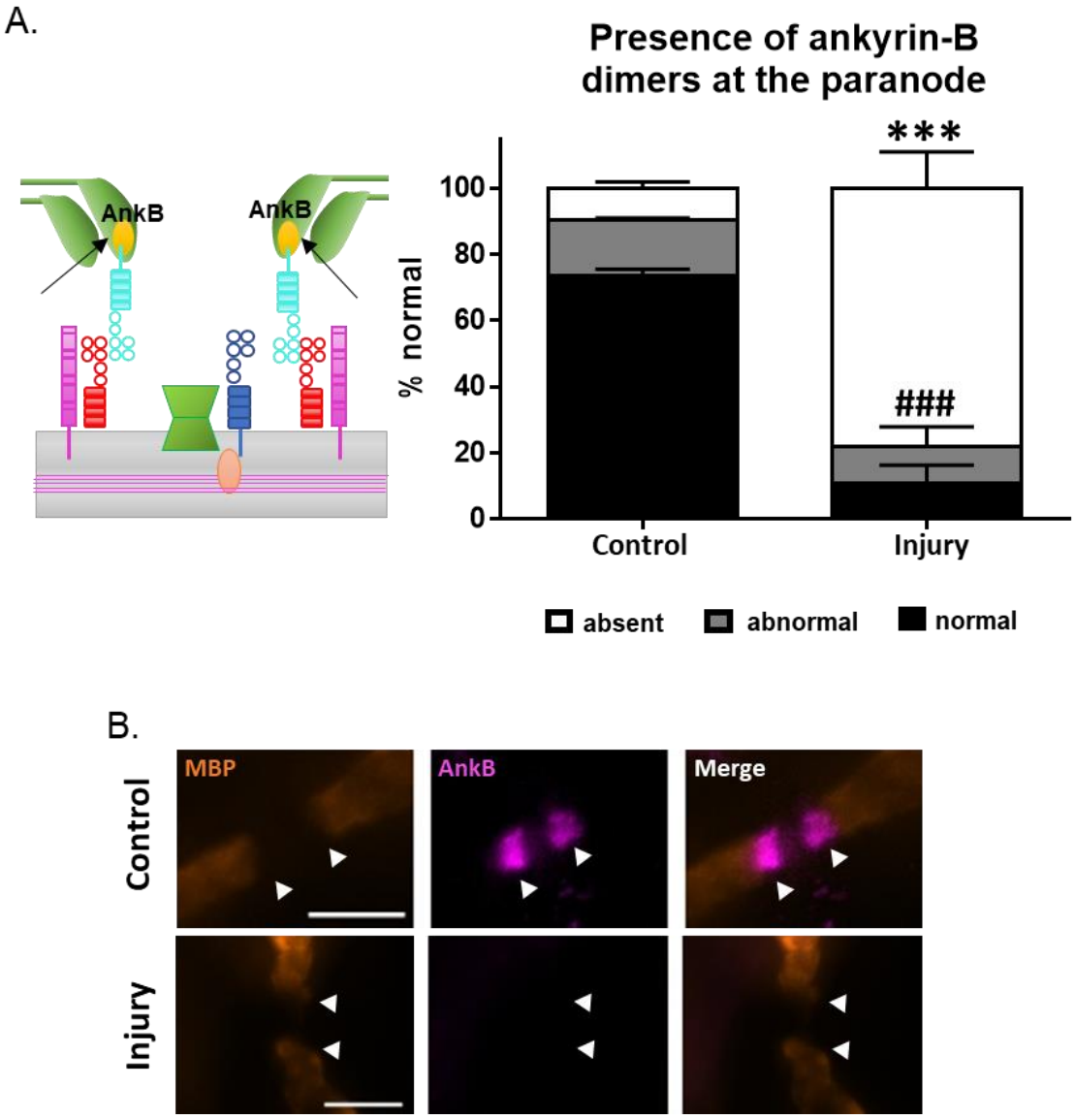

Figure 5.9: Ankyrin-B analysis at the distal paranode. *GalNAc-T$^{-/-}$-Tg(glial)* mice received 50 mg/kg anti-GM1 mAb intraperitoneally (IP). Sixteen hours later, mice were injected IP with 30 µl/g normal human serum (NHS). Control mice received PBS and NHS. The diaphragm was harvested 24-hours post NHS delivery and immunofluorescence analysis was performed on fixed diaphragm sections. A) The presence of ankyrin-B (AnkB) dimers was assessed at the distal paranode. Location of AnkB is illustrated in the schematic. The presence of normal AnkB dimers was significantly reduced in injured mice compared to control (###=p<0.001). There was no significant difference in the percentage of abnormal AnkB dimers. The percentage of distal paranodes with absent AnkB staining was significantly higher in injured mice compared to control (***=p<0.001). B) Illustrative images demonstrate AnkB dimers (magenta) located at the paranode (white arrowheads) in control mice but absent from injured mice. Scale bar = 5 µm. Results represent average ± SEM. Two-way ANOVA with Tukey's multiple comparisons test was performed to determine statistical significance. # = significant difference between paranodes with normal staining; * = significant difference between paranodes with absent staining. n=3/treatment.

5.2.8 Assessment of neurofascin isoforms at the distal NoR

It was not surprising that AnkB dimers in the paranodal cytoplasmic loops were still significantly disrupted 24-hours post injury as they are a known calpain substrate and so are likely cleaved upon calpain activation (Boivin et al., 1990). Complement-mediated injury to the glial membrane resulted in significant loss of NF155 at the paranode in the acute injury model (4.2.10.3); thought to be due to NF155 no longer being tethered to the glial cytoskeleton via AnkB (Chang et al., 2014). It was thus determined whether NF155 dimers become re-localised to the paranode 24-hours post injury. Furthermore, as pan-NFasc binds both NF155 and NF186, the integrity of NF186 at the nodal gap was also assessed to establish whether there was further disruption to this protein in the extended model in comparison to the acute model. The locations of these proteins are illustrated in the schematic in Figure 5.10A. Paranodal pan-NFasc dimers (indicative of NF155) were present at 84 $\pm$ 4% of distal paranodes in control mice; however, the presence of NF155 dimers was significantly reduced to 17 $\pm$ 6% in injured mice ($p<0.001$; Figure 5.10B). Nodal pan-NFasc, representative of NF186, was present at 88 $\pm$ 4% of distal nodal gaps in the control group (Figure 5.10C). On the other hand, the presence of NF186 clusters was significantly reduced to 16 $\pm$ 8% in injured mice ($p<0.01$). Representative images in Figure 5.10D show both nodal and paranodal pan-NFasc present in control mice. Contrastingly, anti-GM1 mAb deposits are present overlying the paranode in injured mice and there is a complete loss of pan-NFasc staining.

These results suggest that NF155 is still mislocalised 24-hours following injury to the glial membrane. Additionally, this data indicates that there is a further reduction in NF186 at the nodal gap, 24-hours after injury to the glial membrane.

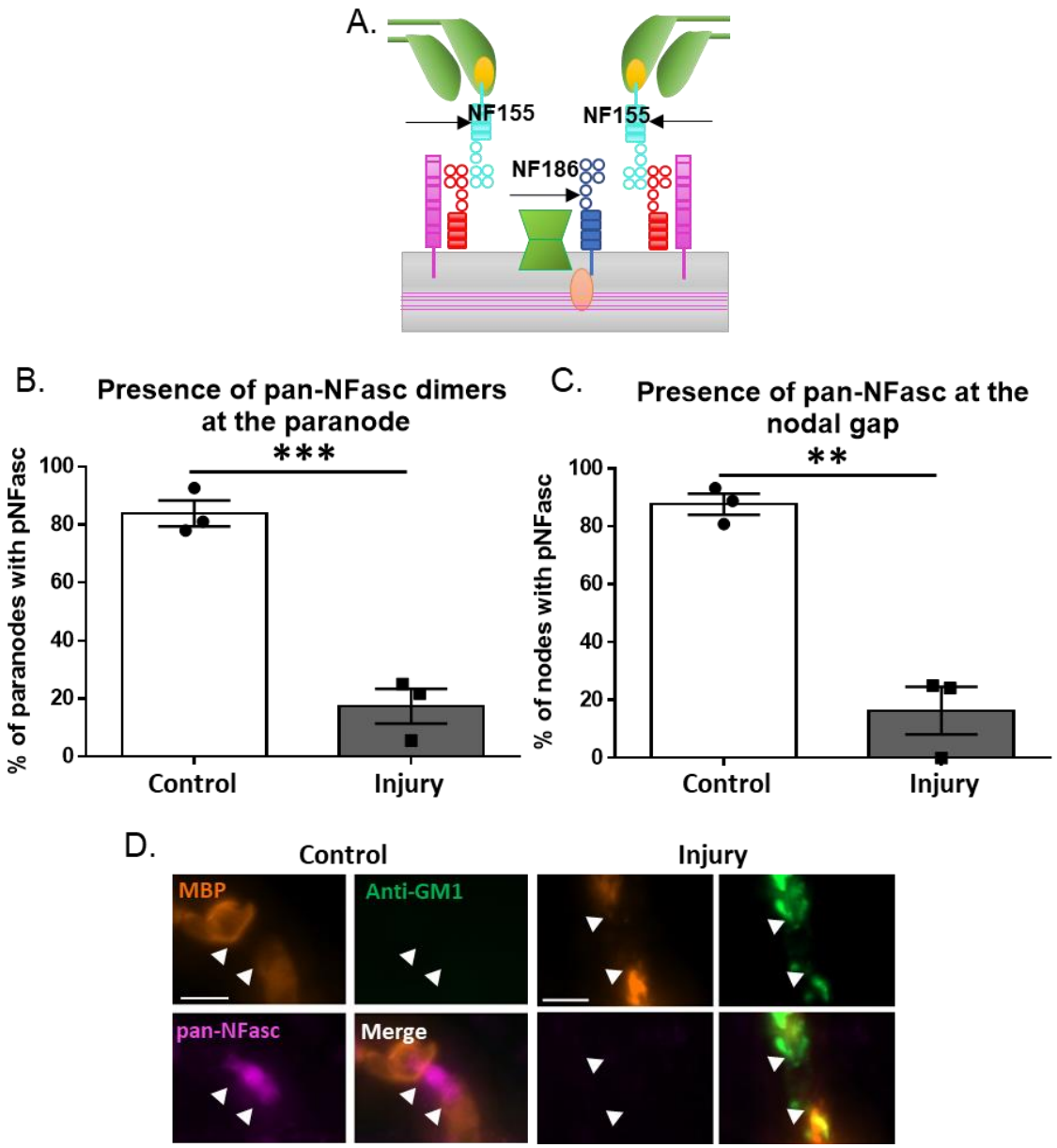

Figure 5.10: Assessment of neurofascin isoforms at the distal NoR. *GalNAc-T$^{-/-}$-Tg(glial)* mice were injected intraperitoneally (IP) with 50 mg/kg anti-GM1 mAb followed 16 hours later with 30 µl/g normal human serum (NHS) delivered IP. Control mice received PBS and NHS. Diaphragm was harvested 24-hours post injury and immunofluorescence analysis was performed on fixed diaphragm sections. A) A pan-NFasc antibody was used to assess the presence of NF186 at the node and NF155 at the paranode, as highlighted by the schematic diagram. B) Paranodal pan-NFasc dimers were significantly reduced in injured mice compared to control (***=$p<0.001$). C) Pan-NFasc was significantly reduced at the nodal gap in injured mice compared to control (**=$p<0.01$). D) Illustrative images demonstrate both nodal and paranodal pan-NFasc (magenta) present at the distal NoR in control mice. Anti-GM1 mAb deposits (green) are present overlying the paranode (white arrowheads) in injured mice and there is a loss of pan-NFasc staining at both the node and paranode. Scale bar = 5 µm. Results represent average $\pm$ SEM. Significance tested by performing unpaired student's t-test. n=3/treatment.

5.2.9 Assessment of Caspr dimers at the distal paranode

Previous results demonstrated significant loss of Caspr dimer staining following injury to the glial membrane in our acute *in vivo* injury model (4.2.10.4). It was hypothesised that injury to the paranodal loops resulted in the mis-localisation of Caspr, located on the axonal membrane at the paranode (see schematic in Figure 5.11A). Therefore, I next determined whether Caspr dimers become re-localised at the paranodes, 24-hours following injury to the glial membrane. Caspr dimers were scored as normal, abnormal, or absent, as previously described for AnkB dimers (Figure 5.8). The results in Figure 5.11A demonstrate that normal Caspr dimers were present at 66 $\pm$ 7% in control mice. Contrastingly, the presence of normal Caspr dimers was significantly reduced to 12 $\pm$ 6% in injured mice. The percentage of paranodes with abnormal Caspr dimer staining was comparable between control (14 $\pm$ 3%) and injured (13 $\pm$ 3%) groups. The percentage of paranodes with absent Caspr dimer staining was significantly higher in the injured group (74 $\pm$ 9%) compared to control (20 $\pm$ 7%). The illustrative images in Figure 5.11B demonstrate Caspr dimers overlying the paranode in control mice but absent from the paranode in injured mice.

Overall, these results suggest that Caspr dimers do not become re-localised to the paranode within 24-hours of injury to the glial membrane.

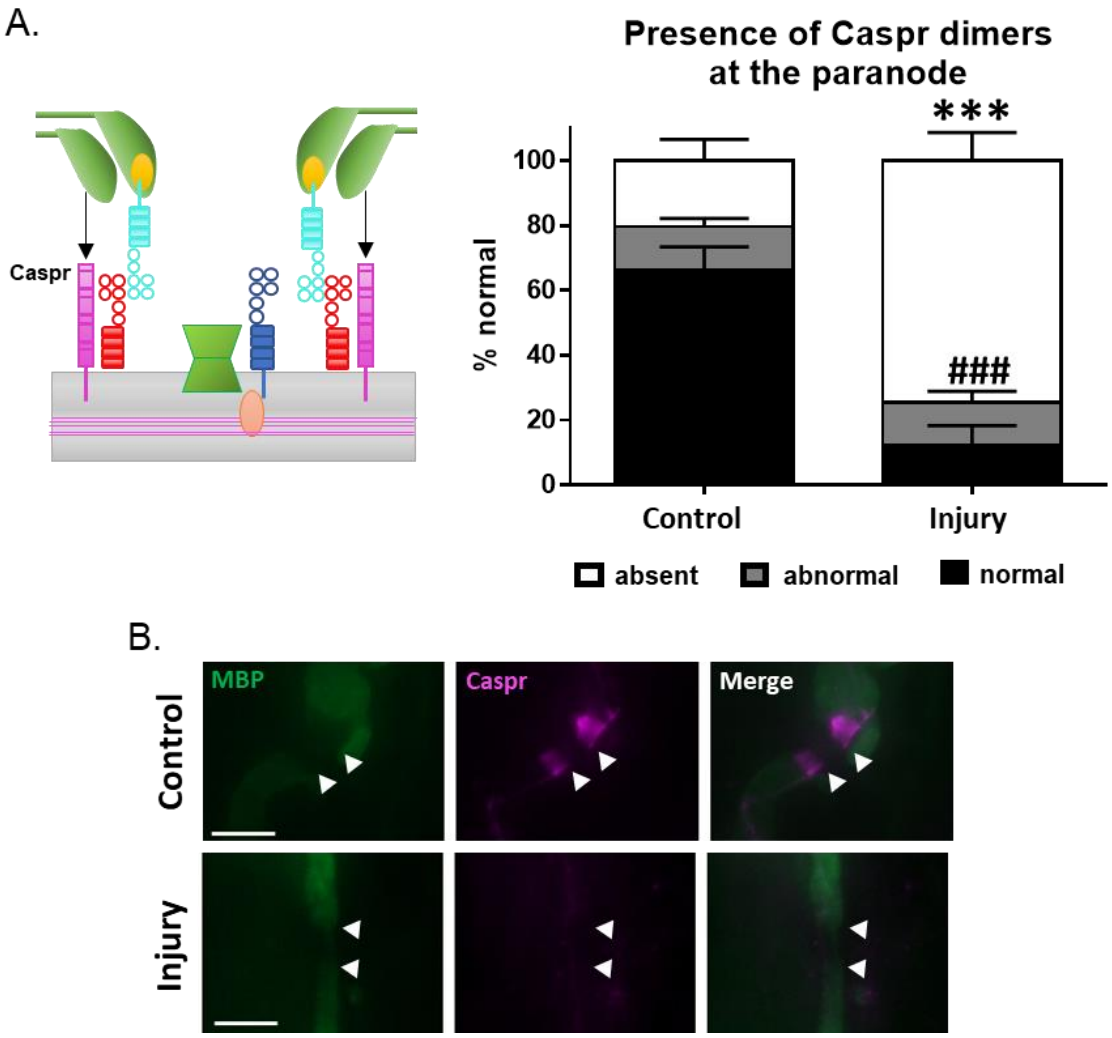

Figure 5.11: Assessment of Caspr dimers at the distal paranode. *GalNAc-T$^{-/-}$-Tg(glial)* mice received 50 mg/kg of anti-GM1 mAb intraperitoneally (IP). Sixteen hours later, mice were injected IP with 30 µl/g normal human serum (NHS). Control mice received NHS only. Diaphragm was harvested 24-hours post injury and immunofluorescence analysis was performed on fixed diaphragm sections. A) The integrity of Caspr dimers at the distal paranode, illustrated by the schematic, was assessed in fixed diaphragm sections. The percentage of normal Caspr dimers was significantly reduced in injured mice compared to control (###=p<0.001). The appearance of abnormal Caspr dimers was comparable between control and injured groups. The percentage of paranodes with absent Caspr dimers was significantly higher in injured mice compared to control (***=p<0.001). B) Representative images demonstrate Caspr dimers (magenta) overlying the paranode (white arrowheads) in control mice. In injured mice, Caspr dimers are absent from the paranode. Nodal gap was identified by a gap in myelin basic protein (MBP; green) staining. Results represent average ± SEM. Two-way ANOVA with Tukey's multiple comparisons test was performed to determine statistical significance. # = significant difference between paranodes with normal staining; * = significant difference between paranodes with absent staining. n=3/treatment.

5.3 Summary

In conclusion, the results of this chapter indicate that axonal integrity is disrupted at the distal NoR following injury to the glial membrane. Axon integrity was not disrupted following acute injury; however, in the temporally extended injury model, the presence of neurofilament at the nodal gap was reduced and there was a significant loss of NF186 and Nav channels located on the axonal membrane at the nodal gap. This was combined with significant disruption to AnkG, which tethers NF186 and Nav to the subaxolemmal cytoskeleton. Overall, these data demonstrate that targeted injury to the glial membrane subsequently leads to secondary injury to the axon at the distal NoR.

5.4 Discussion

Poor prognosis in GBS is associated with axonal degeneration (Martín-Aguilar et al., 2020). The mechanisms resulting in primary injury to the axon are well established in the axonal variant of GBS thanks to many accessible animal models (as outlined previously 1.7.2). However, the downstream events that occur in AIDP leading to secondary axonal degeneration are currently unknown, due to limited availability of animal models representative of the demyelinating variant. The characterisation of the paranodal demyelinating injury model presented here is the first anti-GM1 mAb and complement-mediated mouse model which exclusively targets the glial membrane, independently of the axonal membrane. The results from Chapter 4 demonstrated that axonal integrity was intact at an acute time point of 6-hours post injury. Next, I determined the consequences of injury to the glial membrane on the axon by extending the injury model to 24-hours. In this chapter, I demonstrate injury to the axon at the distal NoR following extended injury to the glial membrane.

The results from the WBP analysis were surprising as there were no significant differences in TV and RR between control and injured groups at any time point, nor compared to baseline. Previous results from the acute injury model demonstrated that the TV of injured *GalNAc-T$^{-/-}$-Tg(glial)* mice was significantly reduced 5-hours post injury to 77 $\pm$ 6% of baseline (4.2.2). The results illustrated in 5.2.1 indicate that the average TV of injured *GalNAc-T$^{-/-}$-Tg(glial)* mice at 6-hours post injury was 77 $\pm$ 18% of baseline, comparable to the acute model. There was increased variation in the results at 6-hours post injury as

demonstrated by the larger SEM. An explanation for this is because one mouse in the injured group had a comparable TV to baseline at each time point; indicating that this mouse may not have been injured. Although, immunofluorescence analysis demonstrated that anti-GM1 mAb and complement deposits were present at over 40% and 50% of NMJs, respectively, confirming the presence of antibody and complement. Thus, it is possible that antibody and complement deposition was not sufficient to cause enough disruption to the distal nerve that would lead to a change in behavioural output. Therefore, the TV of this mouse increased the variation in results for the injured group. Despite this, the TV was comparable with baseline in injured *GalNAc-T$^{-/-}$-Tg(glial)* mice at 12 and 24-hours post injury which is remarkable considering the significant damage to the distal NoR. This could suggest that the safety factor for impulse conduction was not lowered beneath the threshold following injury to the distal paranodes, therefore conduction block did not occur (Uncini and Kuwabara, 2015). Alternatively, evidence from a phrenic nerve injury model in pigs demonstrated that following unilateral and/or bilateral diaphragm paralysis, the nondiaphragmatic respiratory muscles can compensate for diaphragmatic paralysis (LoMauro et al., 2021). Therefore, it is possible that the intercostal and abdominal muscles maintain respiratory function following injury to the diaphragm in this injury model. Additionally, the TV of control and injured mice was comparable at each time point. At 6-hours post injury, one of the control mice had a reduced TV of 42% of baseline which then recovered to 112 and 120% at 12 and 24-hours, respectively. This initial reduction in TV could have been caused by the injection of NHS into the peritoneal cavity; however, I have demonstrated previously that NHS injections have no impact on respiratory function in the acute injury model and so this is unlikely. The control mouse with the lowest TV at 12-hours post injury had the highest baseline value of 0.30 ml in comparison to 0.20 ml and 0.17 ml for the other two control mice (Data not shown). The TV reduced to 0.22, 0.27 and 0.17 ml at 6, 12, and 24-hours post injury, respectively. The normal resting TV of a mouse is 0.15 ml (Guyton, 1947); therefore, the TV of this mouse did not fall below the normal resting TV at any time point. Furthermore, this mouse was the heaviest in the experimental group and Guyton (1947) also demonstrated that heavier mice have larger TVs; thus, providing an explanation for the higher values. There was a large variation in RR results which could suggest that mice were not habituated or settled efficiently prior to recording. Evidence suggests that RR is positively correlated with increased motor activity in rodents (Kabir et al., 2010).

Additionally, there is evidence to show that *GalNAc-T*$^{-/-}$ mice are hyperactive compared to wild type mice (Pan et al., 2005). Therefore, providing an explanation for the increased RR. There was also large variation in the RR data from the acute injury model, further supporting that TV is a more accurate output of respiratory function in this model. Taken together, the results from the respiratory function analysis were very variable and a conclusion could not be made; thus, it would be worth repeating the experiment addressing the issues described above.

Animal models have demonstrated that ablation or injury to pSC does not acutely affect the function or morphology of the nerve terminal in frogs (Reddy et al., 2003) or mice (Halstead et al., 2005). Therefore, suggesting that pSC injury does not lead to axonal injury. It was demonstrated here that anti-GM1 attack to Schwann cells resulted in the death of pSC at the nerve terminal, as indicated by the presence of caspase 3 positive cells. Thus, it was surprising to see that neurofilament occupancy at the nerve terminal was reduced in injured mice in comparison to control, although not significantly. As there is extensive structural damage to the paranodal loops following injury to the glial membrane, the distal NoR will be extremely vulnerable to secondary injury and so it is not surprising to see a loss of neurofilament at the nodal gap (the possible mechanisms involved are discussed below). Transection of the nerve could cause Wallerian degeneration to occur (Llobet Rosell and Neukomm, 2019), inducing degeneration at the terminal, providing a possible explanation for the reduction in NFH occupancy at the NMJ.

Previous studies have established that complement-mediated injury in AGAb dependent injury models causes the activation of the protease calpain, leading to cleavage of cytoskeletal and structural proteins at the NoR ((McGonigal et al., 2010)). In chapter 4, it was determined that there was significant disruption to the axo-glial adhesion molecules at the distal paranode following injury to the glial membrane. Here, I demonstrate that AnkB remains significantly disturbed 24-hours post injury. This was expected as AnkB is a known calpain substrate and so is likely cleaved by calpain (Boivin et al., 1990), activated following the entry of calcium through MAC pores on the glial membrane. It was unknown what would happen to NF155 (glial membrane) and Caspr (axonal membrane) in the extended model. It was found that the presence of these axo-glial adhesion molecules remains reduced from the axonal and glial membrane 24-hours post injury. NF155 and Caspr are not known calpain substrates and so it is unlikely that these are

being cleaved, although the possibility cannot be ruled out. AnkB functions to stabilise the axo-glial junction at the paranode by tethering NF155 to the underlying cytoskeleton (Chang et al., 2014). Therefore, these results strongly suggest that cleavage of AnkB from the glial cytoskeleton causes mis-localisation of both NF155 and Caspr from the paranode. Pillai et al. (2009) demonstrated that genetic ablation of NF155 subsequently results in the disorganisation of Caspr and contactin at the paranode. The indirect mislocalisation of Caspr due to AnkB cleavage in our model, emphasises the importance of NF155 presence to maintain paranodal junction organisation. Another possible explanation could be a result of disruption to the antibody binding epitopes and so, although the protein may still be partially present, the antibody is no longer able to detect the antigen.

As previously mentioned, the mechanisms of secondary injury to the axon are largely unknown. It is thought that secondary axonal degeneration may occur due to Wallerian degeneration, impaired axonal transport, metabolic dysregulation, mitochondrial damage, and/or inflammatory mediated damage, although other mechanisms are also hypothesised to be involved. Herein, I propose that calpain-mediated destruction is involved in the pathogenesis of secondary axonal degeneration (outlined in Figure 5.12). I hypothesise that destruction of the axo-glial adhesion molecules at the paranodes results in the formation of mechanopores in the axonal membrane. Models of diffuse axonal injury (a model of traumatic brain injury) have demonstrated calcium influx through mechanically induced pores in the axonal membrane, leading to axonal degeneration (Kilinc et al., 2008, Kilinc et al., 2009). Mechanopores are transient membrane pores that occur due to mechanical deformation. Thus, it is possible that disruption and mis-localisation of contactin and Caspr on the axonal membrane at the paranode, and detachment of the paranodal loops, generates mechanopores in the membrane resulting in calcium influx and calpain activation. The axonal cytoskeletal protein, AnkG, at the nodal gap is a known calpain substrate (Boivin et al., 1990) as are Nav channels on the axonal membrane (von Reyn et al., 2009); explaining the significant loss of these proteins at the nodal gap. The reduction in NF186 could be a result of mislocalisation following the cleavage of AnkG and Nav. However, NF186 was disrupted following acute injury to the glial membrane, without loss of Nav, as described in chapter 4. It was hypothesised that this was a consequence of disruption to the CAM at the paranode, as it has been demonstrated that the paranodal junction functions as a barrier to prevent lateral

diffusion of nodal proteins (Rosenbluth, 2009). A study performed by Taylor et al. (2017) and colleagues supports this hypothesis, as they demonstrated that when both NF186 and NF155 expression were simultaneously depleted postnatally by tamoxifen, NF155 was depleted first which accelerated the turnover of NF186. Hence, highlighting the importance of paranodal neurofascin in maintaining the stability of the nodal complex. As explained previously, it could be possible that the binding epitope which the pan-neurofascin antibody targets has been altered and therefore, the antibody is unable to detect the antigen.

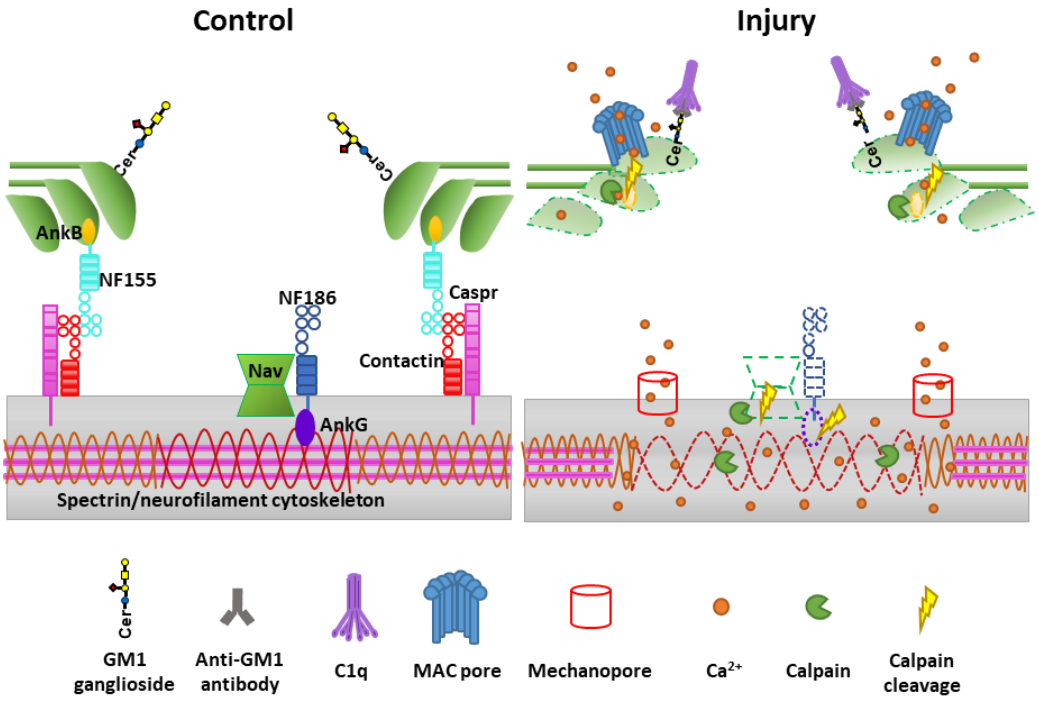

Figure 5.12: Hypothesised mechanism of secondary axonal degeneration.

In conclusion, the results of this chapter demonstrate that exclusive injury to the glial membrane with an anti-GM1 mAb and complement *in vivo*, causes significant impairment of the axo-glial adhesion molecules at the distal paranode, culminating in secondary injury to the axon at the distal NoR. This evidence confirms for the first time that exclusive injury to the glial membrane in a mouse model can induce secondary axonal degeneration. The extended paranodal demyelinating injury model described here will be extremely valuable to study the downstream pathways involved in secondary axonal degeneration; differentiating them from the pathways which induce primary axonal degeneration. Understanding the mechanisms of secondary axonal degeneration is critical for developing targeted therapeutics which will improve the long-term prognosis of GBS.

6 Effects of complement inhibition in models of axonal and paranodal demyelinating peripheral neuropathies

6.1 Introduction

The involvement of the complement pathway in GBS pathogenesis has been demonstrated in both patient autopsies and animal models of GBS (Hafer-Macko et al., 1996a, Hafer-Macko et al., 1996b, Willison et al., 2008). It has been established from animal models that AGAb and complement-mediated injury results in the formation of MAC pores in the membrane (Halstead et al., 2005, Halstead et al., 2004, Halstead et al., 2008). The formation of MAC results in the uncontrolled influx of ions and water into the cell, resulting in swelling and cell lysis. The influx of calcium ions activates the calcium-dependent protease, calpain, leading to cleavage of cytoskeletal structural proteins such as neurofilament, actin and ankyrin (Boivin et al., 1990, Kamakura et al., 1983, Ma et al., 2013, McGonigal et al., 2010, O'Hanlon et al., 2003). Additionally, anaphylatoxins (C3a and C5a) that are produced during complement activation are pro-inflammatory peptides that can cause additional damage, for example through the recruitment of macrophages (Sarma and Ward, 2011). Due to the pathogenic role of complement in GBS, the complement cascade has become of significant interest as a therapeutic target over recent years. Complement inhibition at both the C5 and C1q steps of the classical pathway has been demonstrated to provide effective protection from injury in *in vivo* AGAb-mediated mouse models representative of MFS and the axonal variant of GBS (Halstead et al., 2008, McGonigal et al., 2016). Following the success of these complement inhibitors in animal models, they have now progressed on to clinical trials, some of which are currently ongoing (Davidson et al., 2017, Misawa et al., 2018, Misawa and Suichi, 2020). Due to the limited availability of animal models representative of the demyelinating variant of GBS, it is unknown whether complement inhibition would be an effective therapeutic for patients with AIDP. Following the successful characterization of the anti-GM1 mAb-mediated paranodal demyelinating injury model in *GalNAc-T*$^{-/-}$*-Tg(glial)* mice representative of AIDP, I next determined whether complement inhibition would offer protection to the axo-glial junction at the paranode, to establish the relevance of complement inhibition as a therapeutic for AIDP.

The aim of this chapter was thus to study the effects of inhibiting human C2, an early complement product in the classical pathway, provided under a research agreement in collaboration with Argenx. In summary, the classical complement pathway is activated by complement fixing antibodies binding to the C1q complex. Once activated, C1r cleaves the C1s subunit which activates and cleaves both C4 and C2 into C4a and C4b, and C2a and C2b, respectively. C2a and C4b then form a complex referred to as C3 convertase which is responsible for cleaving C3 (Sarma and Ward, 2011). The anti-C2 humanised antibody that was used (ARGX-117), referred to throughout as C2 inhibitor, binds to the S2 domain of C2, preventing interaction of C2a with C4b and therefore, cleavage of C3 (Van de Walle et al., 2020) (illustrated in Figure 6.1). Blocking C2 will inhibit progression through C3, eliminating production of harmful anaphylatoxins C3a and C5a, and preventing the formation of MAC pores. The effects of human C2 complement inhibition was first evaluated in our established axonal *ex vivo* injury model in *GalNAc-T*$^{-/-}$*-Tg(neuronal)* mice, to determine the efficacy of the C2 inhibitor. Then, it was investigated whether human C2 complement inhibition had any therapeutic effects in our anti-GM1 mAb-mediated paranodal demyelinating *ex vivo* and *in vivo* injury models in *GalNAc-T*$^{-/-}$*-Tg(glial)* mice.

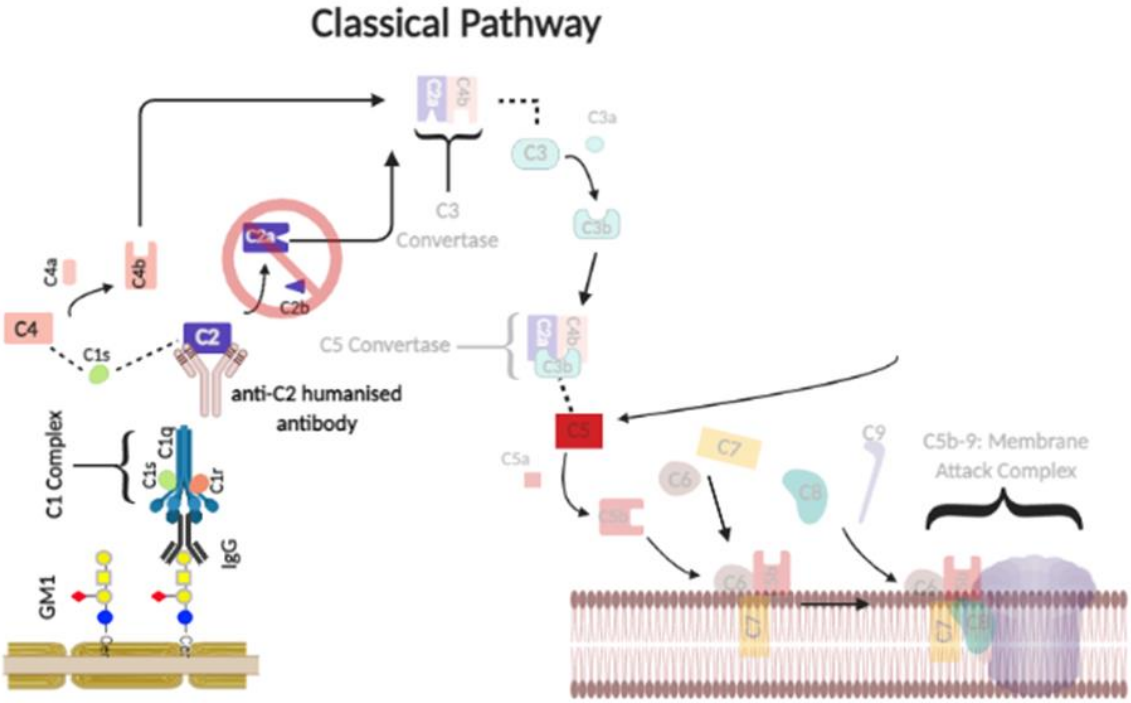

Figure 6.1: Inhibition of C2 blocks progression of classical complement pathway. Created using BioRender.com.

6.2 Results

6.2.1 Effects of C2 inhibition in an *in-vitro* assay

An *in vitro* complement assay was performed on *GalNAc-T$^{-/-}$-Tg(neuronal)* diaphragm sections to determine the concentration of C2 inhibitor required to inhibit progression of the complement pathway. This was performed in triplicate for each treatment group at each concentration. The exception was that there was only an n=1 for 25 μg/ml C2 inhibitor and therefore statistics could not be performed for this concentration. The deposition of anti-GM1 mAb and the early complement component, C3c, overlying the NMJ were assessed indirectly by fluorescent intensity. Anti-GM1 mAb overlying the NMJ decreased from 22.3 $\pm$ 1.5 to 15.5 $\pm$ 1.8 AU as the concentration of the isotype control increased; only differing significantly to the positive control at 50 μg/ml ($p<0.05$; Figure 6.2A). The average anti-GM1 mAb intensity for the C2 inhibitor ranged between 17.6 $\pm$ 0.6 – 23.5 $\pm$ 2.8 AU, which was comparable at all concentrations to the positive control anti-GM1 mAb intensity of 26.2 $\pm$ 1.3 AU. The anti-GM1 mAb intensity was significantly higher to the negative control intensity at all concentrations in both the isotype control and C2 inhibitor groups ($p<0.001$). C3c intensity at the NMJ followed the same trend as the anti-GM1 mAb intensities in the isotype control group (Figure 6.2B). The C3c intensity decreased from 13.7 $\pm$ 1.6 to 8.3 $\pm$ 2.4 AU as the concentration of the isotype control increased; differing significantly to the negative control at all concentrations ($p<0.05$ at 25 and 50 μg/ml; $p<0.01$ at 5 μg/ml; $p<0.001$ at 2.5 and 10 μg/ml). There were no significant differences between the positive control intensity and the intensity of C3c in the isotype control group at any concentration, except 50 μg/ml ($p<0.05$). In contrast, the C3c intensity in the C2 inhibitor group was significantly lower than the positive control intensity at all concentrations ($p<0.001$) but was comparable to the C3c intensity of the negative control. Additionally, the C3c intensity in the C2 inhibitor group was significantly lower compared to the isotype control group at each respective concentration ($p<0.05$ at 50 μg/ml; $p<0.01$ at 5 μg/ml; $p<0.001$ at 2.5 and 10 μg/ml).

The illustrative images in Figure 6.3 demonstrate anti-GM1 mAb and C3c deposits overlying the NMJ in the positive control, whereas there are no deposits found in the negative control. In the isotype control group, anti-GM1 mAb and C3c are detected at the NMJ at all concentrations. On the other hand, although anti-GM1 mAb is present

overlying the NMJ of the C2 inhibitor group, C3c deposits are absent at every concentration.

Overall, the results from the topical complement assay suggested that the C2 inhibitor was highly efficacious at concentrations ranging between 2.5 and 50 µg/ml.

Optimisation of the *in vitro* assay was challenging due to low concentrations of NHS used for the assay, and thus low level of activated complement products. Therefore, a preliminary *ex vivo* experiment was performed to determine the concentration of inhibitor required to block C2 in our *ex vivo* injury model. The results demonstrated that 100 or 200 µg/ml of C2 inhibitor was required to block the complement pathway when targeting the nerve terminal and NoR, respectively; these results are shown in Appendix 8.4 and 8.5.

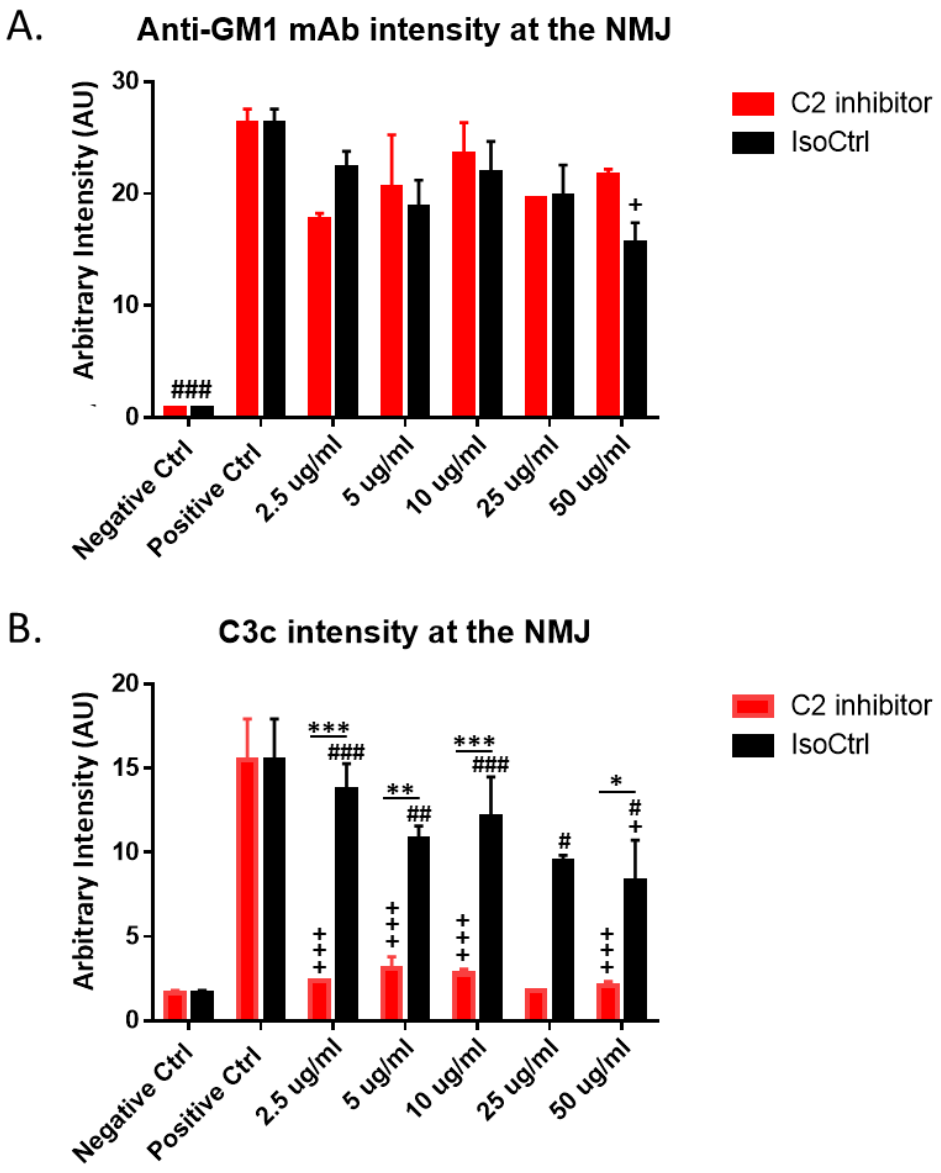

Figure 6.2: *In vitro* complement inhibition assay. Diaphragm sections from *GalNAc-T*$^{-/-}$-*Tg(neuronal)* mice were incubated in 10 µg/ml anti-GM1 mAb, before the relevant concentration of C2 inhibitor or isotype control (isoctrl) was added to the sections along with 4% normal human serum (NHS). Negative control was incubated in Ringer's solution only; positive control was incubated in anti-GM1 mAb and 4% NHS. The intensity of anti-GM1 mAb and C3c overlying the neuromuscular junction (NMJ) was determined. A) The intensity of anti-GM1 mAb at the NMJ was not significantly different from the positive control across all groups, except for sections treated with 50 µg/ml of isoctrl which was significantly reduced compared to the positive control. B) The intensity of C3c was significantly lower at 2.5, 5, 10, and 50 µg/ml of C2 inhibitor compared to the respective concentrations of isoctrl and compared to the positive control (*=p<0.05; **=p<0.01; ***/+++=p<0.001). C3c intensity of the isoctrl differed significantly to the negative control at each concentration (#=p<0.05; ##=p<0.01; ###=p<0.001). n=1 25 µg/ml C2 inhibitor; n=4 for all other concentrations and treatment groups. Two-way ANOVA performed with Tukey's multiple comparisons test. *=significant difference between C2 inhibitor and isoctrl; +=significant difference compared to positive control; #=significant difference compared to negative control.

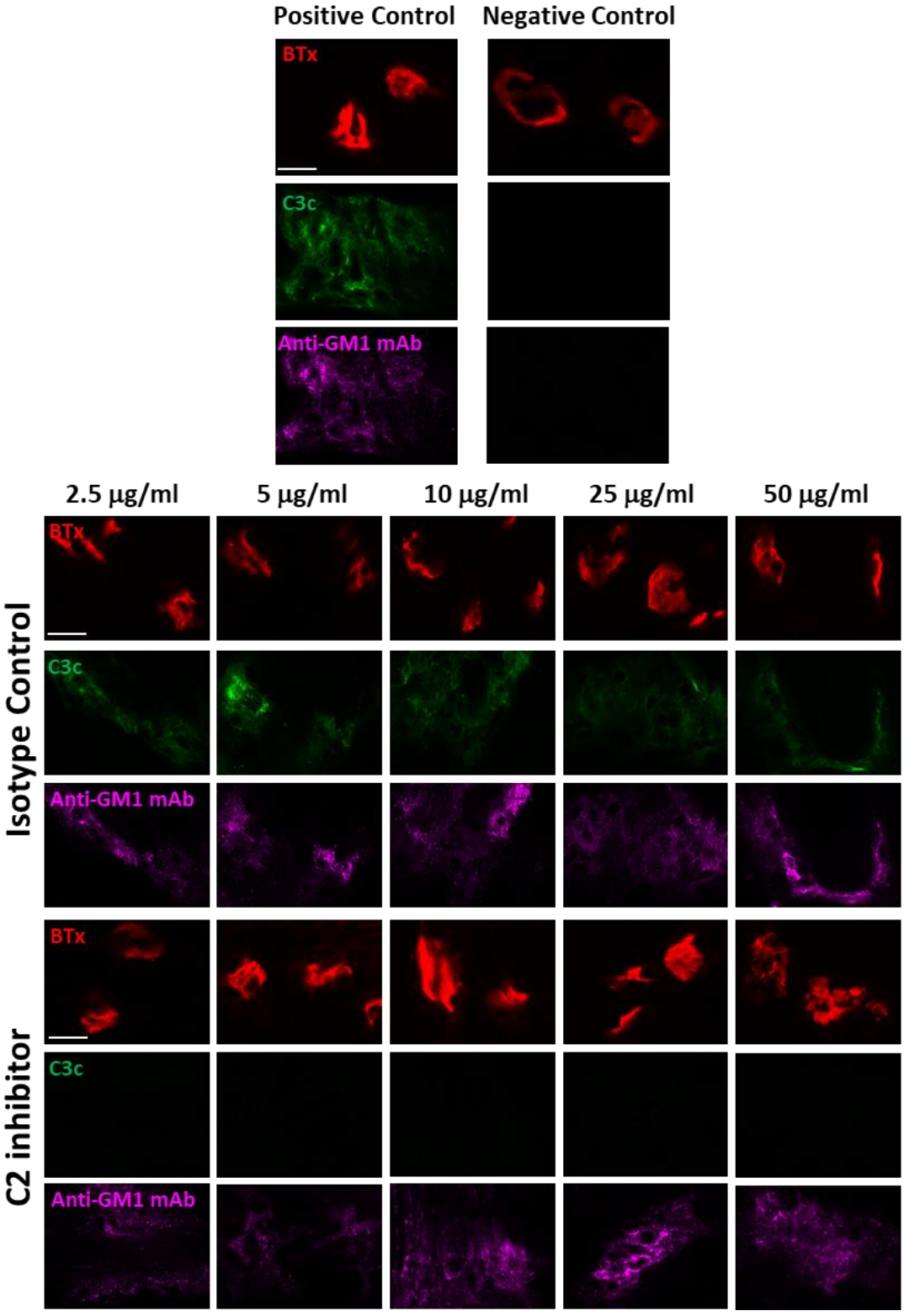
Positive Control
Negative Control
BTx
C3c
Anti-GM1 mAb
2.5 µg/ml
5 µg/ml
10 µg/ml
25 µg/ml
50 µg/ml
Isotype Control
C2 inhibitor

Figure 6.3: Illustrative images of the *in vitro* complement inhibition assay. (See previous page). Diaphragm sections from *GalNAc-T$^{-/-}$-Tg(neuronal)* mice were incubated in 10 µg/ml anti-GM1 mAb, before the relevant concentration of C2 inhibitor or isotype control was added to the sections along with 4% normal human serum (NHS). The negative control was incubated in Ringer's solution only; positive control was incubated in anti-GM1 mAb and 4% NHS. Immunostaining was performed and the fluorescent intensity of anti-GM1 mAb and the early complement component, C3c overlying the neuromuscular junction (NMJ) were determined. Representative images showing anti-GM1 mAb (magenta) and C3c (green) deposits overlying the NMJ, identified by bungarotoxin (BTx, red), in the positive control and at each concentration of the isotype control. C3c deposits were absent at every concentration of C2 inhibitor and from the negative control. Scale bar = 20 µm.

6.2.2 Effects of C2 inhibition in an *ex vivo* axonal injury model

6.2.2.1 Deposition of anti-GM1 antibody and C1q at the distal nerve

First, the effects of C2 inhibition were assessed in our anti-GM1 mAb-mediated axonal *ex vivo* injury model in *GalNAc-T$^{-/-}$-Tg(neuronal)* mice. The presence of anti-GM1 mAb and C1q deposits at the distal nerve (defined as the NMJ, first myelin internode and NoR adjacent to the NMJ) were evaluated to confirm that AGAb had initially activated the complement pathway in the isotype control and C2 inhibitor groups prior to C2 blockade in the latter group. Figure 6.4A demonstrates that there was no significant difference between the percentage of distal nerves with anti-GM1 mAb deposits in the isotype control (100 $\pm$ 0%) and C2 inhibitor groups (96 $\pm$ 2%). The presence of anti-GM1 mAb deposits was significantly lower in the NHS only group compared to all other treatment groups, as no anti-GM1 antibody deposits were found ($p<0.001$). Likewise, 98 $\pm$ 1% and 69 $\pm$ 14% of distal nerves had C1q deposits in the isotype control and C2 inhibitor groups, respectively (Figure 6.4B). Although there was a difference between both groups, this was not significant. The NHS only group had significantly less C1 deposits than all other groups ($p<0.01$ compared to C2 inhibitor; $p<0.001$ compared to isotype control). Illustrative images in Figure 6.4C show anti-GM1 mAb and C1q deposits overlying the NMJ and distal NoR in the isotype control group and the C2 inhibitor group, but absent from the NHS only group. In summary, these results confirm that the complement pathway was activated, indicated by the presence of C1q, by anti-GM1 mAb in both the isotype control and C2 inhibitor groups, despite the presence of the inhibitor in the latter.

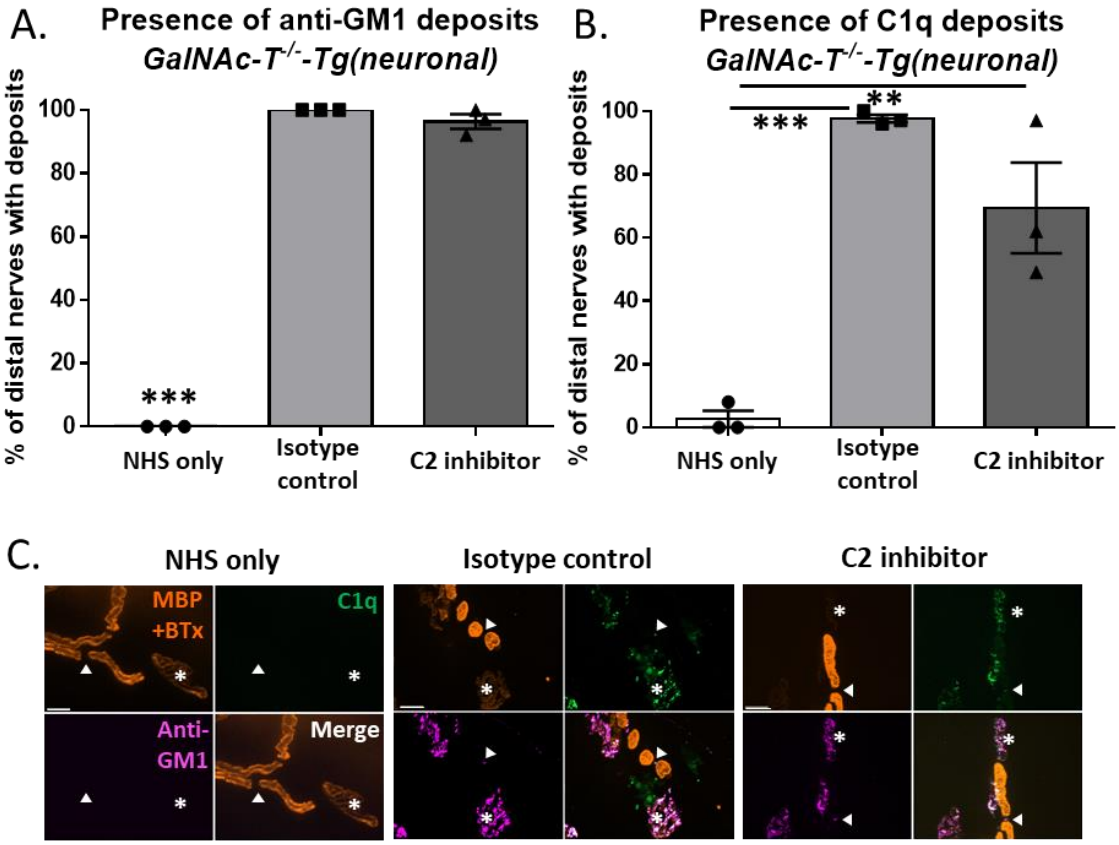

Figure 6.4: Deposition of anti-GM1 mAb and C1q at the distal nerve in *GalNAc-T$^{-/-}$-Tg(neuronal)* mice. Acute *ex vivo* injury performed on triangularis sterni (TS) muscle from *GalNAc-T$^{-/-}$-Tg(neuronal)* mice. TS was incubated in 200 µg/ml C2 inhibitor or isotype control, 40% normal human serum (NHS) and 100 µg/ml anti-GM1 mAb for 4 hours at 32℃. NHS only group was incubated in 40% NHS and Ringer's. Presence of anti-GM1 mAb and C1q deposits was assessed at the distal nerve to confirm activation of the complement pathway. A) The presence of anti-GM1 mAb deposits in the isotype control group and C2 inhibitor group was significantly higher compared to the NHS only group (***=p<0.001). There was no significant difference between the isotype control and C2 inhibitor groups. B) C1q deposits were present at significantly more distal nerves in the isotype control and C2 inhibitor groups compared to the NHS only group (**=p<0.01; ***=p<0.001). There was no significant difference between the isotype control and C2 inhibitor groups. C) Illustrative images show examples of C1q (green) deposits and anti-GM1 mAb (magenta) deposits overlying the neuromuscular junction (identified by bungarotoxin; white asterisks), and at the nodal gap (white arrowheads) in the isotype control and C2 inhibitor groups. Anti-GM1 mAb and C1q deposits are absent from the NHS only group. Scale bar = 10 µm. To test for statistical significance, a one-way ANOVA with Tukey's multiple comparisons test was performed. n=3/treatment.

6.2.2.2 Assessment of axonal integrity at the nerve terminal

The neuroprotective effect of complement inhibition was investigated in an axonal *ex vivo* injury model in *GalNAc-T$^{-/-}$-Tg(neuronal)* mice by first assessing the integrity of the axon at the NMJ. The axonal structural protein, NFH, was used as a marker of axonal integrity. C2 inhibition was confirmed by staining for the early complement component, C3c, as this is present downstream of C2 in the complement pathway (Figure 6.5A). The isotype control group had C3c deposits present at 66 $\pm$ 15% of NMJs, which was significantly higher compared to only 7 $\pm$ 3% and 5 $\pm$ 2% of NMJs in the NHS only and C2 inhibitor groups, respectively ($p<0.01$). There was no significant difference between the NHS only and C2 inhibitor groups. These results confirm that C2 was blocked, preventing cleavage of C3. The results in Figure 6.5B illustrate that NFH was occupying 91 $\pm$ 4% of NMJs in the NHS only group. On the other hand, there were significantly fewer occupied NMJs in the isotype control group, with only 8 $\pm$ 3% of NMJs being occupied by NFH ($p<0.001$). In contrast, when treated with the C2 inhibitor, 63 $\pm$ 17% of NMJs were occupied with NFH, which was significantly higher compared to the isotype control group ($p<0.01$). There was no significant difference between the percentage of occupied NMJs in the NHS only and C2 inhibitor groups. Illustrative images in Figure 6.5C show C3c deposits in the isotype control group, accompanied with a loss of NFH staining at the NMJ. In contrast, there are no C3c deposits present in the NHS only and C2 inhibitor groups and NFH is present occupying the nerve terminal.

In summary, treatment with the C2 inhibitor attenuates injury, offering protection to axonal integrity at the nerve terminal in this acute *ex vivo* injury model in *GalNAc-T$^{-/-}$-Tg(neuronal)* mice.

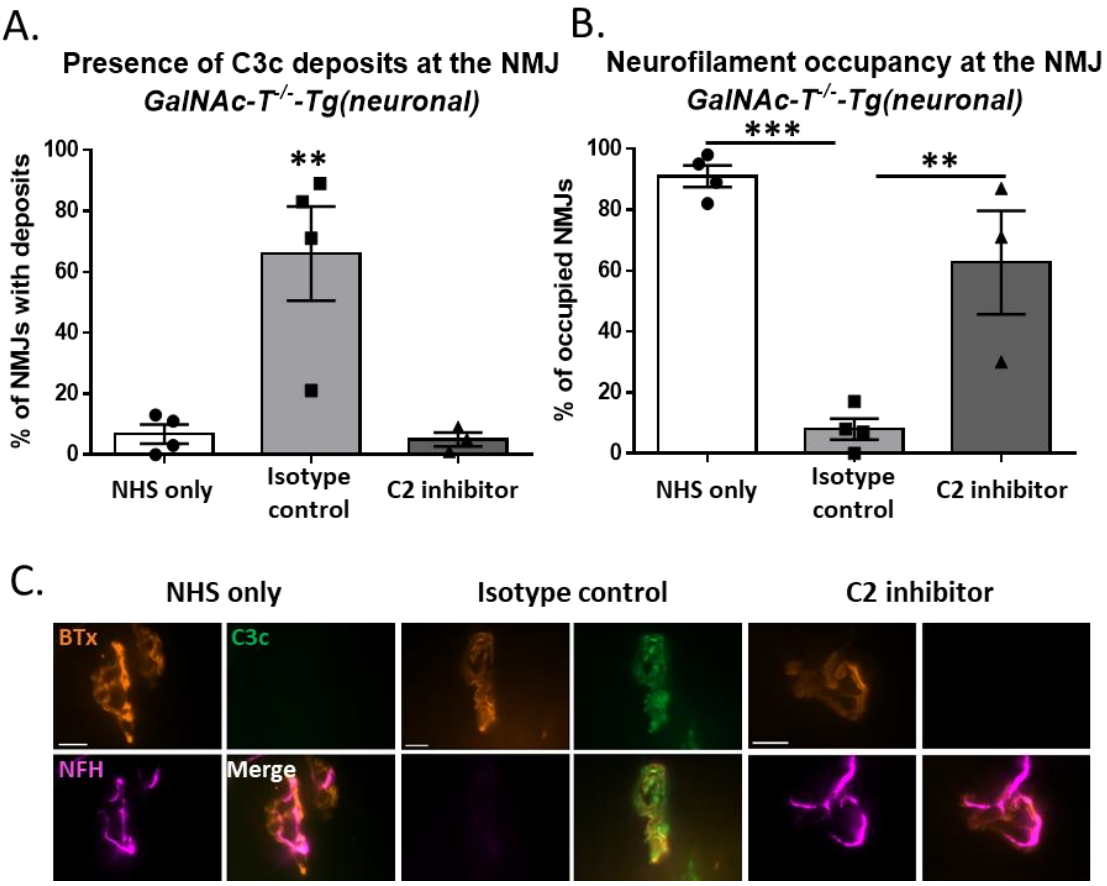

Figure 6.5: Effects of C2 inhibition on axonal integrity at the NMJ in an *ex vivo* axonal injury model. Acute *ex vivo* injury performed on triangularis sterni (TS) muscle from *GalNAc-T$^{-/-}$-Tg(neuronal)* mice. TS was incubated in 100 µg/ml C2 inhibitor or isotype control, 40% normal human serum (NHS) and 100 µg/ml anti-GM1 mAb for 1 hour at 32℃. NHS only group was incubated in 40% NHS and Ringer's. C3c was stained for to confirm that the complement pathway had been blocked and axonal integrity at the neuromuscular junction (NMJ) was assessed by staining for the axonal structural protein, neurofilament heavy (NFH). A) C3c deposits were found at significantly more NMJs in the isotype control group compared to all other groups (**=p<0.01). B) NFH was occupying significantly more NMJs in the NHS only and C2 inhibitor groups compared to the isotype control group (***=p<0.001, **=p<0.01, respectively). C) Representative images illustrate C3c deposits (green) overlying the NMJ, identified by bungarotoxin (BTx, orange) in the isotype control group, accompanied with a loss of NFH (magenta) staining. C3c is absent from the NHS only and C2 inhibitor groups, and NFH is present overlying the NMJ. Scale bar = 10 µm. One-way ANOVA performed with Tukey's multiple comparisons test to determine statistical significance. n=4 NHS only and isotype control; n=3 C2 inhibitor.

6.2.2.3 Presence of voltage gated sodium channels at the node of Ranvier

As previously demonstrated in Chapter 4, complement-mediated injury to the axonal membrane in *GalNAc-T$^{-/-}$-Tg(neuronal)* mice results in the disruption of Nav at the nodal gap. Therefore, the integrity of the axonal membrane at the NoR, following complement inhibition, was investigated in *GalNAc-T$^{-/-}$-Tg(neuronal)* mice by staining for pNav (Figure 6.6).

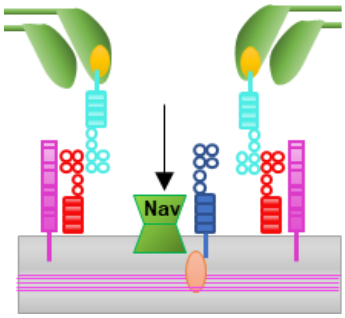

Figure 6.6: Location of voltage gated sodium channels at the node of Ranvier.

C3c deposition at the distal nerve, defined as the first myelin internode and NoR adjacent to the NMJ, was evaluated. Figure 6.7A illustrates that C3c deposits were present at 84 ± 12% of distal nerves in the isotype control group, which was significantly higher compared to both the NHS only (0 ± 0%) and C2 inhibitor groups (6 ± 4%), respectively ($p<0.001$). There was no significant difference between the C2 inhibitor and NHS only groups. Therefore, this data indicates that C2 was successfully blocked by the inhibitor. Next, the presence of Nav clusters was investigated (Figure 6.7B). Results show that pNav clusters were present at 100 ± 0% of distal NoR in the NHS only group. In contrast, the presence of pNav clusters was significantly reduced to 25 ± 2% in the isotype control group ($p<0.001$). When the C2 inhibitor was applied, pNav clusters were present at 98 ± 2% of distal NoR; indicating that pNav clusters were protected and comparable to the percentage of pNav clusters present in the NHS only group. Representative images show that when C3c deposits are present at the distal NoR in the isotype control group, this results in the loss of pNav staining (Figure 6.7C). On the other hand, in the NHS only group and the C2 inhibitor group, complement deposits are absent and pNav clusters are present at the distal NoR. In summary, inhibition of C2 offers protection to pNav at the nodal gap in this acute *ex vivo* axonal injury model.

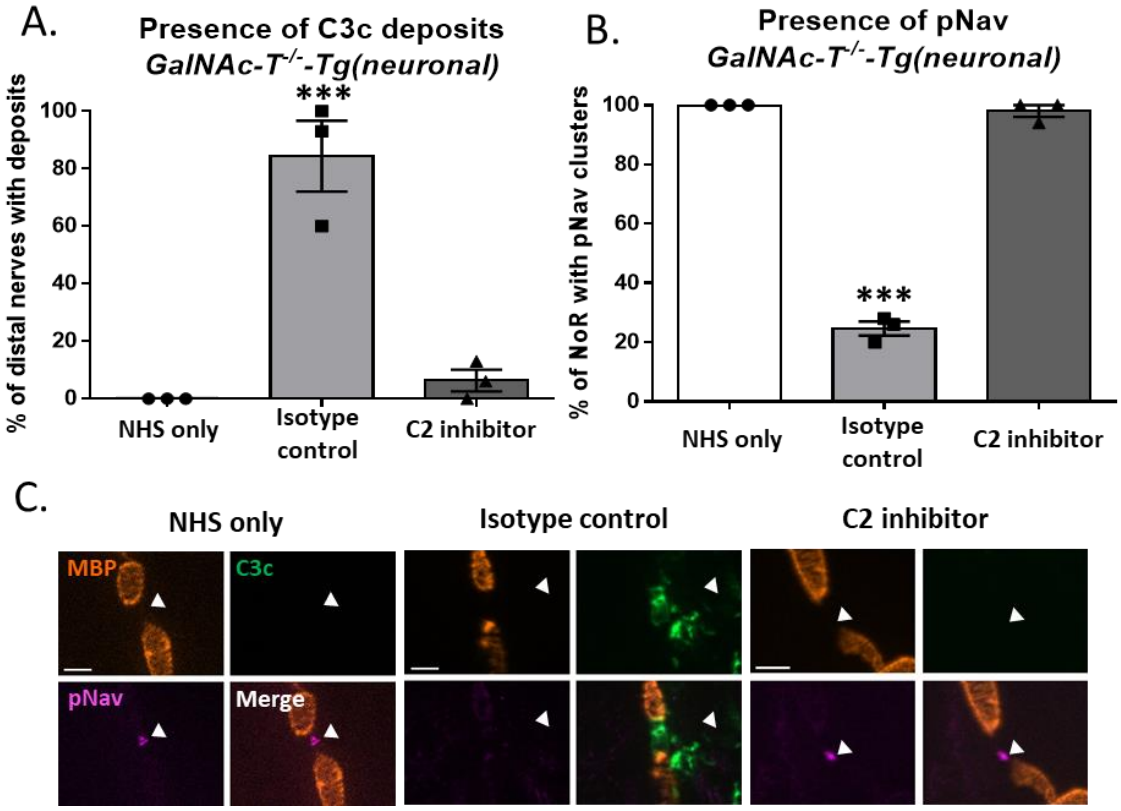

Figure 6.7: Effect of C2 inhibition on the NoR in an *ex vivo* axonal injury model. Acute *ex vivo* injury performed on triangularis sterni (TS) muscle from *GalNAc-T$^{-/-}$-Tg(neuronal)* mice. TS was incubated in 200 µg/ml C2 inhibitor or isotype control, 40% normal human serum (NHS) and 100 µg/ml anti-GM1 mAb for 4 hours at 32°C. NHS only group incubated in 40% NHS and Ringer's. The early complement component, C3c, was stained for to confirm complement pathway inhibition and the integrity of voltage gated sodium channels (Nav) at the node of Ranvier (NoR) were assessed. A) C3c deposits were present at significantly more distal nerves in the isotype control group compared to all other groups (***=p<0.001). There was no significant difference between the percentage of C3c deposits in the NHS only group and the C2 inhibitor group. B) pNav clusters were present at significantly more distal NoR in the NHS only group and C2 inhibitor group compared to the isotype control group (***=p<0.001). There was no significant difference between the C2 inhibitor group and the NHS only group. C) Representative images illustrate C3c deposits (green) at the nodal gap (white arrowhead) in the isotype control group, accompanied with a loss of pNav staining (magenta). On the other hand, C3c was absent from both NHS only and C2 inhibitor groups, and pNav clusters were present at the nodal gap. Scale bar = 5 µm. Statistical significance was determined by performing a one-way ANOVA with Tukey's multiple comparisons test. n=3/treatment.

6.2.3 Effects of C2 inhibition in an *ex vivo* paranodal demyelinating injury model

After demonstrating neuroprotective effects of C2 inhibition in our established *ex vivo* axonal injury model, for the first time, the therapeutic effects of complement inhibition were explored in our *ex vivo* anti-GM1 mAb-mediated paranodal demyelinating injury model in *GalNAc-T$^{-/-}$-Tg(glial)* mice.

6.2.3.1 Deposition of anti-GM1 antibody and C1q at the distal nerve

To determine whether anti-GM1 mAb had bound and subsequently activated the complement pathway in both the isotype control and C2 inhibitor groups, the percentage of distal nerves with anti-GM1 mAb and C1q deposits were determined. Figure 6.8A illustrates that anti-GM1 mAb was deposited at significantly more distal nerves in both the isotype control (97 $\pm$ 1%) and C2 inhibitor groups (97 $\pm$ 2%) compared to the NHS only group but not to each other ($p<0.001$). Similarly, C1q deposits were present at 88 $\pm$ 3% and 77 $\pm$ 6% of distal nerves in the isotype control group and the C2 inhibitor group, respectively; differing significantly from the NHS only group but not to each other ($p<0.001$; Figure 6.8B). The illustrative images in Figure 6.8C demonstrate anti-GM1 mAb and C1q deposits overlying the internode and paranodes in the isotype control and C2 inhibitor groups. On the other hand, antibody and C1q deposits are absent from the NHS only group.

In conclusion, these results confirm that binding of anti-GM1 mAb to glial membranes, activated the complement pathway in both the isotype control and C2 inhibitor groups. Additionally, this further corroborates the findings in 6.2.2.1; demonstrating that the C2 inhibitor does not obstruct C1q activation.

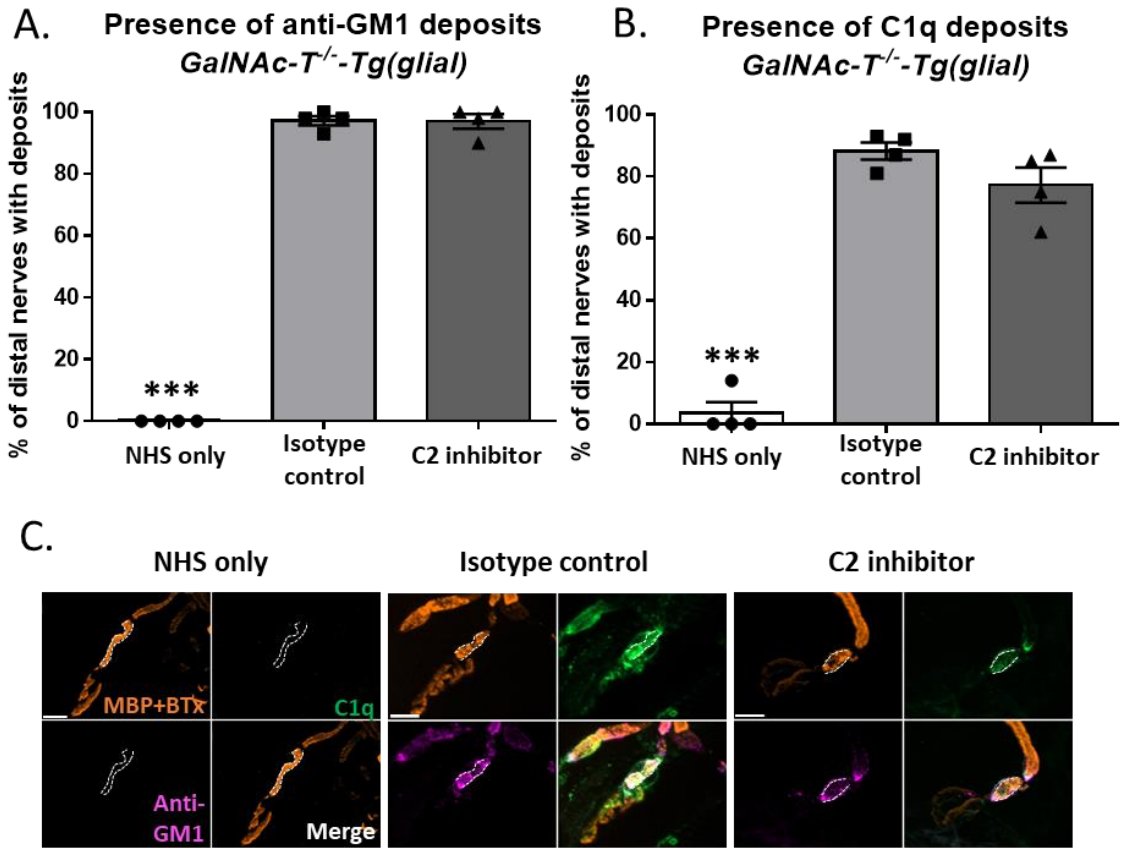

Figure 6.8: Presence of anti-GM1 mAb and C1q deposits at the distal nerve in *GalNAc-T-/--Tg(glial)* mice. Acute *ex vivo* injury performed on triangularis sterni (TS) muscle from *GalNAc-T-/--Tg(glial)* mice. TS was incubated in 200 µg/ml C2 inhibitor or isotype control, 40% normal human serum (NHS) and 100 µg/ml anti-GM1 mAb for 4 hours at 32°C. NHS only group was incubated in 40% NHS and Ringer's. Immunoanalysis performed to determine the percentage of distal nerves with anti-GM1 mAb deposits and subsequent C1q deposits. A+B) Results demonstrate that there were significantly more anti-GM1 mAb and C1q deposits in the isotype control and C2 inhibitor groups compared to the NHS only group (***=p<0.001). There were no significant differences between the isotype control and C2 inhibitor groups. C) Illustrative images show anti-GM1 mAb (magenta) and C1q (green) deposits overlying the distal nerve, identified by myelin basic protein (MBP; orange, broken white line), in the isotype control and C2 inhibitor groups. Scale bar = 10 µm. Statistical significance determined by performing one-way ANOVA with Tukey's multiple comparisons test. n=4/treatment.

6.2.3.2 Integrity of ankyrin-B at the distal paranode

The percentage of distal nerves with C3c deposits was assessed to investigate whether C2 activation had been blocked, preventing the cleavage of C3 and progression of the complement pathway. The results in Figure 6.10A demonstrate that 94 ± 3% of distal nerves in the isotype control group had C3c deposits. This was significantly higher compared to both the NHS only group and the C2 inhibitor group ($p<0.001$). There was no significant difference between the NHS only group and C2 inhibitor group, as C3c deposits were present at 4 ± 4% and 2 ± 2% of analysed distal nerves, respectively. These data therefore indicate that the classical complement pathway was blocked by the C2 inhibitor.

It was established that there was significant complement-mediated disruption to the axo-glial junction when the glial membrane was targeted with anti-GM1 mAb in *GalNAc-T*$^{-/-}$*-Tg(glial)* mice (4.2.10.2). Hence, investigation of the presence of the paranodal cytoplasmic protein and calpain substrate, AnkB, was determined to assess the integrity of the axo-glial junction following complement inhibition (Figure 6.9).

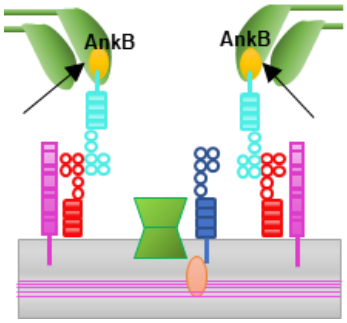

Figure 6.9: Location of ankyrin-B at the node of Ranvier.

AnkB dimers were present at 76 ± 4% of analysed distal paranodes in the NHS only group (Figure 6.10B). On the other hand, the presence of AnkB dimers was significantly reduced to 10 ± 1% in the isotype control group ($p<0.001$). Treatment with the C2 inhibitor resulted in a significantly higher percentage of distal paranodes having AnkB dimers present compared to the isotype control group ($p<0.001$), with 71 ± 1% of distal paranodes having positive staining in the C2 inhibitor group. The presence of AnkB dimers in the C2 inhibitor group was comparable to that of the NHS only group. Representative images in Figure 6.10C show AnkB dimer staining at the paranode of NHS only and C2 inhibitor groups. In contrast, AnkB is absent from the paranode of the isotype control

group and C3c deposits are present overlying the paranode and internode. In conclusion, C2 inhibition attenuated disruption to AnkB dimers, present in the cytoplasmic loops of paranodes, maintaining integrity of the structural protein to comparable levels with control mice.

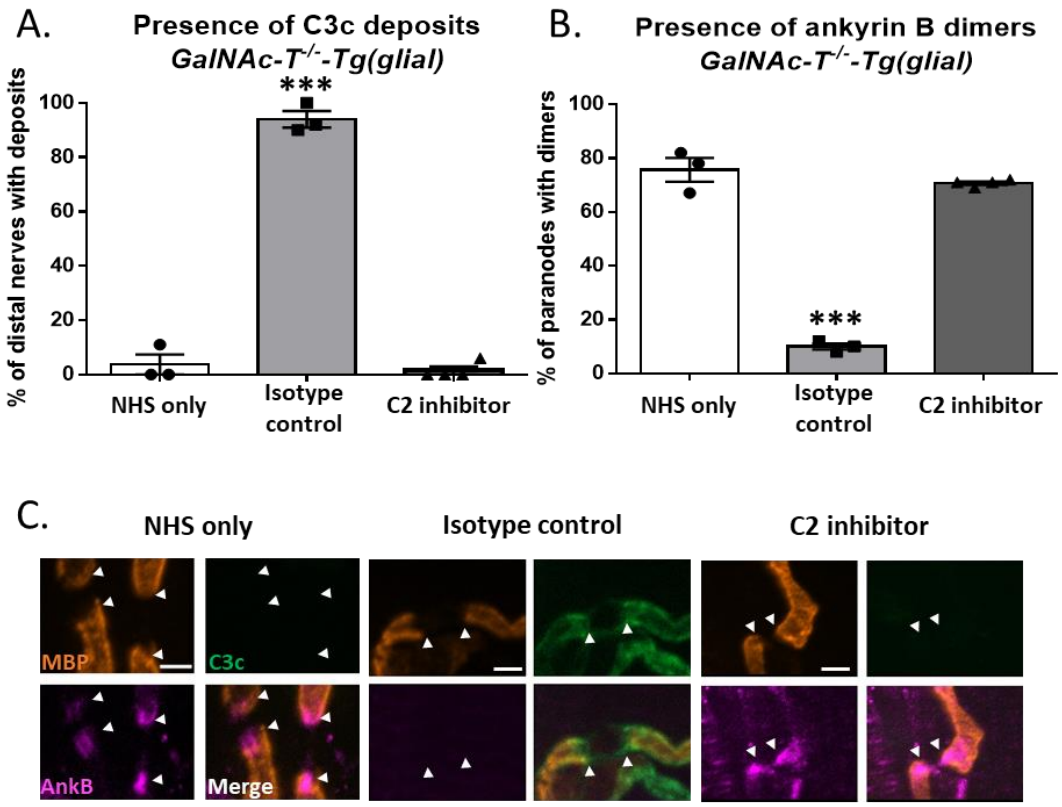

Figure 6.10: Effect of C2 inhibition on ankyrin-B in an *ex vivo* paranodal demyelinating injury model. Acute *ex vivo* injury performed on triangularis sterni (TS) muscle from *GalNAc-T$^{-/-}$-Tg(glial)* mice. TS was incubated in 200 µg/ml C2 inhibitor or isotype control, 40% normal human serum (NHS) and 100 µg/ml anti-GM1 mAb for 4 hours at 32°C. NHS only group incubated in 40% NHS and Ringer's. TS was stained for the early complement component, C3c, to confirm the complement pathway had been blocked. The integrity of ankyrin-B (AnkB) dimers at the paranode following complement inhibition was assessed. A) There were significantly more distal nerves with C3c deposits in the isotype control group compared to the NHS only and C2 inhibitor groups (***=p<0.001). There was no significant difference between the NHS only and C2 inhibitor groups. B) AnkB dimers were present at significantly more paranodes in the NHS only and C2 inhibitor groups compared to the isotype control groups (***=p<0.001). There was no significant difference between the presence of AnkB dimers in the NHS only and C2 inhibitor groups. C) Representative images show AnkB dimers (magenta) present at the paranode (white arrowheads) in NHS only and C2 inhibitor group. AnkB is absent from the paranode in the isotype control group and C3c deposits (green) are present overlying the myelin basic protein staining (orange). Scale bar = 5 µm. One-way ANOVA with Tukey's multiple comparisons test performed to determine statistical significance. n=3 NHS only and isotype control; n=4 C2 inhibitor.

6.2.3.3 Assessment of Caspr dimers at the distal paranode

As described previously, we have established that complement mediated injury to the glial membrane in *GalNAc-T$^{-/-}$-Tg(glial)* mice results in the disruption of proteins located on both the axonal and glial membranes at the paranode, consisting of the paranodal junction. Since complement inhibition protected the integrity of AnkB, an anchoring protein for NF155 located on the glial membrane at the paranode (Chang et al., 2014), I next investigated the presence of Caspr (Figure 6.11) which is the NF155 binding partner protein located on the axonal membrane (Charles et al., 2002), following complement inhibition.

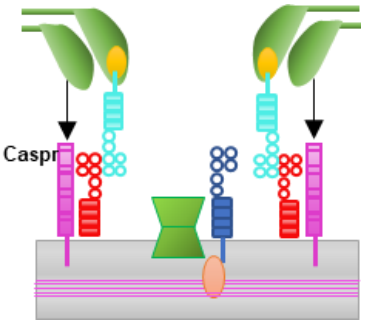

Figure 6.11: Location of Caspr at the Node of Ranvier.

MAC was stained for along with Caspr to confirm C2 inhibition prevented the formation of the terminal complement component. The results in Figure 6.12A illustrate that MAC was present at 72 ± 11% of distal nerves in the isotype control group, which was significantly higher compared to both the NHS only and C2 inhibitor group ($p<0.001$). Only 5 ± 2% of distal nerves had MAC deposits present in the C2 inhibitor group which did not differ significantly compared to NHS only, confirming that MAC pore formation had been blocked by inhibition of C2. Evaluation of the presence of Caspr dimers at the paranode revealed that 91 ± 4% of distal paranodes had Caspr dimers present in the NHS only group (Figure 6.12B). The presence of Caspr dimers was significantly reduced to 41 ± 4% in the isotype control group compared to all other treatment groups ($p<0.001$). In contrast, when C2 was inhibited Caspr dimers were protected to comparable levels to the NHS only group, with 89 ± 2% of distal paranodes having Caspr dimers present. Representative images in Figure 6.12C demonstrate that Caspr dimers are present at the paranode in both the NHS only and C2 inhibitor groups. On the other hand, MAC deposits are found overlying the internode and there is a loss of Caspr dimer staining in the isotype control

group. Overall, these results indicate that C2 inhibition significantly protects the integrity of Caspr dimers at the distal paranode in *GalNAc-T$^{-/-}$-Tg(glial)* mice in this acute *ex vivo* paranodal demyelinating injury model.

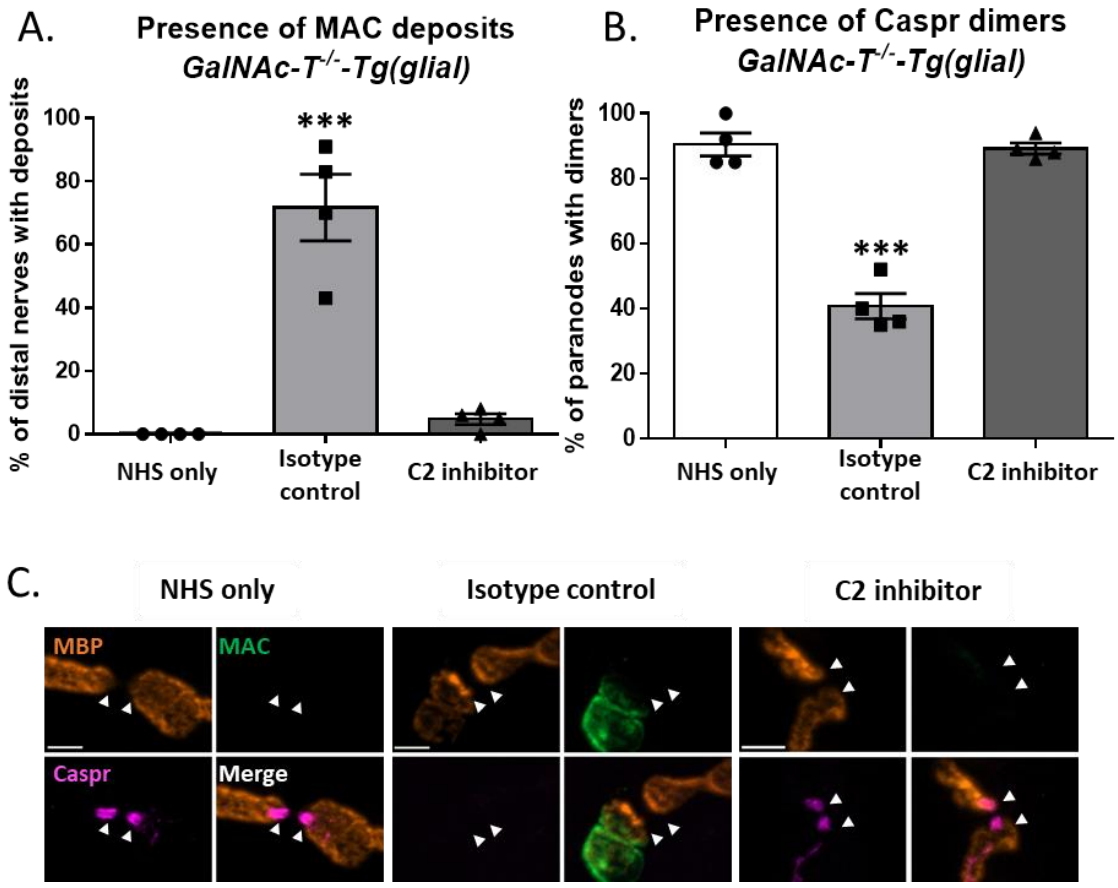

Figure 6.12: Effect of C2 inhibition on Caspr dimers in an *ex vivo* paranodal demyelinating injury model. Acute *ex vivo* injury performed on triangularis sterni (TS) muscle from *GalNAc-T$^{-/-}$-Tg(glial)* mice. TS was incubated in 200 µg/ml C2 inhibitor or isotype control, 40% normal human serum (NHS) and 100 µg/ml anti-GM1 mAb for 4 hours at 32℃. NHS only group incubated in NHS and Ringer's. The terminal complement product, membrane attack complex (MAC) was stained for and the integrity of Caspr dimers at the paranode was assessed. A) MAC deposits were present at significantly more distal nerves in the isotype control group compared to all treatment groups (***=p<0.001). There was no significant difference between the NHS only and C2 inhibitor group. B) The presence of Caspr dimers was significantly reduced in the isotype control group compared to NHS only and C2 inhibitor groups (***=p<0.001). There was no significant difference between the NHS only and C2 inhibitor groups. C) Illustrative images show Caspr dimers (magenta) present at the paranode (white arrowheads) in the NHS only and C2 inhibitor groups. Caspr dimers were absent from the paranode in the isotype control group and MAC deposits (green) are present overlying the myelin basic protein staining (orange). Scale bare = 5 µm. Statistical significance was determined by performing a one-way ANOVA with Tukey's multiple comparisons test. n=4/treatment.

6.2.4 Effects of C2 inhibition in an *in vivo* paranodal loop injury model

After establishing that C2 inhibition offered protection to axo-glial adhesion molecules in our *ex vivo* anti-GM1 mAb dependent complement-mediated paranodal demyelinating injury model, we then studied the neuroprotective effects of human C2 inhibition *in vivo* in *GalNAc-T$^{-/-}$-Tg(glial)* mice. For *ex vivo* studies, the C2 inhibitor used was Bro-2, the precursor molecule of the previously published ARGX-117 (Van de Walle et al., 2020). For *in vivo* studies, ARGX-117 was selected due to the high concentration of the stock solution and the increased half-life of the drug. Prior to performing the *in vivo* experiment, an *ex vivo* experiment was performed, comparing the efficacy of Bro-2 and ARGX-117 in *GalNAc-T$^{-/-}$-Tg(neuronal)* mice. It was determined that the concentration and neuroprotective effects of ARGX-117 were comparable with Bro-2 (see Appendix 8.6).

6.2.4.1 Assessment of respiratory function following complement inhibition

Respiratory function was assessed using WBP to determine the effect of human C2 complement inhibition on diaphragm function in *GalNAc-T$^{-/-}$-Tg(glial)* mice. A baseline WBP recording was taken prior to anti-GM1 mAb and complement delivery. TV and RR were then assessed at 5-hours post injury and compared to the baseline values. Figure 6.13A illustrates the TV at 5-hours post injury in each treatment group as a percentage of the baseline, represented by the broken line. The TV of the naïve control group remained comparable to baseline throughout the recording and at 5-hours, was 96 $\pm$ 6% of baseline. At 5-hours post injury, the TV of the isotype control group was reduced to 65 $\pm$ 9%. This was significantly reduced compared to baseline and to the naïve control group ($p<0.05$ compared to naïve control; $p<0.01$ compared to baseline). On the other hand, the TV was 84 $\pm$ 3% of baseline at 5-hours post injury following C2 inhibition. The TV of the C2 inhibitor group did not differ significantly compared to any other treatment groups nor to baseline. Nevertheless, although not significant, these results suggest that inhibition of human C2 offers protection to TV. The RR at 5-hours post injury for each treatment group is displayed in Figure 6.13B. At 5-hours post injury, the RR of the naïve control group was reduced to 54 $\pm$ 3%, although this did not differ significantly compared to baseline. In contrast, the RR of the isotype control group was elevated to 132 $\pm$ 30%, although not significantly. The RR of the C2 inhibitor group was comparable to naïve control, with a reduced value of 54 $\pm$ 11% of baseline. Despite the differences between the groups, there

were no significant differences in RR between any of the treatment groups. Overall, both TV and RR were protected to comparable levels of the naïve control following inhibition of C2.

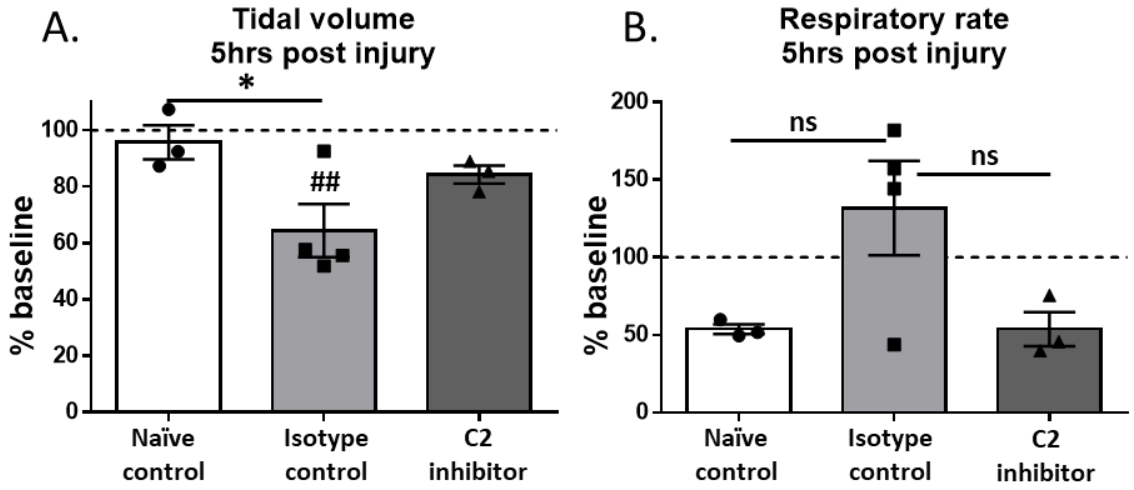

Figure 6.13: Assessment of respiratory function following C2 inhibition. A baseline whole-body plethysmography (WBP) recording was taken prior to *GalNAc-T$^{-/-}$-Tg(glial)* mice receiving 50 mg/kg of anti-GM1 mAb intraperitoneally (IP). The following morning, mice received an intravenous injection of 200 mg/kg of C2 inhibitor (ARGX-117) or IgG1 isotype control, followed 10 minutes later with 30 µl/g normal human serum (NHS) delivered IP. Naïve control mice received PBS only. A WBP recording was taken at 5-hours post injury and the tidal volume (TV) and respiratory rate (RR) for each treatment group was plotted as a percentage of the baseline (represented by broken line). A) The TV of the isotype control group was significantly reduced compared to baseline and naïve control at 5-hours post injury (*=p<0.05; ##=p<0.01). B) The RR of the isotype control group was elevated at 5-hours post injury, although not significantly. A repeated measures two-way ANOVA with Sidak's multiple comparisons test was performed to test for significance between the baseline value and 5-hour value for each treatment group. A one-way ANOVA with Tukey's multiple comparisons test was performed to test for significance of the TV/RR at 5-hours post injury between treatment groups. *=significance between treatment groups; #=significance compared to baseline. Results represented as the average ± SEM; n=4 for isotype control, n=3 for naïve control and C2 inhibitor.

6.2.4.2 Confirmation of anti-GM1 antibody and complement activation

Immunofluorescence analysis was performed on the diaphragm harvested from *GalNAc-T$^{-/-}$-Tg(glial)* mice and the integrity of the paranode was assessed. Prior to quantifying axo-glial adhesion molecules at the paranode, anti-GM1 mAb and the complement activation complex, C1q, were studied to determine whether the complement pathway had been activated in the isotype control and C2 inhibitor groups. Figure 6.14A demonstrates that anti-GM1 mAb deposits were present at 100 ± 0% and 96 ± 3% of

distal nerves in the isotype control and C2 inhibitor groups, respectively, which did not differ significantly. This was significantly higher in comparison to the naïve control group, which as expected, had no anti-GM1 mAb deposits present ($p<0.001$). Quantification of C1q deposition at the distal nerve was then performed and the results are illustrated in Figure 6.14B. These results show that C1q deposits were present at 73 $\pm$ 11% and 66 $\pm$ 10% of distal nerves in the isotype control and C2 inhibitor groups, respectively. Although there was no significant difference between the isotype control and C2 inhibitor groups, the presence of C1q deposits was significantly higher in both groups compared to the naïve control group ($p<0.001$). Illustrative images in Figure 6.14C show anti-GM1 mAb and C1q deposits overlying the distal internode in both the isotype control and C2 inhibitor groups.

In summary, these results provide affirmation that the complement pathway was activated by anti-GM1 mAb in the isotype control and C2 inhibitor groups and that inhibition of C2 does not negatively impact C1q activation.

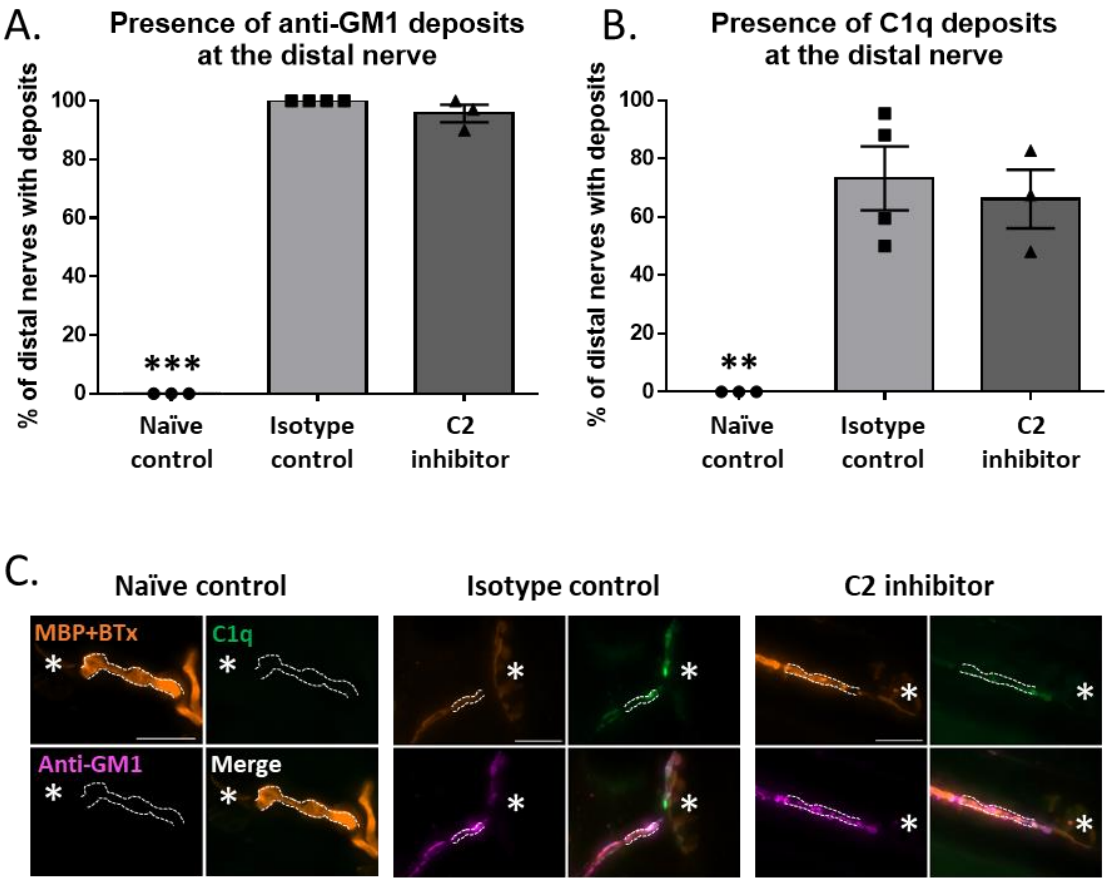

Figure 6.14: Quantification of anti-GM1 mAb and C1q deposition at the distal nerve of *GalNAc-T$^{-/-}$-Tg(glial)* mice. *GalNAc-T$^{-/-}$-Tg(glial)* mice were injected intraperitoneally (IP) with 50 mg/kg anti-GM1 mAb followed 16 hours later, with 200 mg/kg of C2 inhibitor (ARGX-117) or IgG1 isotype control delivered intravenously. Ten minutes later, mice received 30 µl/g normal human serum (NHS) as a source of complement IP. Naïve control mice received PBS only. Diaphragm was harvested 6 hours post NHS injection and immunostaining was performed on fixed diaphragm sections. Anti-GM1 mAb and the complement activation complex, C1q, were stained for to confirm anti-GM1 mAb had activated the complement pathway. A+B) Anti-GM1 mAb and C1q deposits were present at significantly more distal nerves in the isotype control and C2 inhibitor group compared to naïve control (***=p<0.001; **=p<0.01). C) Representative images demonstrate anti-GM1 mAb and C1q deposits present along the distal internode (identified by myelin basic protein, MBP; orange; broken white line) and at perisynaptic Schwann cells surrounding the neuromuscular junction (identified by bungarotoxin; white asterisks). Scale bar = 20 µm. One-way ANOVA with Tukey's multiple comparisons test used to test for statistical significance. Results represented as the average ± SEM. n=4 isotype control; n=3 naïve control and C2 inhibitor.

6.2.4.3 Integrity of axo-glial adhesion molecules at the distal paranode

We have demonstrated that injury to the glial membrane results in significant disruption to the axo-glial junction at the paranode (4.2.10). It is hypothesised that this is a result of complement-mediated injury to the glial membrane. Thus, to test this hypothesis, I studied the integrity of the axo-glial adhesion molecules at the NoR following C2 inhibition. The proteins that were studied are outlined in Figure 6.15.

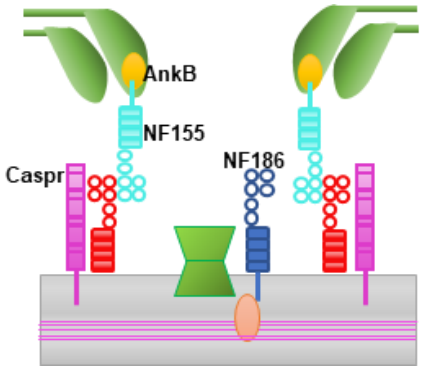

Figure 6.15: Schematic diagram of node of Ranvier.

The presence of C3c deposits was assessed to determine whether the C2 inhibitor had prevented the progression of the complement pathway. Figure 6.16A demonstrates that 95 ± 3% of distal nerves had C3c deposits in the isotype control group, which was significantly higher compared to all other treatment groups ($p<0.001$). Complement deposits were absent from the naïve control group as expected. Only 10 ± 3% of distal nerves had C3c deposits present in the C2 inhibitor group which did not differ significantly in comparison to the NHS only group, therefore demonstrating that the complement pathway had been inhibited in this group.

Next, the effects of complement inhibition on the integrity of the paranodal anchoring protein, AnkB, was investigated. AnkB dimers were present at 97 ± 1% of distal paranodes in naïve control mice (Figure 6.16B). The presence of AnkB dimers was significantly reduced in the isotype control group to 7 ± 3%, compared to all other treatment groups ($p<0.001$). Although AnkB dimers were present at significantly more distal paranodes in the C2 inhibitor group compared to isotype control ($p<0.001$), dimers were present at 57 ± 5% of distal paranodes which was significantly lower compared to naïve control ($p<0.001$). These results are illustrated in Figure 6.16C; AnkB dimers are present at the

paranode in the naïve control and C2 inhibitor groups. However, complement deposits are present at the paranode of the isotype control group and there is a loss of AnkB staining.

Therefore, C2 inhibition provides significant protection to AnkB dimers present in the cytoplasmic loops of the paranode in this acute anti-GM1 mAb-mediated paranodal demyelinating injury model.

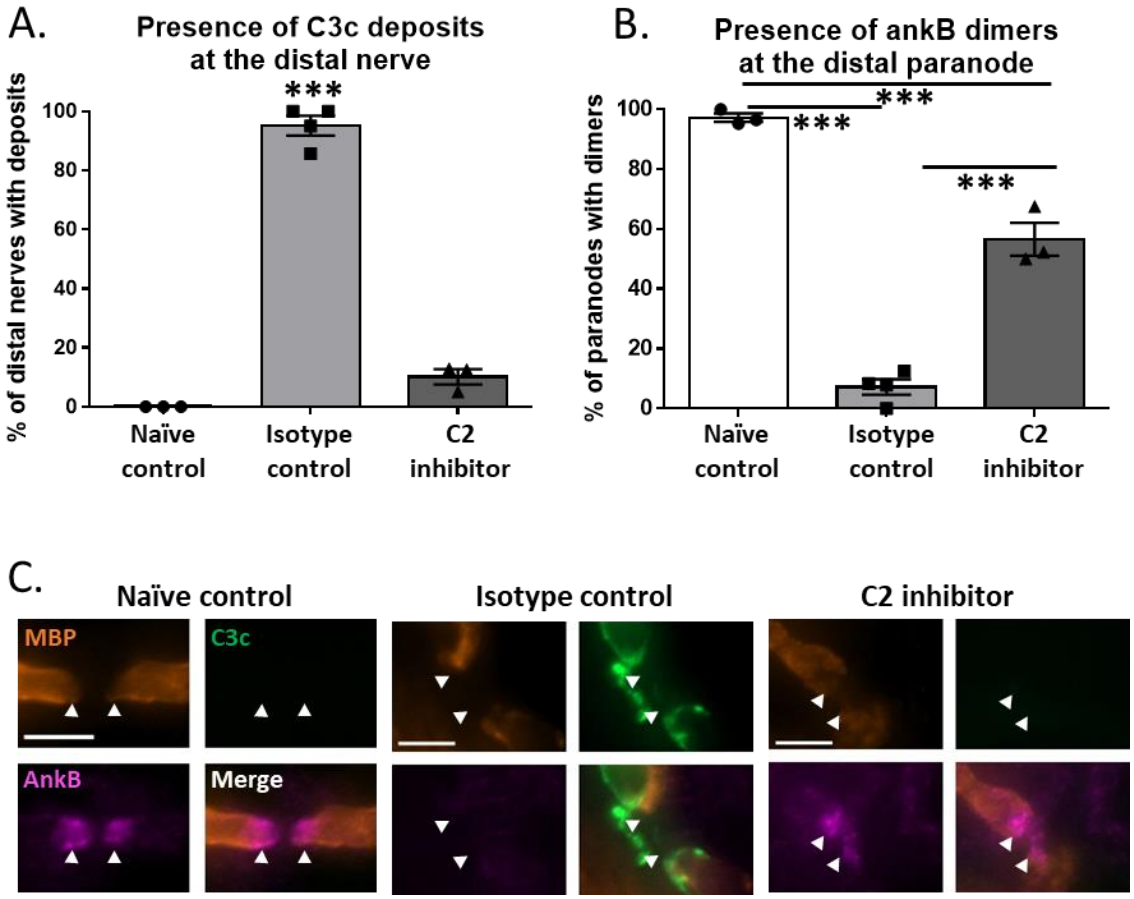

Figure 6.16: Integrity of ankyrin-B dimers at the distal paranode following C2 inhibition in *GalNAc-T$^{-/-}$-Tg(glial)* mice. *GalNAc-T$^{-/-}$-Tg(glial)* mice were injected intraperitoneally (IP) with 50 mg/kg of anti-GM1 mAb followed 16 hours later with 200 mg/kg of C2 inhibitor (ARGX-117) or IgG1 isotype control delivered intravenously. Ten minutes after, mice received 30 µl/g normal human serum (NHS) IP. Naïve control mice were injected with PBS only. Diaphragm was harvested 6-hours post injury and immunofluorescence analysis was performed on fixed diaphragm sections. The early complement product, C3c, was stained for to determine whether C2 was inhibited and the subsequent integrity of AnkB at the distal paranode was assessed. A) C3c deposits were present at significantly more distal nerves in the isotype control group compared to naïve control and C2 inhibitor groups (***=p<0.001). B) The presence of AnkB dimers was significantly reduced in both the isotype control and C2 inhibitor groups compared to naïve control (***=p<0.001). AnkB dimers were present at significantly more distal paranodes in the C2 inhibitor group compared to isotype control (***=p<0.001). C) Illustrative images demonstrate AnkB dimers (magenta) at the paranode (white arrowheads) in both the naïve control and C2 inhibitor groups. C3c deposits (green) are present overlying myelin basic protein (MBP; orange) in the isotype control group and AnkB dimers are absent from the paranode. Scale bar = 5 µm. Statistical analysis performed using one-way ANOVA with Tukey's multiple comparisons test. Results represented as average ± SEM. n=3 isotype control; n=4 naïve control and C2 inhibitor.

As demonstrated previously, injury to the glial membrane in *GalNAc-T$^{-/-}$-Tg(glial)* mice results in significant disruption to the axo-glial junction at the paranode accompanied with a disturbance to NF186 at the nodal gap (4.2.10). The function of AnkB is to tether NF155 to the underlying cytoskeleton at the paranode (Chang et al., 2014). Therefore, I next determined whether complement inhibition also offered protection to NF155 located on the glial membrane. Additionally, pan-NFasc immunostaining was performed that identifies NF186 at the nodal gap and NF155 at the paranode; thus, the presence of NF186 was also investigated. Figure 6.17A illustrates that NF155 dimers, depicted by paranodal pan-NFasc staining, were present at 93 $\pm$ 2% of distal paranodes in the naïve control group. The presence of NF155 dimers were significantly reduced in the isotype control group to 11 $\pm$ 8% ($p<0.001$). In contrast, NF155 dimers were present at significantly more distal nerves in the C2 inhibitor group compared to isotype control ($p<0.05$). Only 57 $\pm$ 14% of distal nerves in the C2 inhibitor group had NF155 dimers present in comparison to 93 $\pm$ 2% in the NHS only group, however this difference was not significant. The results in Figure 6.17B show that NF186, represented by nodal pan-NFasc staining, was present at 99 $\pm$ 1% of distal nodal gaps in naïve control mice (Figure 6.17A). On the other hand, the presence of NF186 was significantly reduced to 67 $\pm$ 9% in the isotype control group ($p<0.05$). NF186 was present at 94 $\pm$ 2% of distal nodal gaps in the C2 inhibitor group which was comparable to naïve control mice. Although not statistically significant, the significance value between the isotype control group and C2 inhibitor group was $p=0.051$. Representative images in Figure 6.17C demonstrate pan-NFasc staining at both the nodal gap and paranode in the naïve control and C2 inhibitor group, despite the presence of anti-GM1 mAb deposits in the latter. In contrast, anti-GM1 mAb deposits are present at the paranode of the isotype control group and pan-NFasc staining is only present at the nodal gap but absent from the paranodes.

Hence, inhibition of C2 protects both axonal NF186 and glial NF155 at the distal NoR following anti-GM1 mAb-mediated injury in this acute paranodal demyelinating *in vivo* injury model in *GalNAc-T$^{-/-}$-Tg(glial)* mice.

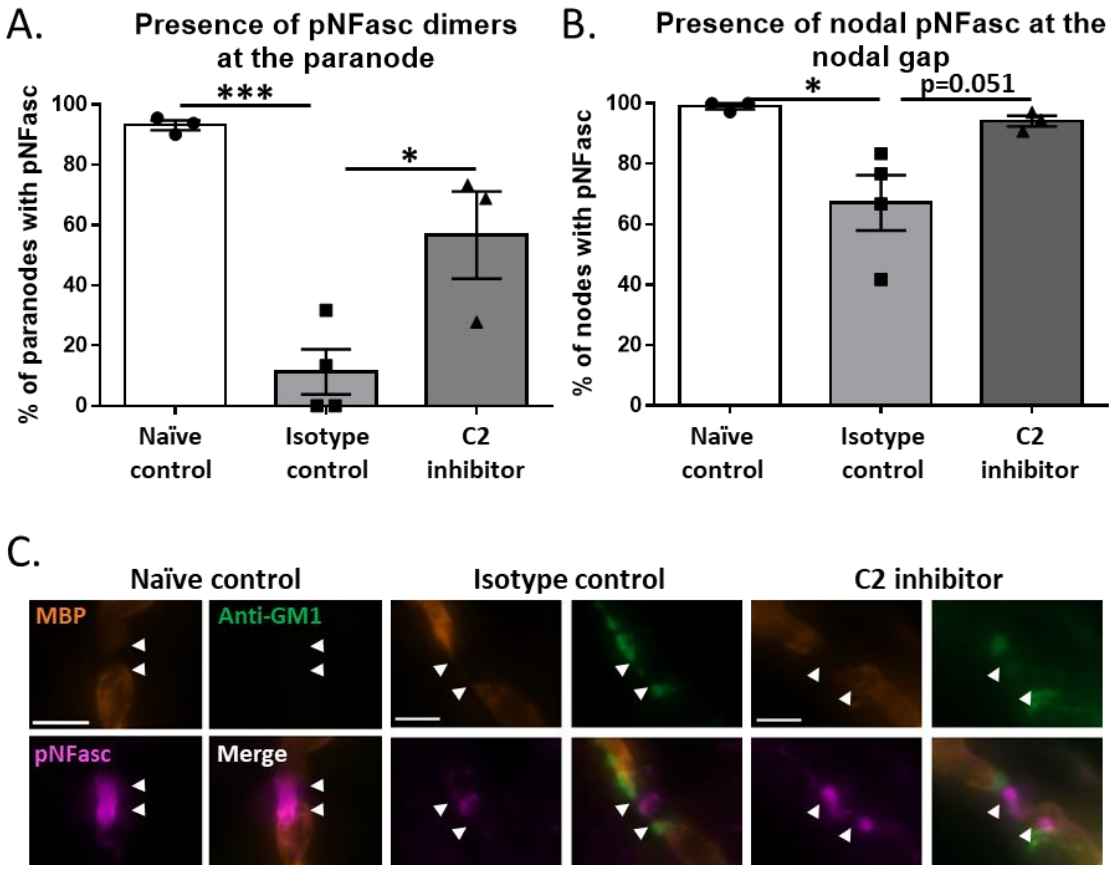

Figure 6.17: Assessment of neurofascin isoforms at the distal node of Ranvier following C2 inhibition in *GalNAc-T$^{-/-}$-Tg(glial)* mice. *GalNAc-T$^{-/-}$-Tg(glial)* mice received an intraperitoneal (IP) injection of 50 mg/kg anti-GM1 mAb. Sixteen hours later, an intravenous injection of 200 mg/kg of C2 inhibitor (ARGX-117) or IgG1 isotype control was administered, followed 10 minutes later with an IP injection of 30 µl/g normal human serum (NHS). Naive control mice received PBS only. Diaphragm was harvested six hours post NHS injection and immunofluorescence analysis was performed on fixed diaphragm sections. The effect of complement inhibition on the neurofascin isoforms (NF155 and NF186) were determined by staining for pan-NFasc. A) The presence of paranodal pan-NFasc dimers was significantly reduced in the isotype control group compared to both naïve control and C2 inhibitor groups (*=p<0.05; ***=p<0.001). B) Nodal pan-NFasc clusters were significantly reduced in the isotype control group compared to naïve control (*=p<0.05). Nodal pan-NFasc clusters were protected in the C2 inhibitor group. C) Representative images demonstrate the presence of both nodal and paranodal pan-NFasc (magenta) in the naïve control group. Anti-GM1 mAb deposits (green) are present at the paranode (white arrowheads) in the isotype control group and paranodal pan-NFasc dimers are absent. On the other hand, both nodal and paranodal pan-NFasc are present in the C2 inhibitor group despite the presence of anti-GM1 mAb deposits. Scale bar = 5 µm. One-way ANOVA with Tukey's multiple comparisons test used to determine statistical significance. Results represented as average ± SEM. n=4 isotype control; n=3 naïve control and C2 inhibitor.

After determining that AnkB and NF155 were significantly protected following human C2 inhibition, I investigated the effects of complement inhibition on Caspr, the axonal binding partner of NF155 (Charles et al., 2002). The terminal complement product, MAC, was studied alongside Caspr to confirm that MAC pore formation had been inhibited in the C2 inhibitor group. The results in Figure 6.18A demonstrate that MAC deposits were present at 69 ± 6% of distal nerves in the isotype control group. This was significantly higher compared to both naïve control (0 ± 0%) and C2 inhibitor groups (9 ± 5%; $p<0.001$). There was no significant difference in MAC deposition between the NHS only group and C2 inhibitor group; therefore, confirming that formation of MAC pores had been prevented by blockade of C2.

When investigating the presence of Caspr dimers at the distal paranode, it was found that Caspr dimers were present at 96 ± 2% of paranodes in the naïve control group (Figure 6.18B). Conversely, the presence of Caspr dimers was significantly reduced to 20 ± 4% in the isotype control group ($p<0.001$). Treatment with the C2 inhibitor resulted in Caspr dimers being present at 58 ± 11% of distal paranodes. Although this was significantly lower in comparison to the naïve control group ($p<0.05$), this was significantly higher in comparison to the isotype control group ($p<0.01$). Therefore, C2 inhibition provides significant protection to Caspr dimers present on the axonal membrane at the paranode in this acute *in vivo* paranodal demyelinating injury model in *GalNAc-T$^{-/-}$-Tg(glial)* mice.

Overall, these results strongly indicate that C2 inhibition significantly attenuates injury to the axo-glial adhesion molecules on both the axonal and glial membranes at the paranode in this anti-GM1 mAb and complement-mediated *in vivo* paranodal demyelinating injury model.

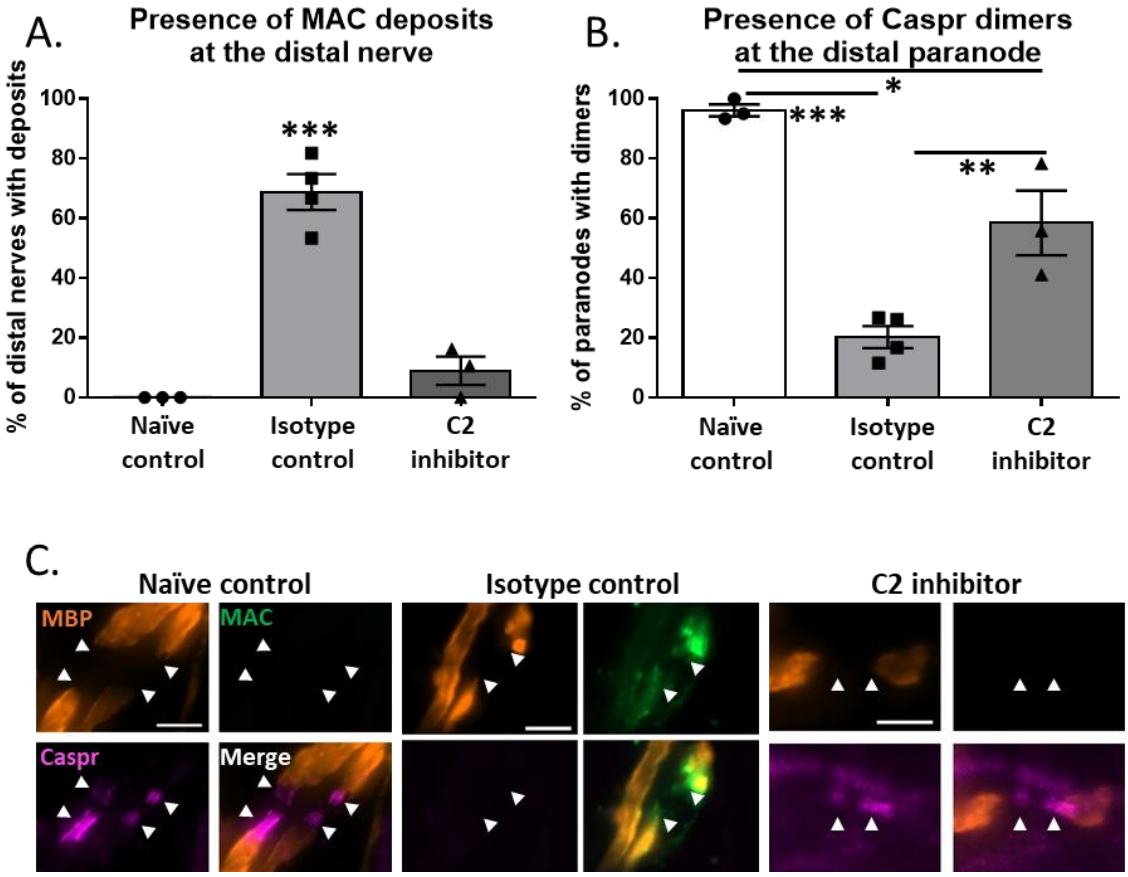

Figure 6.18: Effects of C2 inhibition on the presence of Caspr dimers at the distal paranode in *GalNAc-T$^{-/-}$-Tg(glial)* mice. *GalNAc-T$^{-/-}$-Tg(glial)* mice were injected intraperitoneally (IP) with 50 mg/kg anti-GM1 mAb. Sixteen hours later, mice received an intravenous injection of 200 mg/kg of C2 inhibitor (ARGX-117) or IgG1 isotype control, followed 10 minutes later by 30 µl/g normal human serum (NHS) IP. Naïve control mice received PBS only. Immunofluorescence analysis was performed on fixed diaphragm sections to assess the presence of the membrane attack complex (MAC) and consequent integrity of Caspr dimers on the axonal membrane at the paranode. A) MAC deposits were present at significantly more distal nerves in the isotype control group compared to naïve control and C2 inhibitor groups (***=p<0.001). There was no significant difference between the NHS only and C2 inhibitor groups. B) Caspr dimers were significantly reduced in the isotype control and C2 inhibitor groups compared to naïve control (*=p<0.05; ***=p<0.001). Caspr dimers were present at significantly more paranodes in the C2 inhibitor group compared to isotype control (**=p<0.01). C) Illustrative images show Caspr dimers (magenta) present at the paranode (white arrowheads) in the naïve control and C2 inhibitor group. In contrast, MAC deposits (green) are present overlying myelin basic protein (MBP; orange) in the isotype control group and there is a loss of Caspr dimers. Scale bar = 5 µm. One-way ANOVA with Tukey's multiple comparisons test was performed to test for statistical significance. Results represented as average ± SEM. n=4 isotype control; n=3 naïve control and C2 inhibitor.

6.3 Summary

In conclusion, inhibition of human C2 offers protection from nerve injury in both the anti-GM1 mAb dependent complement-mediated *ex vivo* axonal and paranodal demyelinating injury models. Furthermore, C2 inhibition provided protection to respiratory function and the integrity of axo-glial adhesion molecules in an *in vivo* anti-GM1 mAb and complement-mediated paranodal demyelinating injury model in *GalNAc-T$^{-/-}$-Tg(glial)* mice.

6.4 Discussion

It was hypothesised that complement may be involved in the pathogenesis of GBS following the discovery of complement deposits on the axonal membrane in patient autopsies with AMAN (Hafer-Macko et al., 1996a). The pathogenic action of complement at the NMJ and NoR was later demonstrated in various axonal and MFS animal models of GBS (Halstead et al., 2005, Halstead et al., 2004, Halstead et al., 2008, McGonigal et al., 2016, McGonigal et al., 2010, Susuki et al., 2007b). Patient autopsy findings have also demonstrated complement deposits on Schwann cell membranes and thus it is hypothesised that complement has a similar pathogenic role in AIDP (Hafer-Macko et al., 1996b). However, it has yet to be confirmed whether complement is involved in the pathogenesis of AIDP due to the limited availability of suitable animal models. Following the generation of the new anti-GM1 mAb and complement-mediated paranodal demyelinating injury model, representative of AIDP, I evaluated the efficacy of an anti-C2 humanised antibody (ARGX-117) both in our established axonal injury model in *GalNAc-T$^{-/-}$-Tg(neuronal)* mice and determined whether this attenuated injury in our newly developed paranodal demyelinating injury model in *GalNAc-T$^{-/-}$-Tg(glial)* mice.

In the last few decades, the complement pathway has become the focus for developing new therapeutics to treat GBS. Clinical trials are ongoing testing the efficacy of the anti-C5 antibody, Eculizumab, in GBS patients following the demonstration that it successfully attenuated injury in a mouse model of GBS (Halstead et al., 2008, Davidson et al., 2017, Misawa et al., 2018). As a result of these studies, Eculizumab has now been awarded SAKIGAKE fast-track status in Japan for use in GBS (Tanaka et al., 2021). The mechanisms of action of the drug involve inhibiting the formation of MAC pores in the membrane, and

therefore, as MAC is the terminal complement component common to all three complement pathways, this results in their blockage. As a consequence, this has been found to put patients treated with Eculizumab at potential risk of microbial infections, such as meningococcal disease (Cullinan et al., 2015, McNamara et al., 2017). Furthermore, anaphylatoxins (C3a and C5a) are still produced as a by-product from downstream complement components, despite the inhibition of MAC. Generation of anaphylatoxins results in potent proinflammatory effects, such as mediating cellular chemotaxis (Fernandez et al., 1978). Hence, targeting the early complement component, C2, with the anti-C2 humanised antibody (ARGX-117) overcomes these potential limitations, as does the use of anti-C1q as we previously reported below (McGonigal et al., 2016). ARGX-117 specifically inhibits the classical and lectin complement pathways, leaving the alternative complement pathway to respond to potential microbial infections. Additionally, ARGX-117 prevents the cleavage of C3 by intercepting the formation of the C3 convertase complex, C4bC2a; thereby, blocking formation of the harmful anaphylatoxin by-products (Van de Walle et al., 2020).

It has also been demonstrated that inhibition of the complement initiating complex, C1q, alleviates dysfunction and pathology in an *in vivo* axonal injury model in *GalNAc-T$^{-/-}$-Tg(neuronal)* mice (McGonigal et al., 2016). Consequently, clinical trials are now ongoing to test the safety and efficacy of C1q in patients with GBS (Islam et al., 2020)(Clinicaltrials.gov; NCT04035135). Here, I established that inhibition of C2 in an *ex vivo* axonal injury model in *GalNAc-T$^{-/-}$-Tg(neuronal)* mice, also results in neuroprotective effects at the NMJ. The considerations that might influence the use of different inhibitors at different stages of the early complement pathway are complex and beyond the scope of my studies. Issues including the half-lives, the distribution and quantities of the target molecules and the side effect profiles will come into play as the clinical programmes in these areas develop. The ARGX-117 mAb binds in a pH and Ca^{2+} dependent manner to C2 and the Fc region has been engineered to increase half-life. These features enable ARGX-117 to release C2 in the endosome to be degraded by lysosomes, and ARGX-117 to be recycled into the circulation to bind additional C2 molecules, leading to a longer serum half-life (Van de Walle et al., 2020). C2 also has a low concentration in comparison with other classical and lectin pathway components (Porter and Reid, 1979), thus requiring lower dosage of inhibitors. Overall, these properties make C2 an attractive therapeutic

target amongst the many complement components and inhibitors currently being studied (Mastellos et al., 2019).

Targeting C2 as a therapeutic target is a novel concept and so the effects of C2 inhibition have not been studied in humans. A phase 1 clinical trial is currently recruiting healthy participants to evaluate the safety and immunogenicity of ARGX-117 (ClinicalTrials.gov; NCT04532125). Nevertheless, ARGX-117 has been demonstrated to prevent complement-mediated cytotoxicity in an *in vitro* model for autoimmune haemolytic anaemia and antibody-mediated rejection of organ transplants (Van de Walle et al., 2020). Therefore, inhibition of the classical and lectin complement pathways by targeting C2 will be beneficial to treat diseases driven by complement fixing autoantibodies.

Following the characterization of the anti-GM1 mAb paranodal demyelinating injury model in *GalNAc-T*$^{-/-}$*-Tg(glial)* mice and determining that the injury outputs differ significantly depending on which membrane is targeted, the mechanism(s) involved in injury to the glial membrane was hypothesised to be complement-mediated (as discussed in Chapter 4). The results in this chapter indicate that disruption to the axo-glial adhesion molecules is a result of complement-mediated damage (outlined by schematic diagram in Figure 6.19). Taken together, it is hypothesised that binding of anti-GM1 mAb to the glial membrane, particularly at the paranodal loops, activates the complement pathway resulting in the formation of MAC pores in the glial membrane. As already established, MAC pores in the membrane induces the uncontrolled movement of water and ions, particularly calcium ions which subsequently, activates the calcium-dependent protease calpain [reviewed by (Morgan, 2016)]. Various components of the underlying cytoskeleton are known calpain substrates, including actin and AnkB present in the cytoplasmic paranodal loops. Therefore, it is likely that actin and AnkB are cleaved upon calpain activation. AnkB functions to stabilize the axo-glial junction by tethering NF155 to the F-actin cytoskeleton (Chang et al., 2014); thus, providing an explanation for the disruption to NF155. Furthermore, calpain is associated with the disruption of Caspr (McGonigal et al., 2010). The mislocalization of nodal and paranodal proteins is hypothesised to be a causal effect of proteolysis of the underlying subaxolemma cytoskeleton [reviewed by (Ma et al., 2013)], thus it is very likely that cleavage of the glial cytoskeleton would also result in the mislocalization of these proteins. Hence, providing an explanation for disruption to the axo-glial complex at the paranode, consisting of

NF155 on the glial membrane and Caspr and contactin1 on the axonal membrane. The significant damage to the paranodal junction could culminate in the detachment of the cytoplasmic paranodal loops, causing leakage of current from the paranodal region, reducing the safety factor for impulse transmission leading to conduction block (Uncini and Kuwabara, 2015).

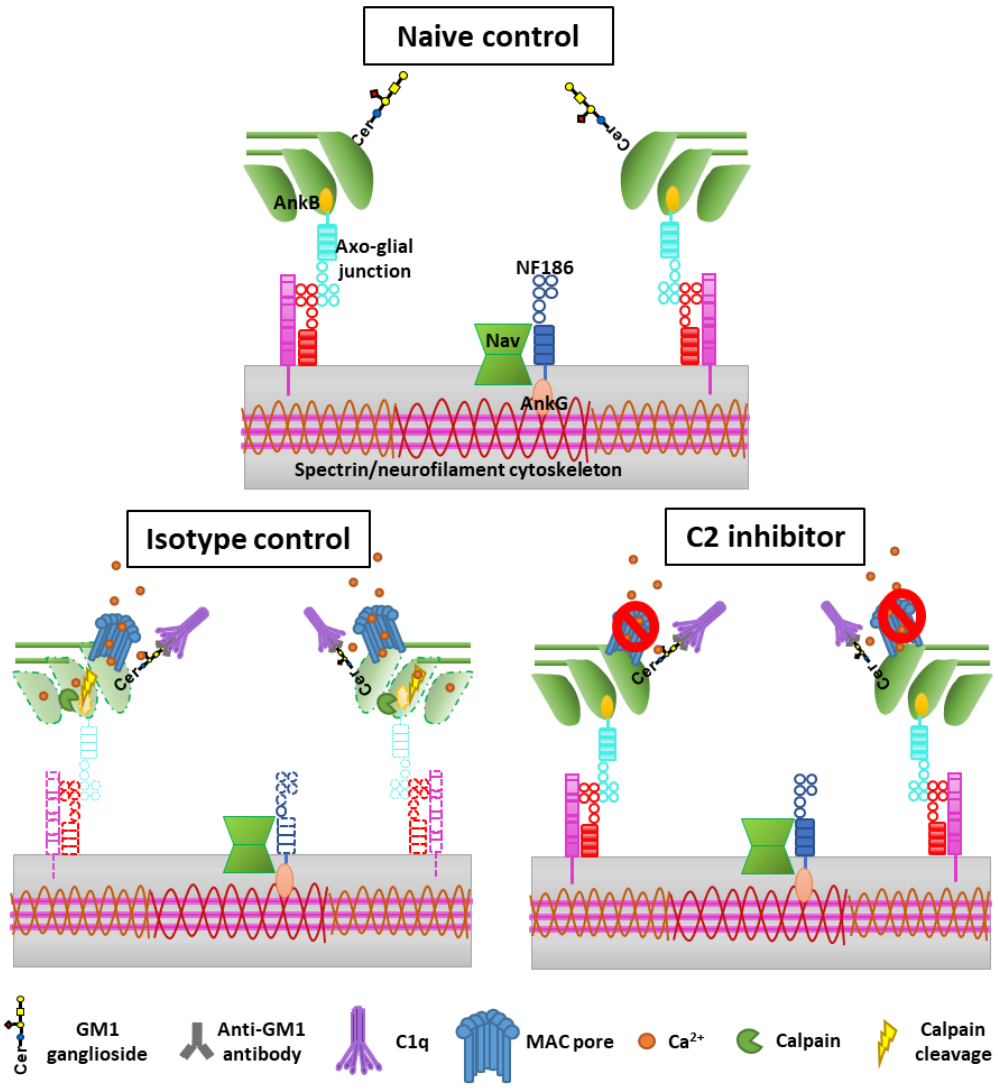

Figure 6.19: Schematic diagram of injury at the node of Ranvier in each treatment group.

The *in vitro* results demonstrate that the C2 inhibitor is extremely efficacious at blocking the classical pathway in a topical assay. A possible reason why there was no dose-dependent effect could be due to the low concentration of NHS (4%) used in the assay. C2 has the lowest serum concentration in comparison to the other components of the classical complement pathway (Porter and Reid, 1979); therefore, very low doses of inhibitor would be required to inhibit C2. For this reason, optimisation of the *in vitro* assay was difficult and thus, dose studies were performed in the *ex vivo* injury model

which uses a higher concentration of complement. There was some variation present in the anti-GM1 mAb and C3c intensities in the isotype control group from the *in vitro* assay, particularly at 50 μg/ml which differed significantly to the positive control for both anti-GM1 mAb and C3c intensity. The significantly reduced C3c intensity can be explained by the lower intensity of anti-GM1 mAb, indicating that there were fewer deposits of antibody present and therefore, fewer complement deposits. It is unclear why there were fewer anti-GM1 mAb deposits present when incubated with 50 μg/ml isotype control. The results from the *ex vivo* experiment suggest that the isotype control is not interfering with anti-GM1 mAb binding. Therefore, the reduced presence of anti-GM1 mAb deposits could be a result of biological variability.

The integrity of axo-glial adhesion molecules was significantly protected in the *in vivo* paranodal demyelinating injury model in *GalNAc-T$^{-/-}$-Tg(glial)* mice following C2 inhibition, although not to comparable levels of the naïve control group. An explanation for the difference between the naïve control group and C2 inhibitor group could be due to the low levels of C3c and MAC deposits still present in the C2 inhibitor group, indicating that complete inhibition of the complement pathway was not achieved. MAC pores are very efficient at lysing cells and rupturing the membrane, causing disruption to ionic homeostasis (Dourmashkin and Rosse, 1966). Therefore, it is not surprising that even low levels of MAC pore formation can cause major disruption to axo-glial adhesion molecules. Additionally, as ARGX-117 is specific for human C2, it was speculated that active mouse C2 could compensate for human C2 and interact with the human complement pathway, resulting in development of MAC pores. However, *in vitro* experiments that replicated the conditions of our *in vivo* model were performed by ARGX-117 to explore this possibility. The results demonstrated that mouse complement was not interacting with the human pathway when ARGX-117 was applied (data not shown). A possible explanation for this is because of the low levels of complement products in laboratory mice relative to humans (Ong and Mattes, 1989). We have demonstrated previously, the inability of complement fixing AGAbs to activate mouse complement in our injury models (Goodyear et al., 1999); hence, a heterologous source of complement is required in our injury models. Despite the difference in structural protection between naïve control and C2 inhibitor mice, the respiratory phenotype was attenuated following C2 inhibition to comparable levels with naïve control.

In addition, the neuroprotective effects of C2 inhibition demonstrated in the *ex vivo* paranodal demyelinating injury model in *GalNAc-T$^{-/-}$-Tg(glial)* mice was greater than that described in the *in vivo* model. A possible explanation for this is because the inhibitor was pre-mixed with NHS prior to applying to the tissue in the *ex vivo* model; however, in the *in vivo* model, the C2 inhibitor and NHS injections were administered via different delivery routes. Therefore, in the *ex vivo* model, the C2 inhibitor would have bound free circulating C2 that was present in the NHS prior to AGAb fully activating the complement pathway. Furthermore, in the *in vivo* model, the C2 inhibitor was administered straight into the blood stream but the NHS was injected into the peritoneum; thus, preventing immediate inhibition of complement. The protocol used in the *in vivo* model does not replicate what would happen in a clinical situation, as treatment would be administered following the induction of injury in the patient. Therefore, treatment would have to be administered early in the course of clinical presentation to mitigate further damage already caused by complement activation and development of MAC pores. Nevertheless, as our injury model uses NHS as a source of complement, our models are closely related to complement-mediated injury in patients. Furthermore, the inhibitor used in this experiment is specific for human C2 and thus, the neuroprotective effects of the drug are as a direct result of human complement inhibition, and it would be expected to have similar effects in patients. Future work would involve investigating the efficacy of C2 inhibition in the extended anti-GM1 mAb paranodal loop injury model, whereby the inhibitor would be given post injury.

Overall, the significant findings of this chapter are that C2 inhibition mitigates injury to the axo-glial adhesion molecules in an *in vivo* anti-GM1 mAb and complement-mediated paranodal demyelinating injury model. These results establish that damage to the paranodal loops in this injury model is mediated by complement fixation. Therefore, demonstrating for the first time that complement inhibition attenuates injury in a demyelinating model, representative of the demyelinating variant of syndromes associated with anti-GM1 antibodies like GBS and MMN. Additionally, C2 inhibition is likely to attenuate injury in any disease mediated by complement fixing autoantibodies. This outcome is very insightful for future clinical trials as it suggests that both AMAN and AIDP patients should be included in complement inhibition trials, along with future possibilities in MMN.

7 Discussion

The pathogenesis of AIDP and secondary bystander axonal injury are poorly understood due to the limited availability of suitable animal models, in comparison to the established mechanisms involved in primary axonal degeneration in AMAN. Both primary and secondary axonal degeneration are associated with a poor prognosis in GBS (Altmann et al., 2020, Martín-Aguilar et al., 2020); thus, understanding the diverse degenerative mechanisms is essential to develop targeted treatments to improve long-term prognosis.

It is considered that a peripheral nerve antigen drives the immune response in GBS, and evidence from patient serology and autopsy studies suggests the involvement of the complement system (Hafer-Macko et al., 1996a, Hafer-Macko et al., 1996b, Hartung et al., 1987). Evidence indicates that autoantibodies directed towards gangliosides, such as GM1, are responsible for the pathogenesis of GBS (Willison, 2018, Yuki et al., 2001, Yuki et al., 1990). GM1 antibodies predominantly bind to the motor axolemma, hence providing an explanation for the association between AMAN and GM1 antibodies (Yuki et al., 2001). However, AIDP patients with a preceding *C. jejuni* infection also have anti-GM1 antibodies present in their sera (Rees et al., 1995b). GM1 is expressed in both axonal and glial membranes in wild type mice (Gong et al., 2002, Sheikh et al., 1999, Susuki et al., 2007b); thus, providing an explanation for the presence of anti-GM1 antibodies in both the axonal and demyelinating variants of GBS. It is currently unknown whether the pathological phenotype mediated by anti-GM1 antibodies arises from injury to one or other, or both membranes in AMAN and AIDP. Current animal models are unable to segregate the differences between axonal and glial-directed anti-GM1 antibody attack.

Thus, the aim of this thesis was to use *GalNAc-T$^{-/-}$-Tg(neuronal)* and *GalNAc-T$^{-/-}$-Tg(glial)* mice to target the axonal and glial membranes independently of each other and subsequently, differentiate between injury to the axonal and glial membrane at the NoR. In addition, membrane-specificity of complex ganglioside expression allowed us to target the glial membrane independently of the axonal membrane in *GalNAc-T$^{-/-}$-Tg(glial)* mice, to determine whether secondary bystander axonal degeneration occurred. Furthermore, complement inhibition has been demonstrated to attenuate injury in animal models of AMAN (McGonigal et al., 2016, Phongsisay et al., 2008) but it has yet to be established whether this would be a suitable treatment for AIDP patients, due to the lack of

demyelinating injury models. Hence, the newly developed paranodal demyelinating injury model in *GalNAc-T$^{-/-}$-Tg(glial)* mice allowed us to also investigate the effects of complement inhibition.

7.1 Main findings

Below, I highlight the main findings of the thesis and discuss how they impact the wider field of GBS research.

7.1.1 Models of peripheral neuropathy

As mentioned previously, GM1 is expressed in both axonal and glial membranes in wild type mice, and therefore we are unable to differentiate between primary injury and the consequences of cell-specific membrane injury. The main aim of this thesis was thus, to generate and characterise injury in *GalNAc-T$^{-/-}$-Tg(neuronal)* and *GalNAc-T$^{-/-}$-Tg(glial)* mice following targeted injury to the axonal or glial membrane, respectively, with a single anti-GM1 mAb.

Direct injury to the axonal membrane in *GalNAc-T$^{-/-}$-Tg(neuronal)* mice resulted in the acute loss of axonal integrity and disruption of axonal structural proteins at the distal motor nerve terminal, comparable to previously published findings (McGonigal et al., 2016). Assessment of injury to the NoR revealed that there was significant disturbance to Nav clustering at the nodal gap. However, the axo-glial junction at the paranode remained largely intact in *GalNAc-T$^{-/-}$-Tg(neuronal)* mice. The disruption to the NoR was accompanied with a slight elongation to the nodal gap; possibly due to axonal membrane swelling as a result of uncontrolled influx of ions through MAC pores (Podack et al., 1982). As a consequence of this axonal injury, mice presented with functional loss in this acute injury paradigm, likely due to a combination of injury to the distal motor nerve terminal and disruption to Nav clusters at the distal nodal gap. Overall, these results highlight the importance of axonal integrity and suggest that AGAb-mediated injury directed to the axon is entirely responsible for injury to the nerve terminal. Moreover, the evidence presented in Chapter 4 suggests that nodal lengthening observed in early AMAN pathology (Griffin et al., 1996, Susuki et al., 2007b) is not due to detachment of the paranodal loops but instead, is an effect of injury to the axonal membrane. Overall,

GalNAc-T$^{-/-}$-Tg(neuronal) mice can be used to study the pathogenesis of primary axonal degeneration and to test appropriate treatment strategies.

The downstream mechanisms involved in demyelinating pathogenesis have yet to be established. However, patient autopsy studies demonstrated the presence of complement deposits on the outer surface of Schwann cells resulting in vesicular demyelination, prior to the invasion of macrophages into the myelin sheath (Hafer-Macko et al., 1996b). The authors hypothesised that complement was activated by antibodies binding to glycolipids in the abaxonal Schwann cell membrane. Antibodies to gangliosides, notably GM1, have been found in patients with AIDP, although no significant correlation has been determined (Rees et al., 1995a, Sinha et al., 2007). The anti-GM1 mAb-mediated paranodal demyelinating mouse model developed in this thesis utilised exclusive ganglioside expression in glia to target the glial membrane, independent of the axonal membrane. The aim was to generate a mouse model to investigate the consequent pathogenesis of glial membrane injury. Characterization of AGAb-mediated injury to the glial membrane demonstrated the formation of MAC pores in the Schwann cell membrane at the paranodal loops. It is hypothesised that this consequently leads to an influx of calcium ions, activating the calcium-dependent protease, calpain. Upon activation, calpain then cleaves components of the underlying cytoskeleton - actin and AnkB (as they are known calpain substrates (Villa et al., 1998, Boivin et al., 1990)). Cleavage of AnkB causes the detachment of the axo-glial junction, consisting of NF155 in the glial membrane bound to Caspr and contactin in the axonal membrane (Charles et al., 2002). The loss of the axo-glial junction from the paranodes leads to the mis-localisation of NF186 from the nodal gap and disruption to Kv1.1 at the juxtaparanode (Figure 7.1). This emphasises the importance of the axo-glial junction and suggests that the tethering of NF155 to the cytoskeleton via AnkB is crucial in maintaining the stability of the junction (Chang et al., 2014). Overall, these results highlight the structural damage which can occur to the NoR following AGAbs binding to the paranodal loops. It is possible that detachment of the paranodal loops could result in compact myelin vesiculation followed by macrophage infiltration, culminating in segmental demyelination. This is the first description of an AGAb-mediated paranodal demyelinating *in vivo* mouse model. Developing an animal model representative of the demyelinating variant was imperative to investigate the pathways involved in nodal injury. Not only will this model be beneficial for studying GBS pathogenesis, but this is relatable to any antibody-dependent,

complement-mediated immune attack in demyelinating PNS disorders, other than GBS. Detachment of the paranodal loops and conduction block are key events in nodopathies (Uncini and Kuwabara, 2015); therefore, this animal model closely resembles the early paranodal demyelinating features of nodopathies, such as GBS.

7.1.2 Mechanisms of secondary axonal degeneration

Secondary 'bystander' axonal degeneration is a characteristic of AIDP (Asbury et al., 1969, Feasby et al., 1993). In GBS, a poor prognosis is associated with axonal degeneration; demonstrated by recent studies that determined high serum levels of the axonal structural protein, neurofilament, was an indicator of poor patient outcome (Altmann et al., 2020). The pathogenesis of primary axonal degeneration is well understood due to numerous animal models that have uncovered the involvement of complement and calpain pathways (McGonigal et al., 2010, O'Hanlon et al., 2003, Willison et al., 2008). However, the mechanisms leading to secondary axonal degeneration in AIDP are unknown. A rodent model of EAN (animal model with features representative of AIDP) exhibited histological evidence of secondary axonal degeneration (Lonigro and Devaux, 2009). The authors did not comment on the possible mechanisms involved; however, there was strong evidence supporting nodal disturbance and cytoskeletal disorganisation. Peripheral nerve Schwann cells functions in establishing the molecular architecture of the NoR and cytoskeletal organisation [reviewed by (Moss et al., 2021)], and supplying trophic support to the axon [for review, see (Bouçanova and Chrast, 2020)]. Therefore, it is possible that injury to the paranodal cytoplasmic loops disturbs these functions, culminating in secondary injury to the axon. We used *GalNAc-T*$^{-/-}$*-Tg(glial)* mice to test this hypothesis, by selectively injuring the glial membrane, independently of the axonal membrane, and investigating the consequences to axon integrity.

In the acute injury model (6 hours), the axo-glial adhesion molecule on the axonal membrane, Caspr, was significantly disturbed. This was thought to be an indirect effect of detachment of NF155 from the glial cytoskeleton via calpain-mediated cleavage of AnkB. In addition, there was a moderate loss of NF186 at the nodal gap and Kv1.1 from the juxtaparanode; likely becoming mis-localised due to disruption of the axo-glial junction and loss of NF155 from the paranodes (illustrated in Figure 7.1). However, there was no evidence of axonal degeneration. In contrast, in the extended injury model (24 hours),

there was a reduction in neurofilament occupancy at the NoR, although this was not significantly different to control. A further reduction of NF186 was present, accompanied with significant disruption to Nav and AnkG at the nodal gap.

As mentioned previously, it is thought that peripheral nerve Schwann cells supply trophic support to the axon [reviewed by (Bouçanova and Chrast, 2020)]. It has been demonstrated that Schwann cells express glucose transporters and connexins; indicating that they may function in importing and exporting glucose and other metabolites and ions between the glial cytoplasm, the extracellular environment, and underlying axons. Thus, injury to the paranodal loops could disturb energy metabolism in the axon, leaving them susceptible to metabolic imbalances which induce secondary axonal degeneration. Another possible mechanism of secondary axonal degeneration is mitochondrial dysfunction [reviewed by (Moss et al., 2021)]. It has been demonstrated that demyelination alters mitochondrial transport (Kiryu-Seo et al., 2010). As mitochondria are critical in providing the energy required to maintain functional neural connections, impaired axonal transport of mitochondria could cause axon degeneration. Here, we hypothesise that one downstream mechanism resulting from the disturbance of Caspr (and most likely contactin) on the paranodal axolemma might be the formation of mechanopores in the axonal membrane, induced by mechanical strain (Kilinc et al., 2008, Kilinc et al., 2009). These mechanopores then function in the same way as MAC pores, allowing the uncontrolled influx of ions into the axolemma. The increased calcium influx activates calpain, which cleaves Nav, AnkG and the underlying axonal cytoskeleton, leading to secondary axonal degeneration. This hypothesis is illustrated in the schematic in Figure 7.1.

These results suggest that secondary ‘bystander’ injury to the axon occurs over time, following injury to the glial membrane. In relation to humans, antibody binding directly to the axon may occur, in addition to antibody binding the glial membrane, contributing to axonal injury. Overall, this evidence is a clear and compelling demonstration of secondary axonal degeneration occurring following exclusive AGAb-mediated injury to the paranodal loops and indicates the importance of the axo-glial junction in maintaining the molecular architecture of the NoR and its secondary influence on axon integrity. Moreover, this paranodal demyelinating mouse model using *GalNAc-T$^{-/-}$-Tg(glial)* mice will be an

invaluable tool to investigate the mechanisms of secondary axonal degeneration and trialling relevant therapeutics.

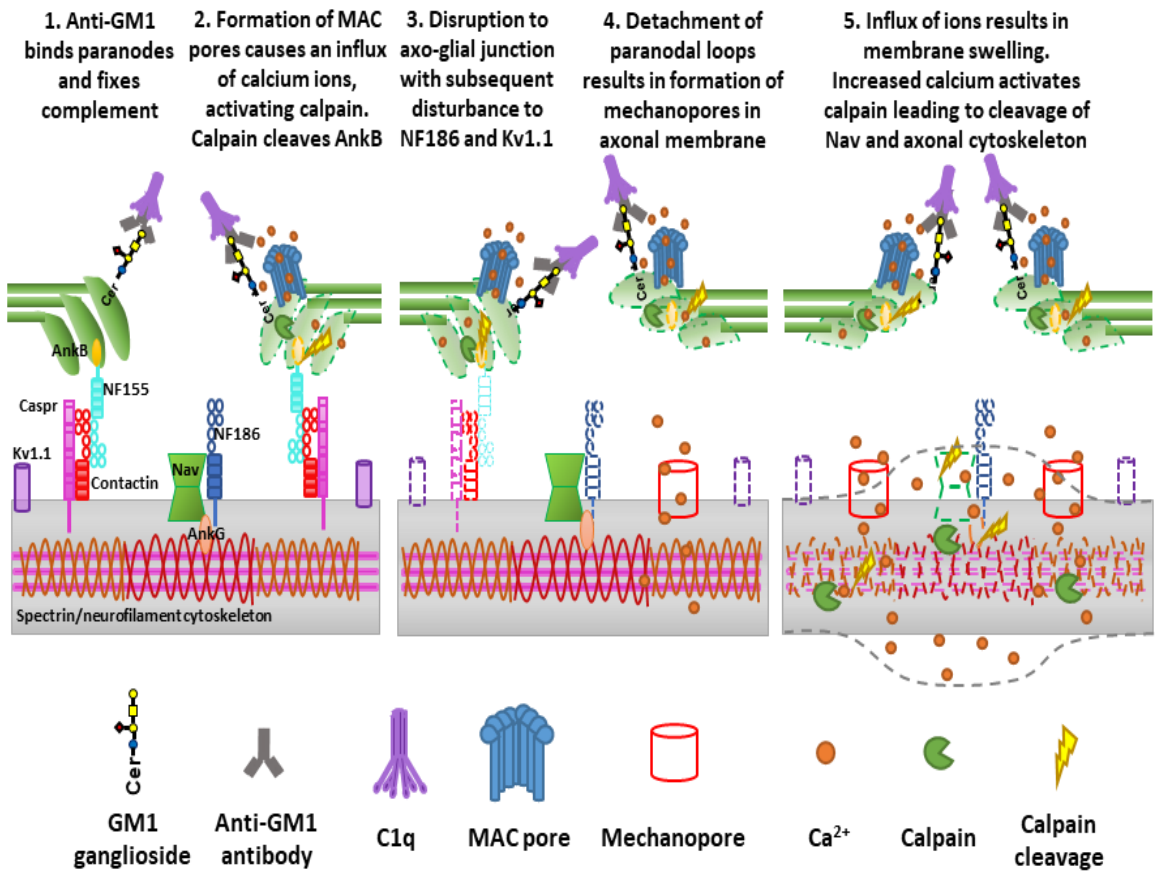

Figure 7.1: Hypothesised pathogenesis of AIDP and secondary axonal degeneration.

7.1.3 Attenuation of complement-mediated injury in a model of paranodal demyelinating peripheral neuropathy

Complement inhibition has been shown to attenuate axonal degeneration in murine mouse models of GBS (Halstead et al., 2008, McGonigal et al., 2016). Consequently, a C5 and a C1q inhibitor have progressed to clinical trials, demonstrating promising results (Davidson et al., 2017, Islam et al., 2020, Misawa et al., 2018, Misawa and Suichi, 2020). However, it has yet to be determined whether complement inhibition would be effective in preventing demyelinating pathology. Following the characterization of the anti-GM1 mAb-mediated paranodal demyelinating injury model, the protective effects of human C2 inhibition were studied. It was established that C2 inhibition mitigates injury to the axo-glial adhesion molecules and improves respiratory function in an *in vivo* paranodal demyelinating injury model.

These results demonstrate for the first time through direct experimentation that paranodal demyelination can occur via complement-dependent pathways. This supports the hypothesis that the early events in AIDP pathogenesis is the binding of complement-fixing antibodies to the surface of the Schwann cell, including paranodal loops (Hafer-Macko et al., 1996b). Although an antigenic target on peripheral nerve myelin has yet to be established in AIDP, *GalNAc-T$^{-/-}$-Tg(glial)* mice can be used to model the downstream consequences of complement activation on the glial membrane. In addition, this model of peripheral demyelination is representative of other syndromes associated with anti-GM1 antibodies like MMN (Pestronk et al., 1988); therefore, corroborating complement inhibition as a possible treatment for MMN patients (Vlam et al., 2013). Moreover, C2 inhibition is likely to attenuate injury in any disease mediated by complement fixing autoantibodies. This outcome is very insightful for future clinical trials as it suggests that both AMAN and AIDP patients should be included in complement inhibition trials.

7.2 Future work

7.2.1 Transgenic mice as experimental models

The generation of *GalNAc-T$^{-/-}$-Tg(neuronal)* and *GalNAc-T$^{-/-}$-Tg(glial)* mice offer the possibility to investigate whether both the axonal and demyelinating variants should be treated in the same way or whether individual treatment strategies are required. Furthermore, the *GalNAc-T$^{-/-}$-Tg(neuronal)* and *GalNAc-T$^{-/-}$-Tg(glial)* mice can be used to trial therapeutics for treating primary and secondary axonal degeneration, respectively.

Recently, we have generated a *GalNAc-T$^{-/-}$-Tg(neuronal)* x *GalNAc-T$^{-/-}$-Tg(glial)* double rescue mice (referred to as neuronal and glial double rescue mice), whereby ganglioside expression is rescued in both neural membranes. The aim is to use the neuronal and glial double rescue mice to investigate the binding patterns of different AGAbs and the consequent downstream mechanisms which occur when the target ganglioside is expressed on both axonal and glial membranes. As these mice do not have global ganglioside expression, it is hypothesised that they will overcome the limitations of using wild type mice for passive immunisation injury studies demonstrated previously (Cunningham et al., 2016), as antibody should not be sequestered. This is important as it

will help us better understand the behaviour of pathogenic antibodies and how they mediate disease in patients.

7.2.2 Investigate the downstream mechanisms involved in demyelinating pathology

Previous studies have demonstrated that calpain inhibition protects axonal integrity from AGAb-mediated injury to the motor nerve terminal (O'Hanlon et al., 2003) and to distal NoR (McGonigal et al., 2010); strongly indicating the involvement of calpain in the pathogenesis of primary axonal degeneration. However, the role of calpain in demyelinating pathology has yet to be determined. To address this, *GalNAc-T$^{-/-}$-Tg(glial)* mice could be used to determine whether inhibition of calpain would offer protection to AGAb-mediated injury to the glial membrane. It is hypothesised that calpain activation is responsible for cleaving AnkB and the underlying cytoskeleton in the paranodal cytoplasmic loops, leading to the mislocalization of the axo-glial junction and detachment of the paranodal loops; consequently, resulting in secondary axonal degeneration. Therefore, it is likely that calpain inhibition would attenuate injury to the glial cytoskeleton and axo-glial junction, protecting the integrity of the paranodal loops.

The development of the extended injury model in *GalNAc-T$^{-/-}$-Tg(glial)* mice also provides the opportunity to administer treatment, such as a complement inhibitor, following the onset of injury; mimicking what would happen in a clinical situation. Pilot studies would initially have to be performed to determine the optimal time between delivery of NHS and complement inhibitor. It is hypothesised that injury would still occur but treatment with the drug would mitigate further damage already caused by complement activation and development of MAC pores.

In addition, the extended injury model in *GalNAc-T$^{-/-}$-Tg(glial)* mice could be used to investigate whether paranodal loop injury leads to myelinating Schwann cell death, inducing segmental demyelination. Caspase-3 can be used as a marker of apoptosis in neural cells (Mukherjee and Williams, 2017); thus, to determine whether myelinating Schwann cells become apoptotic following injury to the paranodal loops, the presence of caspase 3 could be studied. Furthermore, immunoelectron microscopy could be performed to investigate the ultrastructure of compact myelin at complement positive paranodes/internodes. It is hypothesised that signs of vesicular demyelination will be

present along with the presence of macrophages which have been demonstrated to be recruited over 3-7 days post injury (Mueller et al., 2003, Taskinen and Röyttä, 1997).

7.2.3 Investigate the mechanisms involved in secondary axonal degeneration

The *GalNAc-T$^{-/-}$-Tg(glial)* mice will be invaluable tools to model secondary axonal degeneration and investigate the mechanisms involved. Future work would involve investigating the presence of mechanopores in the axonal membrane. There is evidence to support the presence of mechanopores in the axonal membrane in *in vivo* models of spinal cord contusion (Williams et al., 2014) and multiple sclerosis (Witte et al., 2019). In these studies, they demonstrated the uptake of fluorescently conjugated macromolecules in calcium-elevated axons. Therefore, investigating the uptake of fluorescent macromolecules in our extended *in vivo* injury model would be compelling, to determine whether pores in the axonal membrane are present. It is hypothesised that the macromolecules would enter through the mechanopores and fluorescence would be detected within the axolemma. However, the presence of MAC pores in the glial membrane complicates matters and it would be difficult to differentiate between fluorescent molecules in the axolemma with fluorescence in the glial cytoplasm. To overcome this, you could use a glial marker, such as S100, to differentiate between the membranes. In addition, pilot studies would have to be performed to determine the best route of delivery of the macromolecules.

The next step would be to investigate whether a calcium influx is present in the axolemma. One possibility to test this would be to use transgenic mice which endogenously express a fluorescence resonance energy transfer-based calcium biosensor in their neurons, termed Thy1-TNXXL (Mank et al., 2008, Mank et al., 2006). These mice exhibit a significantly enhanced fluorescence change in the presence of increased calcium levels that can be observed during *ex vivo* whole-mount or *in vivo* fluorescence imaging (Mank et al., 2008). The Thy1-TNXXL transgenic mice have been crossed with the *GalNAc-T$^{-/-}$-Tg(glial)* mice, with the aim to investigate the changes in axonal calcium levels following targeted injury to the glial membrane (Unpublished data). It is hypothesised that a fluorescence change would be observed in the axons of *GalNAc-T$^{-/-}$-Tg(glial)* mice, 24 hours after complement-mediated injury to the glial membrane; representative of an

increase of calcium into the axon via mechanopores. Following the influx of calcium ions in to the axolemma, it was considered that the protease, calpain, is activated. Thus, the next steps would be to assess axonal integrity following calpain inhibition in *GalNAc-T$^{-/-}$-Tg(glial)* mice. To achieve this, transgenic mice that overexpress human calpastatin (hCAST), an endogenous calpain inhibitor driven by a neuron specific promoter (Higuchi et al., 2005) could be crossed with *GalNAc-T$^{-/-}$-Tg(glial)* mice. This would allow us to explicitly investigate the consequence of axonal calpain inhibition on secondary axonal degeneration in *GalNAc-T$^{-/-}$-Tg(glial)* mice, without interfering with calpain-mediated injury to the glial membrane. To assess the effects of calpain inhibition, the extended *in vivo* injury model would be performed using hCAST x *GalNAc-T$^{-/-}$-Tg(glial)* mice and axonal integrity at 24 hours would be investigated.

In addition, the *GalNAc-T$^{-/-}$-Tg(glial)* mice could be used to investigate the involvement of other pathways hypothesised to be involved in the pathogenesis of secondary axonal degeneration, such as metabolic disruption, axonal transport, and mitochondrial dysfunction.

7.2.4 Characterize models mediated by human monoclonal antibodies

The *in vivo* models characterized in this thesis are mediated by mouse mAbs. To make the results more transferable to human disease, it would be beneficial to generate animal models mediated by human mAbs or IgG/IgM positive human sera. As demonstrated in chapter 3, the human mAb, BO3, cannot bind to GM1 in live tissue; thought to be due to interactions with other gangliosides within glycolipid rafts on the membrane preventing the antibody from binding. Greenshields and colleagues have previously overcome this issue with other mAbs by pre-treating an *ex vivo* TS preparation with neuraminidase (Greenshields et al., 2009). Treatment with neuraminidase cleaves the sialic acid (neuraminic acid) groups from the gangliosides (except the terminal sialic acid group), therefore creating *de novo* GM1. Following neuraminidase treatment, any antibody which was unable to bind due to steric hinderance between gangliosides, such as GM1 and GD1a (Greenshields et al., 2009), would bind to the membrane. If antibody successfully bound to the tissue following neuraminidase treatment, the next steps would be to determine whether the antibody could activate human complement. Neuraminidase

treated tissue would not be an accurate representation of membrane orientation in humans; however, it would provide a model to determine whether human mAb can activate complement and exert neuropathological effects.

7.3 Concluding remarks

These transgenic mice offer many potential roles in the investigation of AGAb mediated binding and injury at specific membrane sites. In patients, AGAb mediated injury occurs only on peripheral nerve membranes even though gangliosides are expressed ubiquitously. Therefore, the use of these mice can mimic the site-specific antibody targeting that is seen in human disease.

The results presented in this thesis demonstrate an animal model representative of AIDP pathology and can be used to study the downstream mechanisms involved following injury to the paranodal loops. Furthermore, these results provide evidence that secondary axonal degeneration occurs subsequently to paranodal demyelination, and the demyelinating injury model can be used to study the mechanisms involved. In addition, complement inhibition attenuated injury to the glial membrane; thereby demonstrating for the first time that complement inhibition would be effective in treating demyelinating neuropathies, such as GBS.

8 Appendices

8.1 Intensity analysis of antibody, complement and neurofilament at the neuromuscular junction

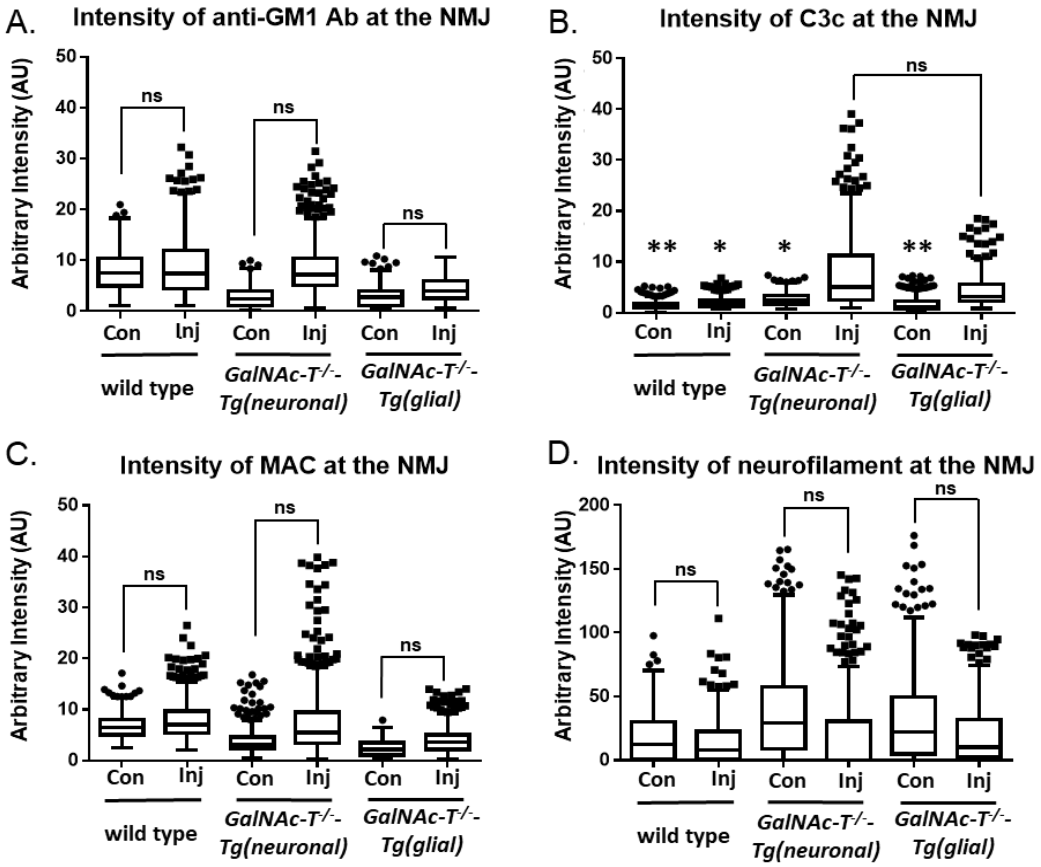

Figure 8.1: Intensity of antibody, complement and neurofilament at the neuromuscular junction. The diaphragm was harvested from wild type, *GalNAc-T$^{-/-}$-Tg(neuronal)* and *GalNAc-T$^{-/-}$-Tg(glial)* mice following intraperitoneal (IP) injection of 50 mg/kg anti-GM1 mAb followed 16 hours later with an IP injection of 30 µl/g normal human serum (NHS); control mice received PBS and NHS. Fresh frozen diaphragm was sectioned, and immunofluorescence analysis was performed. The intensity of anti-GM1 mAb, C3c, membrane attack complex (MAC), and neurofilament heavy (NFH), overlying the neuromuscular junction (NMJ) was determined and plotted as Tukey box and whisker plots. A) The intensity of anti-GM1 mAb was elevated in control and injured wild type mice and injured *GalNAc-T$^{-/-}$-Tg(neuronal)* mice compared to all other treatment groups, although not significantly. B) The mean C3c intensity in injured *GalNAc-T$^{-/-}$-Tg(neuronal)* mice was significantly higher compared to all other treatment groups, except injured *GalNAc-T$^{-/-}$-Tg(glial)* mice (*=p<0.05; **=p<0.01). C) The intensity of MAC overlying the NMJ was higher in injured groups compared to their respective controls, although not significantly. D) Control and injured wild type mice, injured *GalNAc-T$^{-/-}$-Tg(neuronal)* mice, and injured *GalNAc-T$^{-/-}$-Tg(glial)* mice had a reduced NFH intensity compared to both *GalNAc-T$^{-/-}$-Tg(neuronal)* and *GalNAc-T$^{-/-}$-Tg(glial)* control mice, although this was not significant. Results represent mean ±SEM. n=4/treatment/genotype. Two-way ANOVA with Tukey's multiple comparisons test was performed to test for statistical significance on mean intensity.

8.2 Presence of pNav clusters and Caspr dimers at the distal NoR in wild type mice

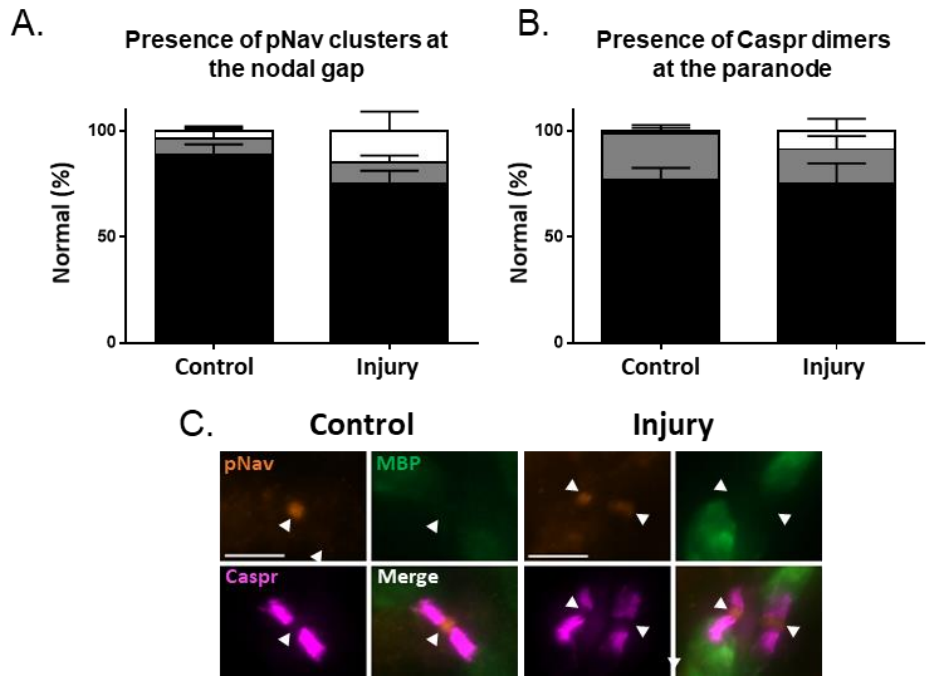

Figure 8.2: Assessment of pNav clusters and Caspr dimers at the distal NoR in wild type mice. Wild type mice were injected intraperitoneally (IP) with 50 mg/kg anti-GM1 mAb followed 16 hours later with an IP injection of 30 µl/g normal human serum (NHS). Control mice received PBS and NHS. Diaphragm was harvested at 6 hours post NHS injection and immunofluorescence analysis was performed on fresh frozen diaphragm. The presence of condition of pNav clusters and Caspr dimers were assessed and categorised into normal, abnormal, or absent. A) There were no significant differences in the presence of pNav clusters between control and injured mice. B) The percentage of normal, abnormal and absent Caspr dimers were comparable between control and injured wild type mice. C) Representative images illustrate pNav clusters (orange) at the nodal gap (white arrowhead, indicated by a gap in myelin basic protein staining (MBP; green)) and Caspr dimers (magenta) flanking the pNav clusters at the paranode in both control and injured mice. Scale bar = 5 µm. Two-way ANOVA with Tukey's multiple comparisons test was performed to test for significance. n=4/treatment.

8.3 Confirmation of anti-GM1 mAb in the circulation 40 hours after delivery

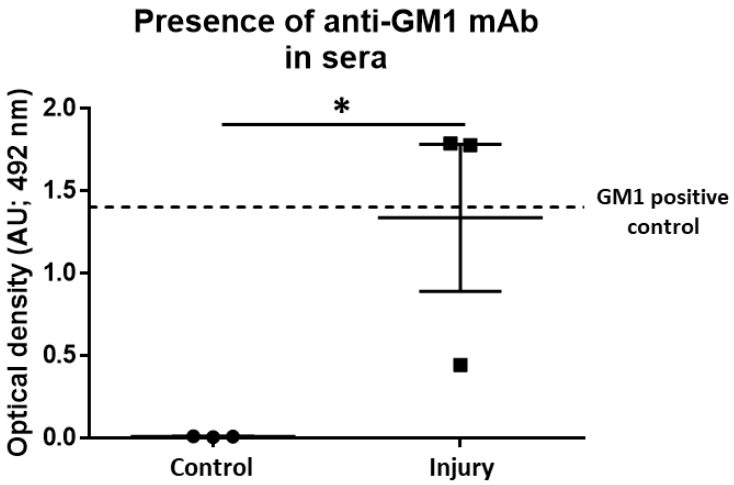

Figure 8.3: Confirmation of anti-GM1 mAb in the sera of *GalNAc-T$^{-/-}$-Tg(glial)* mice. *GalNAc-T$^{-/-}$-Tg(glial)* mice received an intraperitoneal (IP) injection of 50 mg/kg anti-GM1 mAb followed 16 hours later with an IP injection of 30 µl/g normal human serum (NHS). Control mice received PBS and NHS. A blood sample was collected 24-hours post NHS injection; and an ELISA was performed to confirm the presence of anti-GM1 mAb. Anti-GM1 mAb was used as a GM1 positive control (broken line). Anti-GM1 mAb was present in the sera of all injured mice as demonstrated by the positive optical density values (OD). The average OD value was significantly higher in the injury group compared to control mice (*=$p<0.05$). Results represent mean $\pm$ SEM. An unpaired t-test was performed to determine statistical significance. n=3/treatment.

8.4 *Ex vivo* C2 inhibition dose study at the neuromuscular junction

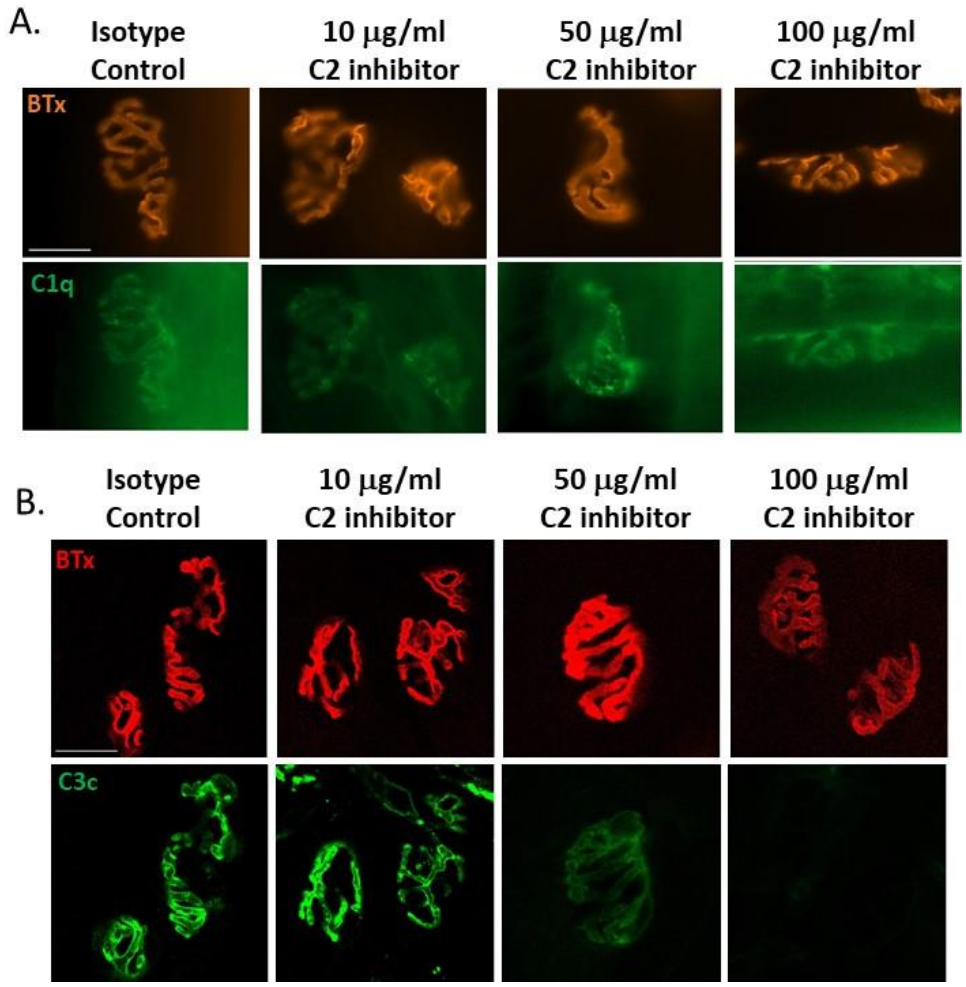

Figure 8.4: C2 inhibition dose study in 1-hour *ex vivo* injury model. The triangularis sterni muscle was harvested from *GalNAc-T*$^{-/-}$*-Tg(neuronal)* mice and incubated in 100 µg/ml anti-GM1 mAb, 40% normal human serum (NHS), as a source of complement, and either 10, 50 or 100 µg/ml of C2 inhibitor for 1 hour at 32°C. This injury paradigm targets the nerve terminal; therefore, immunoanalysis was performed and the presence of C1q and C3c deposits overlying the neuromuscular junction (NMJ) were assessed. A) The complement initiation complex, C1q, was stained for to confirm that the complement pathway had been activated. C1q deposits (green) were present overlying the NMJ (identified by BTx; orange) at every concentration. B) The early complement component, C3c, was stained for to determine whether C2 activation had been blocked. Illustrative images show that the intensity of C3c (green) at the NMJ (identified BTx, red) reduced when the concentration of C2 inhibitor increased. C3c deposits were absent when 100 µg/ml of the C2 inhibitor was applied and therefore this concentration was selected to use when targeting the NMJ in *ex vivo* experiments. Scale bar = 20 µm.

8.5 *Ex vivo* C2 inhibition dose study at the distal nerve

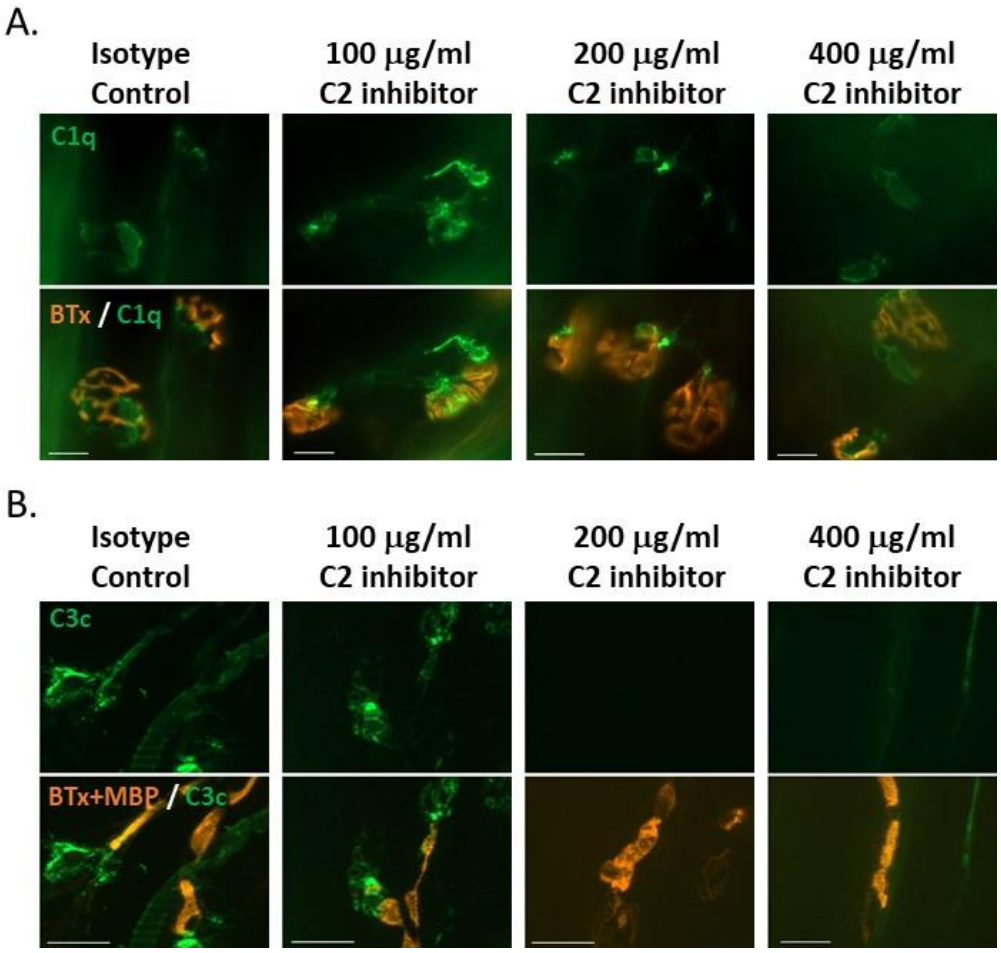

Figure 8.5: C2 inhibition dose study in 4-hour *ex vivo* injury model. The triangularis sterni muscle was harvested from *GalNAc-T*$^{-/-}$*-Tg(glial)* mice and incubated in 100 µg/ml anti-GM1 mAb, 40% normal human serum and either 100, 200 or 400 µg/ml C2 inhibitor for 4 hours at 32℃. This injury paradigm targets the distal nerve at the node of Ranvier (NoR); therefore, immunoanalysis was performed and the presence of C1q and C3c deposits overlying the neuromuscular junction (NMJ) distal nerve were assessed. A) C1q (green) was present surrounding the NMJ (identified by BTx; orange) and at the terminal heminode, indicating the complement pathway was activated in the presence of the C2 inhibitor. B) C3c deposits (green) were present surrounding the NMJ and the distal nerve (orange) in the isotype control and 100 µg/ml C2 inhibitor. C3c was absent when 200 and 400 µg/ml C2 inhibitor was applied, indicating that complement was inhibited at both concentrations. Therefore, 200 µg/ml C2 inhibitor was selected to use when targeting the NoR for *ex vivo* experiments. Scale bar = 20 µm.

8.6 *Ex vivo* comparison: Bro-2 vs ARGX-117

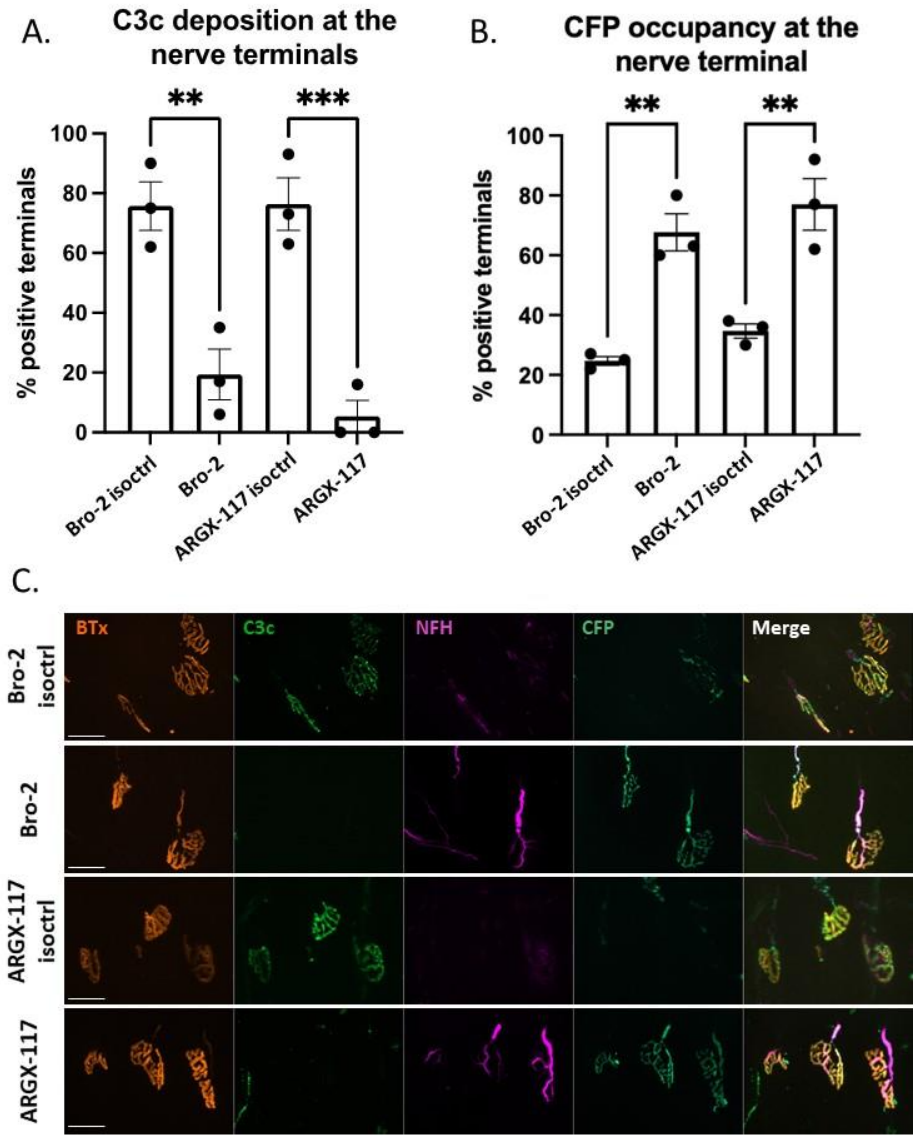

Figure 8.6: Comparison between the efficacy of Bro-2 and ARGX-117 in an *ex vivo* axonal injury model in *GalNAc-T$^{-/-}$-Tg(neuronal)* mice. The triangularis sterni muscle was harvested from *GalNAc-T$^{-/-}$-Tg(neuronal)* mice and incubated in 100 µg/ml anti-GM1 mAb, 40% normal human serum and 100 µg/ml of either Bro-2 or ARGX-117 for 1 hour at 32℃. Immunoanalysis was performed to assess the integrity of the axon at the nerve terminal. A) C3c was stained for to confirm inhibition of C2. The presence of C3c deposits was significantly reduced in both the Bro-2 and ARGX-117 treatment groups in comparison to their respective isotype controls (**=p<0.01; ***=p<0.001). B) The mice used in this experiment endogenously expressed cyan fluorescent protein (CFP) in their axons. The presence of CFP was used as a marker of axonal integrity. CFP was occupying significantly more nerve terminals in the Bro-2 and ARGX-117 treatment groups in comparison to their respective controls (**=p<0.01). C) Representative images illustrate the presence of C3c deposits (green) overlying the nerve terminal (BTx; orange) in both the Bro-2 and ARGX-117 isotype controls which corresponds to a loss of neurofilament (magenta) and CFP (cyan) staining. In contrast, C3c is absent from Bro-2 and ARGX-117 treatment groups and neurofilament and CFP are present occupying the nerve terminal. Scale bar = 20 µm. Statistical significance assessed by performing one-way ANOVA with Tukey's multiple comparisons test. Results presented ± SEM; n=3/treatment.

List of Abstracts

Clare I. Campbell, Rhona McGonigal, Madeleine E. Cunningham, Denggao Yao, Hugh J. Willison (2021). *Progress towards integrated mouse models of neuronal and glial membrane injury in anti-GM1 antibody-mediated neuropathy.* Peripheral Nerve Society (PNS) virtually anywhere meeting, Online, June 12-13 and 25-27, 2021.

Clare I. Campbell, Rhona McGonigal, Denggao Yao, Hugh J. Willison (2019). *Targeting axonal or glial membranes with anti-GM1 antibody to model axonal and demyelinating peripheral neuropathies.* PNS annual meeting, Italy, June 22-26, 2019.

Clare I. Campbell, Rhona McGonigal, Denggao Yao, Hugh J. Willison (2019). *Restricted expression of complex gangliosides to neurons or Schwann cells allows autoantibody targeting to specific axonal or glial membranes in peripheral neuropathy models.* 7th Molecular Mechanisms of Axon Degeneration meeting, Scotland, March 11-14, 2019.

Clare I. Campbell, Rhona McGonigal, Denggao Yao, Hugh J. Willison (2018). *Generation of novel transgenic mice with complex ganglioside expression restricted to either neuronal or glial membranes and their potential uses for modelling injury in axonal and demyelinating variants of Guillain-Barré syndrome.* Molecular Medicine of Sphingolipids meeting, Israel, October 14-19, 2018.

List of References

ACOSTA, J. A., BENZAQUEN, L. R., GOLDSTEIN, D. J., TOSTESON, M. T. & HALPERIN, J. A. 1996. The transient pore formed by homologous terminal complement complexes functions as a bidirectional route for the transport of autocrine and paracrine signals across human cell membranes. *Molecular Medicine,* 2**,** 755-765.

AGUILAR-NASCIMENTO, J. E. D. 2005. Fundamental steps in experimental design for animal studies. *Acta cirurgica brasileira,* 20**,** 2-3.

ALBERS, J. W., DONOFRIO, P. D. & MCGONAGLE, T. K. 1985. Sequential electrodiagnostic abnormalities in acute inflammatory demyelinating polyradiculoneuropathy. *Muscle & nerve,* 8**,** 528-539.

ALHINDI, A., BOEHM, I., FORSYTHE, R. O., MILLER, J., SKIPWORTH, R. J., SIMPSON, H., JONES, R. A. & GILLINGWATER, T. H. 2021. Terminal Schwann cells at the human neuromuscular junction. *Brain communications,* 3**,** fcab081.

ALTMANN, P., DE SIMONI, D., KAIDER, A., LUDWIG, B., RATH, J., LEUTMEZER, F., ZIMPRICH, F., HOEFTBERGER, R., LUNN, M. P. & HESLEGRAVE, A. 2020. Increased serum neurofilament light chain concentration indicates poor outcome in Guillain-Barré syndrome. *Journal of Neuroinflammation,* 17**,** 1-10.

AMOR, V., ZHANG, C., VAINSHTEIN, A., ZHANG, A., ZOLLINGER, D. R., ESHED-EISENBACH, Y., BROPHY, P. J., RASBAND, M. N. & PELES, E. 2017. The paranodal cytoskeleton clusters Na+ channels at nodes of Ranvier. *Elife,* 6**,** e21392.

ARTHUR-FARRAJ, P. J., LATOUCHE, M., WILTON, D. K., QUINTES, S., CHABROL, E., BANERJEE, A., WOODHOO, A., JENKINS, B., RAHMAN, M. & TURMAINE, M. 2012. c-Jun reprograms Schwann cells of injured nerves to generate a repair cell essential for regeneration. *Neuron,* 75**,** 633-647.

ASBURY, A. K., ARNASON, B. G. & ADAMS, R. D. 1969. The inflammatory lesion in idiopathic polyneuritis. *Medicine,* 48**,** 173.

ASBURY, A. K. & CORNBLATH, D. R. 1990. Assessment of current diagnostic criteria for Guillain-Barré syndrome. *Annals of Neurology: Official Journal of the American Neurological Association and the Child Neurology Society,* 27**,** S21-S24.

ATKINSON, J. P., DU CLOS, T. W., MOLD, C., KULKARNI, H., HOURCADE, D. & WU, X. 2019. The Human Complement System: Basic Concepts and Clinical Relevance. *Clinical Immunology.* Elsevier.

BARBI, L., COELHO, A. V. C., ALENCAR, L. C. A. D. & CROVELLA, S. 2018. Prevalence of Guillain-Barré syndrome among Zika virus infected cases: a systematic review and meta-analysis. *Brazilian Journal of Infectious Diseases,* 22**,** 137-141.

BEKKU, Y. & SALZER, J. L. 2020. Independent anterograde transport and retrograde cotransport of domain components of myelinated axons. *Journal of Cell Biology,* 219.

BERGHS, S., AGGUJARO, D., DIRKX, R., MAKSIMOVA, E., STABACH, P., HERMEL, J.-M., ZHANG, J.-P., PHILBRICK, W., SLEPNEV, V. & ORT, T. 2000. βIV spectrin, a new spectrin localized at axon initial segments and nodes of Ranvier in the central and peripheral nervous system. *The Journal of cell biology,* 151**,** 985-1002.

BHAT, M. A. 2003. Molecular organization of axo-glial junctions. *Current opinion in neurobiology,* 13**,** 552-559.

BHAT, M. A., RIOS, J. C., LU, Y., GARCIA-FRESCO, G. P., CHING, W., MARTIN, M. S., LI, J., EINHEBER, S., CHESLER, M. & ROSENBLUTH, J. 2001. Axon-glia interactions and the domain organization of myelinated axons requires neurexin IV/Caspr/Paranodin. *Neuron,* 30**,** 369-383.

BOHLSON, S. S., GARRED, P., KEMPER, C. & TENNER, A. J. 2019. Complement nomenclature-deconvoluted. *Frontiers in immunology,* 10**,** 1308.

BOIKO, T., RASBAND, M. N., LEVINSON, S. R., CALDWELL, J. H., MANDEL, G., TRIMMER, J. S. & MATTHEWS, G. 2001. Compact myelin dictates the differential targeting of two sodium channel isoforms in the same axon. *Neuron,* 30**,** 91-104.

BOIVIN, P., GALAND, C. & DHERMY, D. 1990. In vitro digestion of spectrin, protein 4.1 and ankyrin by erythrocyte calcium dependent neutral protease (calpain I). *International Journal of Biochemistry,* 22**,** 1479-1489.

BOUÇANOVA, F. & CHRAST, R. 2020. Metabolic interaction between Schwann cells and axons under physiological and disease conditions. *Frontiers in cellular neuroscience,* 14**,** 148.

BOWES, T., WAGNER, E. R., BOFFEY, J., NICHOLL, D., COCHRANE, L., BENBOUBETRA, M., CONNER, J., FURUKAWA, K., FURUKAWA, K. & WILLISON, H. J. 2002. Tolerance to self gangliosides is the major factor restricting the antibody response to lipopolysaccharide core oligosaccharides in Campylobacter jejuni strains associated with Guillain-Barre syndrome. *Infection and immunity,* 70**,** 5008-5018.

BOYD, J. G. & GORDON, T. 2003. Neurotrophic factors and their receptors in axonal regeneration and functional recovery after peripheral nerve injury. *Molecular neurobiology,* 27**,** 277-323.

BOYLE, M. E., BERGLUND, E. O., MURAI, K. K., WEBER, L., PELES, E. & RANSCHT, B. 2001. Contactin orchestrates assembly of the septate-like junctions at the paranode in myelinated peripheral nerve. *Neuron,* 30**,** 385-397.

BRETTLE, R., GROSS, M., LEGG, N., LOCKWOOD, M. & PALLIS, C. 1978. Treatment of acute polyneuropathy by plasma exchange. *The Lancet,* 312**,** 1100.

BROSTOFF, S., LEVIT, S. & POWERS, J. 1977. Induction of experimental allergic neuritis with a peptide from myelin P 2 basic protein. *Nature,* 268**,** 752-753.

BROWN, W. F. & SNOW, R. 1991. Patterns and severity of conduction abnormalities in Guillain-Barre syndrome. *Journal of Neurology, Neurosurgery & Psychiatry,* 54**,** 768-774.

BULLENS, R. W., O'HANLON, G. M., WAGNER, E., MOLENAAR, P. C., FURUKAWA, K., FURUKAWA, K., PLOMP, J. J. & WILLISON, H. J. 2002. Complex gangliosides at the neuromuscular junction are membrane receptors for autoantibodies and botulinum neurotoxin but redundant for normal synaptic function. *Journal of Neuroscience,* 22**,** 6876-6884.

CALUPCA, M. A., HENDRICKS, G. M., HARDWICK, J. C. & PARSONS, R. L. 1999. Role of mitochondrial dysfunction in the Ca2+-induced decline of transmitter release at K+-depolarized motor neuron terminals. *Journal of neurophysiology,* 81**,** 498-506.

CAMPBELL, A. 1958. The aetiology of polyneuritis. SAGE Publications.

CARESS, J. B., CASTORO, R. J., SIMMONS, Z., SCELSA, S. N., LEWIS, R. A., AHLAWAT, A. & NARAYANASWAMI, P. 2020. COVID-19–associated Guillain-Barré syndrome: The early pandemic experience. *Muscle & nerve,* 62**,** 485-491.

CARROLL, S. L. 2017. The molecular and morphologic structures that make saltatory conduction possible in peripheral nerve. *Journal of Neuropatholgy & Experimental Neurology,* 76**,** 255-257.

CATALA, M. & KUBIS, N. 2013. Gross anatomy and development of the peripheral nervous system. *Handbook of clinical neurology.* Elsevier.

CHANG, K.-J. & RASBAND, M. N. 2013. Excitable domains of myelinated nerves: axon initial segments and nodes of Ranvier. *Current topics in membranes.* Elsevier.

CHANG, K.-J., ZOLLINGER, D. R., SUSUKI, K., SHERMAN, D. L., MAKARA, M. A., BROPHY, P. J., COOPER, E. C., BENNETT, V., MOHLER, P. J. & RASBAND, M. N. 2014. Glial ankyrins facilitate paranodal axoglial junction assembly. *Nature neuroscience,* 17**,** 1673.

CHARLES, P., TAIT, S., FAIVRE-SARRAILH, C., BARBIN, G., GUNN-MOORE, F., DENISENKO-NEHRBASS, N., GUENNOC, A.-M., GIRAULT, J.-A., BROPHY, P. J. & LUBETZKI, C. 2002. Neurofascin is a glial receptor for the paranodin/Caspr-contactin axonal complex at the axoglial junction. *Current Biology,* 12**,** 217-220.

CHENG, S.-Y., WANG, S.-C., LEI, M., WANG, Z. & XIONG, K. 2018. Regulatory role of calpain in neuronal death. *Neural regeneration research,* 13**,** 556.

CHIAVEGATTO, S., SUN, J., NELSON, R. J. & SCHNAAR, R. L. 2000. A functional role for complex gangliosides: motor deficits in GM2/GD2 synthase knockout mice. *Experimental neurology,* 166**,** 227-234.

CHIBA, A., KUSUNOKI, S., OBATA, H., MACHINAMI, R. & KANAZAWA, I. 1993. Serum anti-GQ1b IgG antibody is associated with ophthalmoplegia in Miller Fisher syndrome and Guillain-Barré syndrome: clinical and immunohistochemical studies. *Neurology,* 43**,** 1911-1911.

CHIBA, A., KUSUNOKI, S., SHIMIZU, T. & KANAZAWA, I. 1992. Serum IgG antibody to ganglioside GQ1b is a possible marker of Miller Fisher syndrome. *Annals of Neurology: Official Journal of the American Neurological Association and the Child Neurology Society,* 31**,** 677-679.

CISTERNA, B. A., ARROYO, P. & PUEBLA, C. 2019. Role of connexin-based gap junction channels in communication of myelin sheath in schwann cells. *Frontiers in Cellular Neuroscience,* 13**,** 69.

COURT, F. A., GILLINGWATER, T. H., MELROSE, S., SHERMAN, D. L., GREENSHIELDS, K. N., MORTON, A. J., HARRIS, J. B., WILLISON, H. J. & RIBCHESTER, R. R. 2008. Identity, developmental restriction and reactivity of extralaminar cells capping mammalian neuromuscular junctions. *Journal of cell science,* 121**,** 3901-3911.

CULLINAN, N., GORMAN, K. M., RIORDAN, M., WALDRON, M., GOODSHIP, T. H. & AWAN, A. 2015. Case report: benefits and challenges of long-term eculizumab in atypical hemolytic uremic syndrome. *Pediatrics,* 135**,** e1506-e1509.

CUMMINGS, J. & HAAS, D. 1972. Animal model for human disease: Idiopathic polyneuritis, Guillain-Barré Syndrome. Animal model: Coonhound paralysis, idiopathic polyradiculoneuritis of coonhounds. *The American journal of pathology,* 66**,** 189.

CUNNINGHAM, M. E., MCGONIGAL, R., MEEHAN, G. R., BARRIE, J. A., YAO, D., HALSTEAD, S. K. & WILLISON, H. J. 2016. Anti-ganglioside antibodies are removed from circulation in mice by neuronal endocytosis. *Brain,* 139**,** 1657-1665.

CUNNINGHAM, M. E., MEEHAN, G. R., ROBINSON, S., YAO, D., MCGONIGAL, R. & WILLISON, H. J. 2020. Perisynaptic Schwann cells phagocytose nerve terminal debris in a mouse model of Guillain-Barré syndrome. *Journal of the Peripheral Nervous System,* 25**,** 143-151.

CUSTER, A. W., KAZARINOVA-NOYES, K., SAKURAI, T., XU, X., SIMON, W., GRUMET, M. & SHRAGER, P. 2003. The role of the ankyrin-binding protein NrCAM in node of Ranvier formation. *Journal of Neuroscience,* 23**,** 10032-10039.

DAILEY, A. T., AVELLINO, A. M., BENTHEM, L., SILVER, J. & KLIOT, M. 1998. Complement depletion reduces macrophage infiltration and activation during Wallerian degeneration and axonal regeneration. *Journal of Neuroscience,* 18**,** 6713-6722.

DALAKAS, M. C. 2002. Mechanisms of action of IVIg and therapeutic considerations in the treatment of acute and chronic demyelinating neuropathies. *Neurology,* 59**,** S13-S21.

DANEMAN, R. & PRAT, A. 2015. The blood–brain barrier. *Cold Spring Harbor perspectives in biology,* 7**,** a020412.

DAVIDSON, A. I., HALSTEAD, S. K., GOODFELLOW, J. A., CHAVADA, G., MALLIK, A., OVERELL, J., LUNN, M. P., MCCONNACHIE, A., DOORN, P. & WILLISON, H. J. 2017. Inhibition of complement in Guillain-Barré syndrome: the ICA-GBS study. *Journal of the Peripheral Nervous System,* 22**,** 4-12.

DAVIS, J. Q., MCLAUGHLIN, T. & BENNETT, V. 1993. Ankyrin-binding proteins related to nervous system cell adhesion molecules: candidates to provide transmembrane and intercellular connections in adult brain. *The Journal of cell biology,* 121**,** 121-133.

DE CHAVES, E. P. & SIPIONE, S. 2010. Sphingolipids and gangliosides of the nervous system in membrane function and dysfunction. *FEBS letters,* 584**,** 1748-1759.

DENISENKO-NEHRBASS, N., OGUIEVETSKAIA, K., GOUTEBROZE, L., GALVEZ, T., YAMAKAWA, H., OHARA, O., CARNAUD, M. & GIRAULT, J. A. 2003. Protein 4.1 B associates with both Caspr/paranodin and Caspr2 at paranodes and juxtaparanodes of myelinated fibres. *European Journal of Neuroscience,* 17**,** 411-416.

DESMAZIERES, A., ZONTA, B., ZHANG, A., WU, L.-M. N., SHERMAN, D. L. & BROPHY, P. J. 2014. Differential stability of PNS and CNS nodal complexes when neuronal neurofascin is lost. *Journal of Neuroscience,* 34**,** 5083-5088.

DEVAUX, J. 2014. New insights on the organization of the nodes of Ranvier. *Revue neurologique,* 170**,** 819-824.

DEVAUX, J. J., ODAKA, M. & YUKI, N. 2012. Nodal proteins are target antigens in Guillain-Barré syndrome. *Journal of the Peripheral Nervous System,* 17**,** 62-71.

DHADKE, S. V., DHADKE, V. N., BANGAR, S. S. & KORADE, M. B. 2013. Clinical profile of Guillain Barre syndrome. *J Assoc Physicians India,* 61**,** 168-72.

DICESARE, J. L. & DAIN, J. A. 1971. The enzymic synthesis of ganglioside: IV. UDP-N-acetylgalactosamine:(N-acetylneuraminyl)-galactosylglucosyl ceramide N-acetylgalactosaminyl-transferase in rat brain. *Biochimica et Biophysica Acta (BBA)-Lipids and Lipid Metabolism,* 231**,** 385-393.

DIONNE, A., NICOLLE, M. W. & HAHN, A. F. 2010. Clinical and electrophysiological parameters distinguishing acute-onset chronic inflammatory demyelinating polyneuropathy from acute inflammatory demyelinating polyneuropathy. *Muscle & Nerve: Official Journal of the American Association of Electrodiagnostic Medicine,* 41**,** 202-207.

DOPPLER, K., APPELTSHAUSER, L., VILLMANN, C., MARTIN, C., PELES, E., KRÄMER, H. H., HAARMANN, A., BUTTMANN, M. & SOMMER, C. 2016. Auto-antibodies to contactin-associated protein 1 (Caspr) in two patients with painful inflammatory neuropathy. *Brain,* 139**,** 2617-2630.

DOURMASHKIN, R. R. & ROSSE, W. F. 1966. Morphologic changes in the membranes of red blood cells undergoing hemolysis. *The American journal of medicine,* 41**,** 699-710.

ELDAR, A. H. & CHAPMAN, J. 2014. Guillain Barre syndrome and other immune mediated neuropathies: diagnosis and classification. *Autoimmunity reviews,* 13**,** 525-530.

ESHED, Y., FEINBERG, K., POLIAK, S., SABANAY, H., SARIG-NADIR, O., SPIEGEL, I., BERMINGHAM JR, J. R. & PELES, E. 2005. Gliomedin mediates Schwann cell-axon interaction and the molecular assembly of the nodes of Ranvier. *Neuron,* 47**,** 215-229.

FEASBY, T., GILBERT, J., BROWN, W., BOLTON, C., HAHN, A., KOOPMAN, W. & ZOCHODNE, D. 1986. An acute axonal form of Guillain-Barréé polyneuropathy. *Brain,* 109**,** 1115-1126.

FEASBY, T., HAHN, A., BROWN, W., BOLTON, C., GILBERT, J. & KOOPMAN, W. 1993. Severe axonal degeneration in acute Guillain-Barré syndrome: evidence of two different mechanisms? *Journal of the neurological sciences,* 116**,** 185-192.

FERNANDEZ, H. N., HENSON, P. M., OTANI, A. & HUGLI, T. E. 1978. Chemotactic response to human C3a and C5a anaphylatoxins: I. Evaluation of C3a and C5a leukotaxis in vitro and under simulated in vivo conditions. *The Journal of Immunology,* 120**,** 109-115.

FEWOU, S. N., RUPP, A., NICKOLAY, L. E., CARRICK, K., GREENSHIELDS, K. N., PEDIANI, J., PLOMP, J. J. & WILLISON, H. J. 2012. Anti-ganglioside antibody internalization attenuates motor nerve terminal injury in a mouse model of acute motor axonal neuropathy. *The Journal of clinical investigation,* 122**,** 1037-1051.

FISHER, M. 1956. An unusual variant of acute idiopathic polyneuritis (syndrome of ophthalmoplegia, ataxia and areflexia). *New England Journal of Medicine,* 255**,** 57-65.

FREEMAN, S. A., DESMAZIÈRES, A., FRICKER, D., LUBETZKI, C. & SOL-FOULON, N. 2016. Mechanisms of sodium channel clustering and its influence on axonal impulse conduction. *Cellular and Molecular Life Sciences,* 73**,** 723-735.

GABRIEL, C., GREGSON, N. & HUGHES, R. 2000. Anti-PMP22 antibodies in patients with inflammatory neuropathy. *Journal of the Peripheral Nervous System,* 5**,** 239-239.

GABRIEL, C., HUGHES, R., MOORE, S., SMITH, K. & WALSH, F. 1998. Induction of experimental autoimmune neuritis with peripheral myelin protein-22. *Brain: a journal of neurology,* 121**,** 1895-1902.

GANSER, A. L., KIRSCHNER, D. A. & WILLINGER, M. 1983. Ganglioside localization on myelinated nerve fibres by cholera toxin binding. *Journal of neurocytology,* 12**,** 921-938.

GEDDES, J. W. & SAATMAN, K. E. 2010. Targeting individual calpain isoforms for neuroprotection. *Experimental neurology,* 226**,** 6.

GHOSH, A., SHERMAN, D. L. & BROPHY, P. J. 2018. The axonal cytoskeleton and the assembly of nodes of Ranvier. *The Neuroscientist,* 24**,** 104-110.

GOLDMAN, M., SMITH, H. & ULMER, W. 2005. Whole-body plethysmography. *European Respiratory Monograph,* 31**,** 15.

GOLL, D. E., THOMPSON, V. F., LI, H., WEI, W. & CONG, J. 2003. The calpain system. *Physiological reviews*.

GOLLAN, L., SABANAY, H., POLIAK, S., BERGLUND, E. O., RANSCHT, B. & PELES, E. 2002. Retention of a cell adhesion complex at the paranodal junction requires the cytoplasmic region of Caspr. *The Journal of cell biology,* 157**,** 1247-1256.

GONG, Y., TAGAWA, Y., LUNN, M., LAROY, W., HEFFER-LAUC, M., LI, C., GRIFFIN, J., SCHNAAR, R. L. & SHEIKH, K. A. 2002. Localization of major gangliosides in the PNS: implications for immune neuropathies. *Brain,* 125**,** 2491-2506.

GOODFELLOW, J. A., BOWES, T., SHEIKH, K., ODAKA, M., HALSTEAD, S. K., HUMPHREYS, P. D., WAGNER, E. R., YUKI, N., FURUKAWA, K. & FURUKAWA, K. 2005. Overexpression of GD1a ganglioside sensitizes motor nerve terminals to anti-GD1a antibody-mediated injury in a model of acute motor axonal neuropathy. *Journal of Neuroscience,* 25**,** 1620-1628.

GOODFELLOW, J. A. & WILLISON, H. J. 2016. Guillain-Barre syndrome: a century of progress. *Nature Reviews Neurology,* 12**,** 723-731.

GOODYEAR, C. S., O'HANLON, G. M., PLOMP, J. J., WAGNER, E. R., MORRISON, I., VEITCH, J., COCHRANE, L., BULLENS, R. W., MOLENAAR, P. C. & CONNER, J. 1999. Monoclonal antibodies raised against Guillain-Barré syndrome–associated Campylobacter jejuni lipopolysaccharides react with neuronal gangliosides and paralyze muscle-nerve preparations. *Journal of Clinical Investigation,* 104**,** 697.

GREENSHIELDS, K. N., HALSTEAD, S. K., ZITMAN, F. M., RINALDI, S., BRENNAN, K. M., O'LEARY, C., CHAMBERLAIN, L. H., EASTON, A., ROXBURGH, J. & PEDIANI, J. 2009. The neuropathic potential of anti-GM1 autoantibodies is regulated by the local glycolipid environment in mice. *The Journal of clinical investigation,* 119**,** 595.

GRIFFIN, J., LI, C., HO, T., TIAN, M., GAO, C., XUE, P., MISHU, B., CORNBLATH, D., MACKO, C. & MCKHANN, G. 1996. Pathology of the motor-sensory axonal Guillain-Barré syndrome. *Annals of neurology,* 39**,** 17-28.

GRIFFIN, J., LI, C., HO, T., XUE, P., MACKO, C., GAO, C., YANG, C., TIAN, M., MISHU, B. & CORNBLATH, D. 1995. Guillain-Barré syndrome in northern China: the spectrum of neuropathological changes in clinically defined cases. *Brain,* 118**,** 577-595.

GUILLAIN-BARRÉ SYNDROME STUDY GROUP, G. S. G. 1985. Plasmapheresis and acute Guillain-Barré syndrome. *Neurology,* 35**,** 1096-1096.

GUILLAIN, G., BARRÉ, J. & STROHL, A. Radiculoneuritis syndrome with hyperalbuminosis of cerebrospinal fluid without cellular reaction. Notes on clinical features and graphs of tendon reflexes. 1916. Annales de medecine interne, 1916. 24.

GUYTON, A. C. 1947. Measurement of the respiratory volumes of laboratory animals. *American Journal of Physiology-Legacy Content,* 150**,** 70-77.

HADDEN, R., CORNBLATH, D., HUGHES, R., ZIELASEK, J., HARTUNG, H. P., TOYKA, K. & SWAN, A. 1998. Electrophysiological classification of guillain-barré syndrome: Clinical associations and outcome. *Annals of neurology,* 44**,** 780-788.

HAFER-MACKO, C., HSIEH, S. T., HO, T. W., SHEIKH, K., CORNBLATH, D. R., LI, C. Y., MCKHANN, G. M., ASBURY, A. K. & GRIFFIN, J. W. 1996a. Acute motor axonal neuropathy: an antibody-mediated attack on axolemma. *Annals of neurology,* 40**,** 635-644.

HAFER-MACKO, C., SHEIKH, K., LI, C., HO, T., CORNBLATH, D., MCKHANN, G., ASBURY, A. & GRIFFIN, J. 1996b. Immune attack on the Schwann cell surface in acute inflammatory demyelinating polyneuropathy. *Annals of Neurology: Official Journal of the American Neurological Association and the Child Neurology Society,* 39**,** 625-635.

HALSTEAD, S. K., KALNA, G., ISLAM, M. B., JAHAN, I., MOHAMMAD, Q. D., JACOBS, B. C., ENDTZ, H. P., ISLAM, Z. & WILLISON, H. J. 2016. Microarray screening of Guillain-Barré syndrome sera for antibodies to glycolipid complexes. *Neurology-Neuroimmunology Neuroinflammation,* 3.

HALSTEAD, S. K., MORRISON, I., O'HANLON, G. M., HUMPHREYS, P. D., GOODFELLOW, J. A., PLOMP, J. J. & WILLISON, H. J. 2005. Anti-disialosyl antibodies mediate selective neuronal or Schwann cell injury at mouse neuromuscular junctions. *Glia,* 52**,** 177-189.

HALSTEAD, S. K., O'HANLON, G. M., HUMPHREYS, P. D., MORRISON, D. B., MORGAN, B. P., TODD, A. J., PLOMP, J. J. & WILLISON, H. J. 2004. Anti-disialoside antibodies kill perisynaptic Schwann cells and damage motor nerve terminals via membrane attack complex in a murine model of neuropathy. *Brain,* 127**,** 2109-2123.

HALSTEAD, S. K., ZITMAN, F. M., HUMPHREYS, P. D., GREENSHIELDS, K., VERSCHUUREN, J. J., JACOBS, B. C., ROTHER, R. P., PLOMP, J. J. & WILLISON, H. J. 2008. Eculizumab prevents anti-ganglioside antibody-mediated neuropathy in a murine model. *Brain,* 131**,** 1197-1208.

HANSSON, H.-A., HOLMGREN, J. & SVENNERHOLM, L. 1977. Ultrastructural localization of cell membrane GM1 ganglioside by cholera toxin. *Proceedings of the National Academy of Sciences,* 74**,** 3782-3786.

HARTUNG, H.-P., SCHWENKE, C., BITTER-SUERMANN, D. & TOYKA, K. V. 1987. Guillain-Barre syndrome: activated complement components C3a and C5a in CSF. *Neurology,* 37**,** 1006-1006.

HASTINGS, R. L., MIKESH, M., IL LEE, Y. & THOMPSON, W. J. 2020. Morphological remodeling during recovery of the neuromuscular junction from terminal Schwann cell ablation in adult mice. *Scientific Reports,* 10**,** 1-13.

HAYMAKER, W. & KEBNOHAN, J. W. 1949. The Landry-Guillain-Barré syndrome: a clinicopathologic report of fifty fatal cases and a critique of the literature. *Medicine,* 28**,** 59.

HIGUCHI, M., TOMIOKA, M., TAKANO, J., SHIROTANI, K., IWATA, N., MASUMOTO, H., MAKI, M., ITOHARA, S. & SAIDO, T. C. 2005. Distinct mechanistic roles of calpain and caspase activation in neurodegeneration as revealed in mice overexpressing their specific inhibitors. *Journal of Biological Chemistry,* 280**,** 15229-15237.

HO, T., HSIEH, S.-T., NACHAMKIN, I., WILLISON, H., SHEIKH, K., KIEHLBAUCH, J., FLANIGAN, K., MCARTHUR, J. C., CORNBLATH, D. & MCKHANN, G. 1997. Motor nerve terminal degeneration provides a potential mechanism for rapid recovery in acute motor axonal neuropathy after Campylobacter infection. *Neurology,* 48**,** 717-724.

HO, T., MISHU, B., LI, C., GAO, C., CORNBLATH, D., GRIFFIN, J., ASBURY, A., BLASER, M. & MCKHANN, G. 1995. Guillain-Barre syndrome in northern China Relationship to Campylobacter jejuni infection and anti-glycolipid antibodies. *Brain,* 118**,** 597-605.

HO, T., WILLISON, H., NACHAMKIN, I., LI, C., VEITCH, J., UNG, H., WANG, G., LIU, R., CORNBLATH, D. & ASBURY, A. 1999. Anti-GD1a antibody is associated with axonal but not demyelinating forms of Guillain-Barre syndrome. *Annals of neurology,* 45**,** 168-173.

HOLMGREN, J., LÖNNROTH, I., MÅNSSON, J. & SVENNERHOLM, L. 1975. Interaction of cholera toxin and membrane GM1 ganglioside of small intestine. *Proceedings of the National Academy of Sciences,* 72**,** 2520-2524.

HOLMGREN, J., LÖNNROTH, I. & SVENNERHOLM, L. 1973. Tissue receptor for cholera exotoxin: postulated structure from studies with GM1 ganglioside and related glycolipids. *Infection and immunity,* 8**,** 208-214.

HORRESH, I., BAR, V., KISSIL, J. L. & PELES, E. 2010. Organization of myelinated axons by Caspr and Caspr2 requires the cytoskeletal adapter protein 4.1 B. *Journal of Neuroscience,* 30**,** 2480-2489.

HUEBNER, E. A. & STRITTMATTER, S. M. 2009. Axon regeneration in the peripheral and central nervous systems. *Cell biology of the axon.* Springer.

HUGHES, R., SANDERS, E., HALL, S., ATKINSON, P., COLCHESTER, A. & PAYAN, P. 1992. Subacute idiopathic demyelinating polyradiculoneuropathy. *Archives of Neurology,* 49**,** 612-616.

HUGHES, R. A., SWAN, A. V., RAPHAËL, J.-C., ANNANE, D., VAN KONINGSVELD, R. & VAN DOORN, P. A. 2007. Immunotherapy for Guillain-Barré syndrome: a systematic review. *Brain,* 130**,** 2245-2257.

ILYAS, A., WILLISON, H., QUARLES, R., JUNGALWALA, F., CORNBLATH, D., TRAPP, B., GRIFFIN, D., GRIFFIN, J. & MCKHANN, G. 1988. Serum antibodies to gangliosides in Guillain-Barre syndrome. *Annals of neurology,* 23**,** 440-447.

IOGHEN, O., MANOLE, E., GHERGHICEANU, M., POPESCU, B. O. & CEAFALAN, L. C. 2020. Non-Myelinating Schwann Cells in Health and Disease. *Schwann Cells.* IntechOpen.

ISLAM, Z., PAPRI, N., JAHAN, I., AZAD, K. A. K., KROON, H.-A., HUMPHRISS, E., SANKARANARAYANAN, S., YEDNOCK, T., KESWANI, S. & MOHAMMAD, Q. D. 2020. Inhibition of C1q, Initiator of the Classical Complement Cascade, by ANX005 for the Treatment of Guillain-Barré Syndrome: Results from a Phase 1b Study (763). AAN Enterprises.

JACOBS, B., ROTHBARTH, P., VAN DER MECHÉ, F., HERBRINK, P., SCHMITZ, P., DE KLERK, M. & VAN DOORN, P. 1998. The spectrum of antecedent infections in Guillain-Barré syndrome: a case-control study. *Neurology,* 51**,** 1110-1115.

JANEWAY JR, C. A., TRAVERS, P., WALPORT, M. & SHLOMCHIK, M. J. 2001. The complement system and innate immunity.

KABIR, M. M., BEIG, M. I., BAUMERT, M., TROMBINI, M., MASTORCI, F., SGOIFO, A., WALKER, F. R., DAY, T. A. & NALIVAIKO, E. 2010. Respiratory pattern in awake rats: effects of motor activity and of alerting stimuli. *Physiology & behavior,* 101**,** 22-31.

KAIDA, K. 2016. Autoantibodies in Guillain-Barré Syndrome (GBS). *Neuroimmunological Diseases.* Springer.

KAIDA, K., KAMAKURA, K., OGAWA, G., UEDA, M., MOTOYOSHI, K., ARITA, M. & KUSUNOKI, S. 2008. GD1b-specific antibody induces ataxia in Guillain-Barré syndrome. *Neurology,* 71**,** 196-201.

KAIDA, K., KUSUNOKI, S., KAMAKURA, K., MOTOYOSHI, K. & KANAZAWA, I. 2000. Guillain-Barré syndrome with antibody to a ganglioside, N-acetylgalactosaminyl GD1a. *Journal of the Peripheral Nervous System,* 5**,** 237-237.

KAIDA, K. I., MORITA, D., KANZAKI, M., KAMAKURA, K., MOTOYOSHI, K., HIRAKAWA, M. & KUSUNOKI, S. 2004. Ganglioside complexes as new target antigens in Guillain–Barré syndrome. *Annals of neurology,* 56**,** 567-571.

KALDOR, J. & SPEED, B. 1984. Guillain-Barré syndrome and Campylobacter jejuni: a serological study. *Br Med J (Clin Res Ed),* 288**,** 1867-1870.

KAMAKURA, K., ISHIURA, S., SUGITA, H. & TOYOKURA, Y. 1983. Identification of Ca2+-activated neutral protease in the peripheral nerve and its effects on neurofilament degeneration. *Journal of Neurochemistry,* 40**,** 908-913.

KANDA, T. 2013. Biology of the blood–nerve barrier and its alteration in immune mediated neuropathies. *Journal of Neurology, Neurosurgery & Psychiatry,* 84**,** 208-212.

KAWAI, H., ALLENDE, M. L., WADA, R., KONO, M., SANGO, K., DENG, C., MIYAKAWA, T., CRAWLEY, J. N., WERTH, N. & BIERFREUND, U. 2001. Mice expressing only monosialoganglioside GM3 exhibit lethal audiogenic seizures. *Journal of Biological Chemistry,* 276**,** 6885-6888.

KEDDIE, S., PAKPOOR, J., MOUSELE, C., PIPIS, M., MACHADO, P. M., FOSTER, M., RECORD, C. J., KEH, R. Y., FEHMI, J. & PATERSON, R. W. 2021. Epidemiological and cohort study finds no association between COVID-19 and Guillain-Barré syndrome. *Brain,* 144**,** 682-693.

KEMPER, C., PANGBURN, M. K. & FISHELSON, Z. 2014. Complement nomenclature 2014. *Molecular immunology,* 61**,** 56-58.

KERSCHENSTEINER, M., REUTER, M. S., LICHTMAN, J. W. & MISGELD, T. 2008. Ex vivo imaging of motor axon dynamics in murine triangularis sterni explants. *Nature protocols,* 3**,** 1645.

KEVENAAR, J. T. & HOOGENRAAD, C. C. 2015. The axonal cytoskeleton: from organization to function. *Frontiers in molecular neuroscience,* 8**,** 44.

KHALIL, M., TEUNISSEN, C. E., OTTO, M., PIEHL, F., SORMANI, M. P., GATTRINGER, T., BARRO, C., KAPPOS, L., COMABELLA, M. & FAZEKAS, F. 2018. Neurofilaments as biomarkers in neurological disorders. *Nature Reviews Neurology,* 14**,** 577-589.

KILINC, D., GALLO, G. & BARBEE, K. A. 2008. Mechanically-induced membrane poration causes axonal beading and localized cytoskeletal damage. *Experimental neurology,* 212**,** 422-430.

KILINC, D., GALLO, G. & BARBEE, K. A. 2009. Mechanical membrane injury induces axonal beading through localized activation of calpain. *Experimental neurology,* 219**,** 553-561.

KIM, D. D. & SONG, W.-C. 2006. Membrane complement regulatory proteins. *Clinical immunology,* 118**,** 127-136.

KIRYU-SEO, S., OHNO, N., KIDD, G. J., KOMURO, H. & TRAPP, B. D. 2010. Demyelination increases axonal stationary mitochondrial size and the speed of axonal mitochondrial transport. *Journal of Neuroscience,* 30**,** 6658-6666.

KLENK, E. 1942. Über die Ganglioside, eine neue Gruppe von zuckerhaltigen Gehirnlipoiden. *Hoppe-Seyler´ s Zeitschrift für physiologische Chemie,* 273**,** 76-86.

KLEYWEG, R., VAN DER MECHE, F. & MEULSTEE, J. 1988. Treatment of Guillain-Barré syndrome with high-dose gammaglobulin. *Neurology,* 38**,** 1639-1639.

KO, C.-P. & ROBITAILLE, R. 2015. Perisynaptic Schwann cells at the neuromuscular synapse: adaptable, multitasking glial cells. *Cold Spring Harbor perspectives in biology,* 7**,** a020503.

KOGA, M., ANG, C., YUKI, N., JACOBS, B., HERBRINK, P., VAN DER MECHÉ, F., HIRATA, K. & VAN DOORN, P. 2001. Comparative study of preceding Campylobacter jejuni infection in Guillain-Barré syndrome in Japan and The Netherlands. *Journal of Neurology, Neurosurgery & Psychiatry,* 70**,** 693-695.

KOGA, M., GILBERT, M., LI, J., KOIKE, S., TAKAHASHI, M., FURUKAWA, K., HIRATA, K. & YUKI, N. 2005. Antecedent infections in Fisher syndrome: a common pathogenesis of molecular mimicry. *Neurology,* 64**,** 1605-1611.

KOSKI, C., SANDERS, M., SWOVELAND, P., LAWLEY, T., SHIN, M., FRANK, M. & JOINER, K. 1987. Activation of terminal components of complement in patients with Guillain-Barre syndrome and other demyelinating neuropathies. *Journal of Clinical Investigation,* 80**,** 1492.

KUSUNOKI, S., CHIBA, A., HITOSHI, S., TAKIZAWA, H. & KANAZAWA, I. 1995. Anti-Gal-C antibody in autoimmune neuropathies subsequent to mycoplasma infection. *Muscle & Nerve: Official Journal of the American Association of Electrodiagnostic Medicine,* 18**,** 409-413.

KUSUNOKI, S., CHIBA, A., TAI, T., TAI, T. & KANAZAWA, I. 1993. Localization of GM1 and GD1b antigens in the human peripheral nervous system. *Muscle & Nerve: Official Journal of the American Association of Electrodiagnostic Medicine,* 16**,** 752-756.

KUSUNOKI, S., HITOSHI, S., KAIDA, K. I., ARITA, M. & KANAZAWA, I. 1999. Monospecific anti-GD1b IgG is required to induce rabbit ataxic neuropathy. *Annals of neurology,* 45**,** 400-403.

KUSUNOKI, S., SHIMIZU, J., CHIBA, A., UGAWA, Y., HITOSHI, S. & KANAZAWA, I. 1996. Experimental sensory neuropathy induced by sensitization with ganglioside GD1b. *Annals of neurology,* 39**,** 424-431.

KUWABARA, S., YUKI, N., KOGA, M., HATTORI, T., MATSUURA, D., MIYAKE, M. & NODA, M. 1998. IgG Anti-GM1 antibody is associated with reversible conduction failure and axonal degeneration in guillain-barré syndrome. *Annals of neurology,* 44**,** 202-208.

KUWAHARA, M., SUZUKI, S., TAKADA, K. & KUSUNOKI, S. 2011. Antibodies to LM1 and LM1-containing ganglioside complexes in Guillain–Barré syndrome and chronic inflammatory demyelinating polyneuropathy. *Journal of neuroimmunology,* 239**,** 87-90.

KWA, M., VAN SCHAIK, I., BRAND, A., BAAS, F. & VERMEULEN, M. 2001. Investigation of serum response to PMP22, connexin 32 and P0 in inflammatory neuropathies. *Journal of neuroimmunology,* 116**,** 220-225.

LANDON, D. & WILLIAMS, P. 1963. Ultrastructure of the node of Ranvier. *Nature,* 199**,** 575-577.

LANDRY, O. 1859. Note sur la paralysie ascendante aigue. *Gaz Hebd Med Paris,* 472**,** 486.

LEDEEN, R. & WU, G. 2018. Gangliosides of the nervous system. *Gangliosides.* Springer.

LEHMANN, H. C., HUGHES, R. A., KIESEIER, B. C. & HARTUNG, H. P. 2012. Recent developments and future directions in Guillain-Barré syndrome. *Journal of the Peripheral Nervous System,* 17**,** 57-70.

LEONHARD, S. E., MANDARAKAS, M. R., GONDIM, F. A., BATEMAN, K., FERREIRA, M. L., CORNBLATH, D. R., VAN DOORN, P. A., DOURADO, M. E., HUGHES, R. A. & ISLAM, B. 2019. Diagnosis and management of Guillain–Barré syndrome in ten steps. *Nature Reviews Neurology,* 15**,** 671-683.

LEPORE, E., CASOLA, I., DOBROWOLNY, G. & MUSARÒ, A. 2019. Neuromuscular junction as an entity of nerve-muscle communication. *Cells,* 8**,** 906.

LEPOW, I., NAFF, G., TODD, E., PENSKY, J. & HINZ JR, C. 1963. Chromatographic resolution of the first component of human complement into three activities. *The Journal of experimental medicine,* 117**,** 983-1008.

LETERRIER, C., DUBEY, P. & ROY, S. 2017. The nano-architecture of the axonal cytoskeleton. *Nature Reviews Neuroscience,* 18**,** 713.

LI, C., XUE, P., TIAN, W., LIU, R. & YANG, C. 1996. Experimental Campylobacter jejuni infection in the chicken: an animal model of axonal Guillain-Barré syndrome. *Journal of Neurology, Neurosurgery & Psychiatry,* 61**,** 279-284.

LI, X., LYNN, B., OLSON, C., MEIER, C., DAVIDSON, K., YASUMURA, T., RASH, J. & NAGY, J. 2002. Connexin29 expression, immunocytochemistry and freeze-fracture replica immunogold labelling (FRIL) in sciatic nerve. *European Journal of Neuroscience,* 16**,** 795-806.

LIM, R., ZAVOU, M. J., MILTON, P.-L., CHAN, S. T., TAN, J. L., DICKINSON, H., MURPHY, S. V., JENKIN, G. & WALLACE, E. M. 2014. Measuring respiratory function in mice using unrestrained whole-body plethysmography. *JoVE (Journal of Visualized Experiments)***,** e51755.

LININGTON, C., IZUMO, S., SUZUKI, M., UYEMURA, K., MEYERMANN, R. & WEKERLE, H. 1984. A permanent rat T cell line that mediates experimental allergic neuritis in the Lewis rat in vivo. *The Journal of Immunology,* 133**,** 1946-1950.

LLOBET ROSELL, A. & NEUKOMM, L. J. 2019. Axon death signalling in Wallerian degeneration among species and in disease. *Open biology,* 9**,** 190118.

LOMAURO, A., ALIVERTI, A., PERCHIAZZI, G. & FRYKHOLM, P. 2021. Physiological changes and compensatory mechanisms by the action of respiratory muscles in a porcine model of phrenic nerve injury. *Journal of Applied Physiology,* 130**,** 813-826.

LONIGRO, A. & DEVAUX, J. J. 2009. Disruption of neurofascin and gliomedin at nodes of Ranvier precedes demyelination in experimental allergic neuritis. *Brain,* 132**,** 260-273.

LU, X., RONG, Y. & BAUDRY, M. 2000. Calpain-mediated degradation of PSD-95 in developing and adult rat brain. *Neuroscience letters,* 286**,** 149-153.

MA, M., FERGUSON, T. A., SCHOCH, K. M., LI, J., QIAN, Y., SHOFER, F. S., SAATMAN, K. E. & NEUMAR, R. W. 2013. Calpains mediate axonal cytoskeleton disintegration during Wallerian degeneration. *Neurobiology of disease,* 56**,** 34-46.

MANK, M., REIFF, D. F., HEIM, N., FRIEDRICH, M. W., BORST, A. & GRIESBECK, O. 2006. A FRET-based calcium biosensor with fast signal kinetics and high fluorescence change. *Biophysical journal,* 90**,** 1790-1796.

MANK, M., SANTOS, A. F., DIRENBERGER, S., MRSIC-FLOGEL, T. D., HOFER, S. B., STEIN, V., HENDEL, T., REIFF, D. F., LEVELT, C. & BORST, A. 2008. A genetically encoded calcium indicator for chronic in vivo two-photon imaging. *Nature methods,* 5**,** 805-811.

MARTÍN-AGUILAR, L., CAMPS-RENOM, P., LLEIXÀ, C., PASCUAL-GOÑI, E., DIAZ-MANERA, J., ROJAS-GARCÍA, R., DE LUNA, N., GALLARDO, E., CORTÉS-VICENTE, E. & MUÑOZ, L. 2020. Serum neurofilament light chain predicts long-term prognosis in Guillain-Barré syndrome patients. *medRxiv*.

MASTELLOS, D. C., RICKLIN, D. & LAMBRIS, J. D. 2019. Clinical promise of next-generation complement therapeutics. *Nature Reviews Drug Discovery,* 18**,** 707-729.

MATSUMOTO, H., KOBAYASHI, O., TAMURA, K., OHKAWA, T. & SEKINE, I. 2002. Miller Fisher syndrome with transient coma: comparison with Bickerstaff brainstem encephalitis. *Brain and Development,* 24**,** 98-101.

MATTEOLI, M., VERDERIO, C., ROSSETTO, O., IEZZI, N., COCO, S., SCHIAVO, G. & MONTECUCCO, C. 1996. Synaptic vesicle endocytosis mediates the entry of tetanus neurotoxin into hippocampal neurons. *Proceedings of the National Academy of Sciences,* 93**,** 13310-13315.

MAYER, M. M. 1972. Mechanism of cytolysis by complement. *Proceedings of the National Academy of Sciences,* 69**,** 2954-2958.

MCARDLE, J., ANGAUT-PETIT, D., MALLART, A., BOURNAUD, R., FAILLE, L. & BRIGANT, J. 1981. Advantages of the triangularis sterni muscle of the mouse for investigations of synaptic phenomena. *Journal of neuroscience methods,* 4**,** 109-115.

MCGONIGAL, R., CUNNINGHAM, M. E., YAO, D., BARRIE, J. A., SANKARANARAYANAN, S., FEWOU, S. N., FURUKAWA, K., YEDNOCK, T. A. & WILLISON, H. J. 2016. C1q-targeted inhibition of the classical complement pathway prevents injury in a novel mouse model of acute motor axonal neuropathy. *Acta neuropathologica communications,* 4**,** 23.

MCGONIGAL, R., ROWAN, E. G., GREENSHIELDS, K. N., HALSTEAD, S. K., HUMPHREYS, P. D., ROTHER, R. P., FURUKAWA, K. & WILLISON, H. J. 2010. Anti-GD1a antibodies activate complement and calpain to injure distal motor nodes of Ranvier in mice. *Brain,* 133**,** 1944-1960.

MCGONIGAL, R. & WILLISON, H. J. 2021. The role of gangliosides in the organisation of the node of Ranvier examined in glycosyltransferase transgenic mice. *Journal of Anatomy*.

MCKHANN, G., CORNBLATH, D., GRIFFIN, J., HO, T., LI, C., JIANG, Z., WU, H., ZHAORI, G., LIU, Y. & JOU, L. 1993. Acute motor axonal neuropathy: a frequent cause of acute flaccid paralysis in China. *Annals of neurology,* 33**,** 333-342.

MCKHANN, G., CORNBLATH, D., HO, T., GRIFFIN, J., LI, C., BAI, A., WU, H., YEI, Q., ZHANG, W. & ZHAORI, Z. 1991. Clinical and electrophysiological aspects of acute paralytic disease of children and young adults in northern China. *The Lancet,* 338**,** 593-597.

MCNAMARA, L. A., TOPAZ, N., WANG, X., HARIRI, S., FOX, L. & MACNEIL, J. R. 2017. High risk for invasive meningococcal disease among patients receiving eculizumab (Soliris) despite receipt of meningococcal vaccine. *MMWR. Morbidity and mortality weekly report,* 66**,** 734.

MILNER, P., LOVELIDGE, C., TAYLOR, W. & HUGHES, R. 1987. P0 myelin protein produces experimental allergic neuritis in Lewis rats. *Journal of the neurological sciences,* 79**,** 275-285.

MISAWA, S., KUWABARA, S., SATO, Y., YAMAGUCHI, N., NAGASHIMA, K., KATAYAMA, K., SEKIGUCHI, Y., IWAI, Y., AMINO, H. & SUICHI, T. 2018. Safety and efficacy of eculizumab in Guillain-Barré syndrome: a multicentre, double-blind, randomised phase 2 trial. *The Lancet Neurology,* 17**,** 519-529.

MISAWA, S. & SUICHI, T. 2020. Guillain-Barré syndrome: Novel treatment by complement inhibition. *Clinical and Experimental Neuroimmunology,* 11**,** 90-93.

MORGAN, B. P. 2016. The membrane attack complex as an inflammatory trigger. *Immunobiology,* 221**,** 747-751.

MOSS, K. R., BOPP, T. S., JOHNSON, A. E. & HÖKE, A. 2021. New evidence for secondary axonal degeneration in demyelinating neuropathies. *Neuroscience Letters,* 744**,** 135595.

MUELLER, M., LEONHARD, C., WACKER, K., RINGELSTEIN, E. B., OKABE, M., HICKEY, W. F. & KIEFER, R. 2003. Macrophage response to peripheral nerve injury: the quantitative contribution of resident and hematogenous macrophages. *Laboratory investigation,* 83**,** 175-185.

MUKHERJEE, A. & WILLIAMS, D. W. 2017. More alive than dead: non-apoptotic roles for caspases in neuronal development, plasticity and disease. *Cell Death & Differentiation,* 24**,** 1411-1421.

NAGAI, Y., MOMOI, T., SAITO, M., MITSUZAWA, E. & OHTANI, S. 1976. Ganglioside syndrome, a new autoimmune neurologic disorder, experimentally induced with brain gangliosides. *Neuroscience letters,* 2**,** 107-111.

NAIK, G. S., MEENA, A. K., REDDY, B. A. K., MRIDULA, R. K., JABEEN, S. A. & BORGOHAIN, R. 2017. Anti-ganglioside antibodies profile in Guillain-Barré syndrome: Correlation with clinical features, electrophysiological pattern, and outcome. *Neurology India,* 65**,** 1001.

NAVE, K.-A. 2010. Myelination and support of axonal integrity by glia. *Nature,* 468**,** 244.

NELSON, A. D. & JENKINS, P. M. 2017. Axonal membranes and their domains: assembly and function of the axon initial segment and node of Ranvier. *Frontiers in cellular neuroscience,* 11**,** 136.

NG, J. K. M., MALOTKA, J., KAWAKAMI, N., DERFUSS, T., KHADEMI, M., OLSSON, T., LININGTON, C., ODAKA, M., TACKENBERG, B. & PRÜSS, H. 2012. Neurofascin as a target for autoantibodies in peripheral neuropathies. *Neurology,* 79**,** 2241-2248.

NISHIMUNE, H. & SHIGEMOTO, K. 2018. Practical anatomy of the neuromuscular junction in health and disease. *Neurologic clinics,* 36**,** 231-240.

NOCERA, G. & JACOB, C. 2020. Mechanisms of Schwann cell plasticity involved in peripheral nerve repair after injury. *Cellular and Molecular Life Sciences***,** 1-13.

O'HANLON, G. M., PLOMP, J. J., CHAKRABARTI, M., MORRISON, I., WAGNER, E. R., GOODYEAR, C. S., YIN, X., TRAPP, B. D., CONNER, J. & MOLENAAR, P. C. 2001. Anti-GQ1b ganglioside antibodies mediate complement-dependent destruction of the motor nerve terminal. *Brain,* 124**,** 893-906.

O'HANLON, G., PATERSON, G., VEITCH, J., WILSON, G. & WILLISON, H. 1998. Mapping immunoreactive epitopes in the human peripheral nervous system using human monoclonal anti-GM1 ganglioside antibodies. *Acta neuropathologica,* 95**,** 605-616.

O'HANLON, G. M., HUMPHREYS, P. D., GOLDMAN, R. S., HALSTEAD, S. K., BULLENS, R. W., PLOMP, J. J., USHKARYOV, Y. & WILLISON, H. J. 2003. Calpain inhibitors protect against axonal degeneration in a model of anti-ganglioside antibody-mediated motor nerve terminal injury. *Brain,* 126**,** 2497-2509.

OGAWA-GOTO, K., FUNAMOTO, N., ABE, T. & NAGASHIMA, K. 1990. Different ceramide compositions of gangliosides between human motor and sensory nerves. *Journal of neurochemistry,* 55**,** 1486-1493.

OGAWA-GOTO, K., FUNAMOTO, N., OHTA, Y., ABE, T. & NAGASHIMA, K. 1992. Myelin gangliosides of human peripheral nervous system: an enrichment of GM1 in the motor nerve myelin isolated from cauda equina. *Journal of neurochemistry,* 59**,** 1844-1849.

OGAWA, Y., OSES-PRIETO, J., KIM, M. Y., HORRESH, I., PELES, E., BURLINGAME, A. L., TRIMMER, J. S., MEIJER, D. & RASBAND, M. N. 2010. ADAM22, a Kv1 channel-interacting protein, recruits membrane-associated guanylate kinases to juxtaparanodes of myelinated axons. *Journal of Neuroscience,* 30**,** 1038-1048.

OGAWA, Y., SCHAFER, D. P., HORRESH, I., BAR, V., HALES, K., YANG, Y., SUSUKI, K., PELES, E., STANKEWICH, M. C. & RASBAND, M. N. 2006. Spectrins and ankyrinB constitute a specialized paranodal cytoskeleton. *Journal of Neuroscience,* 26**,** 5230-5239.

OGAWARA, K., KUWABARA, S., MORI, M., HATTORI, T., KOGA, M. & YUKI, N. 2000. Axonal Guillain-Barré syndrome: relation to anti-ganglioside antibodies and Campylobacter jejuni infection in Japan. *Annals of Neurology: Official Journal of the American Neurological Association and the Child Neurology Society,* 48**,** 624-631.

OKADA, M., ITOH, M.-I., HARAGUCHI, M., OKAJIMA, T., INOUE, M., OISHI, H., MATSUDA, Y., IWAMOTO, T., KAWANO, T. & FUKUMOTO, S. 2002. b-series Ganglioside deficiency exhibits no definite changes in the neurogenesis and the sensitivity to Fas-mediated apoptosis but impairs regeneration of the lesioned hypoglossal nerve. *Journal of Biological Chemistry,* 277**,** 1633-1636.

ONG, G. L. & MATTES, M. J. 1989. Mouse strains with typical mammalian levels of complement activity. *Journal of immunological methods,* 125**,** 147-158.

PAN, B., FROMHOLT, S. E., HESS, E. J., CRAWFORD, T. O., GRIFFIN, J. W., SHEIKH, K. A. & SCHNAAR, R. L. 2005. Myelin-associated glycoprotein and complementary axonal ligands, gangliosides, mediate axon stability in the CNS and PNS: neuropathology and behavioral deficits in single-and double-null mice. *Experimental neurology,* 195**,** 208-217.

PAN, C.-L., YUKI, N., KOGA, M., CHIANG, M.-C. & HSIEH, S.-T. 2001. Acute sensory ataxic neuropathy associated with monospecific anti-GD1b IgG antibody. *Neurology,* 57**,** 1316-1318.

PATERSON, G., WILSON, G., KENNEDY, P. & WILLISON, H. J. 1995. Analysis of anti-GM1 ganglioside IgM antibodies cloned from motor neuropathy patients demonstrates diverse V region gene usage with extensive somatic mutation. *The Journal of Immunology,* 155**,** 3049-3059.

PESTRONK, A., CORNBLATH, D., ILYAS, A., BABA, H., QUARLES, R., GRIFFIN, J., ALDERSON, K. & ADAMS, R. 1988. A treatable multifocal motor neuropathy with antibodies to GM1 ganglioside. *Annals of Neurology: Official Journal of the American Neurological Association and the Child Neurology Society,* 24**,** 73-78.

PETTY, R., DUNCAN, R., JAMAL, G., HADLEY, D. & KENNEDY, P. 1993. Brainstem encephalitis and the Miller Fisher syndrome. *Journal of Neurology, Neurosurgery & Psychiatry,* 56**,** 201-203.

PHONGSISAY, V., SUSUKI, K., MATSUNO, K., YAMAHASHI, T., OKAMOTO, S., FUNAKOSHI, K., HIRATA, K., SHINODA, M. & YUKI, N. 2008. Complement inhibitor prevents disruption of sodium channel clusters in a rabbit model of Guillain–Barré syndrome. *Journal of neuroimmunology,* 205**,** 101-104.

PIEPERS, S., JANSEN, M. D., CATS, E. A., VAN SORGE, N. M., VAN DEN BERG, L. H. & VAN DER POL, W.-L. 2010. IVIg inhibits classical pathway activity and anti-GM1 IgM-mediated complement deposition in MMN. *Journal of neuroimmunology,* 229**,** 256-262.

PILLAI, A. M., THAXTON, C., PRIBISKO, A. L., CHENG, J. G., DUPREE, J. L. & BHAT, M. A. 2009. Spatiotemporal ablation of myelinating glia-specific neurofascin (NfascNF155) in mice reveals gradual loss of paranodal axoglial junctions and concomitant disorganization of axonal domains. *Journal of neuroscience research,* 87**,** 1773-1793.

PINATEL, D. & FAIVRE-SARRAILH, C. 2021. Assembly and Function of the Juxtaparanodal Kv1 Complex in Health and Disease. *Life,* 11**,** 8.

PLOMP, J. J., MOLENAAR, P. C., O'HANLON, G. M., JACOBS, B. C., VEITCH, J., DAHA, M. R., VAN DOORN, P. A., VAN DER MECHÉ, F. G., VINCENT, A. & MORGAN, B. P. 1999. Miller Fisher anti-GQ1b antibodies: α-Latrotoxin–like effects on motor end plates. *Annals of Neurology: Official Journal of the American Neurological Association and the Child Neurology Society,* 45**,** 189-199.

PLOMP, J. J. & WILLISON, H. J. 2009. Pathophysiological actions of neuropathy-related anti-ganglioside antibodies at the neuromuscular junction. *The Journal of physiology,* 587**,** 3979-3999.

PODACK, E., MÜLLER-EBERHARD, H., HORST, H. & HOPPE, W. 1982. Membrane attach complex of complement (MAC): three-dimensional analysis of MAC-phospholipid vesicle recombinants. *The Journal of Immunology,* 128**,** 2353-2357.

POLIAK, S., GOLLAN, L., MARTINEZ, R., CUSTER, A., EINHEBER, S., SALZER, J. L., TRIMMER, J. S., SHRAGER, P. & PELES, E. 1999. Caspr2, a new member of the neurexin superfamily, is localized at the juxtaparanodes of myelinated axons and associates with K+ channels. *Neuron,* 24**,** 1037-1047.

POLIAK, S. & PELES, E. 2003. The local differentiation of myelinated axons at nodes of Ranvier. *Nature Reviews Neuroscience,* 4**,** 968.

PORTER, R. & REID, K. 1979. Activation of the complement system by antibody-antigen complexes: the classical pathway. *Advances in protein chemistry.* Elsevier.

QUEROL, L., NOGALES-GADEA, G., ROJAS-GARCIA, R., DIAZ-MANERA, J., PARDO, J., ORTEGA-MORENO, A., SEDANO, M. J., GALLARDO, E., BERCIANO, J. & BLESA, R. 2014. Neurofascin IgG4 antibodies in CIDP associate with disabling tremor and poor response to IVIg. *Neurology,* 82**,** 879-886.

QUEROL, L., NOGALES-GADEA, G., ROJAS-GARCIA, R., MARTINEZ-HERNANDEZ, E., DIAZ-MANERA, J., SUÁREZ-CALVET, X., NAVAS, M., ARAQUE, J., GALLARDO, E. & ILLA, I. 2013. Antibodies to contactin-1 in chronic inflammatory demyelinating polyneuropathy. *Annals of neurology,* 73**,** 370-380.

RASBAND, M. N., PARK, E. W., ZHEN, D., ARBUCKLE, M. I., POLIAK, S., PELES, E., GRANT, S. G. & TRIMMER, J. S. 2002. Clustering of neuronal potassium channels is independent of their interaction with PSD-95. *The Journal of cell biology,* 159**,** 663-672.

RASBAND, M. N. & PELES, E. 2016. The nodes of Ranvier: molecular assembly and maintenance. *Cold Spring Harbor perspectives in biology,* 8**,** a020495.

RASBAND, M. N. & PELES, E. 2020. Mechanisms of node of Ranvier assembly. *Nature Reviews Neuroscience***,** 1-14.

RASBAND, M. N. & TRIMMER, J. S. 2001. Developmental clustering of ion channels at and near the node of Ranvier. *Developmental biology,* 236**,** 5-16.

RASBAND, M. N., TRIMMER, J. S., SCHWARZ, T. L., LEVINSON, S. R., ELLISMAN, M. H., SCHACHNER, M. & SHRAGER, P. 1998. Potassium channel distribution, clustering, and function in remyelinating rat axons. *Journal of Neuroscience,* 18**,** 36-47.

REDDY, L. V., KOIRALA, S., SUGIURA, Y., HERRERA, A. A. & KO, C.-P. 2003. Glial cells maintain synaptic structure and function and promote development of the neuromuscular junction in vivo. *Neuron,* 40**,** 563-580.

REES, J. H., GREGSON, N. A. & HUGHES, R. A. 1995a. Anti-ganglioside GM1 antibodies in Guillain-Barré syndrome and their relationship to Campylobacter jejuni infection. *Annals of Neurology: Official Journal of the American Neurological Association and the Child Neurology Society,* 38**,** 809-816.

REES, J. H., SOUDAIN, S. E., GREGSON, N. A. & HUGHES, R. A. 1995b. Campylobacter jejuni infection and Guillain–Barré syndrome. *New England Journal of Medicine,* 333**,** 1374-1379.

REEVES, H. M. & WINTERS, J. L. 2014. The mechanisms of action of plasma exchange. *British journal of haematology,* 164**,** 342-351.

RHODES, K. & TATTERSFIELD, A. 1982. Guillain-Barre syndrome associated with Campylobacter infection. *British medical journal (Clinical research ed.),* 285**,** 173.

RINALDI, S., BRENNAN, K. & WILLISON, H. 2010. Heteromeric glycolipid complexes as modulators of autoantibody and lectin binding. *Progress in lipid research,* 49**,** 87-95.

RINALDI, S., BRENNAN, K. M., KALNA, G., WALGAARD, C., VAN DOORN, P., JACOBS, B. C., ROBERT, K. Y., MANSSON, J.-E., GOODYEAR, C. S. & WILLISON, H. J. 2013. Antibodies to heteromeric glycolipid complexes in Guillain-Barré syndrome. *PLoS One,* 8**,** e82337.

ROBERT, K. Y., TSAI, Y.-T., ARIGA, T. & YANAGISAWA, M. 2011. Structures, biosynthesis, and functions of gangliosides—An overview. *Journal of oleo science,* 60**,** 537.

ROSENBLUTH, J. 2009. Multiple functions of the paranodal junction of myelinated nerve fibers. *Journal of neuroscience research,* 87**,** 3250-3258.

RUPP, A. F. 2016. Spontaneous models of Guillain-Barré syndrome in animals.

RUTS, L., DRENTHEN, J., JACOBS, B. & VAN DOORN, P. 2010. Distinguishing acute-onset CIDP from fluctuating Guillain-Barre syndrome: a prospective study. *Neurology,* 74**,** 1680-1686.

SAID, G. 2006. Chronic inflammatory demyelinating polyneuropathy. *Neuromuscular disorders,* 16**,** 293-303.

SAIDA, T., SAIDA, K., DORFMAN, S. H., SILBERBERG, D. H., SUMNER, A. J., MANNING, M. C., LISAK, R. P. & BROWN, M. J. 1979. Experimental allergic neuritis induced by sensitization with galactocerebroside. *Science,* 204**,** 1103-1106.

SAIDA, T., SAIDA, K., LISAK, R. P., BROWN, M. J., SILBERBERG, D. H. & ASBURY, A. K. 1982. In vivo demyelinating activity of sera from patients with Guillain-Barré syndrome. *Annals of Neurology: Official Journal of the American Neurological Association and the Child Neurology Society,* 11**,** 69-75.

SAIDA, T., SILBERBERG, D., FRY, J. & MANNING, M. 1977. Demyelinating Anti-Galactocerebroside Antibodies in EAN and EAE: 112. *Journal of Neuropathology and Experimental Neurology,* 36.

SALZER, J. L. 2015. Schwann cell myelination. *Cold Spring Harbor perspectives in biology,* 7**,** a020529.

SAMUKAWA, M., HAMADA, Y., KUWAHARA, M., TAKADA, K., HIRANO, M., MITSUI, Y., SONOO, M., KUSUNOKI, S. & GROUP, J. G. S. 2014. Clinical features in Guillain–Barré syndrome with anti-Gal-C antibody. *Journal of the Neurological Sciences,* 337**,** 55-60.

SAMUKAWA, M., KUWAHARA, M., MORIKAWA, M., UENO, R., HAMADA, Y., TAKADA, K., HIRANO, M., MITSUI, Y., SONOO, M. & KUSUNOKI, S. 2016. Electrophysiological assessment of Guillain-Barre syndrome with both Gal-C and ganglioside antibodies; tendency for demyelinating type. *Journal of Neuroimmunology,* 301**,** 61-64.

SARMA, J. V. & WARD, P. A. 2011. The complement system. *Cell and tissue research,* 343**,** 227-235.

SAWAI, S., SATOH, M., MORI, M., MISAWA, S., SOGAWA, K., KAZAMI, T., ISHIBASHI, M., BEPPU, M., SHIBUYA, K. & ISHIGE, T. 2014. Moesin is a possible target molecule for cytomegalovirus-related Guillain-Barré syndrome. *Neurology,* 83**,** 113-117.

SCHERER, S. S., XU, T., CRINO, P., ARROYO, E. J. & GUTMANN, D. H. 2001. Ezrin, radixin, and moesin are components of Schwann cell microvilli. *Journal of neuroscience research,* 65**,** 150-164.

SCHNAAR, R. L. 2019. The Biology of gangliosides. *Advances in carbohydrate chemistry and biochemistry.* Elsevier.

SCHONBERGER, L. B., MCGOWAN JR, J. E. & GREGG, M. B. 1976. Vaccine-associated poliomyelitis in the United States, 1961–1972. *American journal of epidemiology,* 104**,** 202-211.

SEJVAR, J. J., BAUGHMAN, A. L., WISE, M. & MORGAN, O. W. 2011. Population incidence of Guillain-Barré syndrome: a systematic review and meta-analysis. *Neuroepidemiology,* 36**,** 123-133.

SHAHRIZAILA, N. & YUKI, N. 2013. Bickerstaff brainstem encephalitis and Fisher syndrome: anti-GQ1b antibody syndrome. *Journal of Neurology, Neurosurgery & Psychiatry,* 84**,** 576-583.

SHEIKH, K. A., DEERINCK, T. J., ELLISMAN, M. H. & GRIFFIN, J. W. 1999. The distribution of ganglioside-like moieties in peripheral nerves. *Brain,* 122**,** 449-460.

SHEIKH, S. I. & AMATO, A. A. 2010. The dorsal root ganglion under attack: the acquired sensory ganglionopathies. *Practical neurology,* 10**,** 326-334.

SHERMAN, D. L., TAIT, S., MELROSE, S., JOHNSON, R., ZONTA, B., COURT, F. A., MACKLIN, W. B., MEEK, S., SMITH, A. J. & COTTRELL, D. F. 2005. Neurofascins are required to establish axonal domains for saltatory conduction. *Neuron,* 48**,** 737-742.

SINHA, S., PRASAD, K., JAIN, D., PANDEY, C., JHA, S. & PRADHAN, S. 2007. Preceding infections and anti-ganglioside antibodies in patients with Guillain–Barré syndrome: a single centre prospective case-control study. *Clinical microbiology and infection,* 13**,** 334-337.

SINNO, H. & PRAKASH, S. 2013. Complements and the wound healing cascade: an updated review. *Plastic surgery international,* 2013.

STEVENS, J. G., PEPOSE, J. S. & COOK, M. L. 1981. Marek's disease: A natural model for the Landry-Guillain-Barré syndrome. *Annals of Neurology: Official Journal of the American Neurological Association and the Child Neurology Society,* 9**,** 102-106.

STEWART, J. D. 2003. Peripheral nerve fascicles: anatomy and clinical relevance. *Muscle & nerve,* 28**,** 525-541.

SUSUKI, K., BABA, H., TOHYAMA, K., KANAI, K., KUWABARA, S., HIRATA, K., FURUKAWA, K., FURUKAWA, K., RASBAND, M. N. & YUKI, N. 2007a. Gangliosides contribute to stability of paranodal junctions and ion channel clusters in myelinated nerve fibers. *Glia,* 55**,** 746-757.

SUSUKI, K., NISHIMOTO, Y., YAMADA, M., BABA, M., UEDA, S., HIRATA, K. & YUKI, N. 2003. Acute motor axonal neuropathy rabbit model: immune attack on nerve root axons. *Annals of neurology,* 54**,** 383-388.

SUSUKI, K., RASBAND, M. N., TOHYAMA, K., KOIBUCHI, K., OKAMOTO, S., FUNAKOSHI, K., HIRATA, K., BABA, H. & YUKI, N. 2007b. Anti-GM1 antibodies cause complement-mediated disruption of sodium channel clusters in peripheral motor nerve fibers. *Journal of Neuroscience,* 27**,** 3956-3967.

SUSUKI, K., YUKI, N., SCHAFER, D. P., HIRATA, K., ZHANG, G., FUNAKOSHI, K. & RASBAND, M. N. 2012. Dysfunction of nodes of Ranvier: a mechanism for anti-ganglioside antibody-mediated neuropathies. *Experimental neurology,* 233**,** 534-542.

SVENNERHOLM, L. 1994. Designation and schematic structure of gangliosides and allied glycosphingolipids. *Progress in brain research.* Elsevier.

TAKAMIYA, K., YAMAMOTO, A., FURUKAWA, K., YAMASHIRO, S., SHIN, M., OKADA, M., FUKUMOTO, S., HARAGUCHI, M., TAKEDA, N. & FUJIMURA, K. 1996. Mice with disrupted GM2/GD2 synthase gene lack complex gangliosides but exhibit only subtle defects in their nervous system. *Proceedings of the National Academy of Sciences,* 93**,** 10662-10667.

TANAKA, M., IDEI, M., SAKAGUCHI, H., KATO, R., SATO, D., SAWANOBORI, K., KAWARASAKI, S., HATA, T., YOSHIZAKI, A. & NAKAMURA, M. 2021. Achievements and challenges of the Sakigake designation system in Japan. *British Journal of Clinical Pharmacology*.

TASKINEN, H. & RÖYTTÄ, M. 1997. The dynamics of macrophage recruitment after nerve transection. *Acta neuropathologica,* 93**,** 252-259.

TAYLOR, A. M., SAIFETIAROVA, J. & BHAT, M. A. 2017. Postnatal loss of neuronal and glial neurofascins differentially affects node of Ranvier maintenance and myelinated axon function. *Frontiers in cellular neuroscience,* 11**,** 11.

THOMAS, F., TROJABORG, W., NAGY, C., SANTORO, M., SADIQ, S., LATOV, N. & HAYS, A. 1991. Experimental autoimmune neuropathy with anti-GM1 antibodies and immunoglobulin deposits at the nodes of Ranvier. *Acta neuropathologica,* 82**,** 378-383.

THURMAN, J. M. & HOLERS, V. M. 2006. The central role of the alternative complement pathway in human disease. *The Journal of Immunology,* 176**,** 1305-1310.

TOWNSON, K., BOFFEY, J., NICHOLL, D., VEITCH, J., BUNDLE, D., ZHANG, P., SAMAIN, E., ANTOINE, T., BERNARDI, A. & AROSIO, D. 2007. Solid phase immunoadsorption for therapeutic and analytical studies on neuropathy-associated anti-GM1 antibodies. *Glycobiology,* 17**,** 294-303.

TRAKA, M., GOUTEBROZE, L., DENISENKO, N., BESSA, M., NIFLI, A., HAVAKI, S., IWAKURA, Y., FUKAMAUCHI, F., WATANABE, K. & SOLIVEN, B. 2003. Association of TAG-1 with Caspr2 is essential for the molecular organization of juxtaparanodal regions of myelinated fibers. *The Journal of cell biology,* 162**,** 1161-1172.

TRAPP, B. D., ANDREWS, S. B., WONG, A., O'CONNELL, M. & GRIFFIN, J. W. 1989. Co-localization of the myelin-associated glycoprotein and the microfilament components, F-actin and spectrin, in Schwann cells of myelinated nerve fibres. *Journal of neurocytology,* 18**,** 47-60.

TURNBULL, W. B., PRECIOUS, B. L. & HOMANS, S. W. 2004. Dissecting the cholera toxin− ganglioside GM1 interaction by isothermal titration calorimetry. *Journal of the American Chemical Society,* 126**,** 1047-1054.

UNCINI, A. & KUWABARA, S. 2012. Electrodiagnostic criteria for Guillain–Barré syndrome: a critical revision and the need for an update. *Clinical neurophysiology,* 123**,** 1487-1495.

UNCINI, A. & KUWABARA, S. 2015. Nodopathies of the peripheral nerve: an emerging concept. *J Neurol Neurosurg Psychiatry***,** jnnp-2014-310097.

UNCINI, A., SUSUKI, K. & YUKI, N. 2013. Nodo-paranodopathy: beyond the demyelinating and axonal classification in anti-ganglioside antibody-mediated neuropathies. *Clinical Neurophysiology,* 124**,** 1928-1934.

UNCINI, A. & YUKI, N. 2009. Electrophysiologic and immunopathologic correlates in Guillain–Barré syndrome subtypes. *Expert review of neurotherapeutics,* 9**,** 869-884.

VAN DE WALLE, I., SILENCE, K., BUDDING, K., VAN DE VEN, L., DIJKXHOORN, K., DE ZEEUW, E., YILDIZ, C., GABRIELS, S., PERCIER, J.-M. & WILDEMANN, J. 2020. ARGX-117, a therapeutic complement inhibiting antibody targeting C2. *Journal of Allergy and Clinical Immunology*.

VAN DEN BERG, B., WALGAARD, C., DRENTHEN, J., FOKKE, C., JACOBS, B. C. & VAN DOORN, P. A. 2014. Guillain-Barré syndrome: pathogenesis, diagnosis, treatment and prognosis. *Nature Reviews Neurology,* 10**,** 469-482.

VAN DER MECHÉ, F., SCHMITZ, P. & GROUP*, D. G. B. S. 1992. A randomized trial comparing intravenous immune globulin and plasma exchange in Guillain–Barré syndrome. *New England Journal of Medicine,* 326**,** 1123-1129.

VAN DOORN, P. A. 2013. Diagnosis, treatment and prognosis of Guillain-Barré syndrome (GBS). *La Presse Médicale,* 42**,** e193-e201.

VILLA, P. G., HENZEL, W. J., SENSENBRENNER, M., HENDERSON, C. E. & PETTMANN, B. 1998. Calpain inhibitors, but not caspase inhibitors, prevent actin proteolysis and DNA fragmentation during apoptosis. *Journal of Cell Science,* 111**,** 713-722.

VLAM, L., VAN DEN BERG, L. H., CATS, E. A., PIEPERS, S. & VAN DER POL, W. L. 2013. Immune Pathogenesis and Treatment of Multifocal Motor Neuropathy. *Journal of Clinical Immunology,* 33**,** 38-42.

VON REYN, C. R., SPAETHLING, J. M., MESFIN, M. N., MA, M., NEUMAR, R. W., SMITH, D. H., SIMAN, R. & MEANEY, D. F. 2009. Calpain mediates proteolysis of the voltage-gated sodium channel α-subunit. *Journal of Neuroscience,* 29**,** 10350-10356.

VRIESENDORP, F. J., FLYNN, R. E., PAPPOLLA, M. A. & KOSKI, C. L. 1995. Complement depletion affects demyelination and inflammation in experimental allergic neuritis. *Journal of neuroimmunology,* 58**,** 157-165.

WAKSMAN, B. H. & ADAMS, R. D. 1955. Allergic neuritis: an experimental disease of rabbits induced by the injection of peripheral nervous tissue and adjuvants. *Journal of Experimental Medicine,* 102**,** 213-236.

WALLIS, R., MITCHELL, D. A., SCHMID, R., SCHWAEBLE, W. J. & KEEBLE, A. H. 2010. Paths reunited: Initiation of the classical and lectin pathways of complement activation. *Immunobiology,* 215**,** 1-11.

WALPORT, M. J. 2001. Complement. *New England Journal of Medicine,* 344**,** 1058-1066.

WANG, J., CHENG, A., WAKADE, C. & ROBERT, K. Y. 2014. Ganglioside GD3 is required for neurogenesis and long-term maintenance of neural stem cells in the postnatal mouse brain. *Journal of Neuroscience,* 34**,** 13790-13800.

WILLIAMS, P. R., MARINCU, B.-N., SORBARA, C. D., MAHLER, C. F., SCHUMACHER, A.-M., GRIESBECK, O., KERSCHENSTEINER, M. & MISGELD, T. 2014. A recoverable state of axon injury persists for hours after spinal cord contusion in vivo. *Nature communications,* 5**,** 1-11.

WILLISON, H., VEITCH, J., PATERSON, G. & KENNEDY, P. 1993. Miller Fisher syndrome is associated with serum antibodies to GQ1b ganglioside. *Journal of Neurology, Neurosurgery & Psychiatry,* 56**,** 204-206.

WILLISON, H. J. 2018. Anti-ganglioside antibodies in peripheral nerve pathology. *Gangliosides***,** 173-188.

WILLISON, H. J., HALSTEAD, S. K., BEVERIDGE, E., ZITMAN, F. M., GREENSHIELDS, K. N., MORGAN, B. P. & PLOMP, J. J. 2008. The role of complement and complement regulators in mediating motor nerve terminal injury in murine models of Guillain–Barré syndrome. *Journal of neuroimmunology,* 201**,** 172-182.

WILLISON, H. J., PATERSON, G., KENNEDY, P. G. & VEITCH, J. 1994. Cloning of human anti-GM1 antibodies from motor neuropathy patients. *Annals of Neurology: Official Journal of the American Neurological Association and the Child Neurology Society,* 35**,** 471-478.

WILLISON, H. J. & YUKI, N. 2002. Peripheral neuropathies and anti-glycolipid antibodies. *Brain,* 125**,** 2591-2625.

WITTE, M. E., SCHUMACHER, A.-M., MAHLER, C. F., BEWERSDORF, J. P., LEHMITZ, J., SCHEITER, A., SÁNCHEZ, P., WILLIAMS, P. R., GRIESBECK, O. & NAUMANN, R. 2019. Calcium influx through plasma-membrane nanoruptures drives axon degeneration in a model of multiple sclerosis. *Neuron,* 101**,** 615-624. e5.

YAKO, K., KUSUNOKI, S. & KANAZAWA, I. 1999. Serum antibody against a peripheral nerve myelin ganglioside, LM1, in Guillain-Barré syndrome. *Journal of the neurological sciences,* 168**,** 85-89.

YANG, Y., OGAWA, Y., HEDSTROM, K. L. & RASBAND, M. N. 2007. βIV spectrin is recruited to axon initial segments and nodes of Ranvier by ankyrinG. *The Journal of cell biology,* 176**,** 509-519.

YAO, D., MCGONIGAL, R., BARRIE, J. A., CAPPELL, J., CUNNINGHAM, M. E., MEEHAN, G. R., FEWOU, S. N., EDGAR, J. M., ROWAN, E. & OHMI, Y. 2014. Neuronal expression of GalNAc transferase is sufficient to prevent the age-related neurodegenerative phenotype of complex ganglioside-deficient mice. *Journal of Neuroscience,* 34**,** 880-891.

YU, R. K., MACALA, L. J., TAKI, T., WEINFELD, H. M. & YU, F. S. 1988. Developmental changes in ganglioside composition and synthesis in embryonic rat brain. *Journal of neurochemistry,* 50**,** 1825-1829.

YUAN, A., RAO, M. V. & NIXON, R. A. 2012. Neurofilaments at a glance. The Company of Biologists Ltd.

YUKI, N., KUWABARA, S., KOGA, M. & HIRATA, K. 1999. Acute motor axonal neuropathy and acute motor-sensory axonal neuropathy share a common immunological profile. *Journal of the neurological sciences,* 168**,** 121-126.

YUKI, N., SATO, S., TSUJI, S., HOZUMI, I. & MIYATAKE, T. 1993a. An immunologic abnormality common to Bickerstaff's brain stem encephalitis and Fisher's syndrome. *Journal of the neurological sciences,* 118**,** 83-87.

YUKI, N., SUSUKI, K., KOGA, M., NISHIMOTO, Y., ODAKA, M., HIRATA, K., TAGUCHI, K., MIYATAKE, T., FURUKAWA, K. & KOBATA, T. 2004. Carbohydrate mimicry between human ganglioside GM1 and Campylobacter jejuni lipooligosaccharide causes Guillain–Barré syndrome. *Proceedings of the National Academy of Sciences,* 101**,** 11404-11409.

YUKI, N., TAKI, T., INAGAKI, F., KASAMA, T., TAKAHASHI, M., SAITO, K., HANDA, S. & MIYATAKE, T. 1993b. A bacterium lipopolysaccharide that elicits Guillain-Barré syndrome has a GM1 ganglioside-like structure. *The Journal of experimental medicine,* 178**,** 1771-1775.

YUKI, N., WATANABE, H., NAKAJIMA, T. & SPÄTH, P. 2011. IVIG blocks complement deposition mediated by anti-GM1 antibodies in multifocal motor neuropathy. *Journal of Neurology, Neurosurgery & Psychiatry,* 82**,** 87-91.

YUKI, N., YAMADA, M., KOGA, M., ODAKA, M., SUSUKI, K., TAGAWA, Y., UEDA, S., KASAMA, T., OHNISHI, A. & HAYASHI, S. 2001. Animal model of axonal Guillain-Barré syndrome induced by sensitization with GM1 ganglioside. *Annals of neurology,* 49**,** 712-720.

YUKI, N., YOSHINO, H., SATO, S. & MIYATAKE, T. 1990. Acute axonal polyneuropathy associated with anti-GM1 antibodies following Campylobacter enteritis. *Neurology,* 40**,** 1900-1900.

YUKI, N., YOSHINO, H., SATO, S., SHINOZAWA, K. & MIYATAKE, T. 1992. Severe acute axonal form of Guillain–Barré syndrome associated with IgG anti-GD1a antibodies. *Muscle & Nerve: Official Journal of the American Association of Electrodiagnostic Medicine,* 15**,** 899-903.

ZHANG, A., DESMAZIERES, A., ZONTA, B., MELROSE, S., CAMPBELL, G., MAHAD, D., LI, Q., SHERMAN, D. L., REYNOLDS, R. & BROPHY, P. J. 2015. Neurofascin 140 is an embryonic neuronal neurofascin isoform that promotes the assembly of the node of Ranvier. *Journal of Neuroscience,* 35**,** 2246-2254.

ZHANG, C., SUSUKI, K., ZOLLINGER, D. R., DUPREE, J. L. & RASBAND, M. N. 2013. Membrane domain organization of myelinated axons requires βII spectrin. *Journal of Cell Biology,* 203**,** 437-443.